University of Alberta

Solubility and Diffusion of Vanadium Compounds and Asphaltene Aggregates

by

Greg Paul Dechaine

A thesis submitted to the Faculty of Graduate Studies and Research
in partial fulfillment of the requirements for the degree of

Doctor of Philosophy

in

Chemical Engineering

Department of Chemical and Materials Engineering

©Greg Paul Dechaine

Spring 2010

Edmonton, Alberta

Examining Committee

Murray R. Gray, Chemical and Materials Engineering, University of Alberta

John M. Shaw, Chemical and Materials Engineering, University of Alberta

Philip Y. K. Choi, Chemical and Materials Engineering, University of Alberta

Jeffrey M. Stryker, Chemistry, University of Alberta

Kevin J. Smith, Chemical and Biological Engineering, University of British Columbia

Abstract

Most crude oils contain traces of vanadyl porphyrins within their asphaltene fraction. Although these metals are only present in trace quantities, they have a significant detrimental impact on crude oil processing units; therefore, their selective removal is highly desirable. The current work studied the interaction of these vanadyl porphyrins with asphaltenes using two approaches: 1) equilibrium solubility measurements of model porphyrins and 2) membrane diffusion measurements in dilute solution.

Solubility measurements with model porphyrins showed that simple model porphyrins fit the operational definition for asphaltenes, exhibiting negligible solubility in n-heptane and orders of magnitude higher solubility in toluene. Measurement of the melting point properties enabled modeling of their solubility behaviour and showed that simple models incorporating solubility parameters (Regular solution and Flory-Huggins) were not capable of describing the observed behaviour.

Diffusion measurements were done using model vanadyl porphyrins, asphaltenes, and petroporphyrins in toluene using a stirred diffusion cell equipped with ultrafiltration membranes (Ultracel YM® and Anopore®). The pore sizes were varied between 3-20 nm to retain aggregates while allowing free molecules to diffuse. The permeate was continuously monitored using *in situ* UV/Visible spectroscopy. These experiments determined that the size of the asphaltene aggregates at 1 g/L in toluene at 25°C were in the range of 5-9 nm. An increase in temperature results in an increase in asphaltene mobility but does not reduce the size of the asphaltene structures below 5 nm. Likewise, a decrease in concentration to 0.1 g/L did not result in a decrease in size. It was also observed that the exclusion of a large portion of the total asphaltenes by pores < 5 nm

eliminates the absorbance of visible light (>600 nm) indicating the presence of Rayleigh scattering for the aggregated species in solution.

The petroporphyrins are larger than the model vanadyl porphyrins as indicated by pore hindrance effects within smaller pores. An increase in temperature results in an increase in petroporphyrin mobility, although decreasing the asphaltene concentration does not. The mobility of the vanadyl petroporphyrins is affected by the origin of the sample (Safaniya, Venezuela, Athabasca) and is therefore not universal.

Acknowledgements

I would first like to sincerely thank my supervisor and mentor, Professor Murray R. Gray. His direct input and guidance were instrumental in accomplishing this body of work. But perhaps even more important to me was his indirect guidance and mentorship, which will likely have a much longer lasting impact on my career and life and is so aptly summed up by the following quote:

> "My father didn't tell me how to live; he lived, and let me watch him do it."
> *Clarence Buddinton Kelland*

I would like to thank my lab assistant, Brenden Boddez. His contribution to this work cannot be understated as he helped keep me productive during a very busy stretch of teaching assignments. I would like to thank Tuyet Le, Dr. Xiaoli Tan, Dr. Cindy Yin, and Andree Koenig for their contributions to my work, mostly in the form of technical advice on the finer points of laboratory procedures and countless technical discussions. I would like to also thank Dr. James Dunn and Dr. Cornelia Bohne for their input and insightful technical discussions.

I would like to thank all of my family: Mom & Dad, Frank and Cathy, all of my brothers and sisters, and all of my close friends for helping me keep some semblance of sanity during the dog days of my research project and reminding me that there is more to life than work.

And finally, but most importantly, I would like to thank my beautiful wife Jen and my son Henri. Although they couldn't write my thesis for me, nor be in the lab doing my experiments, their constant support was the single biggest factor in accomplishing what I have. It was their smiles and love that kept me going and for that I am eternally grateful.

Table of Contents

List of Tables

List of Figures

Nomenclature

CHEMICAL ABBREVIATIONS

AA   Athabasca asphaltenes
APDA   Athabasca partially demetallated asphaltenes
DCM   dichloromethane
DMF   dimethyl formamide
DMSO   dimethyl sulfoxide
H_2OEP octaethylporphyrin
H_2TPP meso-tetraphenylporphyrin
IgG   Immunoglobin-G
KCl   potassium chloride
PAH   polycyclic aromatic hydrocarbon
PBP   4,4'-Bis-(2-pyren-1-yl-ethyl)-[2,2']bipyridinyl
PdTPP   palladium meso-tetraphenylporphyrin
PEG   polyethylene glycol
SA   Safaniya asphaltenes
VA   Venezuelan asphaltenes
VOBenzo   Vanadyl Benzoetioporphyrin
VODPEP   vanadyl deoxophylloerythroetioporphyrin
VOEtio   vanadyl etioporphyrin
VOOEP   vanadyl octaethylporphyrin
VOTPP   vanadyl meso-tetraphenylporphyrin
ZnTPP   zinc meso-tetraphenylporphyrin

SYMBOLS

$a_{C,A}$ absorption cross section (cm^2)
$a_{C,S}$ Rayleigh scattering cross section (cm^2)
A   surface area of membrane (cm^2)
                absorbance
$(A/\ell)_{eff}$ effective surface area to length ratio for membranes (cm)
b   pathlength (cm)
C   concentration of solute (mol/L)
ΔC_P differential heat capacity at the melting point (J/mol·K)
ΔC concentration difference (mol/L)
$\overline{D}$ integral diffusivity (cm^2/s)
D or D_{AB} diffusivity (cm^2/s)
D_e effective diffusivity with pore hindrance (cm^2/s)
D_∞ diffusivity in the absence of pore hindrance (cm^2/s)
d_S Stokes diameter (nm)

Δe	cohesive energy (J/mol)
f	fugacity (Pa)
f°	standard state fugacity (Pa)
I	light intensity
k	convective mass transfer coefficient (cm/s)
	Boltzmann's constant = 1.30866×10^{-23} (K^{-1})
ℓ	thickness of membrane (m)
MW	molecular weight (g/mol)
MWCO	nominal molecular weight cutoff
ΔH_m	enthalpy of fusion (kJ/mol)
ΔH_v	enthalpy of vaporization (kJ/mol)
N_A	molar flux of A through membrane (mol/m^2·s)
	Avogadro's number (6.0221415×10^{23} molecules/mol)
n_P	refractive index of particle
n_S	refractive index of solvent
R	ideal gas constant, 8.314 J/mol·K
r_P	pore radius (nm)
r_S	Stokes radius (nm)
S	mass solubility (g/L)
ΔS_m	entropy of fusion (J/mol·K)
t	time (s, min, h)
T	system temperature (°C or K)
T_m	melting point temperature (°C or K)
u_C	uncertainty in concentration (mol/L)
$u_{\overline{D}}$	uncertainty in the integral diffusivity (cm^2/s)
v	molar volume (m^3/mol)
V	compartment volume (mL)
w	mass concentration (mg/L)
x	mole fraction
z	position/length variable (m)

GREEK SYMBOLS

β	diffusion cell calibration constant
γ	liquid phase activity coefficient
δ	hildebrand solubility parameter (MPa$^{1/2}$)
ε	membrane porosity
	molar absorptivity or extinction coefficient (L/mol·cm)
η	dynamic viscosity (Pa·s)
θ	ratio of molecule radius to pore radius
λ	ratio of membrane volume to diffusion cell compartment volume
	wavelength of light

ξ	constant in Rayleigh scattering equation
ρ	density (kg/m^3 or kmol/m^3)
τ	membrane pore tortuosity
φ	volume fraction

SUBSCRIPTS

0	initial
1	solvent
2	solute
m	mixture
P	permeate
R	retentate
t	at time t

SUPERSCRIPTS

L	Liquid
S	Solid

Chapter 1

Introduction

Most crude oils contain traces of organometallic complexes of various forms. The most abundant and troublesome metal complexes present in the organic portions of fossil fuel deposits are vanadium and nickel. Although these metals are only present in trace quantities, they have a significant detrimental impact on conventional crude oil processing units. In particular, these metals lead to deactivation of both desulphurization and cracking catalysts[1]. For heavy oils and bitumen, the concentrations of these metals are generally much higher, which poses a problem for the economical upgrading of these feedstocks into saleable products. As well, the presence of vanadium compounds in product coke leads to the formation of vanadium pentoxide during combustion. This vanadium pentoxide product poses a toxicity concern[2-4] if emitted directly to the environment from a stack as well as a corrosion concern for turbines when used in power generation applications[5]. These problems are magnified by the fact that the world reserves of conventional light oils are dwindling and being replaced by an ever increasing amount of heavier feedstocks. Therefore, the selective removal of these metal contaminants from heavy oils and bitumen residua is highly desirable.

The current industrial technologies that are applied on a large scale for removal of vanadium fall into one of three categories: coking, de-asphalting, and catalytic hydrodemetallation. The most widely used technology is coking, which almost quantitatively captures the vanadium in the coke byproduct[6]. However, as indicated above, the presence of vanadium in this product poses problems during combustion. In cases where the byproduct coke is stockpiled this is not a concern, although stockpiling of coke represents a significant loss of product and hence a loss of a potential revenue stream. The precipitation of some or all of the asphaltene fraction from the feed also results in significant removal of vanadium[7] since the vanadium partitions preferentially

within this highly polar, highly aromatic fraction[8] (see Chapter 2 for detailed discussion). However, this precipitation process is non-selective and results in a significant loss of product in the form of a contaminated asphaltene stream. Finally, catalytic hydroprocessing selectively removes the vanadium as a vanadium sulfide deposit on the catalyst in ebullated bed reactors[9]. Although this process is the only selective process of the three, this selectivity comes at a substantial cost in catalyst as well as energy in the form of elevated temperatures, pressures, and hydrogen consumption.

The fact that the majority of the vanadium is contained within the highly aromatic, highly polar asphaltene fraction does pose some significant difficulties. The asphaltene fraction is defined as the portion of a petroleum feed that is toluene soluble and n-alkane insoluble (e.g. n-heptane). This operational definition means that asphaltenes represent a solubility class and as such are a heterogeneous mixture of molecules. As is discussed later (Chapter 2), this fraction of petroleum has been shown to associate/aggregate significantly in most (if not all) solvents. This aggregation poses some major difficulties in removing the vanadium compounds.

To this end, the long-term objective of this research is to develop new technologies for the removal of vanadium from bitumen. The first step, and the objective of this specific project, is to understand the physical form that the vanadium components are taking within the bitumen (aggregated vs. free, adsorbed vs. chemically bound in the aggregates) and to also understand under which conditions the vanadium compounds are susceptible to removal (i.e. free). This information is essential in selecting the conditions for successful separation of these components. This work is divided into two primary themes: 1) solubility behaviour of vanadyl porphyrins and 2) stability of asphaltene-porphyrin aggregates via diffusion measurements.

1.1 Solubility Behaviour Properties of Model Porphyrins

The primary goal of this portion of the work (Chapter 3) is to elucidate the equilibrium solubility behaviour of model porphyrins as well as a model asphaltene in n-heptane (standard asphaltene precipitation solvent), toluene (standard solvent in the definition of asphaltenes), dichloromethane (another reference solvent for asphaltenes) and mixtures thereof. Determining the equilibrium solubility of porphyrins in these solvents will provide a benchmark for the amount of vanadyl porphyrins that can be in

solution under ideal solvent conditions (i.e. no association or asphaltenes present). Some of this work has already been done[10] in some solvents at ambient temperature, although toluene, n-heptane, and mixtures thereof were not included in the list of solvents studied.

Also, the melting point properties of the model porphyrins and model asphaltene were also determined as part of this work in order to facilitate theoretical analysis of the aforementioned solubility data. No data exist for these pure component properties which makes any predictive modeling of their thermodynamic behavior extremely difficult.

1.2 Stability of Asphaltene-Porphyrin Aggregates via Diffusion Measurements

The primary goal of this portion of the work (Chapter 4) is to probe the association behaviour of native petroporphyrins and asphaltenes in toluene. This was done using a variation of the stirred diaphragm diffusion cell technique[11-13]. The current variation of this technique used a cell capable of accommodating standard ultrafiltration membranes of varying pore sizes. The membrane pore size was selected to exclude asphaltene-porphyrin aggregates but pass molecules that are in free solution. The spectra of the permeate was continuously monitored using an *in situ* UV/Visible spectrophotometer probe. By continuously monitoring the permeate spectrum, insight is gained as to the chemical nature of the species that are diffusing across the membrane and hence not in an aggregated state.

This apparatus was used to probe the effects of operating conditions (temperature, concentration, asphaltene origin) on the nature of the diffusing species. Analysis of the permeate species coupled with knowledge of the pore size of the membrane allows for inferences to be drawn about the physical state of the species on the retentate side of the membrane. As well, analysis of the rate of transport across the membrane allows for inferences to be drawn about the stability of the aggregated species and the rate of exchange of molecules (whether porphyrin or asphaltene) between the aggregated state and free solution. In this way, the nature and stability of the porphyrin-asphaltene aggregation interactions are elucidated further. The relevance of these results and the implications to current technology for selective removal of vanadium is discussed in Chapter 5.

Chapter 2

Current Understanding of Vanadium in Petroleum

2.1 Distribution of Vanadium Amongst Bitumen Fractions

Information on the distribution of vanadium is important in order to develop processes for the removal of vanadium. In order to properly develop processes for the removal of vanadium from bitumen, it is important to first understand within which fractions the vanadium is present. Barwise and Whitehead[14] measured the concentration of vanadium for various boiling point fractions of a Boscan crude and found that very little of the vanadium is contained in the distillates (350° - 500°C) while the majority of the vanadium is present with the residue fractions (>500°C). Reynolds[8] separated several atmospheric residua using a modified ASTM 2007 separation (saturate, aromatic, resin, asphaltene or SARA) and determined that the majority (>90% in all cases, >95% for most) of the metals were contained in the polar fractions (both resin and asphaltene), with a further majority concentrated in the asphaltenes.

Pearson and Green[15, 16] studied the distribution of vanadium and nickel compounds across acid-base-neutral (ABN) fractions of Wilmington and Mayan crudes both before and after hydrotreating. They found that for the feed materials, vanadium was present in all of the ABN fractions.

Altgelt and Boduszynski[17] measured the concentration of vanadium as a function of atmospheric equivalent boiling point (AEBP) for several heavy oil samples and showed that the concentration of vanadium increases with increasing AEBP. This corroborates the previous findings that the vanadium tends to concentrate in the residue

fraction of petroleum. Filby and Strong[18] observed that vanadium is distributed throughout all fractions of Athabasca bitumen, although the majority (76.1%) is present with the asphaltene fractions while the other 23.1% was present with the pentane soluble maltenes. Pena *et al.*[19] measured the vanadium distribution in Mexican offshore heavy crude and found as other investigators did that the majority of the vanadium was present in the asphaltene fraction of the crude.

Finally, Yang *et al.*[20] measured the distribution of vanadium compounds in various sub-fractions of Athabasca asphaltenes. Each sub-fraction was obtained by precipitation using an increasing amount of n-heptane precipitant. They found that the vanadium was distributed across all of the sub-fractions, with a slight decrease in vanadium content as the ratio of n-heptane to bitumen increased.

The fact that the majority of the vanadium is contained within the highly aromatic, highly polar asphaltene fraction does pose some significant difficulties. As is discussed later (section 2.3), this fraction of petroleum has been shown to associate/aggregate significantly in most (if not all) solvents. This aggregation poses some major difficulties in removing the organometallic components.

2.2 To be or not to be (a Porphyrin), that is the Question? The Characterization of Vanadium Compounds in Bitumen

Although heavy oils and bitumen contain significantly higher concentrations of both vanadium and nickel than conventional oils, the exact molecular form of these metals is still a point of contention among researchers within the field. A wide variety of analytical methods have been employed to attempt to determine the exact molecular form of the vanadium compounds within bitumen and their asphaltene fractions.

Beyond dispute is the fact that a fraction of the vanadium present in petroleum deposits is in the form of vanadyl porphyrins[21]. In this form, the vanadium is axially coordinated to an oxygen atom and also coordinated to the four nitrogen atoms of the porphyrin macrocycle as illustrated in Figure 2-1. These compounds are derived from naturally occurring organic matter such as chlorophyll and protoheme (also shown in Figure 2-1). The most common forms of vanadyl porphyrins identified in petroleum deposits are the Etio form (Figure 2-1b) and the DPEP form (Figure 2-1d). Other forms have been identified, such as the Rhodo or Benzo forms (VOBenzo, Figure 2-1e), although not in the same abundance. Recently, Qian *et al.*[23] successfully identified
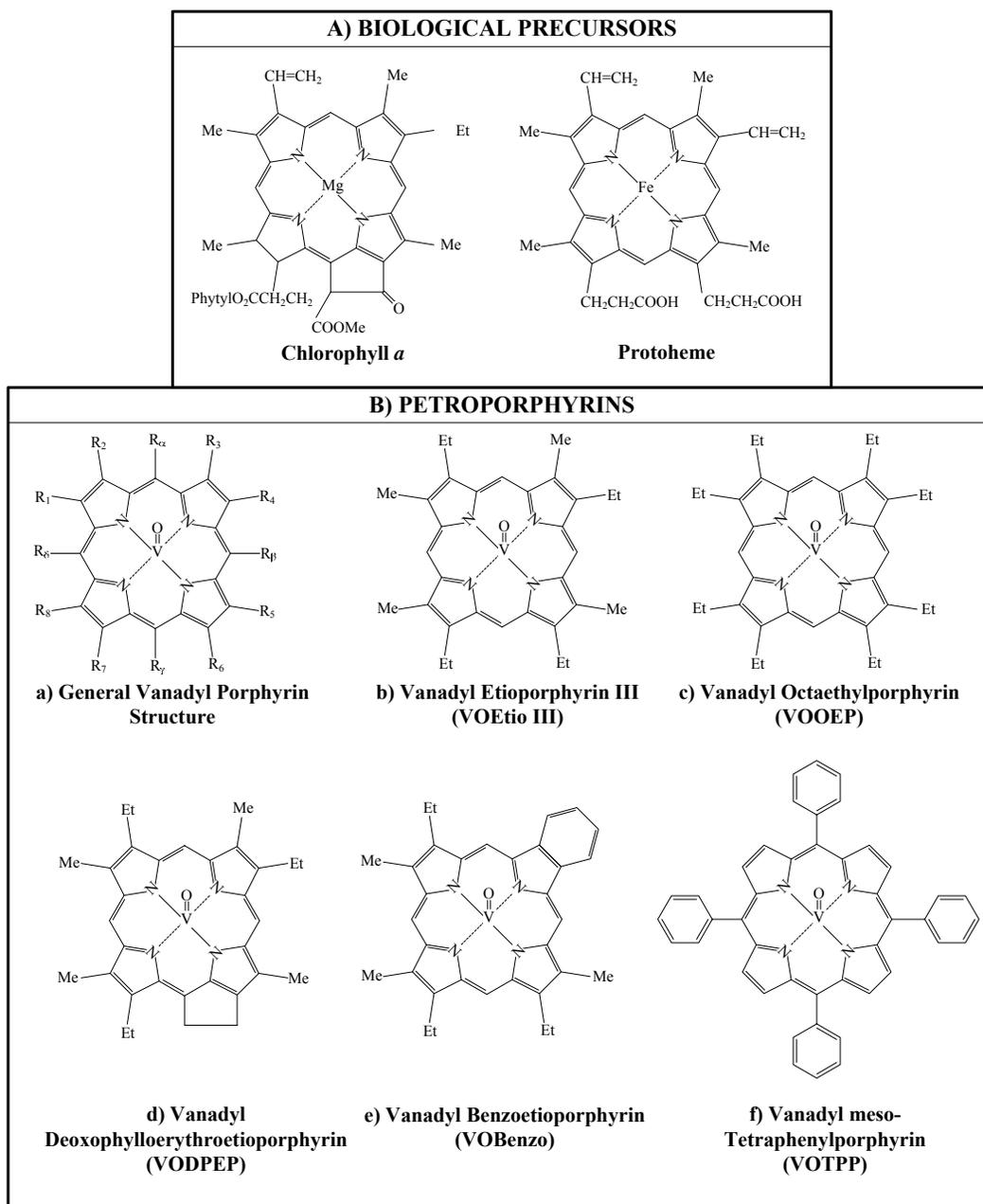
Figure 2-1: General structure and nomenclature of vanadyl porphyrins[22]

vanadyl porphyrins in un-fractionated asphaltenes for the first time, identifying VO-DPEP and VO-Benzo as the dominant types. In addition, they observed cycloalkane-substituted and sulfur-containing porphyrins. Some common vanadyl porphyrins used as model compounds include vanadyl octaethylporphyrin (VOOEP, Figure 2-1c) and vanadyl meso-tetraphenylporphyrin (VOTPP, Figure 2-1f). The nomenclature for the

various vanadyl porphyrins shown in Figure 2-1 will be used throughout the remainder of this review.

One of the primary characteristics of the porphyrin macrocycle is intense absorption of UV/Visible radiation[24]. Because of the intensity and sensitivity of the electronic absorption of UV/Visible radiation by metalloporphyrins, electronic absorption (UV/Visible) spectroscopy has been widely used in their identification and quantification in petroleum samples. However, a significant portion of the vanadium present, particularly the vanadium associated with the asphaltene fraction, does not display this characteristic absorption. If we assume that the extinction coefficient of the petroporphyrins are comparable to model compounds such as VOOEP, then the measured UV/Visible absorbance is much too small to account for the total vanadium content of crude oils [18, 25, 26]. This discrepancy led to a distinction between the porphyrin fraction of the metals, which absorbed as expected, and the "non-porphyrin" fraction which did not.

2.2.1 X-RAY ABSORPTION SPECTROSCOPY

A very powerful method available for characterizing the form of the vanadium in petroleum is the family of X-Ray absorption spectroscopies. In particular, Extended X-ray Absorption Fine Structure (EXAFS) spectroscopy and X-ray Absorption Near-Edge Structure (XANES) spectroscopy can both be used to obtain information regarding the bonding structure surrounding the vanadium atoms within the petroleum and asphaltene matrix.

Goulon *et al.*[27] measured the EXAFS/XANES spectra for Boscan asphaltenes and compared it to those for oxo-vanadyl (VO^{2+}) OEP and thio-vanadyl (VS^{2+}) OEP. As well, the asphaltene spectra was compared to the spectra of authentic petroporphyrins extracted from the original crude sample using dichloromethane + n-hexane mixtures followed by chromatographic separations on aluminum oxide and silica gel columns. Although UV/Visible Soret absorbance (see section 2.2.2) of the asphaltenes accounted for only 13 - 15% of the total vanadium present in the asphaltene fractions, the EXAFS and XANES spectra of the whole asphaltenes were almost completely superimposed on the spectra for pure VOOEP and the authentic petroporphyrins in toluene. This result indicated that although the asphaltenes show very high levels of "non-porphyrinic" vanadium (i.e. vanadium with no UV/Visible absorbance), the vanadium within this

fraction is of the oxovanadyl type coordinated to four nitrogen atoms as in the porphyrin macrocycle. The spectra for thiovanadyl OEP was also recorded and showed a significantly different spectrum than all of the samples tested, indicating that the majority of the vanadium in the asphaltene fraction is in the oxovandyl form. Goulon et al.[28] extended this analysis to Cabimas and Aramco asphaltenes and obtained similar results.

Poncet et al.[29] synthesized a VOEtio compound with the four nitrogen atoms replaced by sulphur atoms. The EXAFS spectrum of this tetra-sulphur porphyrin ligand was dramatically different than the traditional VOEtio spectra. When the spectra of VOEtio were compared to those for authentic petroporphyrins[27], the spectra were nearly identical. Therefore, the vanadium compounds present in asphaltenes are unlikely to be coordinated to four sulphur atoms.

Berthe et al.[30] applied X-Ray Photoelectron Spectroscopy (XPS or ESCA) to the analysis of vanadium compounds in heavy oils. They compared the binding energy of vanadium in both Cabimas and Boscan asphaltenes to the binding energy of vanadium in several model vanadyl compounds with different coordination environments. The binding energy of the vanadium in asphaltenes very closely matched that for the model compounds with a 4-N coordination environment. The binding energy observed with other coordination spheres (i.e. 4-O, 4-S, and various combinations of O, S, and N) showed binding energies significantly different than the asphaltene bound vanadium.

Loos et al.[31] compared the EXAFS spectra of a series of vanadyl porphyrins with varying types of substitution at the periphery of the porphyrin macrocycle: VODPEP, VOEtio, VOOEP, VOtetrabenzyl, VOtetrapyridine etc. The effect of varying the size of the substituents but not location (e.g. Etio vs. OEP) was low for the V=O and V-N bonds and became significant at distances farther from the vanadyl center. Adding meso-tetrasubstitution (e.g. meso-tetraphenylporphyrin) did have a slight impact on the magnitude of the V=O and V-N signals. These slight variations at the center of the porphyrin core arise due to slight distortions induced in the porphyrin macrocycle by the different substituents at the periphery.

Zhang and Boduszynski[32] compared the EXAFS and XANES spectra of asphaltenes to the spectra for VOTPP and several other species with vanadyl coordinated to other types of ligands (vanadyl acetylacetonate and vanadyl sulfate). They found that the vanadium is almost exclusively coordinated to 5 ligands and not 6 ligands. They also found that the XANES and EXAFS spectra of the asphaltenes very closely resembled the

spectra for VOTPP, showing the characteristics of the V=O bond and the 4 V-N bonds, thus indicating that the vanadium present in these asphaltenes are bound in a porphyrinic structure.

Miller *et al.*[33] separated Mayan n-heptane asphaltenes into two fractions by Soxhlet extraction, yielding approx. 25% of the asphaltenes as soluble in n-heptane. Characterization of these 2 fractions using Size Exclusion Chromatography (SEC), Vapor-Pressure Osmometry (VPO), and Small Angle Neutron Scattering (SANS) determined that the soluble fraction did not associate in aromatic solvents while the insoluble fraction did form aggregated structures in aromatic solvents. Therefore, the soluble fraction was named "non-colloidal" asphaltenes and the insoluble fraction "colloidal" asphaltenes. Miller *et al.*[34] then used UV/Visible and EXAFS spectroscopy to determine the form of the vanadium contained in the different fractions of this Mayan asphaltene both before and after hydrocracking. The presence of UV/Visible absorbance peaks in the electronic spectra of the non-colloidal asphaltenes indicates that the metals are present as metalloporphyrins while the colloidal asphaltenes show no such absorbances (consistent with previous investigations). This trend continued for the hydrocracked residuum as well. The EXAFS spectra for the untreated non-colloidal and colloidal asphaltenes were qualitatively similar to the spectra for pure VOTPP. The investigators fit an assumed square planar porphyrin structural model to the EXAFS data and calculated bond distances from the vanadium atom. Their values all agreed within experimental error with the bond distances calculated for VOTPP (both from the EXAFS spectra and XRD data for the model VOTPP compound[34]). In the case of the hydrocracked residuum, the form of the vanadium in the remaining asphaltenes is still that of the vanadyl ion coordinated to four nitrogen atoms in a square planar arrangement. However the form of the vanadium within the chlorobenzene insoluble solids can no longer be fit by the standard porphyrinic model. Rather, a distorted octahedron including 4 N, an O and another O or N closely approximates the measured EXAFS spectra. The presence of this additional ligand is similar to the axial ligation observed between Lewis bases and vanadyl porphyrins in solution (see §2.2.2.3). During processing at high temperatures, heteroatoms within the asphaltene matrix may chemically bind to the vacant ligand site of the vanadium center to form a new chemical bond.

The evidence obtained by the X-Ray methods is very consistent in its assertion that all of the vanadium present in petroleum and asphaltene samples is present as a vanadyl

ion coordinated to four nitrogen ligands. The V-N bond distances observed are indicative of a porphyrin like macrocycle with only slight variations observed. However, as indicated by Loos *et al.*[31], slight variations in the V-N bond distances can be induced by different peripheral substituents. Any EXAFS signal obtained for a heterogeneous sample such as asphaltenes or bitumen will undoubtedly include vanadyl porphyrins with a variety of peripheral substitutions and therefore will represent an "average" spectra. Such an average spectra would have some variation in appearance from model compounds. However, the EXAFS spectra obtained by numerous different investigators on several different asphaltene and petroleum samples all exhibited spectra which were strikingly similar to those for model vanadyl compounds in the vicinity of the vanadyl core (V=O and V-N bonds) indicating that all of the vanadium is coordinated in such an environment. The subsequent variations of the sample spectra from the model compound spectra at greater distances from the vanadyl core are indicative of variation in peripheral substitution, which is anticipated for heterogeneous samples such as asphaltenes and bitumen.

2.2.2   ELECTRONIC ABSORPTION (UV/VISIBLE) SPECTROSCOPY

As mentioned, one of the primary characteristics of the porphyrin macrocycle is intense absorption of UV/Visible radiation[24]. The most intense absorption occurs in the vicinity of 400 nm (near UV/Violet) and is termed the Soret Band. Simple free-base porphyrins also have four characteristic bands in the visible region, the location of which is dependent on the peripheral substitution of the macrocycle. In the case of the metalloporphyrins, these four visible bands are reduced to two bands, referred to as the α and β bands. Generally speaking, the Soret band is much more sensitive than the two visible bands and is the band of choice for quantitative analytical work[24], although as discussed later there are situations where the visible bands are a better choice. Because of the intensity and sensitivity of the electronic absorption of UV/Visible radiation by metalloporphyrins, electronic absorption (UV/Visible) spectroscopy has been widely used in their identification and quantitation in petroleum samples.

2.2.2.1 Effect of Solvent

The solvent system can have an impact on measured UV/Visible spectra[35-37]. Freeman *et al.*[10] used UV/Visible spectroscopy to study the absorbance of VOOEP and VOEtio-I in methylene chloride, chloroform, 1-2 dichloroethane, ethyl acetate, and

toluene. The peak height of the α band (570 nm) was used to quantify the concentration of the metalloporphyrin. Overall their analysis was very thorough and represents a good benchmark for applying UV/Visible spectroscopy to the quantitation of metalloporphyrins in solution. These investigators were capable of detecting concentrations as low as 0.1 μg/mL (~0.1 ppm), despite the reduced intensity of the α band (ε = 28,000 - 32,000 L/mol·cm) versus the Soret band (ε >350,000 L/mol·cm[38]). They also showed that baseline correction of the peak height results in significant improvements in reproducibility for metalloporphyrins. The two main results obtained in this work were to show that the solvent has an impact on the extinction coefficient of metalloporphyrins (as much as 18% variation from one solvent to the next) and to determine the solubility of these metalloporphyrins as a function of the solubility parameter of the solvent (see section 2.2.2.4).

Ferrer and Baran[39] measured the electronic absorption of VOTPP in various different solvents of different polarity and dielectric strength. The solvent had a significant impact on the shape of the spectra when it was capable of axial interaction with the vanadyl atom, such as in the case of DMSO, DMF, methanol and pyridine. No indication was given as to the impact of the different solvents on the intensity of the different peaks.

2.2.2.2 Effect of Peripheral Substitution

Freeman et al.[40] identified the peak locations for various vanadyl porphyrins in dichloromethane solvent using third derivative UV/Visible spectroscopy, and some of the results are shown in Table 2-1. Foster et al.[38] obtained the extinction coefficients and wavelengths for the Soret bands of various vanadyl porphyrins in toluene as shown in Table 2-2. Cantú et al.[41] determined the location of the three peaks for VODPEP in

Table 2-1: Location of absorption maxima for various vanadyl porphyrins in dichloromethane[40]

Vanadyl Porphyrin	Wavelength @ Maximum (nm)		
	Soret Band	β Band	α Band
No substitution	399.4	523.8	559.4
Etio I	406.6	532.8	570.7
Octaethyl	407.3	533.2	570.9
DPEP	410.5	533.3	573.0
Benzo	414.0	544.7	578.7

Table 2-2: Location and extinction coefficient
for the Soret band of various vanadyl porphyrins
in toluene[38]

Vanadyl Porphyrin	Soret Band Wavelength (nm)	Extinction Coefficient $(mM^{-1}cm^{-1})$
Etio I	407	400
DMEP	407	390
OEP	407	364
TPP	424	528

dichloromethane as 410.5 nm (Soret peak, $\varepsilon = 128{,}000$), 533.6 nm (β peak, $\varepsilon = 7{,}060$), and 574.5 nm (α peak, $\varepsilon = 8{,}720$). The results in Table 2-1, Table 2-2, and of Cantú *et al.* indicate that the peripheral substitution of the porphyrin macrocycle can have an impact on the location of the UV/Visible peaks. When the peripheral substituents are in the same location (i.e. OEP, Etio, DMEP), the locations of the Soret and visible peaks remain relatively fixed. However, when the peripheral substituents occupy different locations (such as the meso positions in the case of TPP), the Soret peak is shifted to a higher wavelength (i.e. a red shift). Also, when the substituents begin to exhibit more cyclic (DPEP) and aromatic (Benzo) characteristics, red shifts also occur. Trofimenko *et al.*[42] observed minor shifts in the locations of the absorption peaks for the different isomers of Etioporphyrin (free base form) in benzene and primary alcohols, although the qualitative shape of the spectra remained unchanged. Therefore, even small changes in peripheral substitution (such as isomerization) can impact the electronic absorption characteristics of the porphyrin.

Also worthy of noting is the effect of substitution on the magnitude of the absorption peaks. The extinction coefficient measured by Cantú *et al.*[41] for VODPEP is ~4 times lower than that obtained by Foster *et al.*[38] for VOEtio. Therefore, if the extinction coefficient for VOEtio is used for quantitative studies of a mixture of VOEtio and VODPEP, the total concentration of vanadyl porphyrins will be underestimated.

Peripheral substitution of the porphyrin macrocycle affects the location of the absorption peaks of the electronic spectra since they will impact the electronic structure of the porphyrin macrocycle[43]. The electronic absorption of UV/visible radiation by porphyrins is attributed to π-π* transitions[43-45] and therefore anything that affects the electron structure will have an affect on the location and intensity of the absorption. The

possibility of n-π^* transitions are not considered likely because of the symmetry of the n orbitals and because of the anti-symmetry of the π^* orbitals relative to the plane of the porphyrin macrocycle[44]. A more extensive discussion on the effect of peripheral substituents on the electronic absorption of the porphyrin macrocycle using the so-called "Mutual Atomic Effect" was presented by Berezin[46]. At this point, it is concluded that differences in peripheral substitution of the porphyrin macrocycle will have an impact on both the location and magnitude of electronic absorption peaks and must be accounted for when applying UV/Visible spectroscopy for quantitation.

2.2.2.3 Effect of Coordination and Association

The occurrence of coordination or dimerization/aggregation can alter the UV/Visible spectra of metalloporphyrins[47]. Walker *et al.*[48] monitored the UV/Visible spectra of substituted VOTPP in toluene in the presence of small amounts of piperidine. The addition of piperidine resulted in the formation of a porphyrin-piperidine adduct, causing a red shift of 12 nm for the Soret band with the extinction coefficient remaining unchanged.

Bonnett *et al.*[49] used UV/Visible spectroscopy to monitor the interaction of various basic solvents with VOOEP. They noted a change in the Soret and visible bands when strongly coordinating solvents, in particular primary amines such as n-butylamine, were used. They propose that the primary amines can more readily coordinate to the vanadyl species because of reduced steric hindrance at the final remaining vanadyl coordination site. The importance of steric hindrance on additional ligation of the vanadium atom arises because the vanadium atom lies above the plane of the 4 nitrogen atoms by 0.5 Å[50]. The prospect ligand must be capable of penetrating the micro well created by the elevated vanadium atom in order to create the coordinating bond. Shelnutt *et al.*[51] observed similar tendencies and found that pyrrolidine coordinated much more readily with VOOEP than did pyridine, and this coordination caused a red shift in the Soret band from 407 nm to 425 nm.

Bencosme *et al.*[52] found similar steric effects when studying the axial ligation of various different Lewis bases with VOTPP in dichloromethane. They found that the ability of the different Lewis bases to coordinate with the vanadyl structure followed the order nitrogenated > oxygenated ≥ sulfonated. They also found that the ability of a Lewis base to form an axial ligand with the out of plane vanadyl ion was related to steric factors

(i.e. n-butylamine > tert-butyl amine > diethylamine >> triethylamine). Ozawa and Hanaki[53] compared the ligation tendency of three different oxo-tetraphenyl porphyrins: oxo-vanadium, oxo-chromium, and oxo-titanium. They found that the tendency of these metals to coordinate with Lewis bases was directly related to the distance of the metal atom to the nitrogen basal plane. Oxo-titanium, which has the largest distance showed little or no tendency to coordinate with Lewis bases while oxo-chromium, with the shortest distance, showed the highest tendency to coordinate. The fact that the distance to the porphyrin basal plane dictates the tendency to coordinate would indicate that the coordination occurs axially with the metal centre. Ferrer and Baran[39] observed a similar phenomenon where solvents capable of axial interactions (DMSO, DMF, methanol and pyridine) produced a significant impact on the shape of the spectra.

This tendency of the metal porphyrins to coordinate with various Lewis base heteroatoms could explain their tendency to associate with the asphaltenes in petroleum samples. The asphaltenes are known to have a higher proportion of the total heteroatom (N, O, and S) content of the petroleum. The metalloporphyrins contained within the asphaltene fraction are likely coordinated with heteroatoms within the asphaltene molecules. As indicated above, however, steric hindrance plays a major role in this additional association at the vanadyl center and therefore only those heteroatoms which are present at a pendant position within the asphaltene molecule will be accessible to such a coordination bond. This type of ligand formation would also help to explain the absence of the Soret and visible bands at the usual locations for vanadyl porphyrins. As was observed for model systems, the formation of an additional ligand bond with the vanadium center causes a significant shift in the location of the absorption bands, which may or may not cause them to pass undetected.

The steric hindrance discussed above also reduces the likelihood of dimerization of vanadyl porphyrins[54]. Symmetrical porphyrins such as VOTPP do not form significant amounts of a dimeric species[54] while unsymmetrical porphyrins show a higher tendency to aggregate due to the ability to form head-to-toe species. Although the tendency of vanadyl porphyrins to self-dimerize is well documented[55-58], the conditions generally present in bitumen and asphaltene solutions should not result in any significant self-dimerization[47, 55].

2.2.2.4 UV/Visible Spectroscopy of Authentic Petroporphyrins

A number of authors have attempted to quantify metalloporphyrins in crude oil by using the extinction coefficients of isolated vanadyl compounds or model compounds. Groennings[59] treated crude oil with inorganic acids and organic solvents to isolate a fraction rich in de-metallated porphyrins, which were then used to calibrate the analysis of the whole crude oil. Similar work by Sugihara and Bean[26], Biggs *et al.*[60], Reynolds *et al.*[61], Reynolds *et al.*[62] and Filby and Strong[18] found that the absorbance of the Soret band was 40-50% of the expected value based on model compounds. In each case, this calculation was based on the extinction coefficient of isolated porphyrin compounds in solution.

Van Berkel and Filby[63], and later Pearson and Green[15, 16], studied the effect of thermal processing and hydrotreating, respectively, on the distribution of vanadium and nickel compounds. They found that hydrotreating the crude oils resulted in an increase in the porphyrinic vanadium content for certain fractions. The increase is attributed to one of two possible causes:

1. Hydrotreating leads to a change in the peripheral substitution of highly substituted porphyrins. For porphyrins with peripheral substitution other than octaethyl, etio, or tetraphenyl, it is possible that the absorbance occurs at a wavelength other than that being scanned for in the visible region. During hydrotreating, these large peripheral groups are removed from the porphyrin backbone, causing a shift in the absorbance wavelength to the region being monitored resulting in an apparent increase in porphyrin concentration

2. Large polar asphaltene molecules, which retain metalloporphyrin molecules via molecular association, are converted during hydrotreating thus releasing metalloporphyrins. This type of molecular association is capable of changing the electronic absorption wavelength of a species and hence would shift the wavelength outside of the region being monitored.

Further work by these investigators[64] with other vacuum residue fractions failed to reproduce this same appearance of porphyrins.

Freeman and O'Haver[65] applied derivative UV/Visible spectroscopy to quantify the concentration of metalloporphyrins in de-asphalted bitumen samples. These investigators found significant absorbance by non-porphyrinic compounds in the region of the Soret

Band and therefore had to resort to using the α band. In order to counteract the reduced sensitivity of this peak, data smoothing and second derivative algorithms were applied to the spectrum. These data analysis algorithms serve to improve the signal-to-noise ratio, which is a major difficulty when dealing with complex mixtures where significant background absorbance is present. In the end, they concluded that the optimal algorithm was a second derivative, 3 point sliding average algorithm. Freeman *et al.*[40] extended this analysis further by applying third derivative UV/Visible spectroscopy for the qualitative identification of metalloporphyrins. The use of the third derivative of the absorbance allows for a much more precise identification of the exact wavelength (to within ±0.1 nm) of an absorbance maximum since the third derivative is characterized by a steep zero crossing at an absorbance peak. This method allowed the investigators to differentiate a number of different metalloporphyrins on the basis of the UV/Visible spectra alone. Unfortunately, this method requires that the petroporphyrins be separated and/or purified prior to analysis. Complex bitumen mixtures cannot be analyzed directly to identify the different porphyrins because of significant spectral interferences.

Unfortunately, the majority of the UV/Visible methods employed for the quantitation of metalloporphyrins in bitumen samples rely on chemical extraction of these species from the bitumen sample. As discussed in section 2.3.3, it is unlikely that chemical extraction methods would be capable of completely extracting all of the metalloporphyrins present in a bitumen sample. This is further compounded by the fact that asphaltenes are suspected to form aggregated colloidal structures in most organic solvents, which could further deter the extraction of the metalloporphyrins from the asphaltene phase.

Another major barrier to effective quantitation of vanadyl porphyrins by UV/Visible spectroscopy is the significant absorption of UV/Visible radiation by polycyclic aromatic hydrocarbons (PAH). As the number of aromatic centers increases and as the degree of conjugation increases, the absorbance peak shifts to higher wavelengths due to a higher electron density[66]. Halasinski *et al.*[67] recorded the UV/Visible spectra of a homologous series of PAHs: perylene, terrylene, and quaterrylene and observed absorption peaks in the region of the vanadyl porphyrin bands (both Soret and visible) for all three molecules. Since asphaltenes are large PAHs with sizes resembling these homologues, it is likely that asphaltene molecules will absorb radiation in the vicinity of the vanadyl porphyrin peaks and could easily mask their

presence. Yokota *et al.*[68] used UV/Visible spectroscopy to monitor the absorption spectra of Athabasca asphaltenes as well as various fractions of said asphaltenes separated by SEC. The whole asphaltenes and subsequent subfractions exhibited large structureless absorption bands covering the range 270 – 450 nm, which encompasses the Soret band of the vanadyl porphyrins. This significant interference from the asphaltenes poses significant problems for the quantitation of vanadyl porphyrins since the Soret peak in most cases is virtually invisible.

Antipenko and Zemtseva[69] studied the impact of various chemical species on the electronic spectra of vanadyl porphyrins. A native Russian oil was separated into numerous different representative fractions including the usual SARA fractions (saturates+aromatics, asphaltenes, and resins), nitrogen base fractions, sulphur fractions, naphthenic acids, and other functional groupings. In the case of VOEtio, significant changes in the magnitude of the Soret band were observed in the presence of various pure compounds and oil fractions. In particular, the nitrogen bases and the saturates+aromatics extracted from the native oil sample decreased the intensity of the Soret band by over 30%, while some pure PAH compounds, in particular phenanthrene and anthracene, also decreased the intensity of the Soret band by 30 – 40%. Carbazole, a model aromatic nitrogen compound, also decreased the intensity of the Soret band by over 40%. Therefore, the lack of a vanadyl porphyrin Soret band in asphaltenes could also be attributed to chemical interactions between the asphaltene molecules and the vanadyl porphyrins.

2.2.3   OTHER ANALYTICAL TECHNIQUES

2.2.3.1 Electron Paramagnetic Resonance (EPR) Spectroscopy

Electron Paramagnetic Resonance spectroscopy (EPR), also known as Electron Spin Resonance spectroscopy (ESR), measures the resonant absorption of microwave radiation in the presence of a static magnetic field. The resonant absorption of the radiation in the presence of the magnetic field occurs when there is a magnetic dipole created by the net spin or net orbital angular momentum of an unpaired electron[70]. Such a paramagnetic resonance arises in a quadrivalent vanadium atom (V^{4+}) as a result of an unpaired electron present in a 3d orbital.

Saraceno *et al.*[71] compared the derivative EPR spectra of pure VOEtio to that for a residue fraction with similar concentration of vanadium and found a peak at the same

characteristic location for vanadium. The height of this vanadium peak varied linearly with total concentration with a slope closely matching the slope of a calibration line obtained using pure VOEtio dissolved in a vanadium free heavy oil distillate. The linearity of the peak height vs. concentration plots and the similarity of the curve to that for pure VOEtio indicate that the vanadium species in all of the petroleum samples studied were in the +4 valence state (i.e. V^{4+} as in VO^{2+}).

Tynan and Yen[72] compared the type and shape of EPR spectra obtained for both authentic vanadium compounds in asphaltenes as well as for model vanadium compounds added to a vanadium free asphaltene in various solvents. For non-aggregated vanadium complexes (referred to as free), the EPR spectra is said to be "isotropic" and displays a characteristic derivative spectrum, while an aggregated vanadium compound displays a characteristic "anisotropic" spectrum. When asphaltenes were added to a model vanadyl phthalocyanine complex, the EPR spectra shifted from an isotropic to an anisotropic form indicating association of the vanadium complex with the asphaltenes. As the concentration of asphaltenes increased, so did the degree of anisotropy. A similar effect was observed with the authentic vanadium compounds present in an asphaltene sample. When the temperature of the solution was varied at a fixed asphaltene concentration, the degree of anisotropy decreased with increasing temperature. Using the variation of EPR derivative peak height with temperature, the investigators calculated a vanadium-asphaltene energy of association of 14.3 kcal/mol, regardless of the solvent used. Of the solvents studied (Diphenylmethane, Benzyl n-butyl ether, 1-Ethylnaphthalene, benzene, nitrobenzene, pyridine, and tetrahydrofuran), tetrahydrofuran produced the most isotropic (free) vanadium. In a similar study, Selyutin et al.[73] used ESR spectroscopy to monitor the dimerization of pure VOOEP. They found that although at low temperatures (77 K) VOOEP showed dimerization tendencies, at 20°C in solution the dimeric species disappeared.

Many attempts have been made in the past to use EPR spectra to determine the bonding structure of the vanadium species present in heavy oil and asphaltene samples. Yen et al.[74] combined EPR and UV/Visible spectroscopy and concluded that some of the vanadium was present as non-porphyrins. Dickson et al.[75] and Dickson and Petrakis[76] compared the spin Hamiltonian parameters of native vanadium complexes and pure vanadium complexes[75] obtained by fitting EPR spectra and concluded that a large portion of the vanadium compounds in the oil samples were present with ligand

structures other than the 4 nitrogen coordination sphere. Reynolds *et al.*[77, 78] also concluded on the basis of EPR spin Hamiltonian parameters that the vanadium was present in non-porphyrin coordination, although they were unable to pinpoint an exact coordination type. EPR spin Hamiltonian parameters obtained by Graham[79] for Boscan and Circle Cliffs asphaltenes were similar to VOOEP. Finally, Reynolds[8] and Reynolds *et al.*[80] determined EPR spin Hamiltonian parameters for resins and asphaltene fractions and once again concluded on the basis of these parameters that there are non-porphyrin vanadium coordination environments.

The majority of the work done using spin Hamiltonian parameters (the g-factor, g_o, and the hyperfine splitting constant, A_o) reports and differentiates these values to an extremely high precision (5 significant figures for g_o). Very few analytical techniques are capable of this level of precision, particularly when non-linear regression of a highly complex model such as the spin Hamiltonian is used. Also, bitumen and asphaltene samples are heterogeneous and therefore the calculated values for g_o are average values for the entire sample. This level of precision is probably not justified. Even at a precision of 0.1%, which for most analytical techniques would be deemed excellent, the isotropic g_o value would only be accurate to the 3rd decimal place and would not reveal any significant differences. Malhotra & Buckmaster[81] used high precision 34 GHz EPR spectroscopy along with statistical analysis of variance methods to conclude that the spin Hamiltonian parameters derived from EPR spectra are not capable of differentiating between different coordination structures around the vanadyl ion. This implies that EPR spectroscopy is not a suitable tool for identifying the ligand structure of vanadium in heavy oil, bitumen and asphaltene samples. This method has, however, given us strong proof that the vast majority (if not all) of the vanadium present in petroleum samples is in the form of vanadyl ions. As well, EPR spectroscopy is of value in assessing the aggregation characteristics of the vanadium complexes as shown in the work by Tynan and Yen[72] and Selyutin *et al.*[73].

2.2.3.2 Size Exclusion Chromatography (SEC) with Element Specific Detection

One general class of methods used to study the form of vanadium compounds involves the use of Size Exclusion Chromatography (SEC, also known as Gel Permeation Chromatography or GPC). The basic premise of SEC is that the difference in retention time of different compounds within the column is brought about exclusively on the basis of molecular size. Small molecules penetrate the porous network of the column packing

and are retained in the column for a longer period of time. Larger molecules do not penetrate as extensively and are eluted from the column sooner. In this manner, different molecules are separated on the basis of their size and hence the name size exclusion chromatography. One of the primary assumptions in the application of SEC is that there are no chemical interactions occurring between the sample and the column packing. In order for the method to be valid such interactions must be avoided or minimized [82, 83].

A number of studies have combined SEC of asphaltenes with analysis of fractions for metal content, including Fish and Komlenic[84], Fish et al.[85], Biggs et al.[60, 86], Reynolds et al.[61], Fish et al.[87], Reynolds and Biggs[88], Sundararaman et al.[89], and Reynolds et al.[62] . Unfortunately, the SEC separation of a polydisperse mixture like asphaltenes is not selective for molecular size (Davison et al.[90]). The tendency for asphaltenes to associate in solution changes their apparent size significantly. In addition, asphaltene fractions have a tendency to be adsorbed on the column (chemical interaction), and the elution order of polar fractions is significantly altered by choice of solvent. Both of these effects can shift the apparent size of the eluting material. As well, the response of asphalt samples in an SEC experiment deviates significantly from the response of polystyrene standards to a similar experimental setup[90]. The use of polystyrene standards for calibrating the MW vs. elution volume response of the experiment is not valid for asphaltene samples. These problems make the method invalid for drawing conclusions regarding the size and ligand structure of the vanadium compounds present in the asphaltene fractions of crude oil samples.

2.2.3.3 Interaction of Radioactive Tracers with Asphaltenes

Nguyen and Filby[91] used nickel complexes containing radioactive nickel isotopes (^{63}Ni) to monitor the interaction of model nickel compounds (both porphyrin and non-porphyrin) with Athabasca asphaltenes. When added to a solution of asphaltenes, the model nickel compounds adsorbed/interacted with the asphaltenes. It was not clear whether this interaction was due to association (i.e. chemisorption) or due to ligand interactions between nickel and functional groups within the asphaltene molecules. Attempts to co-precipitate the model compounds with the asphaltenes found that changing the precipitation solvent had little or no impact on the amount of model nickel compounds present in the precipitated asphaltenes. Once again, they were unable to determine whether the asphaltene-Ni interaction was by a π-π interaction or by axial bonding of asphaltene functional groups and the Ni^{2+} ion. Unfortunately, this work did

not investigate the asphaltene-nickel interaction in stronger asphaltene solvents where the asphaltene species are not present as precipitate but rather as smaller colloidal particles.

2.2.3.4 Mass Spectrometry

Mass spectrometry has been applied by numerous investigators to identify the molecular forms of vanadyl porphyrins, as well as the distribution of the various molecular forms in crude oil samples[92-98]. Mass spectrometry is a key analytical method for qualitatively identifying the different porphyrinic forms identified in Figure 2-1.

Beato et al.[99] used electron ionization tandem mass spectrometry (EIMS/MS) to study vanadium compounds in a New Albany bitumen and its pyrolysate using the same separation method as Van Berkel and Filby[63]. Their results indicated that both the bitumen and pyrolysate contained vanadyl porphyrins of similar structure. They also concluded that the appearance of porphyrins in pyrolysate is due to an enhanced solubilisation/desorption mechanism and not due to C-C bond scission indicating that metalloporphyrins are held in the asphaltene/kerogen matrix by association rather than chemically bound.

Grigsby and Green[100] used low-eV High Resolution mass spectrometry (HR/MS) to characterize the non-porphyrinic vanadium present in the >700°C resid fraction of a Cerro-Negro crude. They identified several porphyrinic vanadyl structures within the non-UV absorbing fraction. They explained the discrepancy by identifying several cycloalkyl and aromatic forms of vanadyl porphyrins which would exhibit much lower response in the visible region thus resulting in an underestimation of the porphyrin content. They were also able to identify homologs of the etio and DPEP forms containing additional carbons attached as peripheral substituents.

Rodgers et al.[101] used electrospray ionization Fourier transform ion cyclotron resonance mass spectrometry (ESI-FT-ICR-MS) to characterize the petroporphyrin fractions of a Cerro Negro crude oil extracted using chromatography and solvent based extraction methods. They identified homologs of the VOEtio and VODPEP forms containing additional carbons indicating variation in peripheral substitutions. Their analysis also indicated the presence of dimers of vanadyl porphyrins. However, their analysis requires the addition of ionic species (H^+ and Na^+) to charge the analytes for analysis. The presence of ionic species, and in particular the intentional charging of the porphyrin, can have a significant impact on the dimerization of the porphyrin

monomers[56, 58]. Also, methanol was used to produce the analyte solutions. Methanol has already been identified as a poor solvent for vanadyl porphyrins with a maximum solubility of 3 μg/mL[10]. The solutions used by Rodgers *et al.*[101] are very close to this solubility limit which could result in the formation of aggregates and/or crystals as a result of exceeding saturation in the solvent.

Generally speaking, the samples analyzed with mass spectrometry are chemical extracts of the petroleum rather than the whole sample or even an asphaltene sample. These methods cannot, therefore, help elucidate the form of the vanadyl porphyrins contained with the asphaltene fraction. However, Qian *et al.*[23] analyzed a whole asphaltene sample using atmospheric pressure photoionization (APPI) FT-ICR-MS. Not only did they identify homologs of several of the expected forms of vanadyl porphyrins (VODPEP, VORhodo, and VOEtio), they also identified several sulphur containing vanadyl porphyrins. This report is the first evidence of sulphur species directly attached to vanadyl porphyrins. This is also added proof of the complex nature of the molecular environment surrounding vanadium atoms within the asphaltene fraction.

2.2.4 FINAL ASSESSMENT

Although a number of methods have been used to determine the chemical structures of the organo-vanadium compounds present in crude oils, examination of the primary chemical environment of the vanadium by x-ray spectroscopies (EXAFS, XANES, and XPS) gives a consistent result; the nearest neighbor atoms surrounding the vanadium atom are a single oxygen atom (making a vanadyl ion) and four nitrogen atoms in a square pyramidal structure corresponding to the porphyrin macrocycle. The agreement between the spectra for the model vanadyl porphyrins and the non-absorbing petroporphyrins is excellent.

The majority of studies that identified vanadyl porphyrins from crude oil relied on solvent extracts that did not include all of the vanadium present in the original crude oil; therefore, they provide at best a partial picture of the secondary structure of the vanadium species. By analyzing unfractioned asphaltene, Qian *et al.*[23] were able to indentify elemental compositions consistent with homologous series with one or more fused benzene rings, one or more fused cycloalkyl rings, and vanadyl porphyrins with sulfur. This result indicates a much more diverse range of chemical structures for vanadium than previous studies. The peripheral substitution of the porphyrin ring, coupled with

aggregation with other asphaltenic species, would substantially change the intensity and position of the Soret band.

The evidence suggests, therefore, that the UV-visible studies of porphyrin concentrations in crude oil suffered from overly simplistic assumptions. By ignoring the effect of molecular association in solution and peripheral substitution on the extinction coefficients at a given wavelength, they likely reached a false conclusion, and attempted to define a "non-porphyrin" fraction of vanadium. The evidence indicates that all of the vanadium is in vanadyl porphyrins, although the substitution on the porphyrin ring may be highly variable and extensive.

2.3 Aggregation and Solubility Characteristics of Asphaltenes and Metalloporphyrins

Asphaltenes can adopt a colloidal character in solution, based on various analytical methods including small angle neutron scattering (SANS)[102-104], small angle x-ray scattering (SAXS)[105-108], vapor phase osmometry (VPO)[109-113], and to a lesser extent electron paramagnetic resonance (EPR)[114]. This tendency to aggregate and precipitate in n-alkane solvents (primarily n-pentane or n-heptane) provides the operational definition for asphaltenes. The molecular aggregation of asphaltenes has been detected at surprisingly high temperatures, suggesting that the aggregates may be remarkably stable in the heavy oil or bitumen[102, 115]. As mentioned previously, the majority of the vanadyl porphyrins are concentrated in this asphaltene fraction. This partitioning of the vanadyl compounds in the asphaltene fraction could be attributed to their low solubility in most (if not all) solvents or it could be because the porphyrins are molecularly associated to asphaltene molecules.

2.3.1 SOLUBILITY MODELING OF ASPHALTENE PRECIPITATION

The lack of solubility of porphyrins and their various derivatives in organic solvents has been well documented[116-121]. As discussed in Section 2.2.2.4 (Figure 2-2), Freeman *et al.*[10] determined the solubility of VOOEP and VOEtio in various solvents and found them to be on the order of 10^{-5} mol/L. The type and location of peripheral substituents does have an impact on the solubility of the porphyrin macrocycle. Trofimenko *et al.*[42] showed that the solubility of 4 isomers of Etioporphyrin (free base form) can vary by as much as an order of magnitude due to changes in the crystal packing structure of the

different isomers. Salcedo *et al.*[122] applied DFT theory to investigate the effect of peripheral substitution on solubility of vanadyl porphyrins and found that the addition of peripheral substituents leads to different degrees of out of plane distortion of the porphyrin macrocycle, which in turn leads to variations in the dipole moments of the metalloporphyrin. According to their model, this porphyrin dipole moment, coupled with the solvent dipole moment that dictates the solubility. Many solvents including aromatics, ketones, alcohols, amines etc. have been tested with little or no success for complete dissolution of porphyrins and metalloporphyrins. Therefore, the presence of the vanadyl porphyrins with the insoluble asphaltene fraction could easily be as a result of a co-precipitation mechanism rather than a molecular association mechanism

Two models have been proposed to explain the role of the resins in stabilizing the asphaltene fraction within the oil. The first model proposes that the resins associate at the periphery of an insoluble colloidal particle of asphaltene molecules, forming a steric barrier preventing further aggregation[123]. Upon addition of a low polarity, low solubility-parameter solvent, these resin molecules are dissolved, thus exposing the insoluble asphaltene core and leading to flocculation and precipitation. Subsequent authors proposed smaller clusters of asphaltenes, and suggested an analogy to surfactant micelles[124], eventually reaching the limit suggested by Speight [125] that only a single asphaltene molecule is surrounded by resins. In essence, the resins behave as a surfactant for the asphaltene molecules. Recent work by Andersen and co-workers [126-131] using microcalorimetry showed that the titration of asphaltenes with toluene does not fit the behaviour of a micelle-like system (i.e. critical micelle concentration). Rather, the asphaltene-toluene system fits the behaviour of a step-wise association with aggregates of variable size similar to the dye Rhodamine 6G[130]. Therefore, the analogy of asphaltene aggregates to micelles is false and the use of the term "micelle" in conjunction with asphaltene behavior is not recommended. If this model is accurate, then the metalloporphyrin molecules are not likely to associate with the asphaltenes within the crude oil. Rather, the highly aromatic vanadyl porphyrins are also bound to resins in a similar manner. Upon addition of the solvent and solvation of the resins, the metalloporphyrins are released and precipitate with the asphaltenes.

The second model adopts a thermodynamic approach to explain the stabilizing effect of the resins. This model attributes the destabilization of the asphaltene micelles to a decrease in the solvent power of the medium towards the asphaltene monomers. As the

solvent power of the surrounding medium decreases, the solubility of the asphaltene monomers decreases up to a point where these monomers are no longer fully soluble. Because the size of the asphaltene aggregates is dependent on temperature, concentration, and solvent identity, the aggregation mechanism is thought to be reversible and hence governed by thermodynamic equilibrium. If this model is correct, then the high concentration of metalloporphyrins in the asphaltene fraction is controlled by the solubility (or lack thereof) of the metalloporphyrins in the solvent medium and not by association of the metalloporphyrin molecules with the asphaltenes.

Yarranton and co workers have developed two types of models, one for molecular association, to explain apparent molecular weight measurements. Agrawala and Yarranton[112] proposed that the aggregation of the asphaltene molecules occurs via a pseudo-polymerization mechanism whereby the aggregation of the asphaltene molecules occurs via active hetero-atom centers within the asphaltene molecule. Resins act as a terminator in the process since they contain little or no active hetero-atomic centers. In the presence of a significant amount of resins, little or no association of asphaltenes occurs. This idea was extended to modeling of precipitation. Yarranton *et al.*[112, 132-135] successfully modeled the precipitation behavior of asphaltenes in various solvents using a modification of the Flory-Huggins regular solution model initially developed by Cimino *et al.*[136, 137]. The asphaltene fraction is assumed to consist of monomeric asphaltene species which aggregate to form larger particles similar to polymerization. The pure component properties of the asphaltenic fraction (i.e. solubility parameter, density, molar mass etc.) are then modeled using various fitted distribution functions incorporating this step-wise association model. The model parameters were tuned to fit the experimental density and precipitation data.

One of the main drawbacks of the regular solution model of Yarranton *et al.* is that the results are highly sensitive to the values of the solubility parameters of the various components. Unfortunately, these values for asphaltenes and various other SARA fractions are not well known. In an effort to overcome this shortcoming, Akbarzadeh *et al.*[138] applied the SRK EOS to predict the heat of vaporization and density, and in turn the solubility parameter, of SARA fractions. Their method relied on correlations obtained with model PAHs to predict the pure component properties of SARA fractions based on molecular weight. The model was tuned to experimental density and precipitation data. This approach was taken one step further by Sabbagh *et al.*[139], whom

modeled asphaltene precipitation as a liquid-liquid equilibrium using the Peng-Robinson EOS. Their methodology was similar to Akbarzadeh et al.[138] and produced similar results.

The fact that relatively simple thermodynamic theories such as the regular solution model and cubic EOSs can successfully predict the solid-liquid equilibrium behavior of a complex mixture of asphaltenes lends credibility to the claim that the aggregation of asphaltenes is indeed a thermodynamically controlled equilibrium process. The use of property distributions rather than discrete properties to describe the entire asphaltene fraction is appropriate since this fraction is composed of a large number of species and hence would exhibit a range of properties. However, all of these models require fitting of experimental fractionation (SARA) and precipitation data and therefore are tuned to the specific system being modeled. This requires a greater amount of experimental data to ensure reasonable accuracy and therefore is not entirely predictive. More advanced molecular association models (e.g. SAFT) have been proposed [140, 141] to model the asphaltene precipitation phenomenon with moderate success, although the complexity of these models makes them somewhat less attractive.

In light of the success of these Flory-Huggins regular solution models for predicting the extent of asphaltene precipitation, this same model could also successfully model the precipitation behavior of the vanadyl porphyrins in similar solutions. In fact, the work of Freeman and O'Haver[10] indicates that the solubility parameter of the solvent does play a significant role in the solubility of vanadyl porphyrins.

2.3.2 PROPOSED MECHANISMS FOR ASPHALTENE AGGREGATION

Akbarzadeh et al.[142] investigated the association behavior of model pyrene compounds in solution with different types of polar substituents. They found that the non-polar poly-aromatic compounds pyrene and dipirenyl decane did not associate in o-dichlorobenzene. When ketone and hydroxyl functional groups were added to the molecules, significant association took place. This result supported the contention that the associations in asphaltene molecules occurs via hetero-atomic sites rather than only simple π interactions. Rakotondradany et al.[143] performed similar tests using symmetric, non-polar alkyl substituted hexabenzocoronene (HBC) and observed significant association in toluene. Molecular simulations indicated that the most stable association configurations occurred as a result of π stacking of the polyaromatic core. Tan et al.[144,

[145] demonstrated that multiple interactions, including π-bonding between PAH groups, polar nitrogen groups, and hydrogen bonds in a single molecule could combine to give association in solution when each single interaction was too weak on its own.

Vanadium compounds have been implicated in schemes for aggregation of asphaltenes since Yen *et al.*[72, 74]. Vanadyl porphyrins are capable of forming additional ligand structures with hetero-atoms and vanadyl porphyrins have a flat, aromatic core rich in π electrons, very similar to the HBC core. Yudin *et al.*[146] observed that as the vanadium content of asphaltenes increases, so too does the tendency of the asphaltenes to aggregate. The expectation of π-bonding of vanadyl porphyrins to other aromatic species was tested systematically by Yin *et al.*[147]. They found no evidence of measurable interactions of VOOEP or VOTPP in solution with PAHs, alkyl PAHs such as HBC, or pyrene derivatives. They suggested that the porphyrin ring must be more substituted in order for association with asphaltenic compounds to occur in solution. This observation implies that simple vanadyl porphyrins will be at most weakly bound to aggregates of asphaltenes, while more complex species will be strongly held

Sirota[148] presents a much different view of the observed asphaltene phase behaviour. Rather than using a colloidal model to explain the precipitation and morphology of asphaltenes, Sirota adopts a liquid-liquid phase separation model to explain the observed phenomena. He argues that the fractal morphology observed in precipitated asphaltenes can be explained on the basis of liquid viscosity and surface tension restrictions which prevent the coalescence of nanoscale liquid droplets to form larger liquid regions. If these droplets are cooled below the glass transition point of the asphaltene entity, then these minute droplets solidify in a fractal like structure giving the appearance of colloids that have aggregated to form a large precipitate. This theory was illustrated by precipitating polystyrene in cyclohexane. If the polystyrene solution was slowly cooled across the glass transition point, the resulting morphology was that of smooth droplets of polystyrene in the cyclohexane solvent. However, if the polystyrene solution was cooled rapidly by injecting some of it into cold iso-octane, a fractal-like structure was formed similar to that observed with asphaltenes. The fact that a well defined model compound (which could be operationally defined as an asphaltene since it is toluene soluble but n-heptane insoluble) behaved in virtually the same manner as actual asphaltenes provides compelling evidence for the liquid-liquid glass transition theory. However, the length scales observed by Sirota were on the order of μm and as such are

more in line with the precipitation behaviour observed in n-heptane and other asphaltene precipitants and as such is not necessarily applicable to nano-aggregates in solvents such as toluene. This type of liquid-liquid formalism was used by Yarranton *et al.*[132-134] along with regular solution theory to model the precipitation of asphaltenes in n-alkanes.

The interactions between the vanadyl porphyrins and the asphaltenes is very complex, and a combination of solubility interactions, hetero-atomic associations, and π-π associations likely lead to the partitioning of the vanadyl porphyrins with the asphaltene fraction.

2.3.3 SOLUTION BASED METALLOPORPHYRIN EXTRACTION METHODS

A number of researchers have used solvent precipitation and extraction schemes to enrich vanadium compounds in a single fraction. The work of Freeman *et al.*[10] showed that vanadyl porphyrins have very low solubilities in common organic solvents (see Figure 2-2). Chlorinated solvents (chloroform and dichloromethane) showed the highest solubility while all other solvents showed very little solvent power for the vanadyl porphyrins.

Several patents have been issued for processes to extract vanadyl porphyrins using polar solvents such as 2-Pyrrolidone[149] and butyrolactone[150], although the data provided
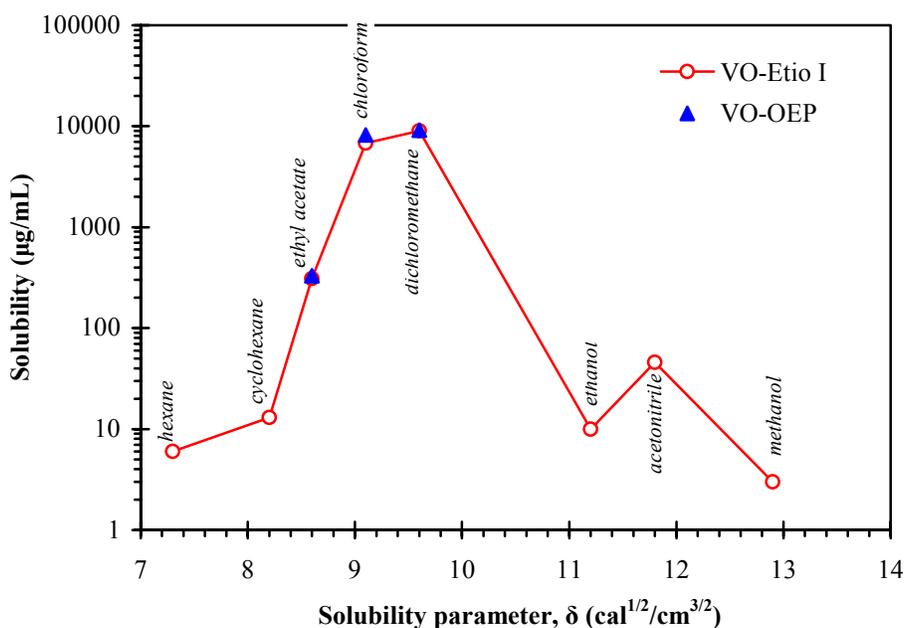
Figure 2-2: Solubility of vanadyl porphyrins at 23 ± 2°C as a function of solubility parameter of the solvent[10]

28

in the patents are for low vanadium oils with little or no asphaltenes present. Overfield[151] used a specific range of Hansen solubility parameters to identify optimal solvents, and identified ethylene carbonate, propylene carbonate, dimethyl sulfone, and ethylene trithiocarbonate as optimum solvents for vanadyl porphyrin extraction. However, once again the data presented in the patent was for low vanadium oil although in this case it did contain asphaltenes (vacuum resid). These solvents were capable of extracting the vanadium compounds selectively, although the process required a large number of equilibrium stages to be effective.

Galimov *et al.*[152] examined the efficacy of a large variety of polar solvents at their boiling point for the extraction of vanadyl porphyrins from Russian asphaltene samples. None of the solvents examined were capable of extracting more than 65% of the free porphyrins initially present.

Yin *et al.*[153] chemically tagged the vanadyl porphyrins within asphaltene samples by reacting with oxalyl chloride followed by a primary amine to replace the oxygen atom with nitrogen coupled to an octadecyl or perfluoroctyl side chain. These tagged species were then subjected to selective affinity chromatography. As was observed with the solvent based extraction methods above, the highest removal of vanadyl porphyrins achieved with this method was 57%. The lack of full recovery of the vanadyl porphyrins was attributed mainly to the aggregation behaviour of the asphaltenes in solution.

Chemical extraction methods are, therefore, not likely to be capable of completely extracting all of the metalloporphyrins present in a petroleum sample. This chemical limitation is further compounded by the fact that asphaltenes form aggregated colloidal structures in most organic solvents, which could further deter the extraction of the metalloporphyrins from the asphaltene phase.

2.4 Implications for Selective Removal of Vanadium Components from Vacuum Residues

The commercial processes for processing of vacuum residue give distinctly different fates for the vanadium components. The most widely used technology is coking, which almost quantitatively captures the vanadium in the coke byproduct. The primary chemical environment of the vanadium is unchanged through this process, although the secondary structure is significantly altered by thermal cracking, dehydration and addition reactions[6]. Similarly, residue fluid catalytic cracking would trap vanadium in coke

deposits on the catalyst pellets, which would then be burned when the catalyst is regenerated. The resulting vanadium on the FCC catalyst destroys the catalyst structure[154, 155]. Deasphalting gives a metal-rich and a metal-depleted fraction, but the separation is non-selective in that complete removal is only achieved with a very large yield of asphalt[7]. Catalytic hydroprocessing selectively removes the vanadium as vanadium sulfide, which accumulates in the catalyst and eventually renders it inactive, therefore, high metal content feeds require high addition rates of catalyst in ebullated bed reactors[9]. Only catalytic demetallation can be considered a truly selective removal technique, but it comes at a substantial cost in catalyst.

Several different reactive demetallation schemes have been explored including oxidative demetallation[156-159], biological demetallation[160-162], electrolytic demetallation[163, 164], ultrasonic irradiation + adsorption[165], photochemical reaction + liquid extraction[166], and absorption by Mo complexes[167]. These varied processes yield vanadium removals ranging between 20-78%, although in many cases the overall mass balance is not considered indicating that a portion of the vanadium removal is not selective and results in significant product loss. The inability of the aforementioned schemes to fully account for the vanadium is linked to the associative behaviour of the asphaltene fraction to which a large portion of the vanadium is linked.

The work of Tanaka *et al.*[115] has important implications for any effort to remove metals from vacuum residue or bitumen by chemical means. If the aggregate persists at temperatures of over 350°C, then a portion of the vanadyl compounds will always be segregated from the free solution. No catalyst or adsorbent can efficiently access the metal centers when they are in such a cluster. Similarly, photochemical or electrochemical processing will be ineffective for this fraction of the metal. Small molecules could possibly penetrate such clusters and react with the vanadyl group, but the resulting products may be no more accessible to separation than the original material[153].

What are the prospects for completely dispersing the asphaltenes to render the metals accessible for catalytic reaction, adsorption, or derivatization for separation? While increasing temperature and solvent strength reduce the degree of aggregation, these conditions have not been demonstrated to completely disaggregate asphaltenes. Given that multiple interactions between poly-functional molecules likely account for the strength of asphaltene aggregation, then a successful strategy must interrupt π-π

interactions, hydrogen bonding, and polar interactions simultaneously. The Hansen solubility parameter approach[168, 169] suggests that a mixed solvent could offer benefits that cannot be achieved by a single solvent that interrupts only one type of intermolecular interaction. Yarranton's observation that the apparent molecular weight of asphaltenes can be suppressed by the presence of polar aromatic compounds[112] suggests that a high concentration of such material could effectively disperse the asphaltene material, although the kinetics of such a disaggregation are not known. Any scheme that seeks to use a sorbent to remove the metals selectively then needs to ensure that the metal species interact more with the surface than with the other species in solution.

2.5 Closing Remarks

Based on the discussion above, the goal of selectively removing the vanadium compounds from bitumen samples would seem to be out of reach. Agreement on the actual form of the organometallic compounds within these samples hasn't even been achieved yet. Nevertheless, the experiments proposed herein will certainly help shed a great deal of light on the nature of the interactions of these organo-vanadium compounds with the asphaltene fractions as well as on their ability to move about within the oil and solvents. This will help point us in the right direction towards the ultimate goal of selectively removing these troublesome contaminants from bitumen and crude oils.

Chapter 3

Solubility of Model Porphyrins and Model Asphaltenes

As discussed in Chapter 2, since asphaltenes are defined by their solubility (or lack thereof), the inclusion of porphyrins with this petroleum fraction is likely tied to solubility phenomena. To this end, the solubility of a series of model porphyrins and model asphaltenes were measured to ascertain whether or not solubility phenomena could explain their inclusion with the asphaltene fraction. As well, these data can be used to test the validity of the various solution models (Regular solution theory and Flory-Huggins theory) and group contribution methods that are so prevalent in the asphaltene literature.

3.1 Experimental Methods

The four model porphyrin compounds (see Figure 3-1) used in this study were all obtained from Sigma Aldrich: meso-tetraphenylporphyrin (H$_2$TPP, sigma-Aldrich #247367), octaethylporphyrin (H$_2$OEP, Sigma-Aldrich #252409), vanadyl meso-tetraphenylporphyrin (VOTPP, Sigma-Aldrich #283649), and vanadyl octaethylporphyrin (VOOEP, Sigma-Aldrich #363715). Both H$_2$TPP and H$_2$OEP were used as received from Sigma-Aldrich, with stated purities of 99.9% and 97.3%, respectively. VOTPP and VOOEP were both purified by flash chromatography (Biotage) using silica gel (see Appendix D). VOTPP was chromatographed twice using a gradient of p-xylene+n-heptane+Dichloromethane (DCM) as the mobile phase, while VOOEP was chromatographed once using a gradient of DCM+n-heptane as the mobile phase. 4,4'-bis-(2-pyren-1-yl-ethyl)-[2,2']bipiridynyl (PBP, see Figure 3-1) was synthesized as per

meso-tetraphenylporphyrin
(H₂TPP)

vanadyl tetraphenylporphyrin
(VOTPP)

Ph =

octaethylporphyrin
(H₂OEP)

vanadyl octaethylporphyrin
(VOOEP)

Et = C₂H₅

4,4'-Bis-(2-pyren-1-yl-ethyl)-[2,2']bipyridinyl
(PBP)
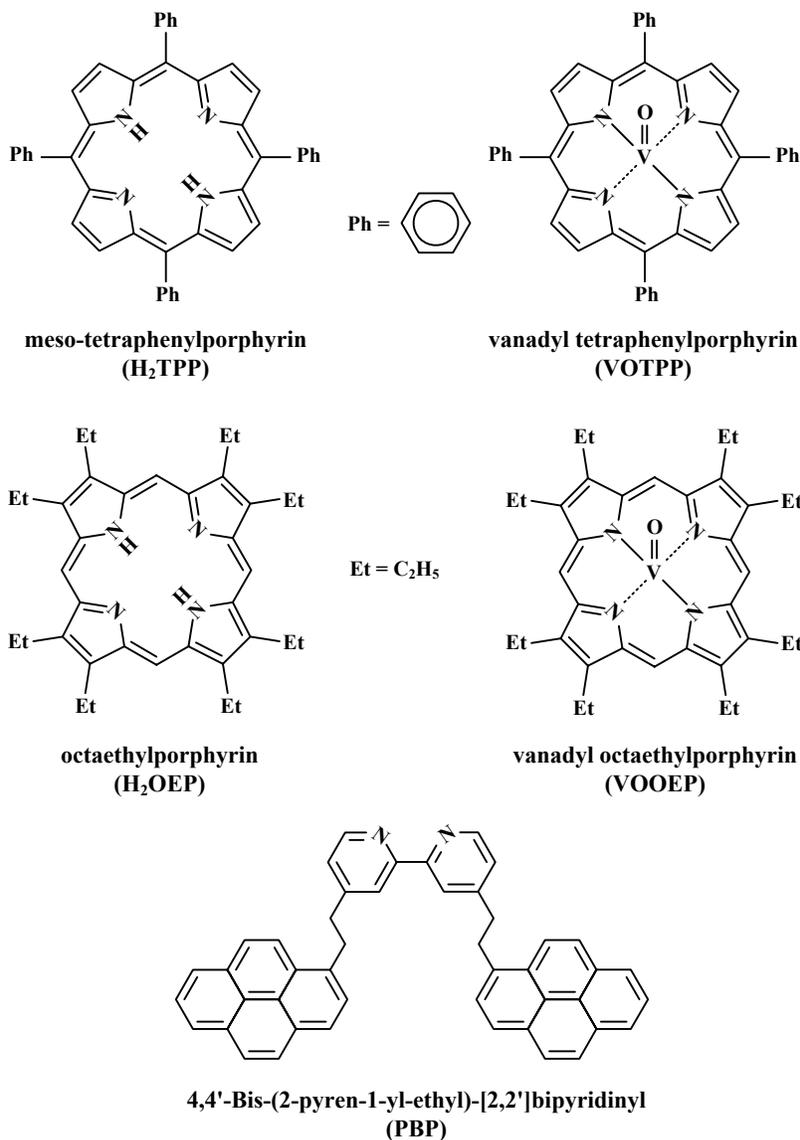
Figure 3-1: Chemical structures of model compounds used in this study

literature methods[144]. The solvents were all HPLC grade and used as obtained from Fisher Scientific.

The solubility was measured by placing an excess of solid in a 16mm x 100mm glass tube with a Teflon lined screw cap. The tube was filled with 5 mL of the desired solvent mixture and capped tightly. The tubes were then subjected to cycles of heating + sonication to speed up the dissolution process. In the case of the toluene+n-heptane solutions, the tubes were heated to 50-60°C for 6-8 hr while being sonicated. The DCM+n-heptane mixtures were heated to 35°C for 6-8 hr while being sonicated. The

tubes were then cooled to ambient temperature (20±2°C) and continuously agitated in a tube roller to allow the solids to slowly re-crystallize. This cycle of heat + sonication was repeated at least three times for each tube to ensure that the solution had reached equilibrium. The tubes were given a minimum of one week at ambient temperature following a heat + sonication treatment prior to sampling and analysis of the liquid composition. The sampling and analysis procedure described below was carried out following each course of heating + sonication to test whether or not the liquid solution had reached its saturation point. If the measured composition deviated significantly from the previous measurement, then another course of sonication + heating was done and the process repeated until the liquid composition remained constant.

The compositions of the equilibrium liquid solutions were measured in triplicate using UV-Visible Spectroscopy (see Appendix B for calibrations). The tubes were removed from the tube roller and allowed to settle for a minimum of one day prior to analysis. A sample of the saturated liquid was taken with a 100 µL gastight syringe, being careful not to disturb the solids on the bottom of the tube. This sample was diluted such that the measured absorbances were within the linear calibration range for the analyte. The dilution ratio was quantified both volumetrically and gravimetrically and the measured concentrations represent the mean of these two methods.

The diluted solutions were then scanned in a 10 mm cuvette at 20±2°C using an SI-Photonics (Tucson, AZ.) model 440 spectrophotometer. This is a fiber optic instrument equipped with a 3,648 element linear CCD array detector. This type of detector allows for collecting an entire spectrum in a single pass, without the need for a scanning monochromator prior to the detector. As a result, full spectra are possible in a matter of seconds. A holographic grating is used to fractionate the light source into discrete wavelengths upstream of the sample. The instrument is equipped with two light sources, a deuterium (D_2) source and a tungsten (W) source. The D_2 source is used for the UV range and can extend up to ~ 500 nm. The W source is primarily for the visible range and can be used from 350 -980 nm, although below 400 nm the intensity of the source declines rapidly. There is some overlap between the 2 sources, although the optimum crossover point between the sources is at 460 nm. The specifications for this instrument are shown in Table 3-1.

This instrument is capable of working with a cuvette holder or fiber optic probes. The cuvette holder is manufactured by SI Photonics specifically to accompany this

instrument. The cuvette holder is capable of using both light sources simultaneously, and all measurements done with cuvettes were done using a crossover between sources at 460 nm. Two sizes of cuvette were used in this work, 10.00±0.01 mm cuvettes as well as 1.00±0.01 mm cuvettes. The size of the cuvette used will be noted where appropriate.

Table 3-1: Instrument specifications for SI Photonics 440 spectrophotometer

Wavelength Range	190 - 980 nm
Spectral Bandwidth	1.0 nm
Photometric Range	0.002 -3.2 AU
Photometric Accuracy	0.005 AU
Baseline Stability	<0.005 AU/hour (@340 and 600 nm)
Stray Light	<0.02% (@ 340 and 600nm)
Typical Speed	1 spectra/sec

The melting points and enthalpies of fusion were measured by Dr. Yadollah Maham using a TA Instruments model Q1000 Differential Scanning Calorimeter.

3.2 Solubility & Melting Point Results

3.2.1 MELTING POINT DATA

In order to apply the regular solution theory and/or the Flory-Huggins theory for solubility modeling, the melting point properties of the solutes are required (see section 3.3). The normal melting point temperature and the enthalpy of fusion for each solid were determined and are summarized in Table 3-2 below.

Table 3-2: Crystal density, melting point temperature, and enthalpy of fusion for the model compounds studied

Solid	MW (g/mol)	Crystal Density (g/cm^3)	Melting Point, T_m (°C)	Enthalpy of Fusion, ΔH_m (J/g)
H$_2$TPP	614.74	1.34[170]	453	62.4
VOTPP	679.66	1.31[50]	511	60.9
H$_2$OEP	534.78	1.19[171]	343	71.0
VOOEP	599.70	1.25[172]	352	63.7
PBP	612.77	1.34[144]	233	85.1

3.2.2 SOLUBILITY DATA

The solubility of the aforementioned model compounds was tested in two series of solutions: toluene + n-heptane mixtures and DCM + n-heptane mixtures. The solubility parameters of the solvent mixtures, δ_{mix}, were calculated using the volume average mixing rule:

$$\delta_{mix} = \frac{\sum_i x_i v_i \delta_i}{\sum_i x_i v_i} \quad \text{...} \quad \{3.1\}$$

where x_i = mol fraction of component i
v_i = molar volume of component i
δ_i = the solubility parameter of component i.

The solubility parameters of the pure solvents were estimated using the definition of the solubility parameter[173]

$$\delta_i = \sqrt{\frac{\Delta H_{v,i} - RT}{v_i}} \quad \text{...} \quad \{3.2\}$$

where ΔH_v = enthalpy of vaporization of component i
T = system temperature

along with the correlations for molar volume and enthalpy of vaporization given by DIPPR[174]:

$$\rho^L \left(kmol / m^3 \right) = \frac{A}{B^{\left[1 + \left(1 - \frac{T(K)}{C} \right)^D \right]}} \quad \text{................................} \quad \{3.3\}$$

$$\Delta H_v \left(kJ / mol \right) = A \left[1 - T(K)/B \right]^C \quad \text{..................................} \quad \{3.4\}$$

The constants necessary to apply equations {3.3} and {3.4} are summarized in Table 3-3 for the three solvents used herein.

The measured solubilities of the 5 solids in various solvent mixtures are summarized below in Table 3-4. Each data point represents the mean of at least 4 replicates of the entire sampling, dilution, and analysis procedure for each mixture. For all of the model compounds, the solubility in toluene was several orders of magnitude higher than in n-heptane, which indicates that all five of these compounds meet the

operational definition of asphaltenes: they are "soluble" in toluene and insoluble in n-heptane.

Table 3-3: Pure solvent properties[174]

Property	TOLUENE		N-HEPTANE		DCM	
	Equation Parameters	Value @ 293 K	Equation Parameters	Value @ 293 K	Equation Parameters	Value @ 293 K
MW (g/mol)	92.14		100.2		84.93	
ρ^L (kmol/m³)*	A = 0.87920 B = 0.27136 C = 591.75 D = 0.29241	9.43	A = 0.61259 B = 0.26211 C = 540.2 D = 0.28141	6.84	A = 1.3897 B = 0.25678 C = 510 D = 0.29020	15.63
ΔH_V (kJ/mol)†	A = 49.507 B = 591.75 C = 0.37742	38.24	A = 50.015 B = 540.2 C = 0.38795	36.92	A = 41.860 B = 510 C = 0.40920	29.50
δ (MPa$^{1/2}$)	18.37		15.36		20.57	

Table 3-4: Equilibrium solubility of model compounds at 20°C

Solvent Composition* (vol%)	$\delta_{20°C}$‡ (MPa$^{1/2}$)	Equilibrium Solubility @ 20°C, S (g/L)§				
		PBP	H₂TPP	H₂OEP	VOTPP	VOOEP
n-heptane	15.4	0.0110±0.0006	0.029±0.001	0.016±0.001	0.0008±0.0001	0.0112±0.0003
20% toluene	16.0	0.089±0.006	0.0629±0.0004	0.042±0.002	0.0045±0.0006	0.0547±0.0007
40% toluene	16.6	0.240±0.002	0.198±0.001	0.073±0.002	0.0167±0.0008	0.139±0.001
60% toluene	17.2	0.480±0.004	0.533±0.001	0.124±0.001	0.0538±0.0002	0.32±0.01
80% toluene	17.8	0.60±0.01	1.34±0.01	0.171±0.001	0.154±0.002	0.639±0.005
Toluene	18.4	1.19±0.02	2.68±0.02	0.202±0.002	0.355±0.003	1.20±0.02
40% DCM	17.4	0.86±0.01	0.879±0.004	0.513±0.002	0.194±0.002	7.58±0.07
60% DCM	18.5	1.82±0.06	2.212±0.007	1.13±0.01	0.627±0.003	19.2±0.3
80% DCM	19.5		3.99±0.03	1.541±0.008	1.36±0.03	
DCM	20.6	4.4±0.7	5.48±0.04	1.76±0.01	2.12±0.03	

*The composition indicates the percentage of the strong solvent, with the balance made up by n-heptane.

‡ This is the solubility parameter of the mixture calculated using the volume average mixing rule (equation {3.1}). The solubility parameters of the pure solvents were estimated using the correlations for molar volume and enthalpy of vaporization given by DIPPR[174].

§ The uncertainty values given are the standard deviations for multiple measurements (minimum of 4) for each solution.

3.3 Solubility Modeling Using the Regular Solution and Flory-Huggins Theories

The equilibrium solubility of a solid (component 2) in a liquid (component 1) is described by the following thermodynamic relation[173]:

$$f_2^s = f_2^{solution} = \gamma_2 x_2 f_2^\circ \dots\dots\dots\dots\dots\dots \{3.5\}$$

where f_2^s = the fugacity of the pure solid solute

          γ_2 = the activity coefficient of the solute in the liquid phase, referenced to f_2°

          x_2 = the mole fraction of solute in the liquid phase

          f_2° = the standard state fugacity to which γ_2 refers

It should be noted that equation {3.5} assumes that the solvent is not soluble in the solid phase and hence both the activity coefficient and mole fraction of solute in the solid phase are one. The fugacity ratio f_2^s / f_2° in equation {3.5} can be determined by using an appropriate thermodynamic cycle to give[173]:

$$\ln \frac{f_2^\circ}{f_2^s} = \frac{\Delta H_m}{RT_m}\left(\frac{T_m}{T} - 1\right) + \frac{\Delta C_P}{R}\left[\ln\left(\frac{T_m}{T}\right) - \frac{T_m}{T} + 1\right] \dots\dots\dots \{3.6\}$$

where ΔH_m = the enthalpy of fusion of the solid (J/mol)
          R = the ideal gas constant (8.314 J/mol·K)
          T_m = the normal melting temperature (K)
          ΔC_P = the difference between the heat capacity of the liquid and solid at the normal melting point = $C_P^L - C_p^S$ (J/mol·K)

          T = the temperature of the solution (K)

Equation {3.6} was derived by choosing the standard state fugacity, f_2°, to be the fugacity of the pure subcooled liquid solute at the same temperature and pressure as the solution. Equation {3.6} assumes that the normal melting point is not far removed from the triple point such that the values for ΔH_t and T_t are replaced by the values at the normal melting point[173].

3.3.1 REGULAR SOLUTION (RS) THEORY.

In order to model the solubility of the solute (2) in the liquid (1) using equations {3.5} and {3.6}, it is necessary to estimate the activity coefficient of the solute in the

liquid phase. According to the Scatchard-Hildebrand regular solution theory, the activity coefficient of the solute in the liquid phase can be estimated from pure component properties[173]:

$$\ln \gamma_2 = \frac{v_2^L \left(\delta_1 - \delta_2 \right)^2 \phi_1^2}{RT}$$ .... {3.7}

where v_2^L = the molar volume of subcooled liquid solute at temperature T (m^3/mol)
δ_1, δ_2 = the solubility parameter of solvent and solute, respectively (Pa$^{1/2}$)
ϕ_1 = the volume fraction of solvent

Combining equations {3.5}-{3.7} gives:

$$\ln \left(\frac{1}{x_2} \right) = \frac{v_2^L \left(\delta_1 - \delta_2 \right)^2 \phi_1^2}{RT} + \frac{\Delta H_m}{RT_m} \left(\frac{T_m}{T} - 1 \right) + \frac{\Delta C_P}{R} \left[\ln \left(\frac{T_m}{T} \right) - \frac{T_m}{T} + 1 \right]$$ .... {3.8}

3.3.2 FLORY-HUGGINS (FH) THEORY.

The activity coefficient of the solute, γ_2, can also be predicted using the Flory-Huggins theory for polymer solutions. This theory was developed for use with asymmetric polymer solutions where the solute molecules are much larger than the solvent molecules. According to this theory, the activity coefficient of the solute is[175]:

$$\ln \gamma_2 = \ln \left(\frac{v_2^L}{v_m^L} \right) + \phi_1 \left(1 - \frac{v_2^L}{v_1^L} \right) + \frac{v_2^L}{RT} \left(\delta_1 - \delta_2 \right)^2 \phi_1^2$$ .... {3.9}

where v_1^L = the liquid molar volume of the solvent (m^3/mol)

v_m^L = the liquid molar volume of the mixture = $v_1^L + v_2^L$ (m^3/mol)

At the limit of low solute solubility ($x_2 \ll 1$), the mixture molar volume approaches that of the solvent and the solvent volume fraction approaches one, yielding the following form used by Yarranton and co-workers[133-135]:

$$\ln \gamma_2 = \ln \left(\frac{v_2^L}{v_1^L} \right) + 1 - \frac{v_2^L}{v_1^L} + \frac{v_2^L}{RT} \left(\delta_1 - \delta_2 \right)^2$$ .... {3.10}

Combining equation {3.9} with equations {3.5} and {3.6} gives:

$$\ln\left(\frac{1}{x_2}\right) = \ln\left(\frac{v_2^L}{v_m^L}\right) + \phi_1\left(1 - \frac{v_2^L}{v_1^L}\right) + \frac{v_2^L}{RT}\left(\delta_1 - \delta_2\right)^2 \phi_1^2 + \frac{\Delta H_m}{RT_m}\left(\frac{T_m}{T} - 1\right) + \frac{\Delta C_P}{R}\left[\ln\left(\frac{T_m}{T}\right) - \frac{T_m}{T} + 1\right]$$

.... {3.11}

3.3.3 SOLUBILITY MODELING FOR A TEST SUBSTANCE: PYRENE

For both of the theories outlined above, assuming the properties of the solute (ΔH_m, T_m, ΔC_P, and v_2^L) and the solvent (v_1^L and δ_1) are known, then the only unknown in equations {3.8} and {3.11} is the solubility parameter of the solute, δ_2. Therefore, given a set of solubility measurements for a solid solute as a function of solubility parameter of the solvent, it should be possible to determine δ_2 by least squares non-linear regression using equations {3.8} and {3.11}. Before applying these two models to the solubility data for the model compounds, this non-linear least squares regression method will be tested on a solid solute for which all of the pertinent data are available: pyrene.

Because pyrene is a relatively high melting compound ($T_m = 150.7°C^{[176]}$) with a fused-ring aromatic structure, its behaviour should be a good representation of the behaviour of the model compounds in this study. The solubility of pyrene in toluene + n-heptane mixtures has been measured experimentally by Ali *et al.*[177] at 293 K (Table 3-5) and will be used from hereon to test the regression scheme.

Table 3-5: Solubility of Pyrene in n-heptane + toluene mixtures

Solvent (vol% Toluene)	x_{Pyrene} (mol fraction) @ 293 K
0	0.0114
10	0.0155
20	0.0226
30	0.0292
40	0.0300
50	0.0310
60	0.0376
70	0.0412
80	0.0488
90	0.0536
100	0.0569

3.3.3.1 Toluene + n-Heptane Solvent Properties

The main properties necessary for modeling the pure solvents are listed in Table 3-3. In the case of the mixed solvent systems, the solvent will be treated as a pseudo-single solvent with properties calculated using molar averages. In the case of the molar volume, this takes the form:

$$v_m^L = x_1 v_1^L + x_2 v_2^L \quad\text{..} \quad \{3.12\}$$

where x_1, x_2 = the mole fractions of each component

The above mixing rule assumes ideal mixing of the two components. According to Holzhauer and Ziegler[178], the excess molar volume for toluene + n-heptane mixtures does not exceed 0.1% and therefore using equation {3.12} will not result in significant errors. An analogous equation can be written for the molar heat capacity of the mixture and once again results in less than 0.1% error[178]. Equation {3.1} is used to calculate the molar average solubility parameter for the mixture.

Since the compositions of the solvent mixtures are given as volume fractions, the mole fractions are determined as follows:

$$x_i = \frac{\phi_i / v_i^L}{\sum_i \phi_i / v_i^L} \quad\text{...} \quad \{3.13\}$$

where v_i^L = the molar volume of component I (m^3/mol)

ϕ_i = the volume fraction of component i

This equation assumes ideal mixing, which as discussed above is a reasonable assumption for these mixtures.

3.3.3.2 Pyrene Solute Properties

Equations {3.8} and {3.11} require several additional properties for the solute in addition to those listed for the solvent.

Temperature and Enthalpy of Fusion, T_m and ΔH_m

The temperature and enthalpy of fusion measured by Wong and Westrum[176] were 423.81 and 17.36 kJ/mol, respectively.

Differential Heat Capacity, ΔC_P

The heat capacities of both the liquid and solid were measured over a range of temperatures by Wong and Westrum[176]. Their value of ΔC_P at the melting point is -23.39 J/mol·K.

Subcooled Liquid Molar Volume, v_2^L

As is the case for the model compounds in this study, pyrene is a solid at room temperature with a melting point far removed from 20°C. Therefore, the value of v_2^L will be an estimate rather than an actual measurement. The first possibility would be to extrapolate liquid volume data from the melting point down to 20°C. Using the volume correlation from DIPPR[174] gives a value of 0.1698 m^3/kmol at 20°C. Although this value is reasonably close to the other predictions below, it is always risky to extrapolate an empirical correlation this far from its lower bound (150.7°C) and should be avoided if possible. Shahidi et al.[179] reported a partial molar volume of 0.1665 m^3/kmol for pyrene in carbon tetrachloride (CCl_4). However, the partial molar volume is not necessarily equivalent to v_2^L, not to mention that the behaviour of pyrene in CCl_4 may not be the same as in n-heptane or toluene and as such this value may not be appropriate. Wakeham et al.[180] applied a quantitative structure-property relationship (QSPR) to obtain a value of 0.1778 m^3/kmol at 20°C. The error of their density predictions averaged ~1.2% and as such appears to be reliable.

The final estimate is obtained by assuming that the volume change on melting, $\Delta v_m = v^L - v^S$, remains constant between the normal melting point and 20°C. Using this assumption with the value of Δv_m measured by McLaughlin and Ubbelohde[181] (18.9 cm^3/mol) and the value of v^S listed below gives a value of 0.1780 m^3/kmol at 20°C. This value is nearly identical to the value predicted by Wakeham et al.[180]. It is unlikely that the volume of a solid will decline at the same rate as a liquid with a decrease in temperature. Therefore, this estimate should provide an upper limit for v^L, with the solid molar volume providing the lower limit. Therefore, a value of 0.178 m^3/kmol at 20°C will be used for the remainder of the calculations.

Solid Molar Volume, v_2^S

The density of solid pyrene measured by Baxter and Hale[182] is 0.1591 m^3/kmol at 22.7°C. This value will be used for the density at 20°C since it is not anticipated that a 3°C change in temperature will lead to a significant change in density for a solid. Although this value is not required for the solubility modeling, it will be used to assess the impact of using the solid molar volume as an estimate for the liquid molar volume of the solute since this approximation will be used for modeling the model compounds.

Heat of Vaporization, ΔH_v

The value for the enthalpy of vaporization, although not required explicitly for equations {3.8} and {3.11}, will be used to provide an estimate for the solubility parameter of pyrene to compare to the results of the regression analysis. It is possible to use the empirical correlation provided by DIPPR[174] to extrapolate for the value of ΔH_v at 20°C. However, as stated in the discussion for v^L, it is risky to extrapolate empirical correlations this far out of their usable range. Roux *et al.*[183] provide a value of 89.4 kJ/mol, which is the mean of several estimates that were thoroughly evaluated. As such, this is likely the most appropriate value to use. It should be noted that this is a hypothetical value since pyrene is a solid at these conditions and as such a heat of vaporization at these conditions is not a real value.

Solubility Parameter, δ

This value is required only to compare to the results of the regression analysis on solubility data. Because the solubility parameter is a function of both v^L and ΔH_v (equation {3.2}), and because both of these values are hypothetical and uncertain, the value for δ will also be a hypothetical value and as such there are many ways to estimate this parameter. DIPPR[174] reports a predicted value of 19.7 MPa$^{1/2}$ at 25°C, although they do not provide any details regarding the method used to generate this estimate. They claim an accuracy of <25% which would indicate that this value is only approximate. If the values of ΔH_v and v_2^L previously discussed are used with equation {3.2}, then the predicted value for δ is 22.1 MPa$^{1/2}$. This predicted value will be used to assess the suitability of the regression method for predicting the value of δ.

The pure component properties of pyrene that will be used from hereon are summarized below in Table 3-6.

Table 3-6: Pure component properties for pyrene

Property	Value	Source
T_m	423.81 K	[1]
ΔH_m	17.36 kJ/mol	[1]
ΔC_P	-23.39 J/mol·K	[1]
v^L_{293K}	0.178 m^3/kmol	[2]
v^S_{293K}	0.1591 m^3/kmol	[3]
$\Delta H_{v, 298K}$	89.4 kJ/mol	[4]
δ_{293K}	22.1 MPa$^{1/2}$	[5]

[1] Wong and Westrum[176]
[2] Estimated, see discussion
[3] Baxter and Hale[182]
[4] Roux *et al.*[183]
[5] Estimated, see discussion

3.3.3.3 Pyrene Solubility Modeling – RS Theory

Now that pure component data has been obtained, the solubility data in Table 3-5 can be used with equation {3.8} to determine the solubility parameter of pyrene. Because equation {3.8} cannot be linearized in δ_2, the fitting procedure is iterative. The solver function in Microsoft Excel® was used to minimize the following objective function for the pyrene modeling:

$$\text{objective function} = \sum \left(x_{2,\text{calc}} - x_{2,\text{meas}} \right)^2 \quad\text{............................ \{3.14\}}$$

The results of the best fit obtained using the data in Table 3-6 are shown in Figure 3-2. This model does a reasonable job of describing the data ($R^2 = 0.958$), although the data exhibit some strange behaviour between 16-16.5 MPa$^{1/2}$.

Effect of Liquid Molar Volume, v^L_2

In the case of the model compounds, the liquid molar volume is unknown and as such it is necessary to use the solid molar volume as an approximation. Therefore, it would be
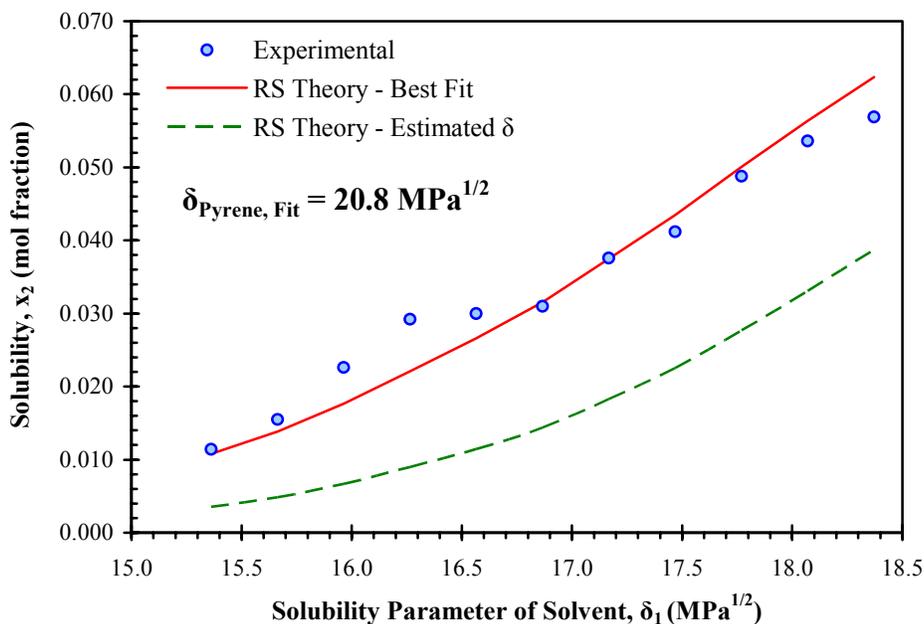
Figure 3-2: Results of the non-linear regression of pyrene solubility data using the RS theory and the pure component properties listed in Table 3-6.

instructive to do the same for the pyrene data to determine the effect on the regression results. Using the solid molar volume represents a decrease of $\approx$ 10% in the value of v^L, and so for comparison the analysis was also done with a value of v^L that was 10% higher than the base value. The results obtained using these modified estimates of v^L are summarized below in Table 3-7.

Table 3-7: Sensitivity analysis of the effect of the subcooled liquid molar volume, v^L, on the regression results with the RS theory.

Method	Base	$v^L \approx v^S$	$v^L = \text{Base} + 10\%$
v^L (m³/kmol)	0.178	0.1591	0.196
δ_{Pyrene} (MPa$^{1/2}$)	20.8	21.0	20.7
Regression R^2	0.958	0.968	0.948

An uncertainty in liquid molar volume of ±10% only results in an uncertainty in the regressed solubility parameter of ±1% indicating a relative insensitivity of the results to this value. In fact, using the solid molar volume as an approximation to the subcooled liquid molar volume actually improves the quality of the fit for the RS model as indicated

by the higher value of R^2. This bodes well for the modeling of the model compounds where the liquid molar volume is not available for these compounds and the solid molar volume must be used as an approximation.

Effect of Enthalpy of Fusion, ΔH_m

A similar sensitivity analysis was done to assess the impact of the value of the enthalpy of fusion, ΔH_m, on the values predicted by the RS theory by varying the value of ΔH_m by ±10%, and the results are summarized below in Table 3-8. These results indicate that the value of ΔH_m has a more significant impact on the predicted solubility parameter than did the liquid molar volume. However, the value of ΔH_m has a physical basis (it is not a hypothetical construct like the subcooled molar volume) and can be measured experimentally. The error in the measured enthalpies is likely on the order of ±2% or less, depending on the type of instrument used and the purity of the sample. In the case of a ±2% deviation in ΔH_m, the error in δ would be ±0.5%.

Table 3-8: Sensitivity analysis of the effect of the enthalpy of fusion, ΔH_m, on the regression results with the RS theory.

Method	Base	$\Delta H_m = $ Base + 10%	$\Delta H_m = $ Base - 10%
ΔH_m (kJ/mol)	17.36	19.10	15.63
δ_{Pyrene} (MPa$^{1/2}$)	20.8	20.3	21.3
Regression R^2	0.958	0.981	0.925

Effect of Differential Heat Capacity, ΔC_P

Finally, a similar sensitivity analysis was done to assess the impact of the value of the differential heat capacity, ΔC_P, on the values predicted by the RS theory by varying the value by ±10%, and the results are summarized below in Table 3-9. One assumption that is commonly made when applying these equations is to assume that the differential heat capacity is negligible and can be ignored[173]. In the case of the model compounds, these data are not available and therefore this term will not be included. Therefore, the calculations were also done assuming $\Delta C_P = 0$ and the results are included in Table 3-9. These results indicate that an uncertainty of ±10% in this value has a negligible effect on the predicted solubility parameter while neglecting this term entirely results in an increase in the calculated solubility parameter of 2.4% with a corresponding decrease in the quality of the fit (as indicated by R^2).

Table 3-9: Sensitivity analysis of the effect of the differential heat capacity, ΔC_P, on the regression results with the RS theory.

Method	Base	$\Delta C_P = 0$	ΔC_P = Base + 10%	ΔC_P = Base - 10%
ΔC_P (J/mol·K)	-23.39	0	-25.73	-21.05
δ_{Pyrene} (MPa$^{1/2}$)	20.8	21.3	20.8	20.9
Regression R^2	0.958	0.926	0.961	0.955

It should be pointed out that the error incurred by ignoring the ΔC_P term in equation {3.8} increases as the system temperature becomes farther removed from the melting point of the solute. This is illustrated in Figure 3-3 where the ΔC_P multiplier (the term in brackets multiplied by ΔC_P in equation {3.8}) is plotted as a function of the ratio of the melting point temperature to the system temperature. As this ratio increases (system temperature decreases), the multiplier increases and would magnify the effect of ΔC_P. In the case of pure pyrene, where ΔC_P is known, this is not a large concern. However, in the case of the model compounds, ΔC_P is not known and therefore this term must be neglected. The error incurred in doing so may become significant since the melting points of the model compounds are very high resulting in a relatively large value for this multiplier and in turn significant potential errors in the predicted solubility behaviour.
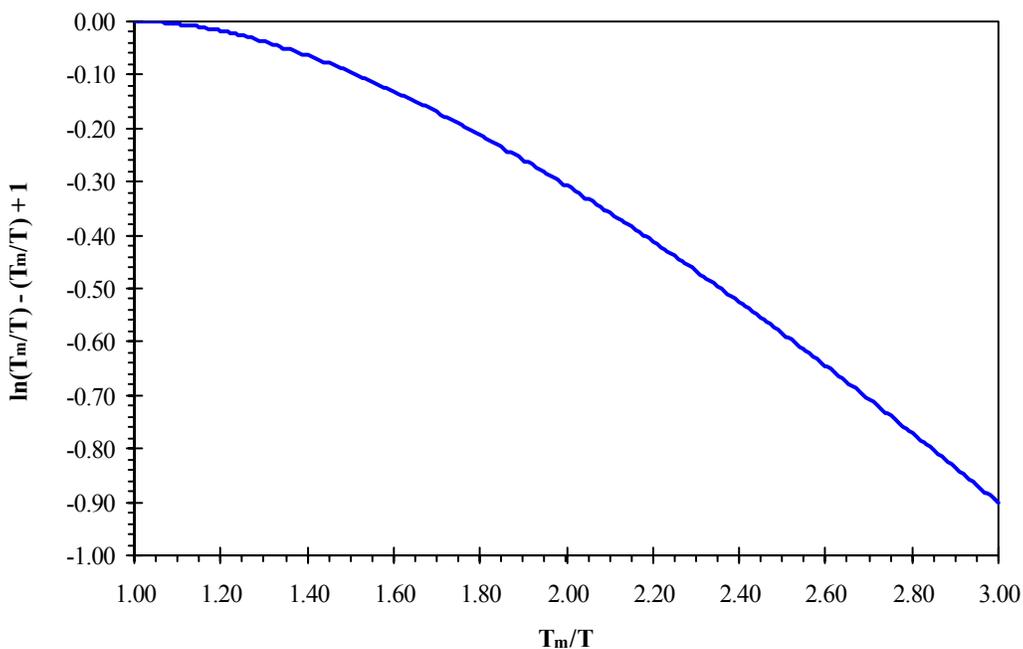
Figure 3-3: Variation in the ΔC_P multiplier with temperature of the system.

Summary of Pyrene RS Modeling

Overall, the value of the solubility parameter for pyrene at 20°C predicted by the solubility modeling varied between 20.3-21.3 MPa$^{1/2}$, resulting in an uncertainty of ±0.5 MPa$^{1/2}$ (±2.4%). The largest contributor to this uncertainty was the enthalpy of fusion, while all other variables showed relative insensitivity to the value of δ obtained via regression of the solubility data. The sensitivity of the analysis to values of ΔH_m and ΔC_P are not specific to the RS model. Rather, these terms represent the ideal solubility of the solid solute as estimated using a standard thermodynamic cycle. Because the thermodynamic cycle uses data at the normal melting point as a reference, operating at a system temperature far removed from this melting point makes for a large extrapolation and hence the potential for incurring significant errors. These ideal solubility terms set the maximum possible solubility while the RS activity coefficient term sets the curvature. Some error incurred by the ideal solubility can be accounted for by the regressed value of δ_2, but not all.

The base value (20.8 MPa$^{1/2}$) does not compare well with the value listed in Table 3-6 (22.1 MPa$^{1/2}$). Although an error of -6.3% may seem like a relatively small discrepancy, the predicted solubility (equation {3.8}) varies exponentially with the square of the terms containing the solubility parameter. Therefore, even small changes in the value for the solubility parameter can result in large discrepancies in the predicted solubility. The solubility predictions obtained with these 2 values of δ are illustrated in Figure 3-2. It is immediately evident that this discrepancy results in significant errors in the solubility modeling, with differences in predicted solubility as high as 100%.

3.3.3.4 Pyrene Solubility Modeling – FH Theory

As was the case for the RS theory, the FH theory (equation {3.11}) cannot be linearized in δ_2 and therefore the fitting procedure is iterative. The solver function in Microsoft Excel® was again used to minimize the same objective function (equation {3.14}). The results of the best fit obtained using the pure property data in Table 3-6 are shown in Figure 3-4. This model does a reasonable job of describing the data ($R^2 =$ 0.918) although the quality of the fit is not as good as the simpler RS theory. The best fit value of the solubility parameter (21.1 MPa$^{1/2}$) is relatively close to the value obtained using the RS theory (20.8 MPa$^{1/2}$).
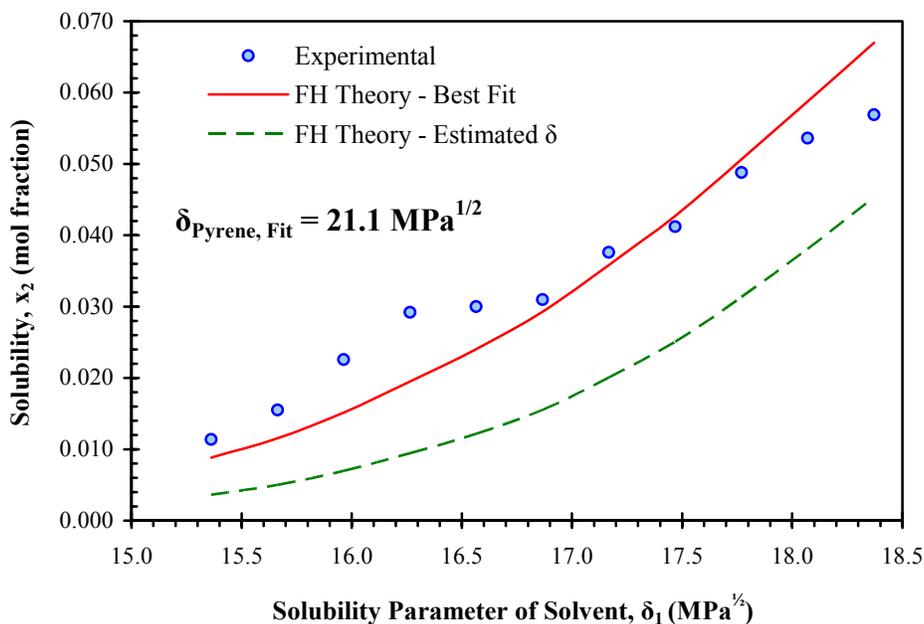
Figure 3-4: Base case results of the non-linear regression of pyrene solubility data using the FH theory and the pure component properties listed in Table 3-6.

Rather than perform a full sensitivity analysis as was done with the RS theory, only the simplifications relevant to the pure compound modeling ($v^L \approx v^S$ and $\Delta C_P = 0$) will be tested for the FH theory. The results with these simplifications are summarized below in Table 3-10. Ignoring ΔC_P decreases the quality of the fit and results in an increase in the value of the solubility parameter (+2.4%). Using the solid molar volume as an approximation to the subcooled liquid molar volume ($v^L \approx v^S$) results in a small increase in the solubility parameter with a corresponding increase in the quality of the fit, indicating that the solid molar volume represents a good approximation for v^L. The relative insensitivity to the value of the solute molar volume is surprising since the FH theory is a much stronger function of the molar volume of the solute. The values

Table 3-10: Sensitivity analysis of the effect of the negligible differential heat capacity, $\Delta C_P = 0$, and $v^L \approx v^S$ on the regression results with the FH theory.

Method	Base	$\Delta C_P = 0$	$v^L \approx v^S$
ΔC_P (J/mol·K)	-23.39	0	-23.39
v^L (m^3/kmol)	0.178	0.178	0.1591
δ_{Pyrene} (MPa$^{1/2}$)	21.1	21.6	21.2
Regression R^2	0.918	0.885	0.946

obtained from regression with the FH theory are all higher than the base value obtained with the RS theory, indicating that the FH volume corrections are serving to reduce the predicted solubility which in turn requires a more significant correction from the solubility parameter term.

The base FH value (21.1 MPa$^{1/2}$) compares better with the estimated value listed in Table 3-6 (22.1 MPa$^{1/2}$), although not much better. As mentioned previously for the RS theory, the predicted solubility (equation {3.11}) varies exponentially with the terms containing the solubility parameter. Therefore, small changes in the value for the solubility parameter can result in large discrepancies in the predicted solubility (see Figure 3-4) and therefore the observed difference of 1 MPa$^{1/2}$ (-4.5%) is significant. Again, considering the hypothetical nature of the solubility parameter for a high melting solid, it is not surprising that this model has difficulty describing the results without an adjustable parameter.

3.3.3.5 Pyrene Solubility Modeling – General Discussion

Overall, the regression analysis of the pyrene solubility data indicates that both of these simple theories can qualitatively describe the solubility behaviour of pyrene in n-heptane + toluene mixtures if the solubility parameter of the solid is used as an adjustable parameter. The simpler RS theory actually does a better job of fitting the observed solubility than does the more complex FH theory. However, both theories can only fit the data by using the solubility parameter of the solute as an adjustable parameter. When an estimated value for the solubility parameter is used, the predictions of both theories are not accurate and lead to a significant under prediction of the solubility.

These discrepancies are not entirely surprising considering that the values for ΔH_v and v^L used to predict the solubility parameter are hypothetical values, which in turn means that the solubility parameter for a solid solute like pyrene is itself a hypothetical value. It cannot have any physical meaning at these low temperature conditions ($T_m/T =$ 1.45) since pyrene cannot exist as a liquid at this low temperature. Therefore, trying to estimate δ using thermodynamic quantities according to its definition (equation {3.2}) is neither meaningful nor accurate. In the case of the value obtained by the regression method, the value obtained cannot hold any physical meaning since it is nothing more than a curve fitting parameter. This best fit parameter can be used to perform engineering design calculations (interpolate solubilities in n-heptane + toluene mixtures); however

drawing specific conclusions regarding the thermodynamics of the solute from this value is not meaningful. Also, extrapolating the regressed solubility parameter to different solvent systems is also inherently risky since intermolecular forces could drastically change the nature of the solvation process and lead to significant errors in prediction.

One of the main advantages of using the RS and FH theories is the ability to predict solubility and solution behaviour from pure component properties without the need for actual solubility data. If a regression of solubility data is required to determine values for δ, then this advantage is no longer relevant since any suitable activity coefficient method (e.g. NRTL, UNIQUAC, WILSON etc.) could just as easily be fit to this type of data. Since the more advanced activity coefficient models are much better equipped to handle non-ideal systems, it is anticipated that these models will do a much better job of describing the solubility data than the very simple RS and FH models.

3.3.4 SOLUBILITY MODELING FOR THE MODEL COMPOUNDS

Now that the methodology has been tested on a solute with well known properties, it will be used to model the solubility behaviour of the model compounds as listed in Table 3-2. Because the measured solubilities of the model compounds were much lower than those of pyrene and spanned several orders of magnitude, the objective function for the non-linear regression was modified as follows:

$$\text{objective function} = \sum \left[\ln \left(\frac{1}{x_{2,\text{calc}}} \right) - \ln \left(\frac{1}{x_{2,\text{meas}}} \right) \right]^2 \quad \text{.................. \{3.15\}}$$

This form of the objective function ensures that the regression results are not as heavily influenced by the high solubility results.

The solvent properties required for this analysis are the same as for the pyrene analysis and are listed in Table 3-3. In the case of the model compounds, the solubility was also measured in dichloromethane (DCM) + n-heptane mixtures. According to Bissell *et al.*[184], the excess molar volume for DCM + n-heptane mixtures does not exceed 0.8% and therefore use of ideal mixing to estimate solvent mixture properties (equations {3.1}, {3.12}, and {3.13}) is appropriate.

The required solute properties for the model compounds were summarized in Table 3-2. As mentioned in the pyrene analysis, the subcooled liquid molar volumes of the model compounds are not known and therefore the solid molar volume will be used as an

approximation for this analysis (i.e. $v^L \approx v^S$). As well, the differential heat capacity (ΔC_P) is not known and therefore all terms including this value will be neglected for the purpose of this analysis.

Both the RS and FH theories (equations {3.8} and {3.11}) are written in terms of mole fractions of the solute in the liquid phase. The measured solubilities were determined using UV/Visible calibrations which give molar concentrations and therefore these values must first be converted to mole fractions using the following equation:

$$x_2 = \frac{S_2 v_1}{MW_2} \quad \text{..} \quad \{3.16\}$$

where S_2 = solubility of solute (g/L)
  v_1 = the molar volume of the solvent (m^3/mol)
  MW_2 = molecular weight of the solute (g/mol)

Equation {3.16} assumes that the solution is dilute ($x_2 \ll 1$) and that the solute has a negligible effect on the molar volume of the mixture (i.e. $v_{mix} = v_1$).

3.3.4.1 Meso-Tetraphenylporphyrin (H₂TPP)

The necessary solute properties for modeling the solubility of H$_2$TPP are listed in Table 3-2. The measured melting point temperature compares reasonably well with the value reported by Rothemund and Menotti[185] (450°C, unknown experimental technique) and Bergstresser and Paulaitis[186] (444°C, DSC). The results obtained in this work using both DSC and TGA showed signs of decomposition upon melting, which was also noted by Rothemund and Menotti[185]. This causes some difficulty in extracting the true enthalpy of melting from the DSC curve and therefore some uncertainty in the measured value for ΔH_m. Unfortunately, no other values for this property were found in the literature for comparison. The solid molar volume is taken from the solid density measurement done by Fleischer *et al.*[170] (1.336 g/mL) along with the molecular weight of the pure compound.

The results of modeling the solubility of H$_2$TPP using both the RS and FH theories are shown in Figure 3-5. Neither theory does a good job of describing all of the observed solubility behaviour for this compound. The FH theory is reasonably close for the toluene data, but deviates by an order of magnitude for the DCM solubility. The primary reason for the poor performance of both models is the relatively high value for both the

melting point temperature (453°C) and the enthalpy of fusion (38.4 kJ/mol) determined for this compound. The maximum (ideal) solubility using these two values is:

$$\ln\left(\frac{1}{x_{2,ideal}}\right) = \frac{\Delta H_m}{RT_m}\left(\frac{T_m}{T}-1\right) = 9.393 \quad\text{.............................} \quad \{3.17\}$$

which gives a maximum solubility of $x_{2,ideal} = 8.33 \times 10^{-5}$. This value is lower than the majority of the measured solubilities and as such, regardless of the value of δ_2 the RS model will never be able to match the measured data. In order to explain/model the measured solubilities with this ideal solubility, the activity coefficient must be less than unity ($\gamma_2 < 1$) which is not possible for the RS theory[173].

One major source of error in the aforementioned ideal solubility calculations was the assumption that the ΔC_P term was negligible. A positive value of ΔC_P would lead to an increase in the ideal solubility and improve the ability of the RS theory to fit the results. Unfortunately, this property is not available and therefore some method of approximating this value is required. According to Neau *et al.*[187], assuming that ΔC_P is zero is not a good assumption for compounds with high melting points, resulting in significant under prediction of the ideal solubility. Assuming that ΔC_P can be approximated by the entropy of fusion (i.e. $\Delta C_P \approx \Delta S_m \approx \Delta H_m/T_m$) results in improved
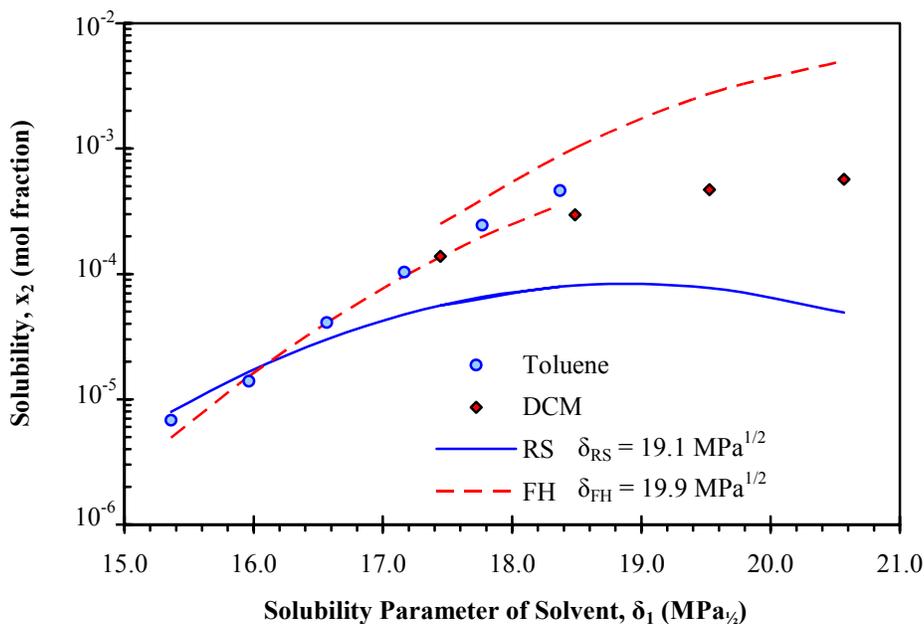
Figure 3-5: Base modeling results for the solubility of H_2TPP using both the RS and FH theories ($v^L \approx v^S$, $\Delta C_P = 0$)

predictions, although they are still too low. According to Neau *et al.*[188], although the different estimates for ΔC_P (i.e. $\Delta C_P \approx 0$ or $\Delta C_P \approx \Delta S_m$) result in different values for the ideal solubility, the best fit value for the solubility parameter obtained from solubility data is not appreciably affected by this difference. This would imply that the magnitude of the ΔC_P terms is small relative to the regular solution correction for the activity coefficient. According to Mishra and Yalkowsky[189], the optimum method for modeling the solubility of polycyclic aromatic hydrocarbons in benzene was the Flory-Huggins (FH) model (for the nonideal portion) combined with the ideal solubility using $\Delta C_P \approx 0$. They also used the UNIFAC model, but found no additional accuracy/benefit over the FH. Neau and Flynn[190] looked at the ΔC_P values for a range of compounds and concluded that in general $\Delta C_P \approx \Delta S_m$ is a better approximation than $\Delta C_P \approx 0$. The exception was for flat, rigid molecules (e.g. benzene and PAH's with no peripheral substitution) where $\Delta C_P \approx 0$ was a much better approximation. For example, in the case of benzene ΔC_P is close to zero while for toluene (where a single methyl group has been added to the periphery of benzene) ΔC_P is much closer to ΔS_m. Therefore, even the addition of a single flexible methyl group is enough to push ΔC_P closer to ΔS_m.

Pappa *et al.*[191] examined in depth the effects of ΔC_P on the predicted ideal solubility and concluded that in cases where the operating temperature is far removed from the melting point (i.e. $T_m/T > 1.4$), the errors introduced by assuming $\Delta C_P \approx 0$ were large (>30%) and as such it is not valid to make this assumption in this case. However, they do go on to state that for fused PAHs, in the absence of actual data the best assumption is $\Delta C_P \approx 0$, rather than $\Delta C_P \approx \Delta S_m$. Wu and Yalkowsky[192] examined various methods for predicting ΔC_P, which included the 2 common assumptions ($\Delta C_P \approx 0$ or $\Delta C_P \approx \Delta S_m$), another assumption ($\Delta C_P \approx 1/2\ \Delta S_m$), as well as various predictive methods. Of the three assumed methods, using $\Delta C_P \approx 1/2\ \Delta S_m$ provided the lowest average absolute error, although they also developed a simple method for predicting the value of ΔC_P from molecular structure that proved to be better than all three of the other simplified assumptions.

It would appear that in the case of H_2TPP, where the system temperature is far removed from the melting point ($T_m/T = 2.5$), assuming $\Delta C_P \approx 0$ is not appropriate although assuming that $\Delta C_P \approx \Delta S_m$ doesn't appear to be much better. This molecule has fused polyaromatic cores with various forms of alkyl bridging and/or alkyl side chains. According to Neau and Flynn[190], once more flexible side chains and/or bridges are

introduced to the PAH core, the ability of these molecules to absorb heat increases significantly and assuming $\Delta C_P = 0$ is no longer valid. In such a case, assuming $\Delta C_P \approx \Delta S_m$ is a better approximation.

The effects of two values of ΔC_P were tested further: $\Delta C_P \approx \Delta S_m \approx \Delta H_m/T_m$ and ΔC_P estimated from the correlation of Wu and Yalkowsky[192]. The results of these calculations are summarized below in Table 3-11 and Figure 3-6. Both of the estimation methods yield very similar values for ΔC_P and therefore the resulting fits are very similar. In the case of the RS theory, the quality of the fit improved significantly, particularly for the toluene solutions. However, this simple theory still cannot describe the entire series of data. In the case of the FH theory, the quality of the fits declined significantly. There was also a significant increase in the value of the regressed solubility parameter for both methods, and the values obtained with the FH theory were consistently higher by a factor of 1 MPa$^{1/2}$ than those from the RS theory.

Table 3-11: Sensitivity analysis of the effect of different values of the differential heat capacity, ΔC_P, on the regression results for H_2TPP.

Method	Base		$\Delta C_P \approx \Delta S_m \approx \Delta H_m/T_m$		Wu and Yalkowsky[192]	
	RS	FH	RS	FH	RS	FH
ΔC_P (J/mol·K)	0		52.82		47.8	
δ_{H2TPP} (MPa$^{1/2}$)	18.9	19.9	21.4	22.5	21.2	22.3
Regression R^2	0.478	0.823	0.891	0.703	0.914	0.710

The best fits occurred with the toluene + n-heptane solvents. In most cases, the models were not capable of accurately capturing the behaviour of the DCM mixtures. Given the much higher density and slightly higher polarity of DCM, it was anticipated that the solubility would be higher in this solvent than it was in toluene, as is predicted by both theoretical models. However, this was not the case. In order to verify that the DCM measurements were not in error, the solubility data in this work were compared to data reported in the literature for H_2TPP in Figure 3-7. From this figure it is apparent that the current measurements fit with other reported solubility measurements. Some of the polar solvents tested (Acetic Acid, Acetone, and 1,4-Dioxane) showed anomalously low solubilities, although given the drastically different physical nature of these solvents, it is difficult to draw any concrete conclusions about these data points. The fact that the data
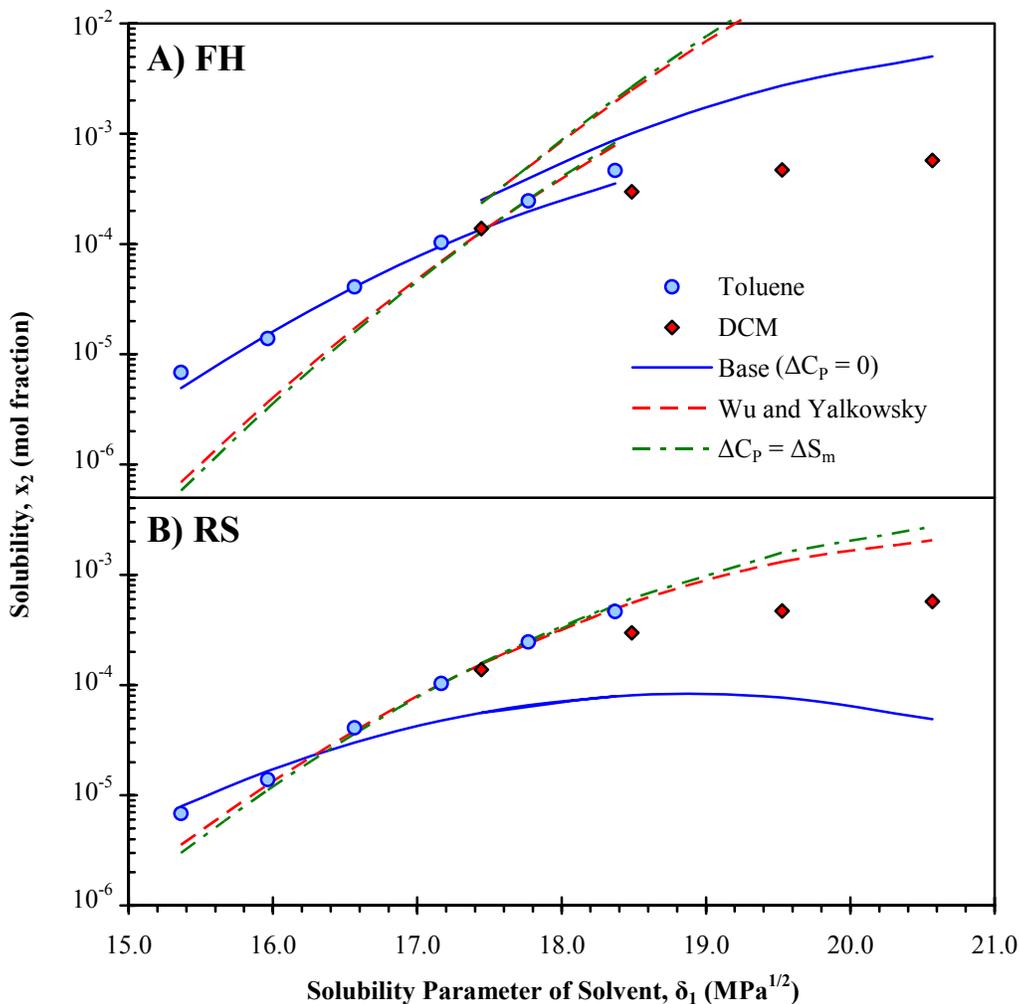
Figure 3-6: Comparison of the effect of different values of ΔC_P on the H_2TPP solubility modeling

exhibit the classical maxima that one would expect for a plot of solubility as a function of solubility parameter is encouraging. As well, the measured solubility in benzene matches very well with the current measurements in toluene indicating that the current measurements are valid and not in error.

3.3.4.2 Vanadyl Meso-Tetraphenylporphyrin (VOTPP)

The necessary solute properties for modeling the solubility of VOTPP are listed in Table 3-2. Unfortunately, no values were available in the literature for comparison of either the temperature or enthalpy of fusion. As was the case for H_2TPP, the DSC and TGA results showed signs of decomposition upon melting, which causes some difficulty in extracting the true enthalpy of melting from the DSC curve and therefore some
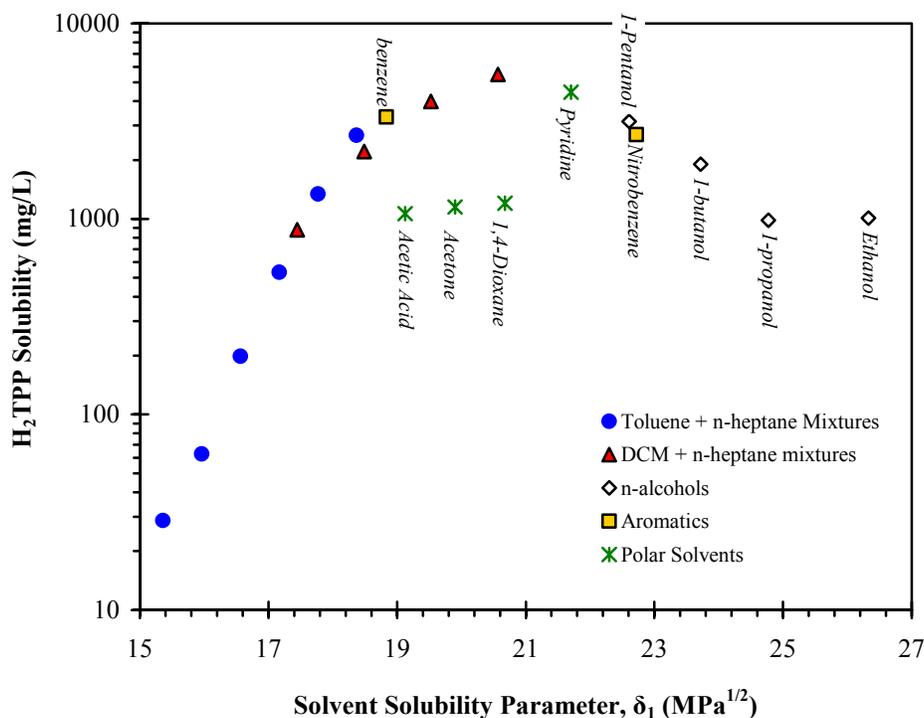
Figure 3-7: Comparison of the current solubility measurements to data reported in the literature for H₂TPP. (n-alcohol data from Berezin *et al.*[120], aromatics and polar solvents from Koifman *et al.*[193]

uncertainty in the measured value for ΔH_m. The solid molar volume is taken from the solid density measurement done by Drew *et al.*[50] (1.31 g/mL) along with the molecular weight of the pure compound.

The results of modeling the solubility of VOTPP using both the RS and FH theories are shown in Figure 3-8. Neither theory does a good job of describing all of the observed solubility behaviour for this compound when $\Delta C_P = 0$. The FH theory is reasonably close for the toluene data, but deviates by an order of magnitude for the DCM solubility. Once again, the poor performance of both models is related to the high values for both the melting point temperature and the enthalpy of fusion which give a maximum (ideal) solubility of $x_{2,ideal} = 2.40 \times 10^{-5}$ (see equation {3.17}). This value is lower than many of the measured solubilities and hence why the RS base model ($\Delta C_P = 0$) cannot adequately describe the behaviour.

The two other estimation schemes outlined previously for ΔC_P were tested as well. The results of these calculations are included in Table 3-12 and Figure 3-8. In the case of the RS theory, the quality of the fit improved significantly when using either estimate of
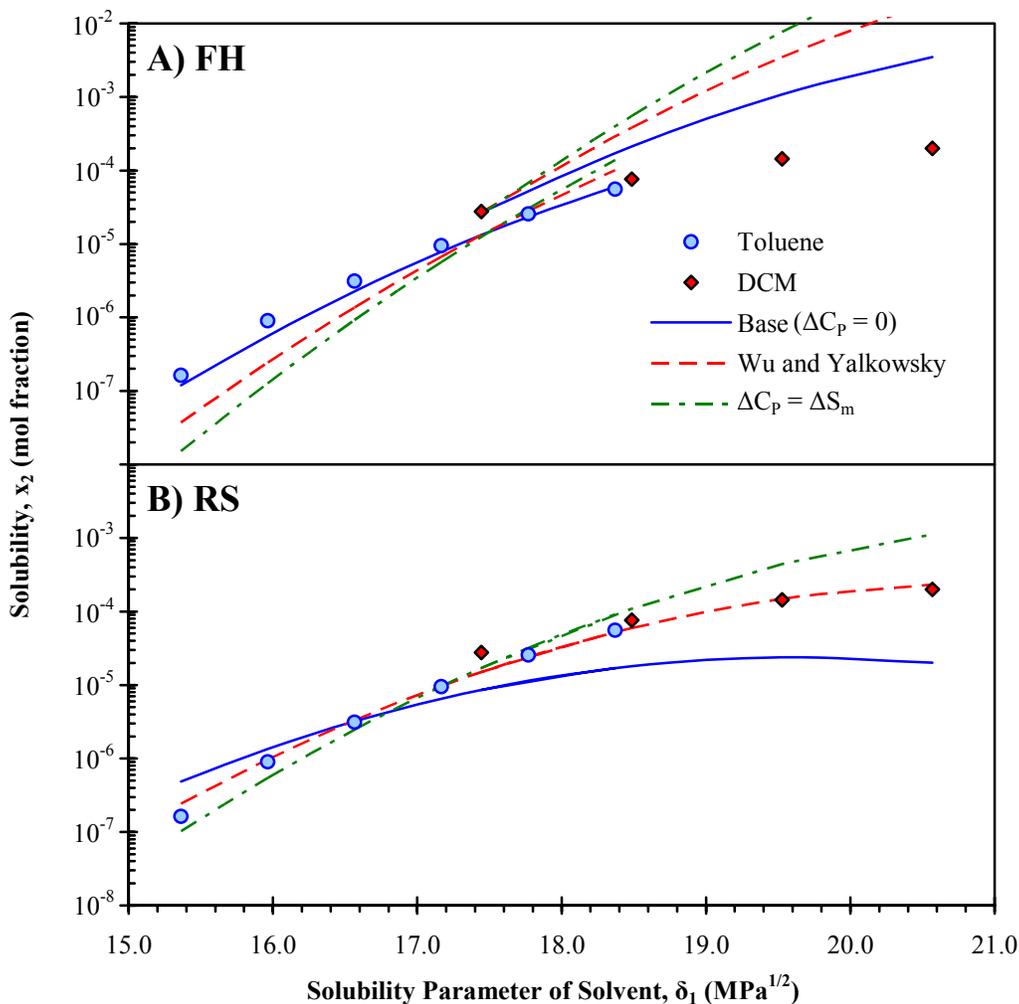
Figure 3-8: Comparison of the effect of different values of ΔC_P on the VOTPP solubility modeling ($v^L \approx v^S$)

Table 3-12: Sensitivity analysis of the effect of different values of the differential heat capacity, ΔC_P, on the regression results for VOTPP.

Method	Base		$\Delta C_P \approx \Delta S_m \approx \Delta H_m/T_m$		Wu and Yalkowsky[192]	
	RS	FH	RS	FH	RS	FH
ΔC_P (J/mol·K)	0		52.7		27.8	
δ_{VOTPP} (MPa$^{1/2}$)	19.6	20.9	22.2	23.2	21.1	22.2
Regression R^2	0.572	0.875	0.934	0.760	0.986	0.800

ΔC_P. The ΔC_P value of Wu and Yalkowsky[192] combined with the RS theory provided the best fit of all of the methods, and for the first time was able to describe the entire series of solubility data including the DCM measurements. In the case of the FH theory, the quality of the fits declined significantly when a non-zero value of ΔC_P is used. The base method ($\Delta C_P = 0$) worked the best with the FH theory, although this base method was only able to account for the behaviour in the toluene mixtures and over predicted the solubility in DCM by an order of magnitude. Once again, there was also a significant increase in the value of the regressed solubility parameter for both methods, and the values obtained with the FH theory were consistently higher by a factor of 1 MPa$^{1/2}$ or more than those obtained with the RS theory.

3.3.4.3 Octaethylporphyrin (H$_2$OEP)

The necessary solute properties for modeling the solubility of H$_2$OEP are listed in Table 3-2. The measured melting point temperature is higher than the values reported by Whitlock and Hanauer[194] (324-325°C, unknown experimental technique) and Eisner *et al.*[195] (318°C, unknown experimental technique). Unfortunately, purity is not stated in these 2 studies and impurities could result in a reduced melting temperature. Unlike the H$_2$TPP samples, the DSC and TGA results did not show signs of decomposition upon melting and therefore the value obtained for ΔH_m is deemed much more reliable. The solid molar volume is taken from the solid density measurement done by Lauher and Ibers[171] (1.19 g/mL) along with the molecular weight of the pure compound.

The results of modeling the solubility of H$_2$OEP using both the RS and FH theories are shown in Figure 3-9. The RS theory does a reasonable job of describing the overall solubility trend with $\Delta C_P = 0$, although it is not capable of capturing the discontinuity in solubility that occurs when switching from toluene to DCM as the strong solvent. The FH theory is capable of capturing the step change in solubility between toluene and DCM, although it is under predicting the toluene solubility and over predicting the DCM solubility by orders of magnitude. In the case of H$_2$OEP, the maximum (ideal) solubility is within a reasonable range for the measured data and therefore using $\Delta C_P = 0$ is still within the range of capability of the two models.

The two other estimation schemes outlined previously for ΔC_P were tested as well. The results of these calculations are included in Table 3-13 and Figure 3-9. Both of the estimation methods yield similar values for ΔC_P and therefore the resulting fits are very
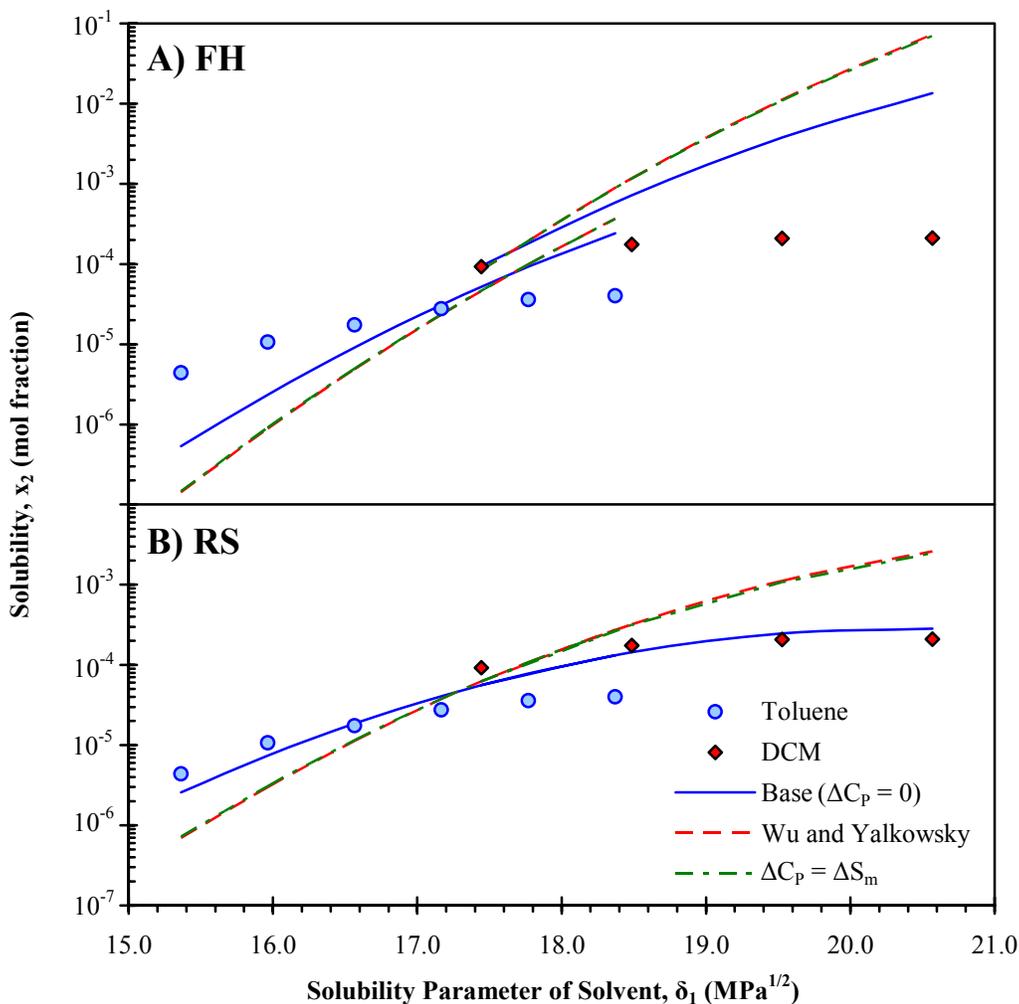
Figure 3-9: Comparison of the effect of different values of ΔC_P on the H_2OEP solubility modeling ($v^L \approx v^S$)

Table 3-13: Sensitivity analysis of the effect of different values of the differential heat capacity, ΔC_P, on the regression results for H_2OEP.

Method	Base		$\Delta C_P \approx \Delta S_m \approx \Delta H_m/T_m$		Wu and Yalkowsky[192]	
	RS	FH	RS	FH	RS	FH
ΔC_P (J/mol·K)	0		61.6		63.5	
δ_{H2OEP} (MPa$^{1/2}$)	20.4	21.6	22.2	23.2	22.3	23.2
Regression R^2	0.877	0.710	0.759	0.664	0.756	0.664

similar. For both theories, the quality of the fit worsened when the non-zero estimate of ΔC_P was used. The base method ($\Delta C_P = 0$) combined with the RS theory worked the best of all of the methods, although this base method was not able to account for the step change in solubility between toluene and DCM. Once again, there was also a significant increase in the value of the regressed solubility parameter for both methods, and the values obtained with the FH theory were consistently higher by a factor of 1 MPa$^{1/2}$ or more than those obtained with the RS theory.

3.3.4.4 Vanadyl octaethylporphyrin (VOOEP)

The necessary solute properties for modeling the solubility of VOOEP are listed in Table 3-2. Unfortunately, no values were available in the literature for comparison of either the temperature or enthalpy of fusion. Unlike the H$_2$TPP and VOTPP samples, the DSC and TGA results did not show signs of decomposition upon melting and therefore the value obtained for ΔH_m is deemed much more reliable. The solid molar volume is taken from the solid density measurement done by Molinaro and Ibers[172] (1.25 g/mL) along with the molecular weight of the pure compound.

The results of modeling the solubility of VOOEP using both the RS and FH theories are shown in Figure 3-10. Both theories do a reasonable job of describing the toluene solubility trend with $\Delta C_P = 0$, although both show signs of deviation at one end or the other of the range. As was the case for H$_2$OEP, the FH theory is capable of capturing the discontinuity in solubility that occurs when switching from toluene to DCM as the strong solvent while the simpler RS theory does not. It should be noted that the solubility data for VOOEP at DCM concentrations > 60 vol% were very high and required excessive amounts of solid solute. As such, they were not measured here.

The two other estimation schemes outlined previously for ΔC_P were tested as well. The results of these calculations are included in Table 3-14 and Figure 3-10. In the case of the RS theory, the quality of the fit improved (R^2 increased) when using either estimate of ΔC_P. However, in no case does the RS theory capture the solubility step-change. In the case of the FH theory, the qualities of the fits were all comparable, although the base method ($\Delta C_P = 0$) worked the best. The FH theory was able to predict a step-change in solubility, but was not able to capture the correct magnitude of this jump. Once again, there was a significant increase in the value of the regressed solubility parameter for both methods, and the values obtained with the FH theory were consistently higher by a factor
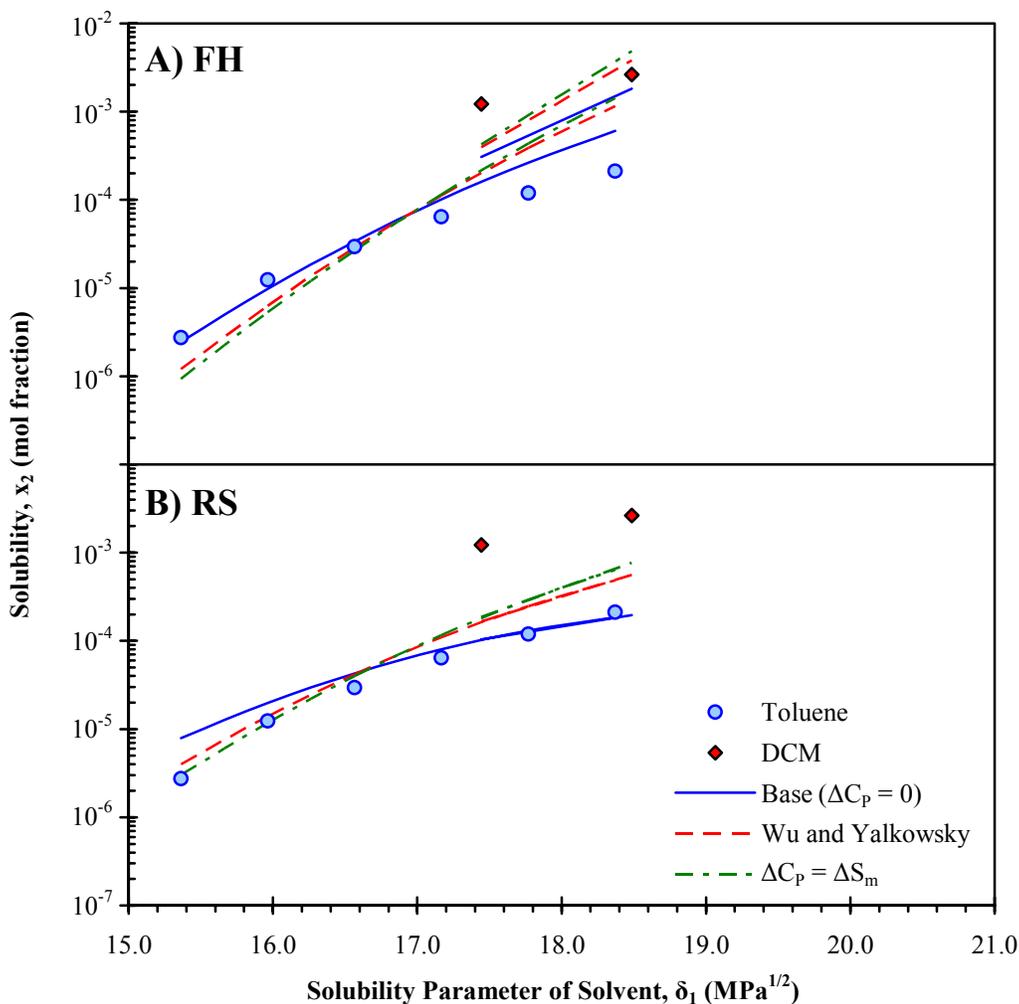
Figure 3-10: Comparison of the effect of different values of ΔC_P on the VOOEP solubility modeling ($v^L \approx v^S$)

Table 3-14: Sensitivity analysis of the effect of different values of the differential heat capacity, ΔC_P, on the regression results for VOOEP.

Method	Base		$\Delta C_P \approx \Delta S_m \approx \Delta H_m / T_m$		Wu and Yalkowsky[192]	
	RS	FH	RS	FH	RS	FH
ΔC_P (J/mol·K)	0		61.1		43.7	
δ_{VOOEP} (MPa$^{1/2}$)	19.5	20.7	21.4	22.3	20.9	21.9
Regression R^2	0.415	0.894	0.781	0.867	0.725	0.880

of 1 MPa$^{1/2}$ or more than those obtained with the RS theory.

The solubilities measured for VOOEP in DCM + n-heptane mixtures are showing anomalously high values. Although a similar increase in solubility was seen with H$_2$OEP, the magnitude of the increase for VOOEP is much greater. The current measurements are compared to the values reported by Freeman *et al.*[10] below in Figure 3-11. The equilibrium solubilities measured by Freeman *et al.* in two chlorinated solvents (DCM and chloroform) are both lower than those measured in this work for a mixture of DCM and n-heptane. The values reported by Freeman *et al.* are definitely higher than the solubility in toluene, but the magnitude of the increase is more inline with the observations with H$_2$OEP. It is suspected that perhaps the solubility measurements done for VOOEP in DCM mixtures are biased high for some reason and may not be reliable.

3.3.4.5 PBP

The necessary solute properties for modeling the solubility of PBP are listed in Table 3-2. No values were available in the literature for comparison of either the
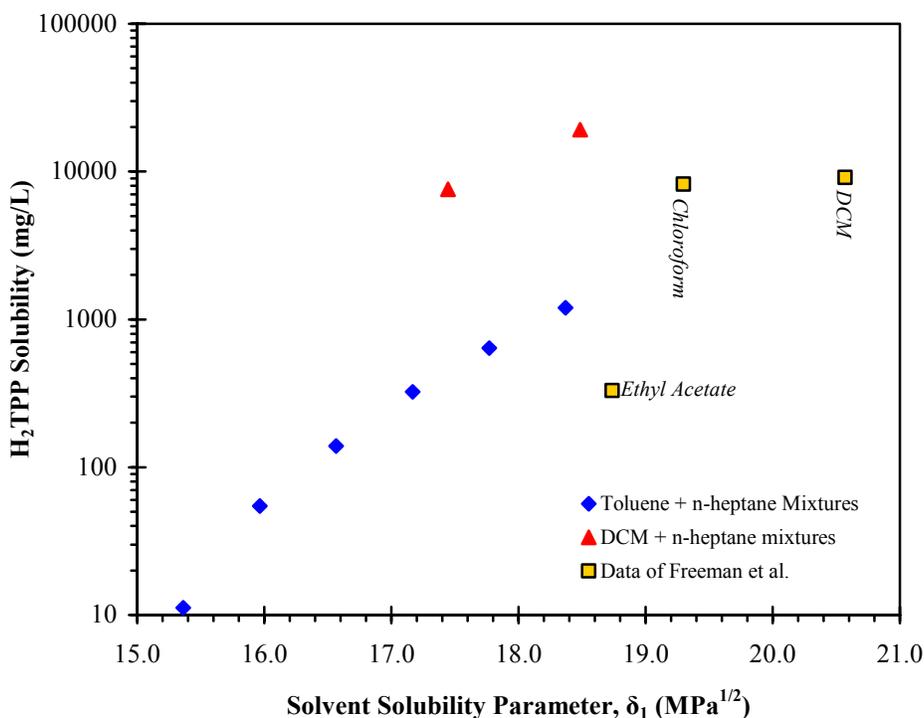
Figure 3-11: Comparison of the current solubility measurements to the data reported by Freeman *et al.*[10] for VOOEP.

temperature or enthalpy of fusion. The DSC and TGA results showed no signs of decomposition upon melting and therefore the measured value for ΔH_m is reliable. The solid molar volume is taken from the solid density measurement done by Tan *et al.*[144] (1.34 g/mL) along with the molecular weight of the pure compound.

The results of modeling the solubility of PBP using both the RS and FH theories are shown in Figure 3-12. Neither theory does a good job of describing all of the observed solubility behaviour for this compound when $\Delta C_P = 0$. The FH theory is reasonably close for the toluene data, but deviates by orders of magnitude for the DCM solubility. The poor performance of both models is related to the high value for the enthalpy of fusion which gives a maximum (ideal) solubility of $x_{2,ideal} = 1.22 \times 10^{-4}$ (see equation {3.17}).
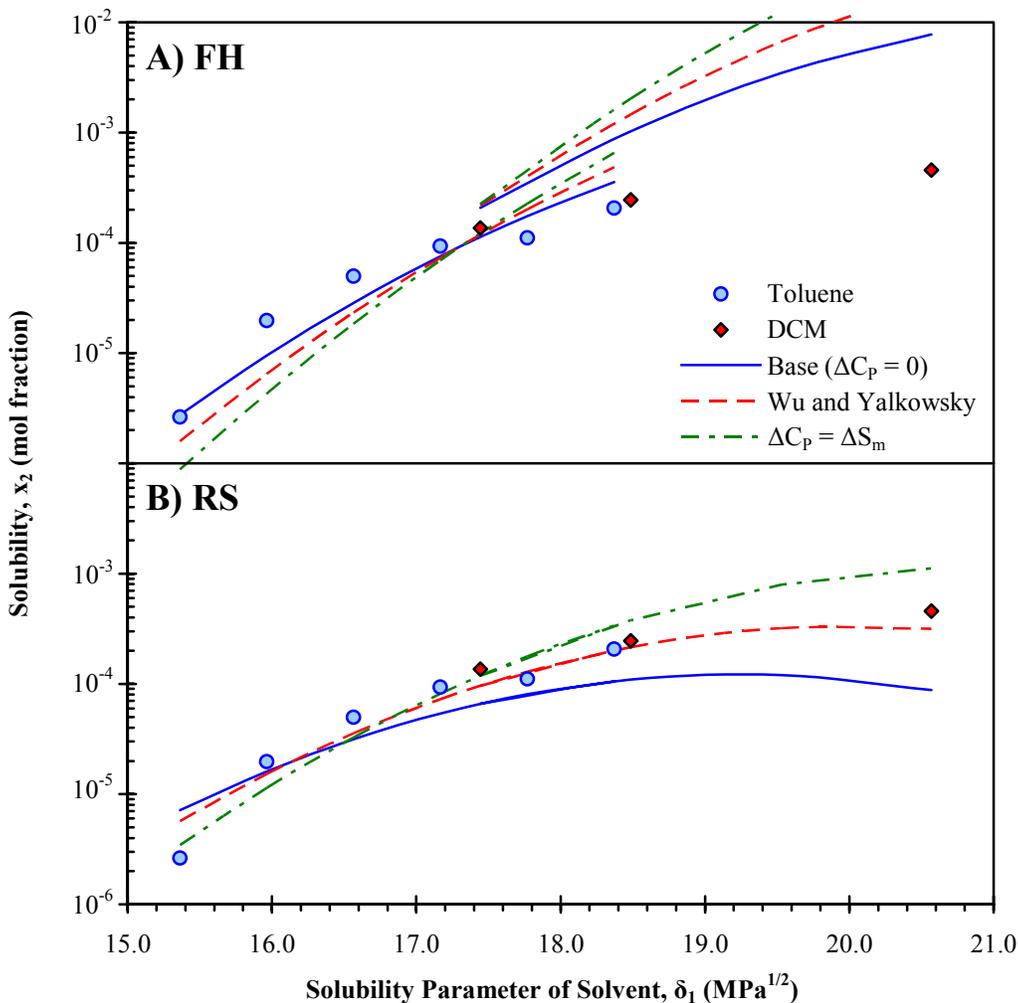
Figure 3-12: Comparison of the effect of different values of ΔC_P on the PBP solubility modeling ($v^L \approx v^S$)

This value is lower than many of the measured solubilities and hence why the RS base model ($\Delta C_P = 0$) cannot adequately describe the behaviour.

The two other estimation schemes outlined previously for ΔC_P were tested as well. The results of these calculations are included in Table 3-15 and Figure 3-12. In the case of the RS theory, the quality of the fit improved when using either estimate of ΔC_P. In the case of the FH theory, the quality of the fits declined when a non-zero value of ΔC_P is used. The base method ($\Delta C_P = 0$) worked the best with the FH theory, although this base method was only able to account for the behaviour in the toluene mixtures and over predicted the solubility in DCM by an order of magnitude. Once again, there was also a significant increase in the value of the regressed solubility parameter for both methods, and the values obtained with the FH theory were consistently higher by a factor of 1 $MPa^{1/2}$ or more than those obtained with the RS theory.

Table 3-15: Sensitivity analysis of the effect of different values of the differential heat capacity, ΔC_P, on the regression results for PBP.

Method	Base		$\Delta C_P \approx \Delta S_m \approx \Delta H_m/T_m$		Wu and Yalkowsky[192]	
	RS	FH	RS	FH	RS	FH
ΔC_P (J/mol·K)	0		103		46.4	
δ_{PBP} ($MPa^{1/2}$)	19.3	20.4	20.9	22.0	20.0	21.2
Regression R^2	0.610	0.807	0.941	0.730	0.935	0.764

3.4 Group-Contribution Modeling

Numerous investigators have attempted to apply group contribution methods for estimating the solubility parameters of asphaltene type molecules[196, 197]. A small cross section of these methods will be tested on the model compounds in this study to determine if it is appropriate to apply these methods to the type of molecules expected in asphaltene fractions.

Jaffe et al.[197] applied the group contribution method of Fedors[198] to estimate the solubility parameters for hypothetical asphaltene structures. The method of Fedors[198] estimates the energy density ($\Delta e = \Delta H_v - RT$) and the liquid molar volume (v) using a group contribution methodology. This method was intended for use with polymers, but was extended by Jaffe et al.[197] to asphaltenes. The results predicted by this method for

some of the model compounds are summarized in Table 3-16. Rogel[196] also used

Fedors' method to predict the solubility parameter for hypothetical asphaltene structures.

These solubility parameters were then correlated to the hydrogen to carbon ratio (H/C)

for the compounds and a linear fit obtained. This linear fit was used to predict the

solubility parameters for the model compounds in this study and the results are included

in Table 3-16. The values for VOTPP and VOOEP were not included in the analysis

since these group contribution methods do not include vanadium or vanadyl as a group.

The δ_{FIT} values included in Table 3-16 are the values which corresponded to the best fit

of all of the methods applied based on the highest R^2 value. These values were chosen

since they best capture the solubility behaviour of the model compounds and as such

represent the best value for the solubility parameter. The exception was pyrene, where

the base fit was chosen since this value was obtained with known pure component

properties and as such this value of δ is a true representation of the full RS theory.

Table 3-16: Comparison of group contribution
predictions of solubility parameters to the best fit
values for the model compounds

Compound	δ (MPa$^{1/2}$)		
	Fedors	**Rogel**	**Best Fit**
H$_2$TPP	26.3	28.7	21.2[a]
H$_2$OEP	22.8	22.4	20.4[b]
PBP	22.4	28.6	20.9[c]
Pyrene	22.8	29.3	21.1[d]

a - δ_{FIT} from RS theory + ΔC_P from Wu and Yalkowsky[192]
b - δ_{FIT} from RS theory + $\Delta C_P = 0$
c - δ_{FIT} from RS theory + $\Delta C_P \approx \Delta S_m \approx \Delta H_m/T_m$
d - δ_{FIT} from Base RS theory

Neither of these methods is able to adequately match the best fit results obtained in

the preceding solubility analysis. With the exception of H$_2$OEP, the results obtained

from the method of Rogel[196] are not even close to the best fit values. As discussed

previously, even small differences in the value of δ can lead to large discrepancies in the

predicted solubility as a result of the exponential dependence of solubility on the square

of the solubility parameter. Therefore, the values obtained by Rogel's method are not

recommended. Fedors' method performed slightly better, although they are still much

higher than the best fit values and as such are not recommended. The fact that Fedors'

method did not perform well is not surprising considering the simple nature of this

method. This method does not have any explicit means/groups for accounting for fused aromatic structures. Since all of these model compounds contain significant aromatic character, this is a major weakness for this method when applied to asphaltenes.

Several other more advanced group contribution methods were considered for modeling the solubility parameters of these model compounds[199-202]. However, all of these models lacked the necessary groups to correctly describe the structures of the model compounds. In particular, these methods do not have explicit groups to take into account fused aromatic structures nor do they have groups to take into account aromatic nitrogen structures such as pyridine or pyrrole, both of which are abundant in the current model structures. Therefore, it was not deemed necessary to apply these models when they are deficient from the start.

One group contribution method which does take into account fused aromatic structures as well as various forms of aromatic nitrogen is the method of Marrero and Gani[203]. This method uses a three level group contribution approach which corrects for larger molecular structures (e.g. fused aromatics and isomers). Therefore, this model should be able to represent the model structures being considered herein. Unfortunately, this model does not include the liquid molar volume or the solubility parameter explicitly and therefore it cannot be used to predict these values. It is capable of predicting the melting point properties and these values are summarized in Table 3-17. Once again, VOTPP and VOOEP were not included since vanadium and vanadyl groups are not included in the method. Within the framework of the Marrero-Gani method, the porphyrin backbone can be described in two ways: as a large fused aromatic structure or as a cyclic structure. Both of these predictions are included in Table 3-17 below.

This method does a very good job of describing the pyrene properties, which is not surprising since pyrene is a fundamental building block within the method and its properties are included explicitly in the regression of the group contributions. Therefore, this method has been optimized for pyrene and it should yield good results.

In the case of the porphyrins, this method significantly under predicts the melting point temperatures, with the aromatic formalism yielding better results in both cases. As for the enthalpy of fusion, this method seems to over predict the value by quite a large margin with the exception of the aromatic formalism for H_2OEP which was very close to the actual value. The fact that this method has difficulty describing the porphyrins is not surprising. The porphyrin backbone is a very special case with some unique molecular

Table 3-17: Comparison of Marrero-Gani group contribution predictions of melting point parameters to the measured values for the model compounds

Compound	Measured		Predicted			
	ΔH_m (kJ/mol)	T_m (K)	ΔH_m (kJ/mol)	% error	T_m (K)	% error
H_2TPP^{cyc}	38.4	726	58.2	52%	549	-24%
H_2TPP^{aro}			69.1	80%	579	-20%
H_2OEP^{cyc}	38.0	616	63.9	68%	467	-24%
H_2OEP^{aro}			37.1	-2.4%	521	-15%
PBP	52.1	506	63.3	21%	562	11%
Pyrene	17.4	424	17.3	-0.6%	421	-0.7%

cyc - Assumes an aromatic structure for the porphyrin backbone
aro - Assumes a cyclic structure for the porphyrin backbone

properties. Unless the method takes this into account explicitly (which it doesn't), then it is unlikely that it will be able to accurately model its behaviour.

In the case of PBP, this model does a better job than it did for the porphyrins. Again, this is expected since pyrene and its various substitutions have been accounted for directly by this method. Despite being a better fit for this method, PBP's properties were still only predicted to within an order of magnitude ($\Delta T_m = +56°C$, $\Delta(\Delta H_m) = 11.2$ kJ/mol) and therefore this method cannot be relied upon for anything more than orders of magnitude for asphaltene molecules.

3.5 General Discussion

The relatively simple RS and FH theories, which are so prevalent in the literature for modeling the solution behaviour of asphaltenes, had difficulty capturing the observed solubility behaviour of the model compounds in this study. This is not surprising since the main parameter used to capture the behaviour, the solubility parameter, is a hypothetical construct for these molecules at the conditions considered. Add to this the fact that the reference point (the normal melting point) is far removed from the actual system conditions and these models quickly degrade. The use of the hypothetical subcooled liquid as the reference state for these systems represents a huge extrapolation and is likely not a very appropriate choice for such high melting compounds.

The combination of all of these factors indicates that these simple models are not recommended as a rigorous treatment of the solution behaviour of these model compounds or any such complex, high melting compounds. The best fit solubility parameters obtained herein represent an empirical correlation which may be adequate for engineering design calculations, provided all of the other parameters are kept the same as was used in the fitting procedure (i.e. ΔC_P, ΔH_m, and v^L). However, to attempt to draw any specific conclusions from the solubility parameters obtained herein or to extend these parameters to other models would not be recommended as these values do not necessarily have a sound thermodynamic basis.

Chapter **4**

Diffusion Measurements

Now that the solubility behaviour of pure model porphyrins has been determined, their diffusion properties in toluene will be studied to gain insight into the stability of the aforementioned aggregation behaviour.

4.1 Introduction

The main goal of this portion of the work is to ascertain the stability of the aggregation occurring in solution for the asphaltene fraction. As stated earlier, vanadium is contained within this fraction and as such it is likely that the vanadyl porphyrins are participating in this aggregation phenomenon.

Obviously, in order to selectively remove the metalloporphyrins from the asphaltenes, it is necessary to determine how strongly the metalloporphyrins are retained within the asphaltene aggregates and to determine whether or not there is an exchange of these species between the free solution and the aggregates. This was done using a stirred diaphragm diffusion cell. If a diaphragm is selected with a pore size small enough to retain the aggregated structures yet large enough to allow the free passage of the molecules in free solution, then metalloporphyrin molecules in free solution will diffuse across the diaphragm. This would result in a decrease in the concentration of metalloporphyrins in free solution on the retentate side of the diaphragm. According to LeChatelier's principle, if the aggregation process is reversible, more porphyrins should be released from the aggregates in order to maintain equilibrium. This would result in additional flux of metalloporphyrins across the diaphragm until the two sides of the diaphragm equalize at a concentration equal to half of the total amount loaded to the cell.

That is, unless the porphyrins are so strongly bound by the asphaltenes that the energy barrier is too great and the metalloporphyrins remain in the aggregates. If the latter is true, then the concentration of metalloporphyrins on the permeate side of the diaphragm would plateau at a value well below the expected concentration based on the total amount initially present.

The same type of mechanism would hold true for the asphaltenes. Asphaltene molecules which are in free solution will diffuse across the diaphragm causing a decrease in concentration on the retentate side. Again, under this scenario, if the aggregation is reversible then more asphaltene molecules should be released from the aggregates to maintain equilibrium causing additional flux of asphaltenes across the diaphragm. However, if the aggregation process is irreversible then one would expect the concentration of asphaltenes on the permeate side of the diaphragm to plateau at a concentration well below half of the total initial concentration.

In this way, the stability of the aggregated structures will be probed using the stirred diaphragm diffusion cell technique. By continuously monitoring the composition of the permeate side of the diaphragm, it will be possible to determine the stability of the aggregated species in solution, as well as gain insight into the rate of exchange of molecules between the aggregated state and free solution.

4.2 Analysis of Stirred Diaphragm Diffusion Cells

4.2.1 BACKGROUND

This technique was first applied by Northrup and Anson[204] to study hemoglobin. Their original cell did not incorporate any external stirring mechanism and relied solely on natural convection as a result of density differences to mix the contents of each compartment. The technique in this form was thoroughly reviewed several years later by Gordon[205]. At this point, the general technique still relied on natural convection to mix the compartments, which was enhanced by orienting the cell vertically with the diaphragm oriented horizontally. The higher density (i.e. high concentration) solution was loaded in the upper compartment and the lower density (i.e. low concentration) solution in the lower compartment[205]. In this way, the density differences would enhance the mixing in each reservoir.

Stokes[206] was the first to pioneer a mechanically stirred diaphragm diffusion cell, with magnetic stirrers parallel and of equal size to the diaphragm. The Stokes cell quickly became the standard for diaphragm diffusion measurements and this technique has since become a standard technique for diffusion measurements.

All of the aforementioned diaphragm diffusion cells were operated with the cell oriented vertically and the diaphragm in the horizontal position. Also, in the case of the Stokes cell, the stirrers are placed very close to (if not resting on) the diaphragm surface and are of comparable size to the diaphragm. Holmes *et al.*[207, 208] were the first to apply a stirred diaphragm diffusion cell oriented horizontally with the diaphragm oriented vertically. In their cell, the stirrers are not oriented parallel to the diaphragm, but rather are placed at the bottom of each reservoir (i.e. perpendicular to the diaphragm). These investigators performed a mechanistic study on the impact of external mass transfer (i.e. stirrer speed) on the cell constant for such a horizontal diffusion cell[207]. Their results indicated that the difference in cell constant between free convection and complete stirring (i.e. no external resistance) was ~6.4-6.8%. However, the difference between a stirrer speed of 220 rpm and 350 rpm was much less pronounced and at these speeds the external mass transfer was deemed to account for less than 0.5% of the cell constant. Therefore, it is possible to orient the cell horizontally, which has obvious advantages with respect to supporting and loading the cell as well as driving the magnetic stirrers.

The most common type of diaphragm used for diffusion measurements is a sintered glass frit with 2-10 μm pores (fine grade frit)[209]. As will be discussed in the next section, the choice of this form of diaphragm is born out of considerations for minimizing bulk flow. Other advantages of the glass frit are its universal solvent compatibility (with the obvious exception of hydrofluoric acids) as well as its mechanical stability. Despite these numerous advantages, several investigators have devised cells to use filtration membranes rather than glass frits as the operating diaphragm[210-218]. The primary advantage of the filtration membranes is much shorter experiments as a result of the significantly shorter diffusion path. Most glass frits have thicknesses on the order of 5 mm compared to filtration membrane thicknesses on the order of 150 μm (a decrease by a factor of 33). As will be shown in the next section, the total time required is directly proportional to the length of the diffusion path and therefore membranes result in significantly shorter experiments.

4.2.2 EQUATIONS FOR ANALYZING STIRRED DIAPHRAGM DIFFUSION CELLS

The analysis of this type of experiment has been thoroughly reviewed in the literature numerous times[205, 209, 219] and therefore only a brief introduction to the governing equations will be given here.
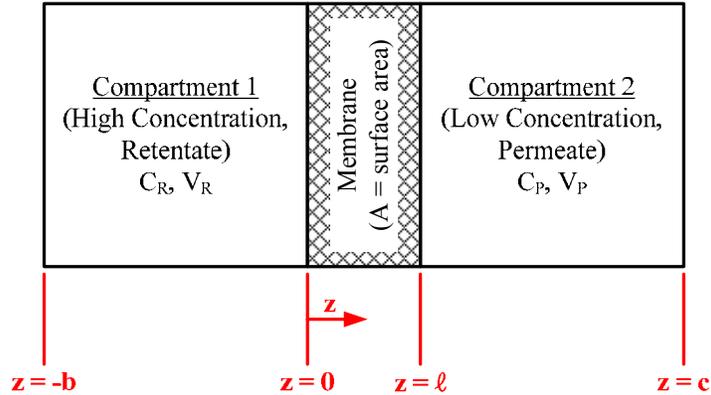
Figure 4-1: Schematic diagram for analysis of diffusion cell. (V_R, V_P = compartment volumes, C_R, C_P = molar concentrations of solute in each compartment, A = membrane surface area)

A schematic diagram for analyzing this apparatus is shown in Figure 4-1. The analysis that follows first assumes that the two compartments are well mixed such that the concentrations in each are uniform throughout. This implies that the mathematical analysis of the diffusion process will be done on the diaphragm itself since no diffusion occurs in the compartments. If it is further assumed that:

1. Diffusion only occurs in the direction normal to the diaphragm surface (i.e. radial symmetry for a circular diaphragm), as denoted by z in Figure 4-1

2. There is no bulk flow through the pores of the diaphragm (i.e. flux is a result of diffusion only)

3. The diffusivity, D_{AB}, is assumed independent of concentration

4. The behaviour of the solute in solution is sufficiently ideal such that the chemical potential can be replaced by concentration as the primary driving force.

then the governing differential equation will take the form of Fick's second law[220] with one initial condition (IC) and two boundary conditions (BC):

$$\frac{\partial C_A}{\partial t} = D_{AB} \frac{\partial^2 C_A}{\partial z^2}$$

IC: $\quad C_A(t,z) = C_0(z)$ for $t = 0$ and $0 \leq z \leq \ell$ .... {4.1}

BC1: $\quad C_A(t, z = 0) = C_R(t)$ for $t > 0$

BC2: $\quad C_A(t, z = \ell) = C_P(t)$ for $t > 0$

The above boundary conditions are particularly difficult to deal with since they vary with time. The above problem was first solved by Barnes[221] for the concentration profile in the membrane. In the case of the diaphragm cell, it is the concentration in the two compartments that we are most interested in and the solution obtained by Barnes can be converted to $C_R(t)$ and $C_P(t)$ with some additional restrictions. For example, if we let λ = the ratio of diaphragm volume to compartment volume and if it is assumed that the diaphragm is initially filled with solvent ($C_A = 0$), then the solution for the concentration in the permeate compartment as a function of time is:

$$C_P(t) = \frac{C_{P,0}}{2}\left[1 - \frac{\lambda}{2} + \frac{\lambda^2}{4} + \left(1 - \frac{\lambda}{6} + \frac{\lambda^2}{60}\right)e^{\left(\frac{-2D_{AB}At}{\ell V_2}\right)\left(1 - \frac{\lambda}{6} + \frac{\lambda^2}{45}\right)} + \sum_{i=1}^{\infty} \frac{4\lambda}{i^2\pi^2}\left(1 - \frac{6\lambda}{i^2\pi^2}\right)e^{\left(\frac{-D_{AB}t}{\ell^2}\right)\left(i^2\pi^2 + 4\lambda\right)}\right]$$

.... {4.2}

This complex infinite sum is prohibitively difficult to apply through the course of a normal diaphragm diffusion cell experiment. A simpler analysis can be done by making the rather LARGE assumption that the concentration gradient in the diaphragm is linear at any given point in time and as such we have a pseudo-steady state process. This assumption simplifies the governing differential equation significantly and results in the following equation for the flux of solute A, N_A, across the membrane at any given time t:

$$N_A\left(mol/m^2 \cdot s\right) = \frac{D_{AB}}{\ell}\left(C_R - C_P\right) \text{.................................. {4.3}}$$

This equation represents a simple solution of Fick's first law of diffusion for a linear concentration gradient through the diaphragm. If we use equation {4.3} to write material balances for each compartment:

$$V_R \frac{dC_R}{dt} = -\frac{AD_{AB}}{\ell}\left(C_R - C_P\right) \text{.................................. {4.4}}$$

$$V_P \frac{dC_P}{dt} = \frac{AD_{AB}}{\ell}\left(C_R - C_P\right) \text{.................................. {4.5}}$$

It should be noted that equations {4.4} and {4.5} assume that the volume of the membrane, and hence the material contained within it, are small and negligible. Taking the sum of equations {4.4} and {4.5} and setting $C_R-C_P = \Delta C$ gives:

$$\frac{d\Delta C}{dt} = -D_{AB}\frac{A}{\ell}\left[\frac{1}{V_1} + \frac{1}{V_2}\right]\Delta C \quad \text{.................................. } \{4.6\}$$

Equation {4.1} can be integrated from $t = 0 \rightarrow t$ and from $\Delta C = \Delta C_0 \rightarrow \Delta C_t$ to give:

$$\ln\left[\frac{\Delta C_o}{\Delta C_t}\right] = \beta D_{AB}t \quad \text{.............................. } \{4.7\}$$

$$\text{where } \beta = \left(\frac{A}{\ell}\right)_{eff}\left[\frac{1}{V_R} + \frac{1}{V_P}\right]$$

Equation {4.7} is the standard equation used for analysis of diaphragm diffusion cells[205, 209, 219] where β is referred to as the cell calibration constant. If only one of the two compartment concentrations is measured, as is the case in this work, then the second concentration must be inferred using an overall mass balance:

$$C_R = C_{R,0} - C_P \quad \text{... } \{4.8\}$$

Equation {4.8} implicitly assumes constant density, negligible diaphragm volume, and equal volumes on both sides of the diaphragm. Substituting this result into equation {4.7} gives

$$\ln\left[\frac{C_{R,0}}{C_{R,0} - 2C_P}\right] = \beta D_{AB}t \quad \text{.. } \{4.9\}$$

Stirred diaphragm diffusion cells, along with equation {4.9}, can be used to determine both self-diffusion coefficients (using isotopically labeled species as the solute) as well as mutual diffusion coefficients. In the current work, all diffusion coefficients determined are mutual diffusion coefficients for the given solute in the solvent (toluene primarily). The derivation of these operating equations relied on several sizeable assumptions which require further discussion prior to its application.

4.2.2.1 All Transport in the Diaphragm is by Diffusive Flux

This implies that convection and/or bulk flow are negligible within the pores of the diaphragm. As long as the size of the pores is sufficiently small, this assumption should

be valid. According to Gordon[205], pore sizes <5 μm are sufficient to eliminate bulk flow. Most if not all filtration membranes that will be used in this work have pore sizes << 5 μm and therefore this assumption does not pose any concerns.

4.2.2.2 No Volume Changes of Mixing

The material balance equations {4.4} and {4.5} assume implicitly that the volume in each compartment remains constant and that the density of each compartment is also constant. For highly non-ideal and/or highly concentrated mixtures, this is not the case. However, the conditions used throughout this work are sufficiently dilute that any changes in density as a result of concentration changes should be negligible.

4.2.2.3 The concentration in Each Compartment is Uniform

The use of an external stirrer will help to minimize these effects.

4.2.2.4 Pseudo-Steady State (i.e. Linear Concentration Profile)

This is the most contentious of the assumptions made to develop the operating equation for this type of apparatus. According to the solution obtained by Barnes[221], this condition is not possible. However, if we recognize that for this type of experiment the ratio of diaphragm volume to compartment volume (λ) is small, then all terms including λ are negligible and equation {4.2} simplifies to equations {4.7} and {4.9}. This is particularly true for diffusion cells using filtration membranes as the diaphragm since the volume of the membrane is very small.

In an effort to meet this assumption, early investigators generally applied a pre-diffusion step as recommended by Gordon[205] in order to establish a linear concentration profile across the membrane. However, as was shown by Holmes *et al*.[207, 208] and Mills *et al*.[222], this is not necessary as long as λ is kept low and the time for the experiment is relatively long. Starting with a diaphragm initially filled with solvent is appropriate and any errors present by doing so will be small. In fact, as long as the calibration experiments are done with the same procedure (see section 4.2.3) then any errors will be accounted for in the value of β.

4.2.2.5 Constant Diffusion Coefficient

This assumption is common to almost all diffusion experiments since the equations become very difficult if not impossible to solve for concentration dependent diffusivity.

For concentrated solutes, it is not generally valid to assume no concentration dependence for D_{AB} and as such the analysis would be incorrect. Diffusion coefficient values obtained from diaphragm cell experiments using equation {4.7} represent an average or "integral" diffusion coefficient spanning the concentration range used for the experiment and is generally denoted by $\overline{D}$. Gordon[205] and later Stokes[11] developed procedures for converting a series of "integral" diffusion coefficients at different average concentrations to true differential coefficients. However, it should be noted that at dilute concentrations as are used in this work, the concentration dependence should be small and the integral coefficients should approach the differential diffusion coefficients at infinite dilution for the solutes of interest.

4.2.3   CALIBRATION OF DIAPHRAGM DIFFUSION CELLS

The cell constant, β, given in equation {4.7} is fixed for a given diaphragm/membrane. However, the surface area and length terms appearing in this equation are not the total surface area and length of the diaphragm itself but rather they are the open pore surface area and length of the pores in the diaphragm. Therefore, the ratio $(A/\ell)_{eff}$ will be a function of the diaphragm properties:

$$\left(\frac{\ell}{A}\right)_{eff} = \frac{\ell \cdot \tau}{A_{membrane} \cdot \varepsilon} \quad \text{..} \{4.10\}$$

where ε = membrane porosity
        τ = pore tortuosity.

Since the tortuosity and porosity are average parameters at best, it is not generally possible to calculate $(A/\ell)_{eff}$ and as such the value of β is usually determined experimentally using a solute with know diffusivity.

The normal calibration standard for determining β is aqueous potassium chloride (KCl)[205, 209, 219] since accurate differential diffusion coefficients are available over a relatively wide range of concentrations making it an ideal calibrant. A more detailed description of the data and procedure for using aqueous KCl to calibrate a stirred diaphragm diffusion cell are given in Appendix A. Since the focus of the present work is for non-aqueous systems, the question arises as to the suitability of using an aqueous system to calibrate a diaphragm for non-aqueous diffusion measurements. Mills[223] has shown that this is indeed a valid procedure to employ. It should be noted, however, that this was done for a standard glass frit diaphragm in a Stokes type vertically stirred cell.

When switching to a non-aqueous system, the calibration obtained from aqueous KCl will hold provided the following conditions are met:

1. The pore properties of the diaphragm do not change when a non-aqueous solvent is used.

2. The external mass transfer characteristics at the membrane face do not change appreciably when a non-aqueous solvent is used.

Condition one is easily met by a glass frit since the non-aqueous solvents do not impact the properties of the glass (e.g. swelling). The second condition is generally met by stirring at a rate such that external mass transfer effects are minimized, which is usually confirmed experimentally. For relatively thick glass frits, the magnitude of the external mass transfer resistance is small relative to the resistance of the diaphragm as a result of the longer diffusion path[207]:

$$\beta = \left(\frac{1}{V_R} + \frac{1}{V_P} \right) \frac{1}{2D/kA + (\ell/A)_{eff}} \quad \text{............................. \{4.11\}}$$

where   k = mass transfer coefficient @ membrane surface (m/s)
        A = membrane total exposed surface area (m^2)
        D = diffusion coefficient (m^2/s)

From equation {4.11}, it is evident that as long as the diffusion path is long (or more importantly the ratio of diffusion pathlength to area, $(\ell/A)_{eff}$ is large compared to 2D/kA) then external mass transfer has a negligible impact on the total value of β.

However, when a filtration membrane is used as the diaphragm, the magnitude of the diaphragm resistance is reduced significantly since they are much thinner than the traditional glass frit. As such the external mass transfer resistance becomes significant[224-226]. Since the external mass transfer resistance is a function of the properties of the solvent (viscosity, μ, and density, ρ), making a switch from an aqueous to a non-aqueous medium will certainly change the external mass transfer resistance at the membrane face and therefore should be accounted for if the standard aqueous KCl calibration is used. As is discussed further in Appendix A, attempts to develop a mass transfer correlation for this cell were not very successful and led to poor results. Also, unlike the traditional glass frits, there is no guarantee that the organic solvent used in this work (toluene) will not have an effect on the pore properties of the polymeric membranes. Even though the materials of the membranes were carefully chosen to

eliminate such effects (see section 4.3.2), it is not possible to eliminate this possibility. Another drawback of using aqueous KCl as the calibrant is the fact that UV/Visible spectroscopy cannot be used for measurement of KCl concentrations. The only suitable technique would be Ion Chromatography (IC) and this technique cannot be done in-situ as in the case for the UV/Visible spectroscopy. The mathematical analysis would not be the same as for the analysis of the porphyrins and asphaltenes and therefore using aqueous KCl does not represent a true calibration of the entire apparatus. Therefore, an alternate method for calibrating the membranes in this work is required.

The best option would be to use a calibration system which has properties that are close to or the same as those at the conditions of interest in this work. Since the solvent used in all of the diffusion work was toluene, the ideal calibration system would use toluene as the solvent. Also, because of the relatively large nature of the molecules being studied herein, it would be ideal to choose a calibration solute with a size that is comparable to the asphaltenes and metalloporphyrins studied in this work. Two possible solutes that meet these requirements are meso-tetraphenylporphyrin (H$_2$TPP) and vanadyl meso-tetraphenylporphyrin (VOTPP). Diffusion coefficient data obtained using Taylor dispersion methods are available for both of these solutes in toluene at 25°C[227, 228]. These data, along with some additional data for the diffusion of palladium[229] (PdTPP) and Zinc[227] (ZnTPP) meso-tetraphenylporphyrin are shown in Figure 4-2. In order to allow for a consistent comparison across multiple solvents, the data are plotted in a linearized form (a generalized form of the Stokes-Einstein equation) that has been corrected for both the viscosity of the solvent and the system temperature.

It would be particularly advantageous to use the VOTPP data point for calibration since it includes the effect of the vanadyl group on the diffusion. However, further inspection of this plot indicates some discrepancies in the data for VOTPP. The data of Saiki *et al.*[227] seem very consistent for both H$_2$TPP and ZnTPP and show a lot less scatter than the VOTPP data of Hejtmánek & Schneider[228]. In fact, the data point for VOTPP in cyclohexane shows an anomalous deviation from the rest of the data. This calls into question the validity of the data generated by these authors and as such it would not seem wise to use this data for calibration purposes. The H$_2$TPP data of Saiki *et al.*[227], along with their corresponding best fit line, seem to fall in the center of the other data points for the metalloporphyrins indicating that the metal atom at the center of the porphyrin ring has little effect on the mobility of the porphyrin backbone and as such the
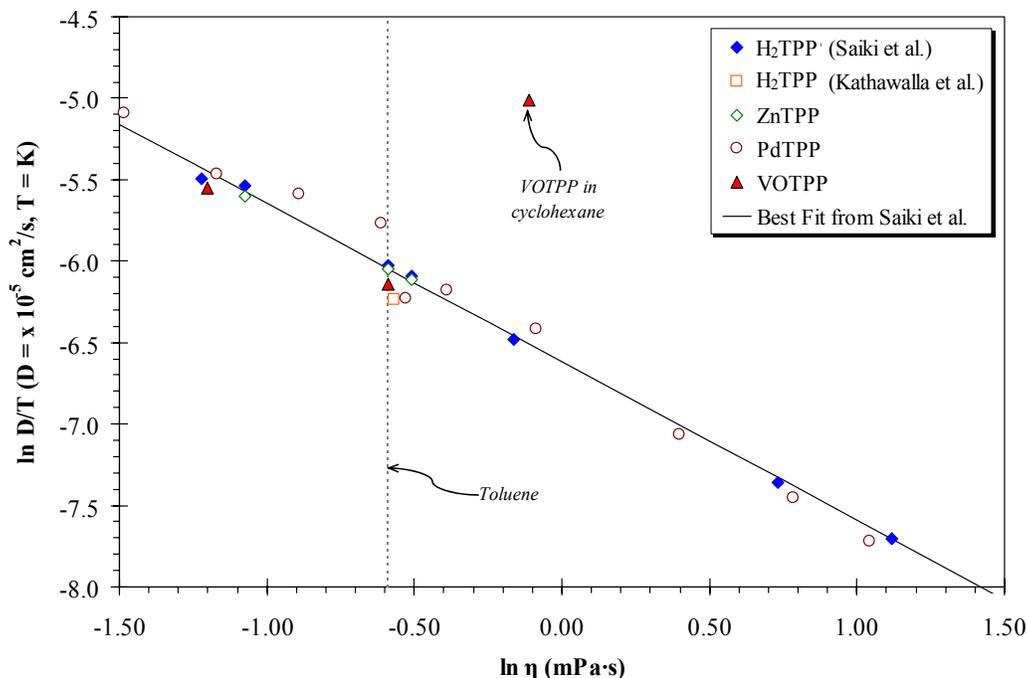
Figure 4-2: Comparison of diffusion data for meso-tetraphenylporphyrins; H_2TPP and ZnTPP – Saiki et al.[227] and Kathawalla et al. [230], VOTPP – Hejtmánek & Schneider[228], PdTPP – Kapinus and Kholodenko[229], viscosity data taken from various sources[231-244].

diffusion coefficient for the metalloporphyrins should be very close to that for the free base porphyrin.

Therefore, the calibration of membranes for the remainder of this work will be done using H_2TPP in toluene as the test solute with a diffusion coefficient of $7.18\pm0.05\times10^{-6}$ cm^2/s[227] at 25°C. By using a test solute dissolved in toluene, there will be no need to correct the calibration for external mass transfer effects, assuming that the presence of the solute does not affect the viscosity of the solution and assuming that the stirrer speed is the same for both the calibration and diffusion runs. Considering the dilute nature of the solutions used in this work, it is not anticipated that viscosity will change appreciably. Also, using a test system with toluene as the solvent ensures that the effects of toluene on the pore structure of the membrane are accounted for. As well, because H_2TPP is of comparable size to the solutes of interest (virtually the same size as the metalloporphyrins, comparable in size to asphaltenes in free solution) the calibration of the membranes will account for hindered diffusion effects. In the case of the metalloporphyrins, this will definitely be the case since the molecules are the same size.

In the case of the asphaltenes, this assumption may become questionable depending on the size of the asphaltene monomers.

An added advantage of using H_2TPP as the test solute is that the quantitative analysis by UV/Visible spectrometry is more accurate than VOTPP as a result of the additional peaks present in the spectrum of H_2TPP (see Appendix B). H_2TPP has 4 visible peaks compared to one for VOTPP. By averaging the response of all 4 peaks, the quantitative determination of H_2TPP is more accurate and more dependable than that for VOTPP, making the calibration more accurate.

4.2.4 OPTIMUM DURATION OF DIFFUSION EXPERIMENTS

One issue that needs to be addressed is the matter of how long to allow each diffusion experiment to run to obtain optimum results. This analysis has been performed by numerous authors[11-13, 209] and will only be summarized here.

Mills and Woolf[209] analyzed the operating equation for the diaphragm diffusion cell and obtained the following expression for the uncertainty in the integral diffusion coefficient ($u_{\overline{D}}$):

$$\frac{u_{\overline{D}}}{\overline{D}} = \frac{u_C \sqrt{2\left(\left[\Delta C_0/\Delta C_t\right]^2 + 1\right)}}{\Delta C_0 \ln\left[\Delta C_0/\Delta C_t\right]} \quad \text{.................................} \quad \{4.12\}$$

where u_C = the uncertainty in concentration (assumed the same for all measurements). At first glance, equation {4.12} indicates that the uncertainty in the integral diffusion coefficient is a strong function of both the uncertainty in concentration as well as the initial concentration difference in the cell. Obviously, it is necessary to maximize the precision of the concentration measurements (minimize u_C) to obtain accurate results. However, it is also necessary to use as large a concentration difference in the cell in order to minimize $u_{\overline{D}}$.

Equation {4.12} does not explicitly contain information about the effect of time on the uncertainty in $\overline{D}$. This information is contained implicitly within the term ΔC_t. At the optimum time, the derivative of equation {4.12} with respect to the permeate compartment, C_P, will be zero[209]:

$$\frac{\partial\left(u_{\overline{D}}/\overline{D}\right)}{\partial C_P} = 0 \quad \text{.................................} \quad \{4.13\}$$

Mills and Woolf[209] performed this differentiation and obtained the following optimum:

$$\beta\overline{D}t_{opt} = \ln[\Delta C_0 / \Delta C_t] = 1.1 \dots\dots\dots\dots\dots\dots\dots\dots \{4.14\}$$

In comparison, Robinson *et al.*[13] obtained $\beta\overline{D}t_{opt} = 1.2$ while Van Geet and Adamson[12] obtained 1.25. Equation {4.12} is plotted in relative terms in Figure 4-3. From this plot, it is evident that the minimum (i.e. optimum) is very flat and there is therefore some latitude in choosing the optimum duration of experiment. From hereon, the value t $\beta\overline{D}t_{opt} = 1.2$ will be used for the length of the experiments.

Finally, it is important to note that the same conditions must be used for both the calibration runs (to determine β) and the resulting diffusion runs (to determine $\overline{D}$). In effect, this requires that $\overline{D}t$ = constant between both the calibration and the diffusion experiments.
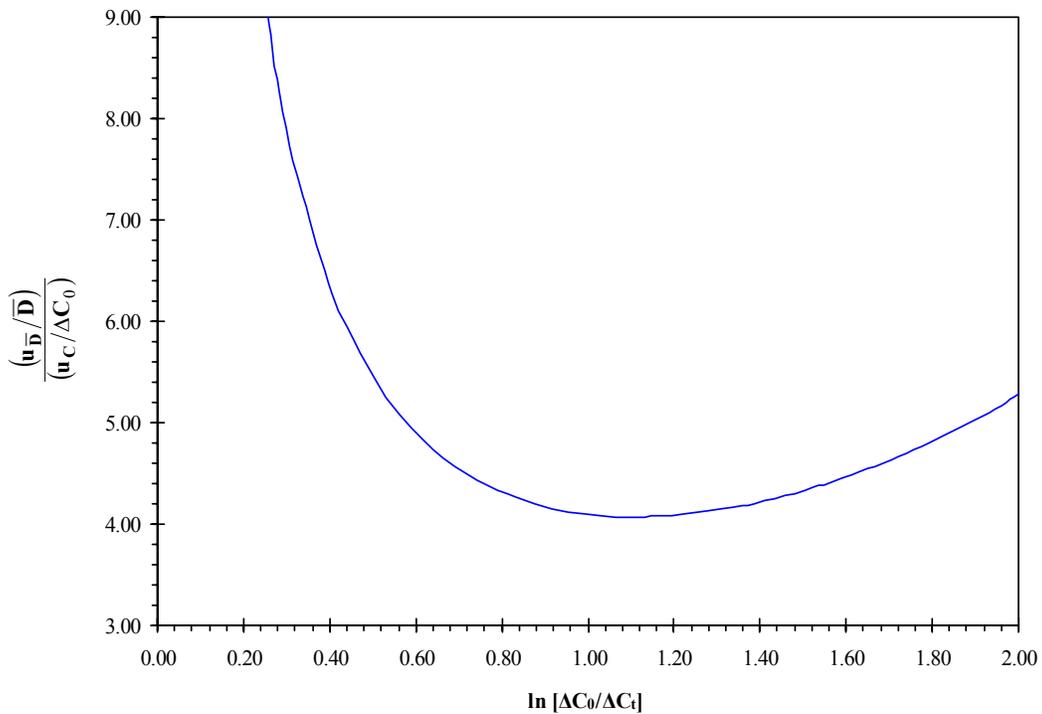
Figure 4-3: Plot of Equation {4.12}

4.3 Experimental Methods

4.3.1 DIFFUSION CELL

The primary apparatus used for this work was the stirred membrane diffusion cell shown schematically in Figure 4-4. The apparatus consists of two fluid reservoirs separated by a suitable membrane with the desired pore characteristics. The cell layout is similar to the horizontal design used by Holmes *et al.*[207, 208], except that the diaphragm is a removable filtration membrane rather than a glass frit.

#	Description
1	Membrane
2	Quartz UV/Vis probe tip
3	K-Type thermocouple
4	Magnetic Stirrer Well
5	Solid glass flanges with ground glass faces, sealed by an expanded teflon gasket & grease
6	Aluminum cell clamp with 8 clamp screws
7	Cell jacket for temperature control
8	0.5 mm Capillary
9	Threaded joint to seal UV/Vis probe
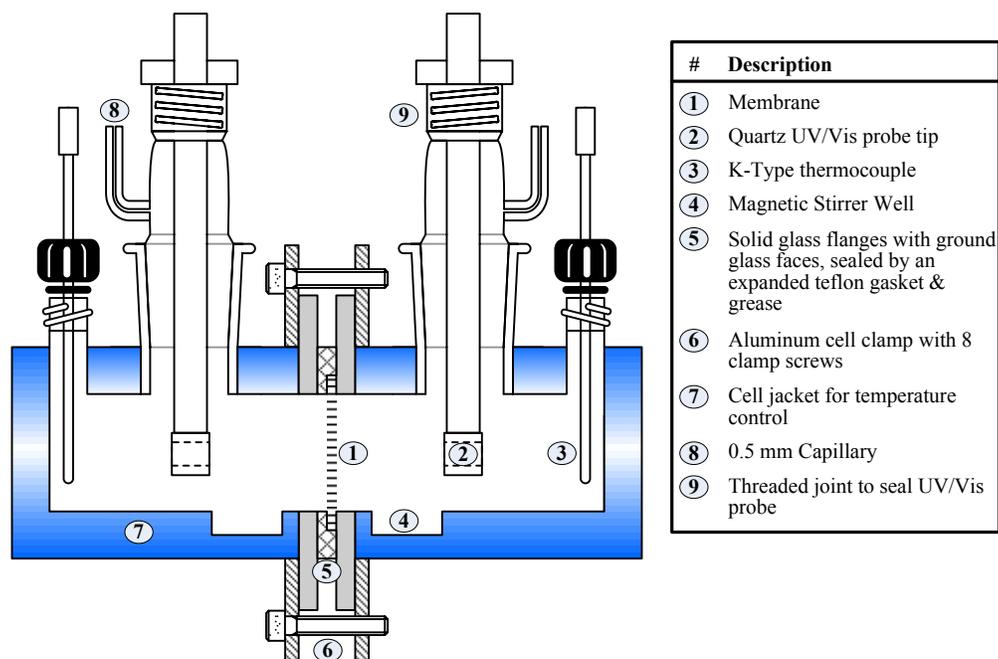
Figure 4-4: Schematic diagram of stirred diaphragm diffusion cell

The cell is constructed entirely of glass. The membrane is sandwiched between two solid glass flanges with their faces ground flat (item 5 in Figure 4-4). The open area of the flange has a diameter of 34 mm. The flange is sealed using a combination of a 0.040" thick expanded Teflon gasket (Teadit® Style 24BB) and solvent resistant grease (Dow-Corning® Molykote® 3451 chemical resistant bearing grease). Expanded Teflon was chosen as the gasket material since it has universal solvent compatibility and because it is soft enough to conform around the edges of the membrane. The Teflon gasket material comes in 4" wide rolls with an adhesive backing on one side. Custom gaskets are cut from these rolls to fit the flange, and the adhesive backing is removed by soaking the gasket in dichloromethane and scraping off the softened adhesive layer. The solvent

resistant grease is required because it is not possible to apply sufficient pressure to the fragile glass flange to get a suitable seal. The flange is compressed using a circular aluminum clamp equipped with 8 #10-32 machine screws (item 6 in Figure 4-4). The screws are first uniformly tightened hand tight to evenly compress the gasket. The screws are then tightened in ¼ turn increments using a standard flange bolt tightening pattern to ensure even compression of the gasket. Consistent alignment of the 2 cell halves is ensured by etched markings on the flanges of each cell. Aligning the marks on each flange ensures that the open areas of each cell are consistently aligned between different experiments/assemblies. The total volume of the cell compartments is ~60 mL which includes the joint housing the UV/Vis probe and capillary adapter. The volume of liquid loaded to each compartment will be less than this total (see section 4.3.4.3)

Each compartment is equipped with a 1" stirrer well (item 4 in Figure 4-4) at the bottom of the compartment, as close as possible to the membrane face, equipped with a ¾" starburst stirrer. Each compartment is also equipped with a 1/8" type-K thermocouple (Omega® KTSS-HH) connected to an Omega® HH502 digital thermometer. The thermometer and thermocouples were calibrated to ±0.2°C using a Hart Scientific 9122 dry-well calibrator. The thermocouples were sealed using Viton® o-rings compressed by a threaded connection (Chemglass CG-350-10). The cell was constructed with jackets (item 7 in Figure 4-4) surrounding each compartment to allow for circulating a heat transfer fluid. The circulating fluid was supplied by a Fisher Isotemp® 3016D digital, refrigerated circulating bath. The circulating fluid was split to supply each compartment simultaneously and ensure consistent temperatures on both sides of the membrane. The temperature read from the two thermocouples never deviated from each other by more than 0.1°C. Initially, the bath was filled with water. However, evaporation caused the liquid level to drop quickly, particularly for high temperature experiments. To avoid such problems, the bath fluid was switched to propylene glycol (Fisher # P355).

For experiments involving porphyrins and asphaltenes, the composition of the permeate side of the membrane was monitored continuously using a C-Technologies, Inc. quartz sleeved Versa Probe. The quartz sleeves are removable and therefore are left in place in the cell (item 2 in Figure 4-4). The size of the custom adapter (item 9 in Figure 4-4) was made of glass to allow for mounting the probe into the cell compartments. This was done using a threaded adapter to compress a Viton® o-ring and seal the quartz sleeve. A quartz sleeve was mounted into each compartment so that the liquid levels on

each side of the membrane remained consistent (i.e. due to volume displacement by the quartz sleeve). This adapter was also equipped with a 0.5 mm capillary (item 9 in Figure 4-4) to ensure that the pressure in the compartments remains equalized at ambient pressure.

The magnetic stirrers in each compartment were driven using a custom built dual magnetic stirrer as illustrated in Figure 4-5. This magnetic stirrer assembly consists of an aluminum plate to which the necessary pulleys are attached. The base plate was equipped with leveling legs on the corners to allow for adjustment of the height of the driven magnets relative to the cell. The main drive shaft is driven by a Caframo BDC-2002 variable speed digital stirrer (speed accuracy = 3% of reading). To ensure that the driven magnets are turning at the same speed as the drive, a timing belt (Boston Gear #3M67060) with matching pulleys (Boston Gear #PA3014DF060) was used. The timing
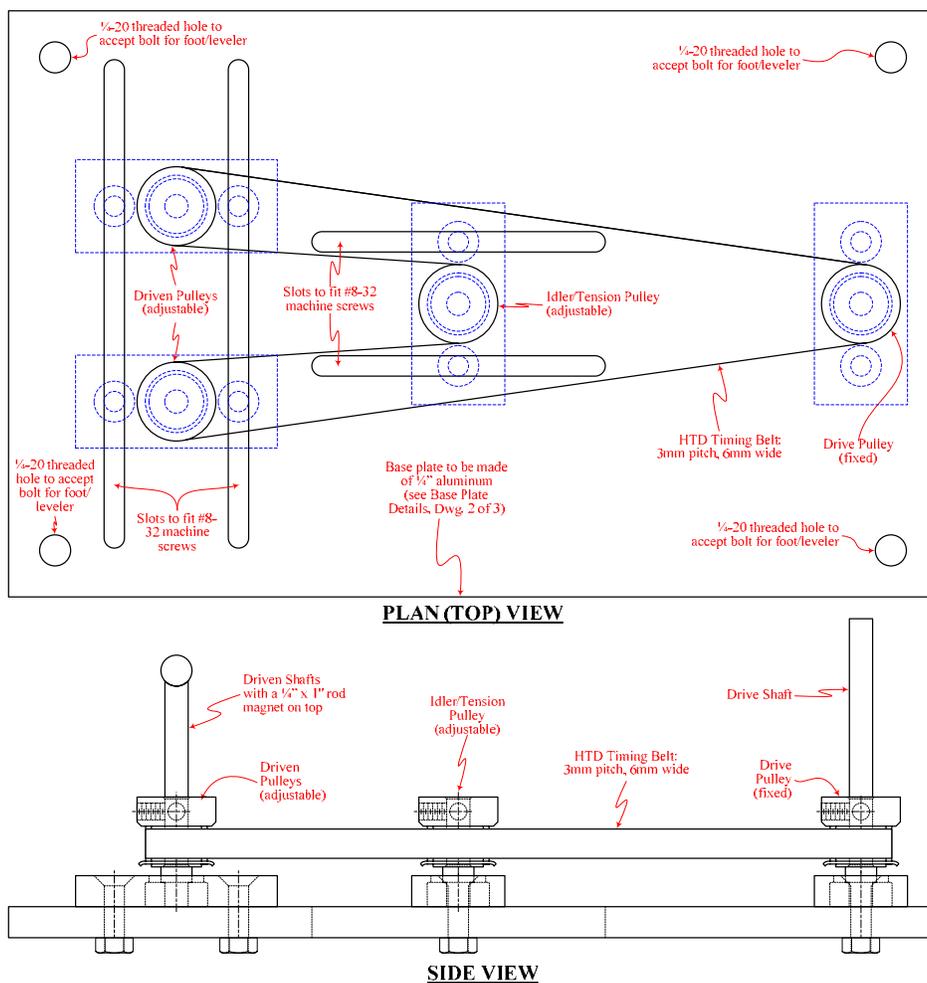
Figure 4-5: Detailed drawing of the magnetic stirrer assembly

belt has small teeth that mesh with matching teeth on the pulleys ensuring that they are turning at the same speed. All of the pulleys are adjustable so that the spacing of the magnets can be adjusted to match the spacing of the stirrer wells in the diffusion cell. An idler pulley was added to keep the belt tight and to force the two magnets to turn in the same direction. Two 1" long by ¼" diameter rare-earth rod magnets (Lee-Valley #99K36.03) were mounted on top of the driven shafts to turn the magnetic stirrers. These bar magnets were centered on the rotating shaft to minimize imbalance and they were then affixed to the shafts using epoxy.

A custom cradle was built out of wood and PVC to support the assembled cell above the magnetic stirrer assembly during the course of an experiment. The base of the cradle was made of ¾" plywood and was secured directly to a lab bench. The lab bench was verified to be plumb and level prior to securing the base to ensure that the cell will also be level (i.e. horizontal). Two semi-cylindrical PVC cradles (made by cutting a 2" Schedule 40 PVC pipe coupling in half) were then mounted on top of this base to hold the cell. The cell was secured to the cradle using hooks and elastic bands. This allowed for some adjustment of the horizontal positioning of the cell relative to the magnetic stirrer base while remaining relatively secure to the base.

4.3.2 MEMBRANES

The diffusion cell described in the previous section was designed to accommodate any suitable filtration membrane with a diameter > 34 mm. In fact, the size of the cell was designed specifically for standard 45-47 mm diameter filtration membranes. Several different types of membranes were used through the course of this work, depending on the size of pores required. In all cases, the material of the membrane was chosen specifically to be compatible with toluene.

4.3.2.1 Millipore Durapore® 5 μm PVDF Membranes

These membranes were used for the mass transfer studies with aqueous KCl (see Appendix A). Their pore size is large enough to eliminate hindered diffusion effects and small enough to eliminate bulk flow as per section 4.2.2.1. PVDF is a polymer which is compatible with toluene and should be a reasonable choice to use for the solutes in toluene. These membranes have a nominal thickness of 125 μm and a diameter of 47 mm.

4.3.2.2 Whatman Anopore® Alumina Membranes

The 0.02 µm (20 nm) pore size Anopore® membranes were used as the upper size range for the metalloporphyrin and asphaltene diffusion studies. These membranes consist of an inorganic alumina matrix that is made electrochemically (anodic aluminum oxide, AAO). The manufacturing process results in a very uniform pore size distribution, although the structure of these membranes is asymmetric. One side of the membrane has 20 nm pores (the active side) while the back side pores are larger at 0.2 µm (200 nm). This asymmetric construction will not affect their use as a diffusion diaphragm, however, since the backside pores are much larger than the active side and as such they should not present a significant barrier to diffusion. As well, because these membranes are inorganic rather than the more conventional polymeric membranes, the pore structure will not be affected by organic solvents, in particular toluene. Their pore size should be large enough to eliminate hindered diffusion effects and to allow full diffusion of the asphaltenes aggregates. These membranes have a nominal thickness of 60 µm and a diameter of 47 mm.

4.3.2.3 Millipore Ultracel Amicon YM Regenerated Cellulose Ultrafiltration Membranes

These membranes were the primary type of membrane used for the metalloporphyrin and asphaltene diffusion studies. Regenerated Cellulose (RC) is fully compatible with toluene and has a temperature limit of 121°C provided the membrane is submerged in the solvent. These membranes have a nominal thickness of 200 µm and a diameter of 44.5 mm. These membranes consist of a 2 layer construction: the active regenerated cellulose layer and a larger support layer made of polypropylene. These membranes are coated with glycerin to prevent the active layer from drying out and this protective coating must be removed prior to use (see section 4.3.4.1).

Three different pore sizes were used in this work: 10 kDa (YM10), 30 kDa (YM30), and 100 kDa (YM100). As is customary for ultrafiltration membranes, these membranes are rated using a nominal Molecular Weight Cut-Off (MWCO) rather than a pore size. According to Millipore, a membrane with a stated MWCO will retain at least 90% of a globular solute with the stated molecular weight[245]. The MWCO for Ultracel YM membranes are characterized using a series of proteins of differing molecular weight as summarized in Table 4-1.

Table 4-1: Rejection and Stokes diameters of proteins with Ultracel YM membranes

Protein	MW (kDa)	% retained[243]			d_S* (nm)
		YM10	YM30	YM100	
Insulin	5.0	25	-	-	2.7 (5.78)[246], 2.3 (5.73)[247] for monomer **Mean = 2.5±0.3**
Cytochrome C	12.4	>95	<15	-	3.4 (11.7)[248], 4.3 (15.6)[249], 3.8 (13.3)[249] **Mean = 3.8±0.8** **Value @ 12.4 kDa‡ = 3.6±0.8**
Myoglobin	17.0	>98	-	12	3.8 (16.9)[250], 3.8[248], 4.0 (16.9)[246], 3.6[249] **Mean = 3.9±0.4**
Chymotrypsinogen	24.5	>98	>80	10	4.4 (25.7)[248], 4.3 (25.7)[246] **Mean = 4.4±0.1**
Albumin	67.0	>98	>98	20	7.2 (67.0)[250], 6.7 (67.1)[251] **Mean = 6.9±0.8**
Immunoglobin G (IgG)	156.0	>98	>98	>95	11.2 (161)[250], 10.2[248], 11.0[251] **Mean = 11±1**

NOTES:

* d_s is the Stokes diameter, $d_s = 2r_s$, where r_s is defined by equation {4.15}. The values given in brackets are the molecular weight of the protein used in the determination of that particular value of d_S

‡ This value was obtained by using a straight line fit to the three points and interpolating

Several investigators have shown that molecular weight is not a good representation of the sieving mechanism of these membranes[252-254] since the shape of the molecule (i.e. linear vs. globular) can have a large impact on the observed retention of a molecule. Tkacik and Michaels[252] compared the retention of a series of dextrans (globular) and polyethylene glycols (PEG, linear) and observed significantly higher retention of the PEG species than dextrans for the same molecular weight. However, when the data were plotted as a function of the Stokes radius (hydrodynamic radius) of the molecules, the data were in good agreement. Therefore, the retention characteristics of the membrane should be referenced in terms of the Stokes radius rather than MWCO.

In order to convert the rejection values in Table 4-1 to a pore size, the Stokes radii of the individual proteins are used (see Table 4-1). These Stokes radii are also known as hydrodynamic radii and are an indication of the effective size of a molecule as a result of diffusive motion according to the Stokes-Einstein equation:

$$D = \frac{kT}{6\pi\eta r_S} \quad \text{.. \{4.15\}}$$

where D = diffusion coefficient of the protein (m^2/s)
         k = Boltzmann's constant = 1.30866 x 10^{-23} (K^{-1})
         T = absolute temperature (K)
         η = viscosity of the solvent (Pa·s)
         r_s = Stokes radius of the molecule/particle (m)

Unfortunately, the molecular weights of these proteins do not correspond directly to the nominal MWCO of the membranes in question and as such their Stokes radii only give rough approximations for the pore sizes. Another method for estimating the pore sizes of these membranes would be to use the data for dextran[252, 253, 255, 256] (a globular solute) to convert the nominal MWCO of the Ultracel membranes to an effective pore size. The molecular weight of the dextran fraction retained by the particular membrane can be converted to a pore size according to the following relation[255]:

$$r_S(\mathring{A}) = 10^{(0.47 \log MW - 0.513)} \quad \text{..................................... \{4.16\}}$$

where r_s = Stokes radius of the dextran molecule (Å)
         MW = molecular weight of the dextran (Da)

The ranges provided by the proteins are compared with the approximate pore size based on the nominal MWCO and equation {4.16} in Table 4-2. From this information, it would appear that equation {4.16} is predicting pore sizes that are larger than those indicated by the protein retention data provided from Millipore. One explanation for this over-prediction could be that the retention values provided by Millipore[245] are apparent retention values, rather than true retention values corrected for concentration polarization. This effect was shown by Kim *et al.*[253] to result in an over-prediction of the pore size by ≈ 3 nm for a YM30 membrane, where they predict a pore size of 4.4-4.7 nm based on dextran rejection measurements. This value given by Kim *et al.*[253] agrees well with the value obtained from Chymotrypsinogen for the 30 kDa membrane and it appears as though the protein data provided by Millipore are reasonable.

Unfortunately, none of the proteins used by Millipore correspond to the actual MWCO of the membranes. Therefore, some approximations must be made to determine pore sizes. Since the dextran predictions with the nominal MWCO seem to significantly over predict the pore size, these values cannot be used. Equation {4.16} indicates that the correlation between molecular weight and Stokes radii is not a simple linear

Table 4-2: Approximate pore sizes of Ultracel YM membranes used in this work

Membrane	Nominal MWCO (kDa)	Approx. Pore Size (nm)		
		From Data in Table 4-1	equation {4.16}	equation {4.17}
YM10	10	>2.3–2.7, <3.4–4.3	4.7	3.0±1
YM30	30	≈4.4, <<6.7–7.2	7.8	5.0±1
YM100	100	>6.7–7.2, <10.2–11.2	13.7	9.0±1

relationship but rather follows a log-log relationship. The mean protein data from Table 4-1 is plotted in Figure 4-6 in log-log form (along with the predictions from equation {4.16} for comparison) yielding the following relationship:

$$r_S(\text{Å}) = 10^{[0.4287\log_{10} MW(Da) - 0.5181]} \quad \text{...............................} \quad \{4.17\}$$
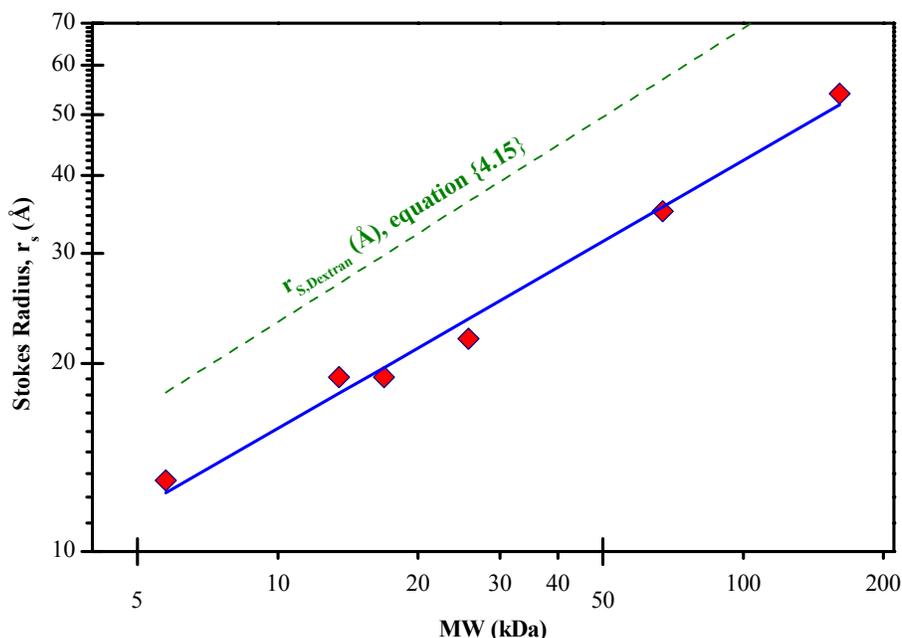
Figure 4-6: Variation of Stokes radii with molecular weight for proteins used to test Ultracel membranes

Equation {4.17} can now be used to estimate the pore sizes of each of the Ultracel membranes. For the YM30 membrane (30 kDa MWCO) equation {4.17} predicts a pore size of 5.0 nm, which fits reasonably well with the measured range of Kim *et al.*[253] and the Chymotrypsinogen measurement. For the YM10 membrane (10 kDa MWCO) equation {4.17} predicts a pore size of 3.1 nm (round down to 3 nm), and for the YM100

membrane (100 kDa MWCO) equation {4.17} predicts a pore size of 8.4 nm, which is between the value for albumin and IgG, and will be rounded up to 9 nm. In all three cases, the accuracy of these values is assumed to be ±1 nm. Therefore, any and all conclusions drawn using the size of the pores will use the values given in the last column of Table 4-2.

4.3.3 ANALYTICAL EQUIPMENT FOR UV/VIS SPECTROSCOPY

All UV/Visible spectroscopic measurements for the asphaltene and metalloporphyrin work was done using an SI-Photonics (Tucson, AZ.) model 440 spectrophotometer (see Chapter 3 for specific details). In the case of the asphaltene and metalloporphyrin diffusion measurements, the composition of the permeate side of the membrane was monitored continuously using a C-Technologies, Inc. (Bridgewater, NJ) quartz sleeved Versa Probe. The quartz sleeves are removable and have a pathlength of 10.00±0.01mm (i.e. same as a cuvette). Unfortunately, this probe is only capable of using one light source at a time. Therefore, all measurements done using the Versa Probe were done using the W source only, spanning from 350 – 950 nm.

4.3.4 EXPERIMENTAL PROCEDURES

4.3.4.1 Preparing Ultracel YM membranes

The procedure recommended by the manufacturer for removing the protective glycerin coating involves soaking or washing the membrane with de-ionized water. However, because the current application uses non-aqueous solvents, introducing water to the membrane poses a problem. Instead, methanol was substituted as the solvent to remove the glycerin. Since glycerin is an alcohol (polyol), it should be soluble in methanol. The added advantage of using methanol is its miscibility with toluene. Therefore, the procedure for conditioning a membrane was as follows:

1. Assemble the cell with the fresh membrane, being sure to orient the active (RC) side of the membrane towards the retentate side of the cell.

2. Load both sides of the cell with methanol and stir @ 600 rpm for 30 minutes.

3. Drain the cell and repeat step 2.

4. Load the retentate side of the cell with fresh methanol and draw it through the membrane using a vacuum applied to the permeate side for 2-4 hours.

5. Drain the cell and rinse both compartments with toluene twice.

6. Repeat step 4 with toluene.

7. Drain and fill the cell with toluene and leave full until the start of the experiment.

4.3.4.2 Solvent & Membrane Degassing

Many of the references using the diaphragm cell technique refer to the process of degassing the solvent/solutions as well as the diaphragm prior to performing the diffusion run. The primary reason for performing this step is to prevent bubbles from forming within the apparatus, and more specifically within the diaphragm, during the course of the run. If bubbles were to form in the diaphragm during the run, this would serve to reduce the available pore area during the run and would skew the results (i.e. would render the calibration invalid).

The most common method employed in the literature for degassing solvents/solutions is to boil them for a short period prior to loading into the cell. However, this method would lead to loss of solvent from the solution which would serve to increase the concentration of solute from the initial value and would skew the results. In general, diaphragm cell diffusion measurements are done using a vertical cell (i.e. horizontal membrane). Therefore, gas bubbles evolved during the experiment would tend to rise and preferentially contact the membrane in the case of the bottom compartment. However, in the case of a horizontal cell (vertical diaphragm), the rising gas bubbles would tend to migrate upwards towards the top of the cell and not towards the membrane. Thus, the impact of this effect is reduced for the present apparatus. Unfortunately, the increased surface area of the membrane material will tend to cause enhanced nucleation of the gas on the surface and therefore there is the potential for gas bubbles to form within the pores of the membrane. This effect is still a factor in the vertical membrane and should be addressed.

The method used in this work was a slightly modified form of the procedure used by Mills and Woolf[209]. The solvents, and in some cases the initial retentate solutions, were passed thru a 0.2 micron Millipore filter twice under vacuum. The filter increases the surface area of the liquids (as well as filters them to remove any particulates) as they pass through into the vacuum flask, thus improving the rate of release of dissolved gases from the solution. As well, this method will minimize the evaporative losses of solvent

from the gravimetrically prepared solutions. In cases where the initial retentate solutions were degassed (only the KCl mass transfer work), the composition of the solution was determined analytically to account for evaporation of solvent during the degassing step.

To ensure that the pores of the membrane were purged of air and filled with degassed solvent, the retentate side of the cell was loaded with degassed solvent and a vacuum applied to the permeate side of the cell via the capillary to draw the liquid into the membrane. This was done until the permeate side of the cell was full of solvent (0.22 μm Durapore® and 0.02 μm Anopore) or long enough to ensure that all pores of the membrane were filled. The liquid level on the retentate side of the cell was kept topped up to ensure that it did not drop below the membrane surface and lead to additional air being drawn into the pores. It was important to keep the vacuum pressure low during this step since the membranes are fragile and it is relatively easy to rupture the membrane with excessive vacuum.

4.3.4.3 Loading the cell & Starting a Run

The liquid loaded to each compartment at the start of each experiment was done using class A volumetric pipettes, 125 mL bottles, and a Sartorius CP 224S analytical balance. For each experiment, 55 mL of liquid (55 mL = 25 mL class A volumetric pipette + 30 mL class A volumetric pipette) was transferred to a clean 125 mL bottle and the mass recorded. The bottles (two for each experiment) were placed in the temperature bath to equilibrate to the temperature of the experiment, after which time they were poured in simultaneously to start the experiment. The empty bottles were then re-weighed to determine how much liquid remained in the bottle, and the difference in weight was taken as the mass of liquid added to the cell. The density of the solutions (usually taken as the density of the solvent) was used to convert the mass of liquid added to volume.

The start of a run was taken as the time when the solutions were fully poured into the cell and the stirrer started. The entire process of pouring in the solutions and starting the stirrer took on the order of 5-10 s and this represents the error in time measurements. In the case of the asphaltene and metalloporphyrin experiments where the composition was measured by a computer, the stopwatch time was synchronized with the computer to ensure that the start time was consistent with the date stamp for each UV/Visible measurement.

4.3.5   CHEMICALS

Through the course of this work, numerous pure chemicals are used along with asphaltenes of various origins.

4.3.5.1 Solvents

The primary solvent used in this work was spectra-analyzed HPLC grade toluene (Fisher Scientific #T330). ACS grade methanol was used for washing and preparing the Ultracel YM membranes (see section 4.3.4.1). Spectra-analyzed HPLC grade n-heptane was used for the calibration experiments.

4.3.5.2 Model Porphyrins

Several model porphyrins were used for the diffusion studies. As discussed in section 4.2.3, free base meso-tetraphenylporphyrin (H_2TPP) from Sigma-Aldrich (#247367, purity = 99.9%) was used as received for calibrating all of the membranes. Vanadyl meso-tetraphenylporphyrin (VOTPP) and vanadyl octaethylporphyrin (VOOEP) were obtained from Sigma-Aldrich (#283649 and #363715, respectively) and were both purified by flash chromatography (see Appendix D) to >99.5% purity.

4.3.5.3 Asphaltenes

Athabasca C_7 Asphaltenes (AA)

The bulk of the work was done using Athabasca C_7 asphaltenes (referred to as AA from hereon) derived from the bottoms stream of a de-asphalting unit processing bitumen from a SAGD operation. The feed material (i.e. de-asphalter bottoms) was processed as follows to recover the pure asphaltenes:

1. The feed was dissolved at a ratio of 40:1 in toluene (sonicated sample for 2 hours to ensure complete dissolution) and filtered over a 0.22 μm Durapore® membrane filter to remove any toluene insoluble material. The total toluene insolubles were <0.05 wt%.

2. The toluene was removed using a rotary evaporator operated under building vacuum at 85°C. The remaining sample was transferred to clean flasks and dissolved in n-heptane at a ratio of at least 40:1. The flasks were sonicated for 1 hour to ensure complete mixing and complete dissolution of the n-heptane

soluble components. The flasks were allowed to cool and settle for at least 3 more hours.

3. The flasks of n-heptane + sample were filtered using a 0.22 μm Durapore® membrane filter to recover the asphaltenes. The samples were washed with additional n-heptane to remove all n-heptane soluble components and leave behind only asphaltenes.

4. The recovered asphaltenes were dried in a vacuum oven at 80°C for 2 days to drive off any residual solvent.

This final asphaltene material is in the form of a fine powder at room temperature and has a vanadium content of 864±9 ppmw as measured by acid digestion and ICP-AES analysis. According to Zhao *et al.*[257], the C_7 asphaltene and vanadium content of a representative Athabasca bitumen is 18.6 wt% and 259 ppmw, respectively.

Venezuelan C_7 Asphaltenes (VA)

A sample of Venezuelan C_7 asphaltenes was obtained from Tuyet Le. The full origin of this sample is unknown other than that it is produced in a similar fashion to the previous Athabasca asphaltenes from bitumen of Venezuelan descent. The vanadium content of this sample is 1162±8 ppmw as measured by acid digestion and ICP-AES analysis. According to Herrington[258], the C_7 asphaltene and vanadium content of a representative Venezuelan (Boscan) crude is 16.5 wt% and 846 ppmw, respectively.

Safaniya C_7 Asphaltenes (SA)

A sample of Safaniya asphaltenes was also obtained from Tuyet Le. The full origin of this sample is again unknown other than that it is produced in a similar fashion to the previous Athabasca asphaltenes from a sample originating in the Safaniya field. The vanadium content of this sample is 217±1 ppmw as measured by acid digestion and ICP-AES analysis. According to Herrington[258], the C_7 asphaltene and vanadium content of a representative Safaniya crude is 13.0 wt% and 65 ppmw, respectively.

Athabasca Partially Demetallated C_7 Asphaltenes (APDA)

A sample of Athabasca bitumen which had been partially demetallated was provided by James Dunn of Imperial Oil Ltd. (Calgary, AB). The asphaltenes were recovered from the bitumen sample in a similar fashion to the previous Athabasca

asphaltenes. The vanadium content of this sample is 180±2 ppmw as measured by acid digestion and ICP-AES analysis.

4.4 Diffusion of Asphaltenes

Some representative spectra from a typical diffusion experiment using an initial solution of 1 g/L AA in toluene at 25°C with an Ultracel YM30 (5 nm) membrane and a stirrer speed of 600 rpm are shown below in Figure 4-7. These spectra were collected in-situ every 10 minutes using the quartz sleeved probe and the W source from 350-950 nm. The permeate spectra at different times are superimposed on the spectra for the whole asphaltenes. The enlarged peak at 407 nm indicates an enrichment of petroporphyrins as a result of the diffusion process, and this will be analyzed in more detail in section 4.5. It is immediately evident from Figure 4-7 that the permeate spectra have a significantly different shape than those of the whole asphaltenes. The permeate spectra are steeper between 350-500 nm and show much lower absorbances at
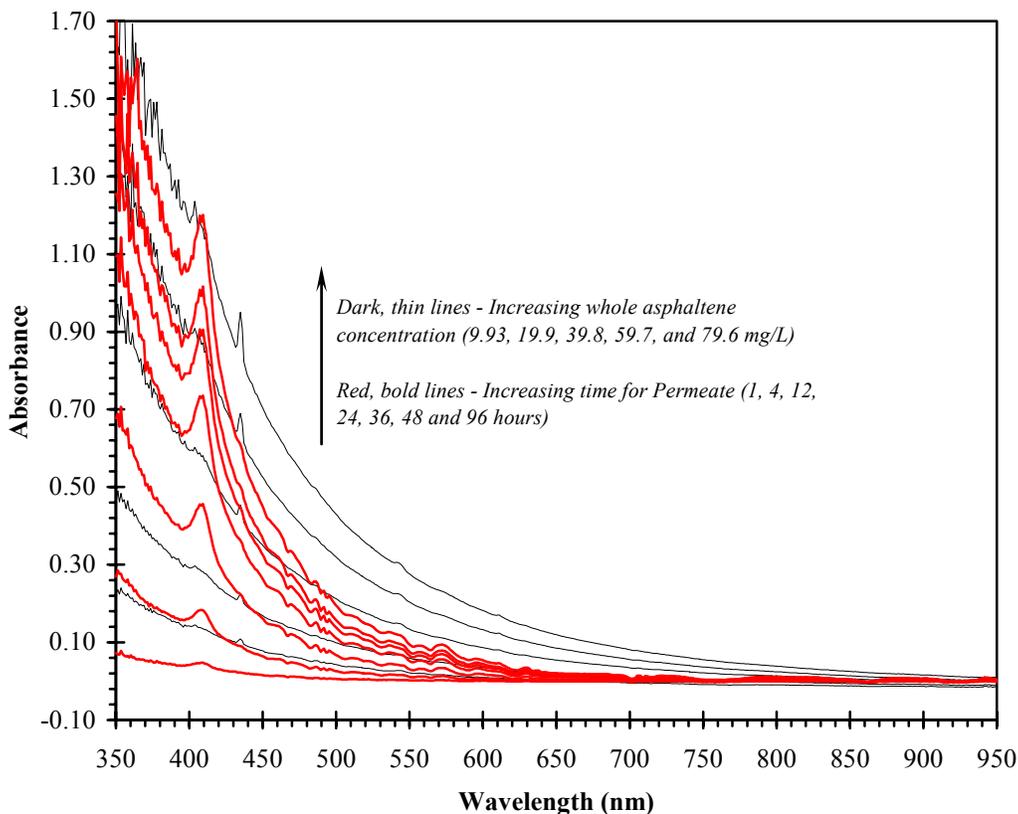
Figure 4-7: Comparison of raw permeate spectra to whole asphaltene spectra for diffusion of AA in toluene (Expt #175): Ultracel YM30 (30 kDa) membrane, T = 25±0.2°C, initial concentration of AA = 1 g/L, stirrer speed = 600 rpm.

wavelengths > 500 nm.

The fact that the permeate spectra are significantly different from the whole asphaltenes indicates that there is some fractionation occurring. In other words, the chemical nature of the retained fractions differs significantly from the chemical nature of the permeated species. The fact that this membrane has a relatively small pore size (5 nm) would lead one to believe that the species that have been retained are in an aggregated state and are too large to diffuse through the membrane while the species that have diffused through the membrane are single molecules or at least much smaller than a nano-aggregate. The fact that the permeated asphaltene species exhibit strong absorbance in the UV region (< 400 nm) is not surprising since asphaltenes are rich in aromatic structures (strong UV absorbers) and one would expect that even single asphaltene molecules would absorb UV radiation. It is the lack of absorbance in the visible region which is surprising and perhaps indicates that the absorbance of asphaltenes in the visible region is due to aggregation.

The permeate absorbance profiles at three different wavelengths (384.7, 500.8, and 600.1 nm) for this same experiment are shown in Figure 4-8. These wavelengths were chosen to coincide with some of the critical features of the permeate spectra shown in Figure 4-7. The absorbance at 384.7 nm occurs in the steepest region of the permeate spectra (UV region) and is an indicator of the concentration of asphaltenes (UV active species). The absorbance at 500.8 is beyond the range of the petroporphyrin peak and is at the tailing end of the steep portion of the spectrum. The absorbance at 600.1 nm is into the region where the absorbances in the permeate spectra are well below those of the whole asphaltenes, and are likely an indicator of the concentration of aggregated species due to scattering (see section 0).

None of the absorbance profiles in Figure 4-8 reached steady state, indicating that the number of asphaltene molecules in free solution that are capable of passing through the membrane's pores has not reached a constant value. It is possible that the aggregated species on the retentate side of the membrane were generating new molecules in free solution. If the aggregation process is reversible then one would expect that as the concentration of molecules in free solution decreases (as a result of diffusion across the membrane) more molecules would break away from the aggregates to maintain equilibrium. The generation of additional free molecules on the retentate side of the membrane results in additional diffusion and hence the continuous, albeit slow, increase
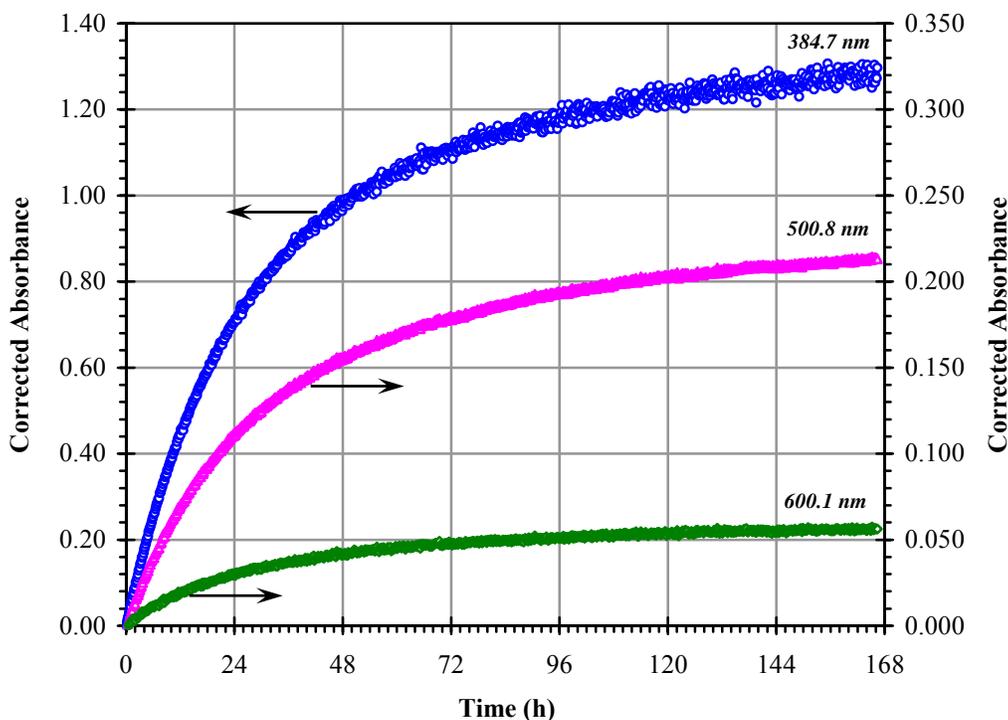
Figure 4-8: Permeate absorbance profiles at three different wavelengths for Expt #175: Ultracel YM30 (30 kDa) membrane, T = 25±0.2°C, initial concentration of AA = 1 g/L

in permeate concentration on the permeate side of the cell. It should be pointed out that the concentration of asphaltenes in the permeate calculated from the absorbance at 384.7 nm is ≈ 75 mg/L at the end of the above experiment, which only corresponds to 7.5% of the total asphaltenes initially loaded to the cell. Therefore, only a small portion of the asphaltene material is diffusing across this membrane over the course of 7 days.

The membrane in the aforementioned experiment was calibrated using H_2TPP in toluene (as discussed in section 4.2.3) and the results of this calibration are shown in Figure 4-9. If it is assumed that the UV/Visible spectrometric calibrations shown in Appendix C remain valid for the permeate species, then it is possible to quantify the diffusion coefficient of the asphaltenes using this membrane calibration data.

One problem that arises when applying the spectrometric asphaltene calibrations in Appendix C, however, is that the measured concentrations are in terms of mass (mg/L) rather than molar concentration (mol/L). Because of the inherent uncertainty in the molar mass of asphaltenes (see Chapter 2), it is difficult to determine the molar concentration of asphaltenes in solution. Unfortunately, the operating equation for analysis of the diffusion cell (equations {4.7} and {4.9}) were derived using molar concentrations. This
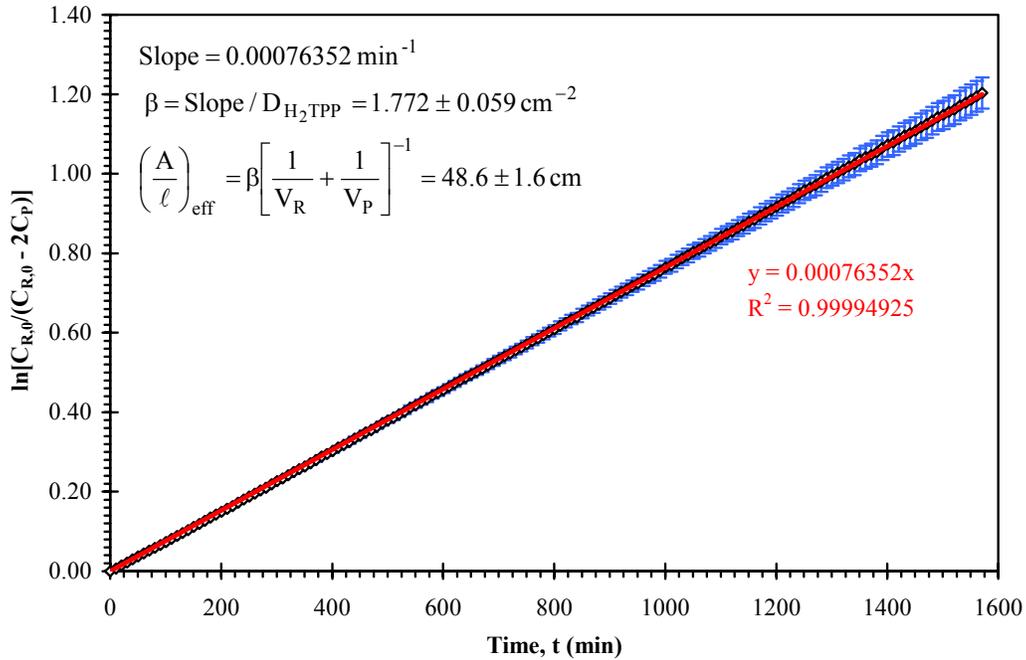
Figure 4-9: Calibration data for Ultracel YM30 membrane using H_2TPP @ $25\pm0.2°C$ (#184)

is not a concern for a system where the molecular weight remains constant (e.g. for a single molecular species) since the ratio of concentrations will be the same.

However, in the current case, it is plausible that the average molecular weight of the asphaltenes on the permeate side are considerably lower than the average molecular weight of the retentate asphaltenes. The latter components are likely aggregated, giving a MW above the cut-off of the membrane. If we let MW_P = the average molecular weight of the permeate asphaltenes and let MW_R = the average molecular weight of the retentate asphaltenes, then equation {4.9} becomes:

$$\ln\left[\frac{w_{R,0}/MW_R}{w_{R,0}/MW_R - 2w_P/MW_P}\right] = \beta D_{AB} t \quad .... \{4.18\}$$

where $w_{R,0}$ = Initial retentate mass concentration of asphaltenes (mg/L)
w_R = Retentate mass concentration of asphaltenes (mg/L)
w_P = Permeate mass concentration of asphaltenes (mg/L)

The derivation of equation {4.18} makes the implicit assumption that the average molecular weight of the retentate asphaltenes does not change over the course of the diffusion experiment. If the permeate average molecular weight is the same as the retentate, equation {4.18} reduces to equation {4.9}.

According to Yarranton and co-workers[111, 112], extrapolating vapor phase osmometry (VPO) data predicts an average molecular weight of an asphaltene monomer to be approximately 1,800 g/mol. The same data predict the molecular weight of aggregated asphaltenes in toluene at 1 g/L to be approximately 4,000 g/mol. Although this measurement was done at 70°C, comparison of their measurements at 50°C and 70°C show that the results were insensitive to temperature at a concentration of 1 g/L, therefore, this value should be a reasonable approximation at 25°C. The results obtained using both forms of analysis are shown in Figure 4-10 using the mean of the concentration determined using the absorbance at 375.8 and 384.7 nm (see Appendix C for calibrations). The first 12 hours of data were regressed in each case since beyond 12 hours the data begin to deviate from linearity.

The resulting slopes can be used with the calibration constant for this membrane (see Figure 4-9) to determine the effective diffusion coefficient of the asphaltenes in each case and these values are included in Figure 4-10. Correcting the molecular weight of the
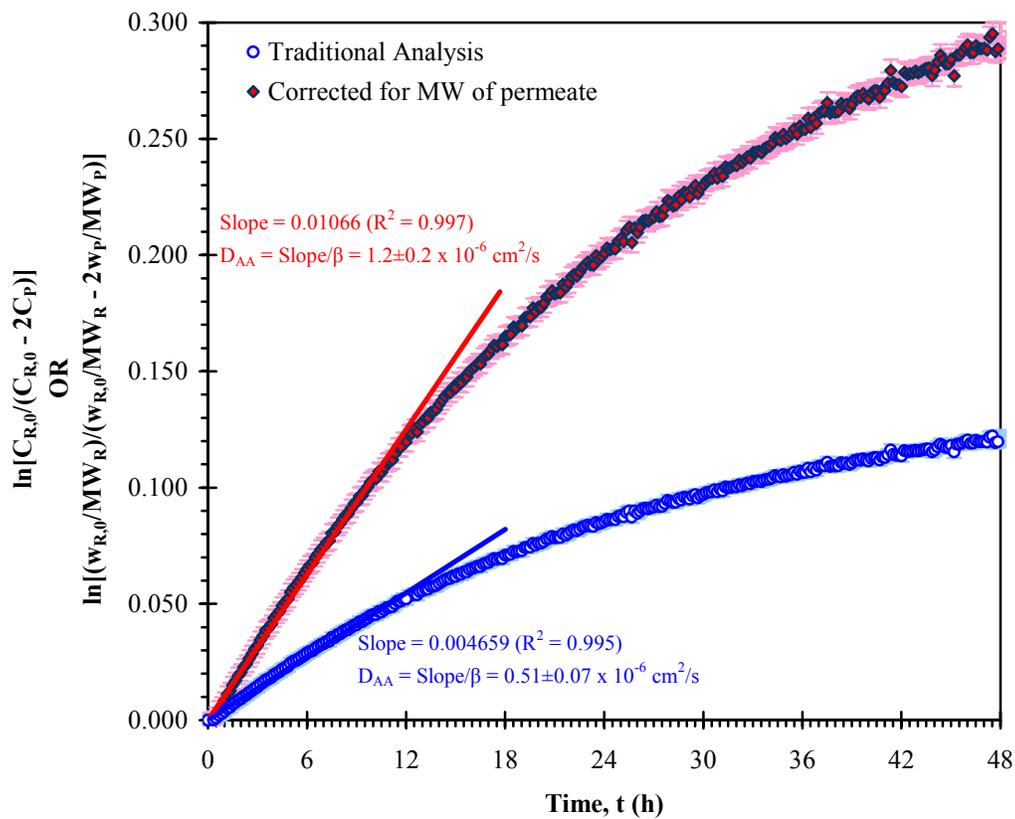
Figure 4-10: Asphaltene diffusion analysis for Expt #175 (Concentrations of asphaltenes determined from the absorbances at 375.8 & 384.7 nm)

permeate results in 94% increase in the effective diffusion coefficient for the asphaltenes. A similar analysis was done using the absorbances at 500.8 and 600.1 nm and the resulting diffusion coefficients are shown in Table 4-3.

Table 4-3: Summary of effective AA diffusion coefficients at different wavelengths obtained from the traditional analysis (equation {4.9}) and the molecular weight corrected analysis (equation {4.18})

Wavelength(s)	$D_{e, AA}$ (x 10^{-6} cm^2/s)		r_s (nm)	
	Equation {4.9}	*Equation {4.18}*	*Equation {4.9}*	*Equation {4.18}*
375.8 & 384.7 nm	0.62±0.04	1.2±0.2	6.0	3.3
500.8 nm	0.33±0.04	0.59±0.09	12	6.7
600.1 nm	0.20±0.06	0.41±0.09	20	13

The fact that the effective diffusivity of the asphaltenes decreases with wavelength would imply that the longer wavelengths correspond to larger asphaltene species. This is consistent with the previous discussion regarding the shape of the permeate spectra. However, the analysis done using equation {4.18} assumed a constant average molecular weight for all of the wavelengths studied and therefore is somewhat misleading. If indeed the longer wavelengths correspond to larger molecules, then this would need to be taken into account in the analysis. Unfortunately, there is no way to assign meaningful molecular weights to the species absorbing at longer wavelengths; therefore, attempting to do so would be nothing more than a guess.

To quantify this result further, the effective diffusion coefficients were converted to Stokes radii using equation {4.15} and a viscosity of 0.5542 mPa·s[241] for toluene at 25°C, and the results are included in Table 4-3. These results confirm the notion that the larger species are responsible for the absorption in the visible region since the Stokes radii increase as the wavelength increases. It should be noted, however, that the Stokes radii calculated for the asphaltenes are much larger than the estimated pore diameter of 5 nm for this membrane. This calls into question the validity of these results. The first problem with the predictions is the assumed average molecular weights of both the retentate and permeates. These values are approximations at best and these could lead to significant errors in the predictions. More recent results of Yarranton *et al.*[113] suggest that perhaps the average molecular weight of the asphaltene monomers may be closer to 1,000 g/mol, which would alter the results significantly. As well, the average molecular

weight of the whole asphaltene aggregates may be higher than the assumed value of 4,000 g/mol. A simultaneous over-prediction of the monomer molecular weight and under-prediction of the aggregate molecular weight produces a compounded error in the calculations. The results in Table 4-3 also indicate that using the standard analysis method (i.e. equation {4.9}) is not appropriate and results in significant under-prediction of the effective diffusivities with a corresponding over-prediction of the size of the asphaltene species in the permeate.

Several investigators have measured the diffusion coefficient of asphaltenes in toluene. Östlund *et al.*[259] found the infinite dilution diffusion coefficient for Venezuelan asphaltenes in toluene to be 2.2×10^{-6} cm^2/s using pulsed field gradient spin echo NMR (PFG-SE NMR). Wargadalam *et al.*[260] obtained a value of 6.26×10^{-6} cm^2/s for a coal derived asphaltene using Taylor dispersion. Östlund *et al.*[261] obtained a value of 5.7×10^{-6} cm^2/s for a North Sea asphaltene using PFG-SE NMR. Ballard *et al.*[262] used fluorescence correlation spectroscopy to obtain a value of 3.4×10^{-6} cm^2/s for a UG8 asphaltene. Finally Lisitza *et al.*[263] used stimulated-echo pulsed field gradient NMR to obtain a value of 2.9×10^{-6} cm^2/s for UG8 asphaltenes at infinite dilution, and a value of $\sim 1 \times 10^{-6}$ cm^2/s at a concentration of 2.1 g/L. Therefore, the values for the infinite dilution diffusion coefficients of asphaltenes in toluene range from 2.2–6.3×10^{-6} cm^2/s. All of the values in Table 4-3 fall outside of this range. In fact, with the exception of the value obtained at wavelengths of 375.8 and 384.7 nm with equation {4.18}, all of the values are an order of magnitude lower.

A major over-simplification present in all of the above analysis is the lack of correction for hindered diffusion effects as a result of the pore size being on the same order as the molecular dimensions of the diffusing species. Baltus and Anderson[264] determined the effects of hindered diffusion of asphaltenes to be well described by the following equation:

$$\frac{D_e}{D_\infty} = e^{-3.89\theta}$$ .... {4.19}

where D_e = effective (measured) diffusivity in the
            presence of pore hindrance
        D_∞ = free diffusivity in the absence of pore
            hindrance effects
        θ = The ratio of molecule diameter to pore diameter
            = r_S/r_P

Assuming that the asphaltenes adhere to the same MW-r_S relationship as the proteins used to characterize the Ultracel membranes (equation {4.17}), the Stokes radius for asphaltenes with a MW of 1,800 g/mol would be 1.5 nm. This agrees well with the Stokes radii calculated using the range of infinite dilution diffusion coefficients reported in the literature (D = 2.2–6.3 x 10^{-6} cm^2/s, r_S = 0.6 – 1.8 nm). This results in θ = 1.5/2.5 = 0.6 and a ratio D_e/D_∞ of 0.1, thus implying that the effective diffusivity values in Table 4-3 are a factor of 10 lower than the free diffusion coefficient for the asphaltenes.

The preceding analysis of hindered diffusion does not take into account the fact that the calibration of the membranes in this work uses a solute that has comparable molecular dimensions to the asphaltenes and therefore a portion of the hindrance effect has already been accounted for. Equation {4.19} can be modified to take into account the calibration with H$_2$TPP as follows:

$$\frac{D_{e,A}}{D_{\infty,A}} = e^{-3.89\left[\frac{r_{S,A} - r_{S,H_2TPP}}{r_P}\right]}$$ .... {4.20}

Equation {4.20} takes into account the effects of hindrance already incurred by the calibrant (H$_2$TPP) when correcting the effective diffusivity of the asphaltenes. The Stokes radius of H$_2$TPP in toluene is r_{S,H_2TPP} = 0.55 nm (calculated using D_{H_2TPP} = 7.18 x 10^{-6} cm^2/s and equation {4.15}) while for the YM30 membrane being considered here the pore radius is r_P = 5/2 = 2.5 nm. These values result in diffusivity ratios, D_e/D_∞, of 0.73 and 0.45 for asphaltenes with molecular weights of 1,800 g/mol and 4,000 g/mol, respectively. Combining these correction factors with the effective diffusivities given in Table 4-3 gives the true (∞) diffusivities as summarized in Table 4-4. The values at the shorter wavelengths were corrected assuming that they are the smaller 1,800 g/mol species while the values at longer wavelengths were corrected assuming they are the larger 4,000 g/mol aggregates. The corrected diffusion values are closer to the values reported in the literature, particularly at the shorter wavelength according to equation {4.18}. The Stokes radii are still larger than the estimated pore size of the membrane which is questionable.

It is clear from the preceding analysis that the diffusion of asphaltenes in the small nano-sized pores (5 nm diameter) of the above membrane is very complex. There is some form of fractionation occurring as a result of these small pores, presumably because

Table 4-4: Summary of the free AA diffusion coefficients, calculated from equation {4.19} at $\theta = 0.6$, at different wavelengths obtained from the traditional analysis (equation {4.9}) and the molecular weight corrected analysis (equation {4.18})

Wavelength(s)	$D_{\infty,AA}$ (x 10^{-6} cm^2/s)		r_s (nm)	
	1,800 Da	*4,000 Da*	*1,800 Da*	*4,000 Da*
375.8 & 384.7 nm (*Equation* {4.9})	0.85±0.05	1.38±0.09	4.6	
375.8 & 384.7 nm (*Equation* {4.18})	1.6±0.3		2.5	
500.8 nm	0.45±0.05	0.73±0.09	8.8	5.4
600.1 nm		0.44±0.10		9.0

large species (nano-aggregates or large molecular weight asphaltene molecules) are retained by the membrane and only small asphaltene species (single molecules or dimers smaller than the pore size) are capable of diffusing across the membrane. The fact that significant portions of the asphaltenes are held back by the membrane complicates the analysis significantly since the molecular weights of the diffusing species are unknown. This phenomenon will now be investigated by varying the conditions of the experiment (pore size, temperature, concentration, and asphaltene origin) to determine what, if any, further conclusions can be drawn from this phenomenon.

4.4.1 FOULING EFFECTS

For any procedure involving the use of a porous membrane, it is important to ascertain the possibility and impact of fouling on the results. This was tested using an Ultracel YM10 membrane and the results are shown in Figure 4-11. These tests were done using pure VOTPP as the test solute. The first (fresh) test was done on the new membrane, while the second test (used) was done following an experiment using 1 g/L AA asphaltenes. The membrane was not washed following the experiment with the asphaltenes. Only the cell compartments were rinsed with toluene to remove any asphaltenes remaining in the cell, but not the membrane. It is immediately apparent from Figure 4-11 that there is some fouling occurring during the course of experiments using asphaltenes. The curve for the used membrane does show some upward curvature, however, which would indicate that whatever is fouling the membrane is being removed slowly and that the fouling is neither irreversible nor permanent.
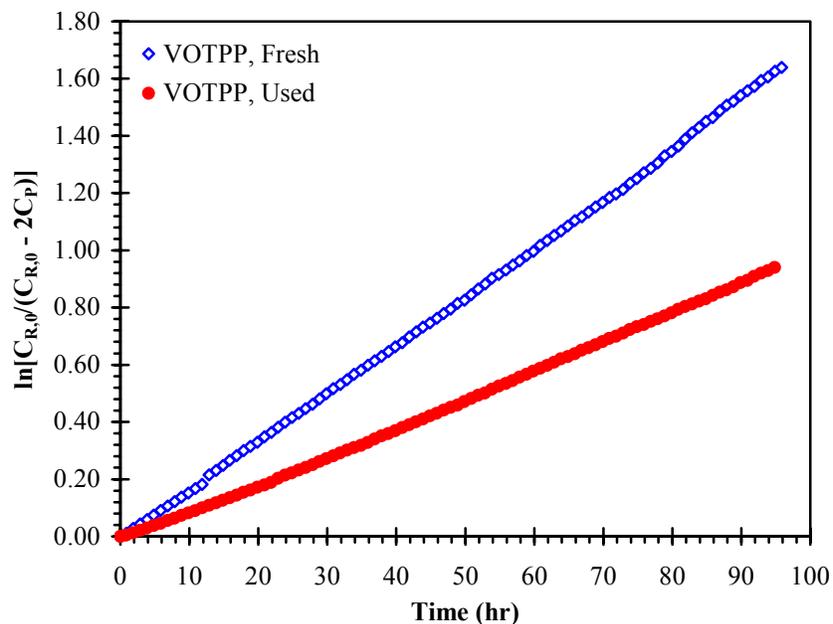
Figure 4-11: Effect of fouling on an Ultracel YM10 membrane. The used membrane was not washed prior to this test.

To test whether or not the fouling is irreversible, a second set of tests was done using H_2TPP and an Anopore® 20 nm membrane. This time, the used membrane (following tests with asphaltenes) was washed by pulling toluene through the membrane using vacuum. The results of these two tests are shown in Figure 4-12. From these results, it appears as though the fouling is indeed reversible and that the asphaltenes that are left behind during a diffusion experiment can be removed by thorough washing of the membrane. In cases where a membrane was reused, great care was taken to thoroughly wash the membrane using degassed toluene.

4.4.2 EFFECT OF PORE SIZE

The effect of pore size on the observed phenomenon was tested using 4 different membranes: Ultracel YM10 (10 kDa, ~3 nm pores), the aforementioned Ultracel YM30 (30 kDa, ~4.5 nm pores), Ultracel YM100 (100 kDa, ~9 nm pores), and Anopore 20 nm membranes. In each case, the starting solution is a 1 g/L solution of AA in toluene and the experiments were all done at 25±0.2°C. A full permeate spectrum was collected every 10 minutes. The absorbance profiles for the above membranes at the same three wavelengths as in Figure 4-8 are shown in Figure 4-13.

As described previously, the absorbance at 600 nm seems to be an indicator of
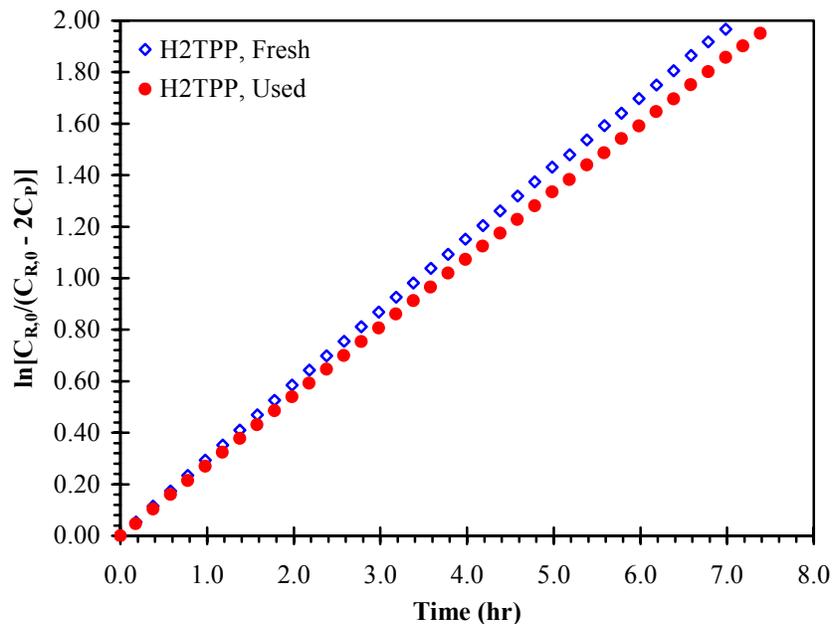
Figure 4-12: Effect of washing on an Anopore 20 nm membrane. The used membrane was washed prior to this test.

larger molecular weight species, and the permeate absorbance profiles at 600 nm seem to bear this out. In the case of the YM10 (3 nm) and the YM30 (5 nm) membranes, there is very little absorbance at 600 nm, even after 7 days. In the case of the Anopore®️ membrane (20 nm), there is significant absorbance at 600 nm indicating that there is little or no retention of asphaltene aggregates by this pore size. If the permeate spectra for the 20 nm Anopore®️ membrane are examined further (Figure 4-14), it is apparent that the permeate spectra match those of the whole asphaltenes closely, indicating that the whole asphaltenes are indeed diffusing across this membrane. There is a slight increase in the absorbance in the UV (350-500 nm), similar to the behaviour of the tighter membranes, indicating that the smaller (UV) species are diffusing slightly faster than the larger aggregated components. This is not entirely surprising since mobility is a function of size and since the larger species are likely to experience more hindrance from the membrane pores (equation {4.19}).

The results with the YM100 membrane (9 nm), shown in Figure 4-15, are very similar to the Anopore®️ 20 nm membrane. The permeate spectra exhibit a similar shape to the whole asphaltenes, with a slightly steeper UV region. This would indicate that this
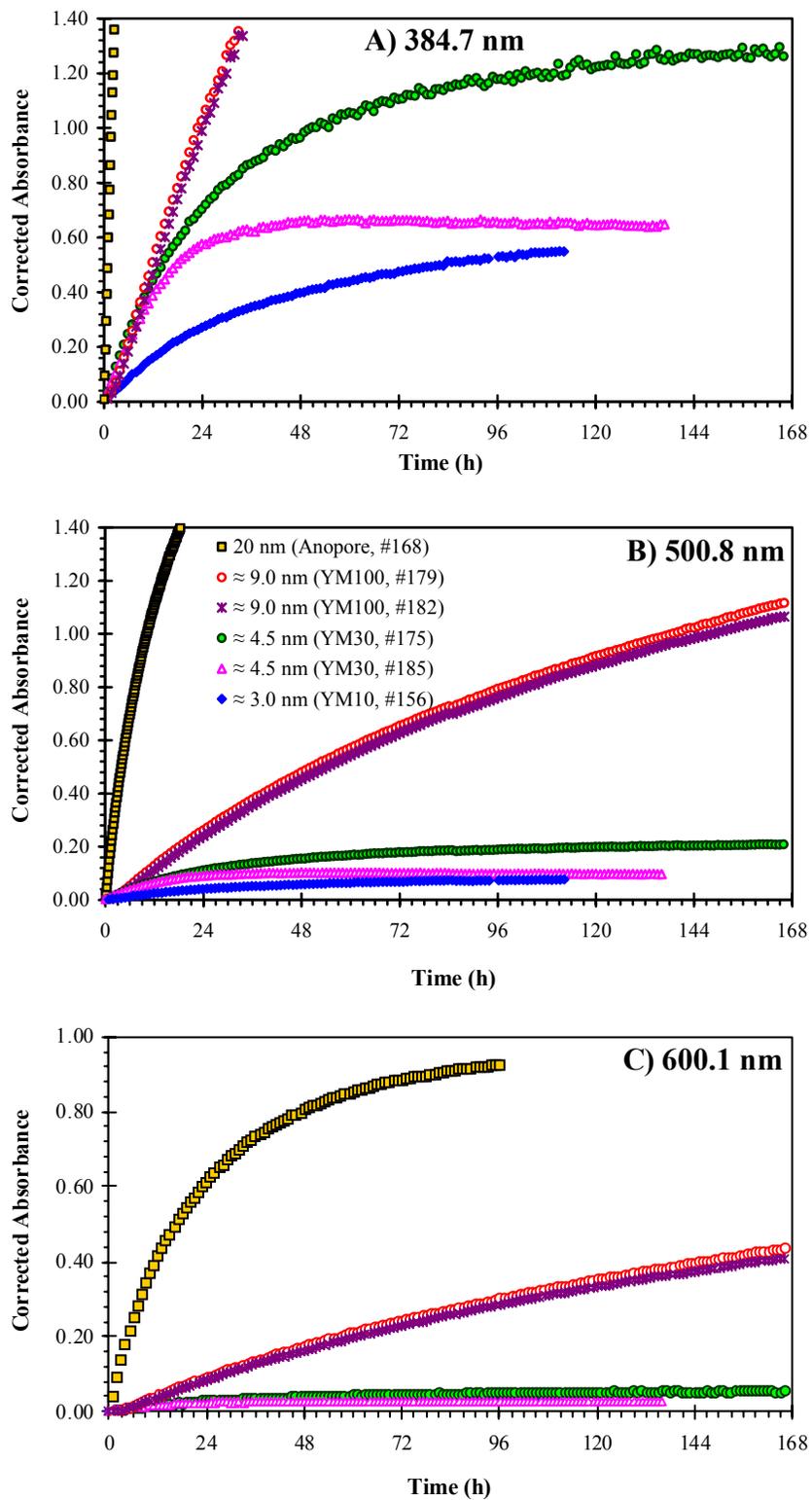
Figure 4-13: Permeate absorbance profiles for diffusion of AA in toluene as a function of membrane pore size: T = 25.0±0.2°C, stirrer speed = 600 rpm, initial AA concentration = 1 g/L. (NOTE: the legend in B applies to all three figures)
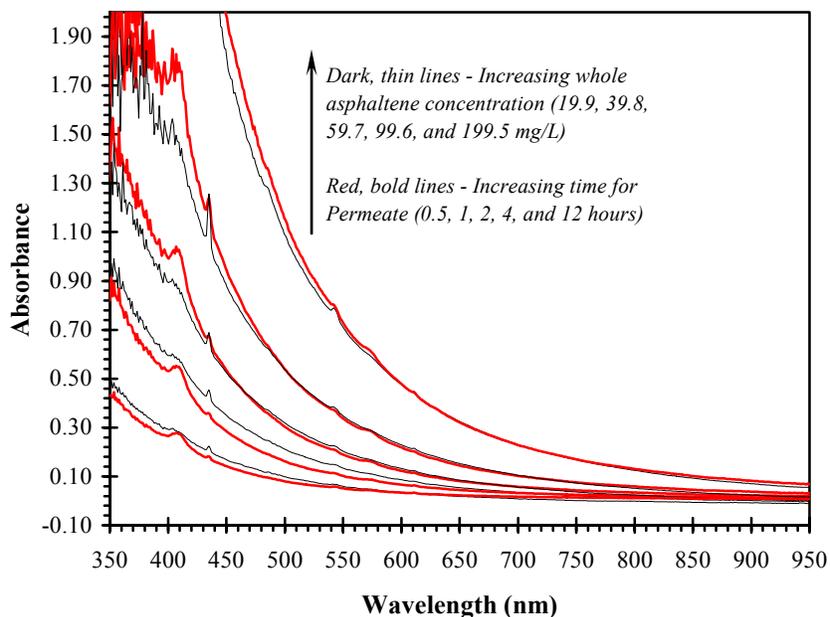
Figure 4-14: Comparison of raw permeate spectra to whole asphaltene spectra for for diffusion of AA in toluene (Expt #168): Anopore® 20 nm membrane, T = 25±0.2°C, initial concentration of AA = 1 g/L, stirrer speed = 600 rpm.
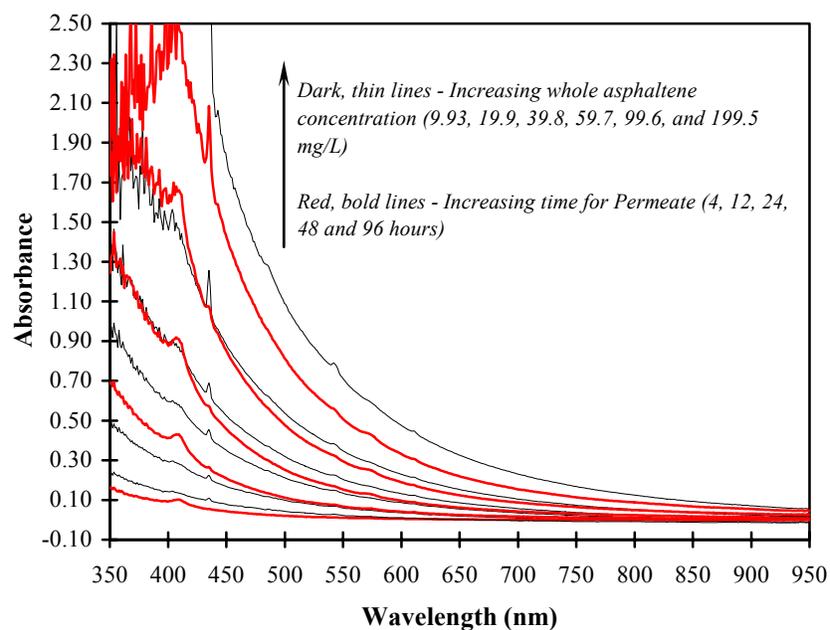
Figure 4-15: Comparison of raw permeate spectra to whole asphaltene spectra for diffusion of AA in toluene (Expt #182): Ultracel YM100 membrane (9.0 nm), T = 25±0.2°C, initial concentration of AA = 1 g/L, stirrer speed = 600 rpm.

membrane also allows the aggregated species to pass and therefore the aggregates are <9 nm in diameter.

The data in Figure 4-13 can now be combined with the asphaltene calibrations in Appendix C to determine the concentration of asphaltenes in the permeate and in turn calculate the effective diffusion coefficients for the AA for each of the four membranes considered above. Each membrane was calibrated using H_2TPP as previously discussed, with the exception of one of the YM30 membranes (#175) which was calibrated using VOTPP (D = 6.4±0.1 x 10^{-6} cm^2/s[228]). The concentration data were then analyzed using either equation {4.9} or equation {4.18}. In general, the first 12 hours of data were regressed in each case, since beyond 12 hours the data began to deviate from linearity, particularly for the YM10 and YM30 membrane. If the data exhibited extended linearity beyond 12 hours (the YM100 membrane exhibited excellent linearity), then the additional data were used. One added benefit of only considering the first 12 hours of data was that the effects of fouling were minimized since it was likely that fouling would require extended times to become significant. The calculated effective diffusivities are summarized for all four membranes in Table 4-5, and plotted in Figure 4-16 for the values from equation {4.9}.

Closer inspection of Table 4-5 and Figure 4-16 shows a couple of interesting trends:

1. There is a pronounced step change in the value of the effective diffusion coefficients between the YM30 (5 nm) and YM100 (9 nm) membranes. This would indicate that the size of the asphaltene aggregates is larger than 5 nm and smaller than 9 nm. This trend holds regardless of the wavelength used to calculate the effective diffusion coefficient.

2. The effective diffusion coefficient always declines as the analytical wavelength increases. This result implies, as previously stated, that the absorbance occurring at longer (visible) wavelengths is due to the larger, possibly aggregated, species.

3. The effective diffusion coefficients obtained for the YM100 (9 nm) and Anopore® (20 nm) membranes are in very good agreement with each other at all wavelengths. This result indicates that the aggregated species were not retained by these membranes and were diffusing through the membrane.

Table 4-5: Summary of effective diffusion coefficients for AA at 25°C

Membrane	$D_{e, AA}$ (x 10^{-6} cm²/s)					
	Equation {4.9}			Equation {4.18}		
	375.8 & 384.7 nm	*500.8 nm*	*600.1 nm*	*375.8 & 384.7 nm*	*500.8 nm*	*600.1 nm*
YM10 (#156)	0.58±0.08	0.32±0.13	0.26±0.49	1.3±0.1	0.72±0.20	0.58±0.72
YM10 (#161)	0.53±0.09	0.37±0.14	0.34±0.40	1.2±0.1	0.82±0.20	0.76±0.59
YM30 (#175)	0.51±0.07	0.26±0.04	0.18±0.05	1.2±0.2	0.59±0.09	0.41±0.08
YM30 (#185)	0.62±0.04	0.32±0.04	0.20±0.06	1.4±0.1	0.73±0.06	0.44±0.08
YM100 (#179)	1.66±0.05	1.31±0.04	1.16±0.04	4.1±0.1	2.23±0.06	2.82±0.08
YM100 (#182)	1.63±0.05	1.28±0.04	1.08±0.03	4.0±0.1	3.16±0.09	2.74±0.08
Anopore 20 nm (#168)	1.70±0.04	1.20±0.03	1.08±0.03	4.2±0.1	4.5±0.2	3.6±0.1
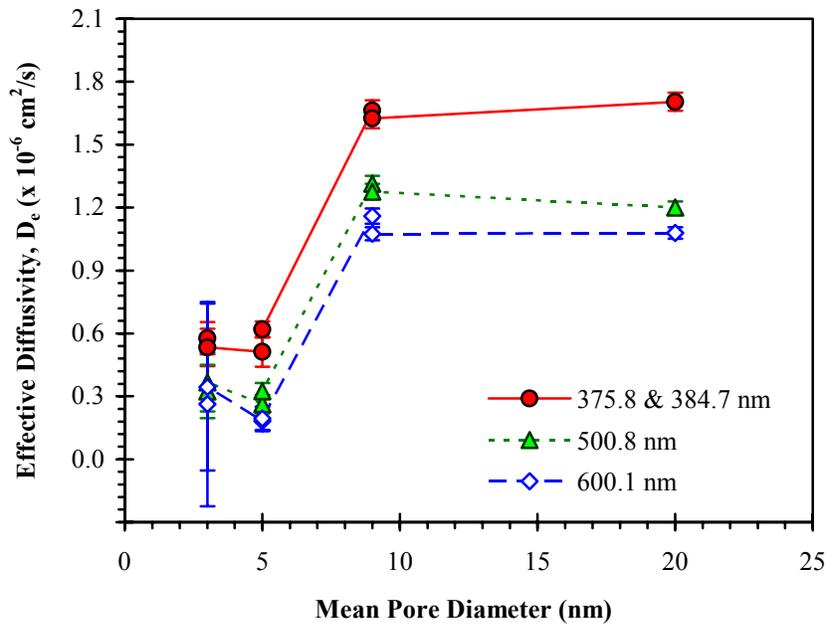
Figure 4-16: Effective diffusivity of AA (Equation {4.9}) as a function of membrane pore size

One point worth noting is that it is not entirely valid to use equation {4.18} to analyze the results from the YM100 and Anopore® membranes. As mentioned in point 3 above, these two membranes allow the aggregates to diffuse and as such the average molecular weight of both the permeate and retentate should be the same. However, the calculations leading to the results in Table 4-5 only used the first 12 hours of data. It is likely that the smaller monomers would diffuse first, followed by the larger, and slower

aggregates. Closer inspection of the spectra in Figure 4-15 shows that this may indeed be the case. The early permeate spectra (<24 hours) have a steeper UV curve relative to the whole asphaltenes than do the later permeate spectra. This observation would support the earlier statements that it is the aggregated asphaltenes which lead to absorption in the visible region.

Finally, it is worth commenting on the effects of hindered diffusion on the results presented above. An analysis was done for the YM30 membrane, which indicated that the effect of the tight pores was to decrease the diffusion coefficient of the monomer by a factor of 0.73 for the YM30 (5 nm) membrane. In the case of the YM100, assuming an aggregate molecular weight of 4,000 g/mol, equation {4.16} predicts a Stokes radius of 1.7 nm and equation {4.20} predicts a decrease in the diffusion coefficient by a factor of 0.64. For the Anopore® membrane, the reduction factor is 0.82. These values indicate that there will be significant hindrance effects, and the effective diffusion coefficients listed in Table 4-5 would change by 56% and 22% for the YM100 and Anopore® membranes, respectively. The corrected diffusivities would then be close to the range of reported values listed previously. In fact, it is anticipated that the diffusivities obtained with these larger pores should be lower than this reported range since the entire asphaltene fraction (aggregates) are diffusing and these larger species should have lower diffusivities. Considering the number of simplifications and assumptions that were required to obtain these values, the fact that they are as close to other reported values is encouraging.

4.4.3   EFFECT OF TEMPERATURE

Diffusion runs were performed at 70.0±0.2°C to assess the effect of temperature on the behaviour of AA. This temperature was chosen to coincide with the VPO data of Yarranton and co-workers[111-113]. Three different membranes were run at this elevated temperature: an Ultracel YM30 (30 kDa, ~4.5 nm pores), an Ultracel YM100 (100 kDa, ~9 nm pores), and an Anopore 20 nm membrane. In each case, the starting solution was a 1 g/L solution. A full permeate spectrum was collected every 10 minutes and the stirrer was operated at 600 rpm. The absorbance profiles at 500.8 and 600.1 nm are shown in Figure 4-17 for the above experiments, along with the corresponding data at 25°C. The resulting effective diffusion coefficients for the runs at 70°C are summarized in Table 4-6. In the case of the Anopore® and YM30 membranes, the increase in temperature causes the absorbance profiles at both wavelengths to rise, although not drastically. This
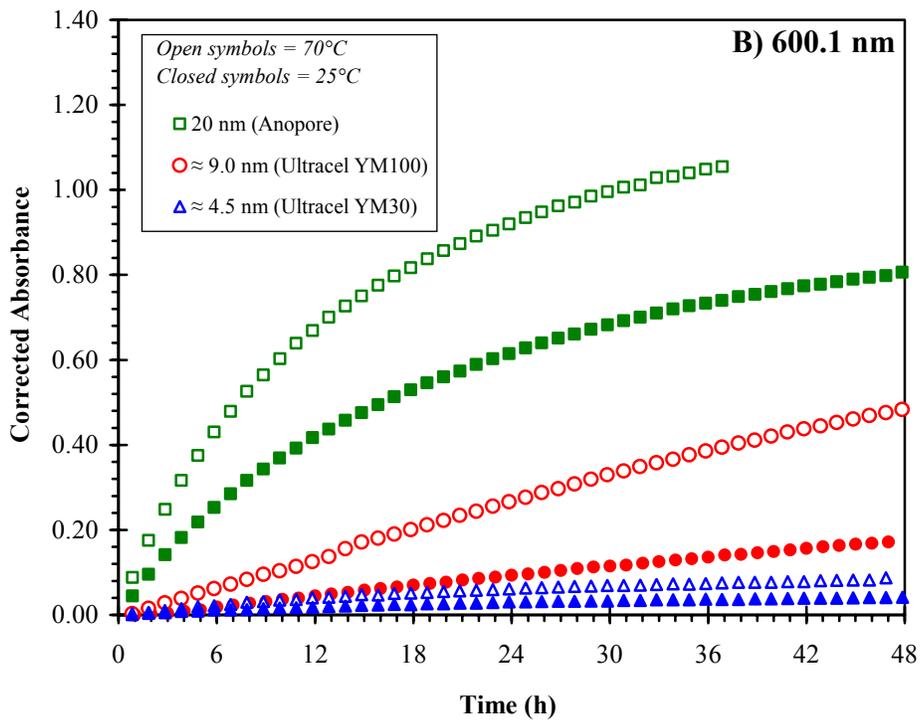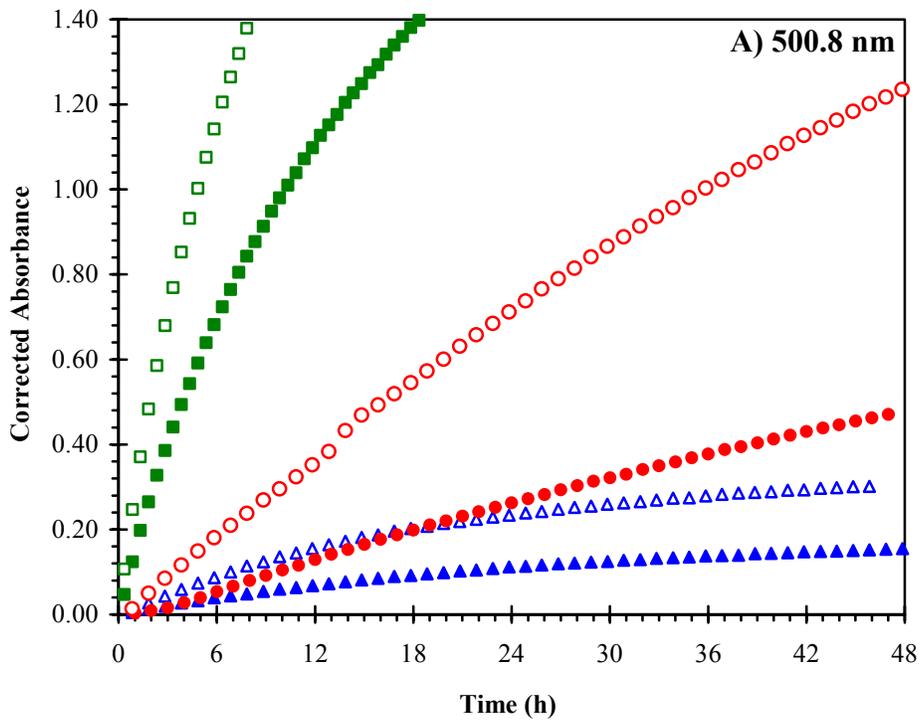
Figure 4-17: Permeate absorbance profiles for diffusion of AA in toluene as a function of pore size and temperature: stirrer speed = 600 rpm, initial AA concentration = 1 g/L.

Table 4-6: Summary of effective diffusion coefficients for AA at 70°C

Membrane	$D_{e, AA}$ (x 10^{-6} cm²/s)					
	Equation {4.9}			Equation {4.18}		
	375.8 & 384.7 nm	*500.8 nm*	*600.1 nm*	*375.8 & 384.7 nm*	*500.8 nm*	*600.1 nm*
YM30 (#176)	1.2±0.2	0.68±0.09	0.43±0.07	2.8±0.4	1.6±0.2	0.98±0.1
YM100 (#192)	3.7±0.1	3.13±0.09	2.84±0.08	9.0±0.3	8.5±0.2	7.5±0.2
Anopore 20 nm (#172)	3.8±0.1	2.64±0.06	2.36±0.06	9.3±0.2	13.5±0.8	11.1±0.5

makes sense since one would expect the asphaltenes to become more mobile at higher temperatures. If the effective diffusion coefficients in Table 4-6 are compared with those in Table 4-5, the values at 70°C are higher by a factor of ~2 with both of these membranes. According to the Stokes-Einstein relation (equation {4.15}) if the size of the diffusing species does not change, then the ratio Dη/T remains constant and we can write:

$$\frac{D_1}{D_2} = \frac{\eta_2}{\eta_1} \frac{T_1}{T_2} \quad \text{...} \quad \{4.21\}$$

Using viscosities of 0.5542 and 0.3482 mPa·s at 25°C and 70°C, respectively[241], the ratio of diffusion coefficients would then be 1.83. This is reasonably close to the observed ratios which ranged from 1.9-2.3. This would imply that an increase in temperature to 70°C did not result in a substantial decrease in the size of the aggregates at the concentration in these experiments. This observation agrees with the VPO measurements of Yarranton *et al.*[111-113] which showed that at concentrations below 2 g/L, temperature had a small effect on the observed size of the aggregates.

4.4.4 EFFECT OF CONCENTRATION

Two runs were performed at a concentration of 0.1 g/L to assess the effect of concentration on the behaviour of AA. Two different membranes were tested at this concentration: an Ultracel YM10 (10 kDa, 3 nm pores) and an Anopore 20 nm membrane. In each case, the temperature was 25.0±0.2°C. A full permeate spectrum was collected every 10 minutes and the stirrer was operated at 600 rpm. Because the concentration is so much lower than the previous data, plotting the absorbance profiles would not be instructive. Rather, the operating line plots (i.e. equation {4.9}) of these low concentration runs were compared to those at the higher concentration at a

wavelength of 384.7 nm in Figure 4-18. The effective diffusion coefficients of these low concentration measurements are listed in Table 4-7.

Table 4-7: Summary of effective diffusion coefficients for AA with 0.1 g/L initial concentration

Membrane	$D_{e, AA}$ (x 10^{-6} cm²/s), Equation {4.9}		
	375.8 & 384.7 nm	*500.8 nm*	*600.1 nm*
YM10 (#157)	0.52±0.7		
Anopore 20 nm (#170)	1.7±0.5	2.64±0.06	2.36±0.06

In the case of the Anopore® membrane, the results of the low concentration and the high concentration measurements completely overlap. Unfortunately, for the high concentration experiment, the detector is quickly saturated at this wavelength and therefore it is not possible to extend this curve to see if this overlapping trend continues. Based on the measured effective diffusivities (1.70±0.04 at 1 g/L, 1.70±0.5 at 0.1 g/L) it would appear that they are indeed the same. This is not surprising since this membrane has relatively large pores and allows full diffusion of all asphaltenes even at 1 g/L. Therefore, diluting the solution doesn't really change the ability of the asphaltenes to pass through the pores, particularly those species which absorb at a wavelength of 384.7 nm.

A similar behaviour was observed with the YM10 membrane. The two operating lines essentially overlap, although the experimental error at the low concentrations is large and hence the much larger scatter in the data. It should be noted that the analysis for the YM10 membrane was only done at a wavelength of 384.7 nm because the absorbances at 500.8 and 600.1 nm were too low for quantitation. The effective diffusion coefficient at the lower concentration is virtually identical to the value obtained at 1 g/L indicating that the size of the aggregates are essentially the same at both concentrations.

4.4.5 EFFECT OF ASPHALTENE ORIGIN

Three runs were performed using asphaltenes from different origins: Safaniya asphaltenes (SA), Venezuelan asphaltenes (VA), and asphaltenes from an Athabasca bitumen that has been partially demetallated (APDA, see section 4.3.5.3). These tests were all carried out using an Ultracel YM30 membrane with an initial asphaltene concentration of 1 g/L and a temperature of 25.0±0.2°C. A full permeate spectrum was
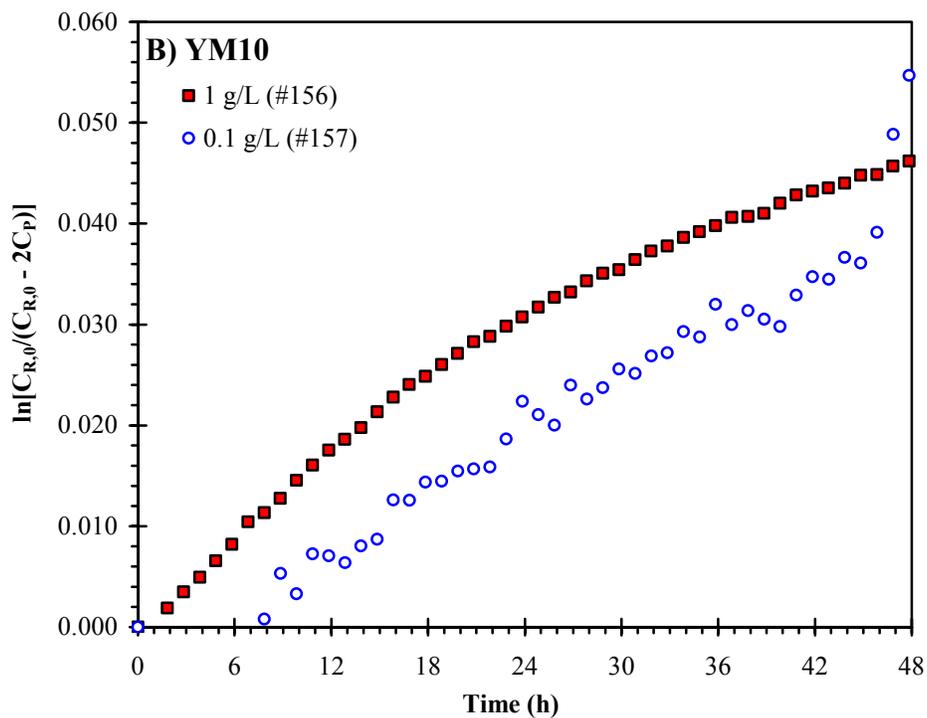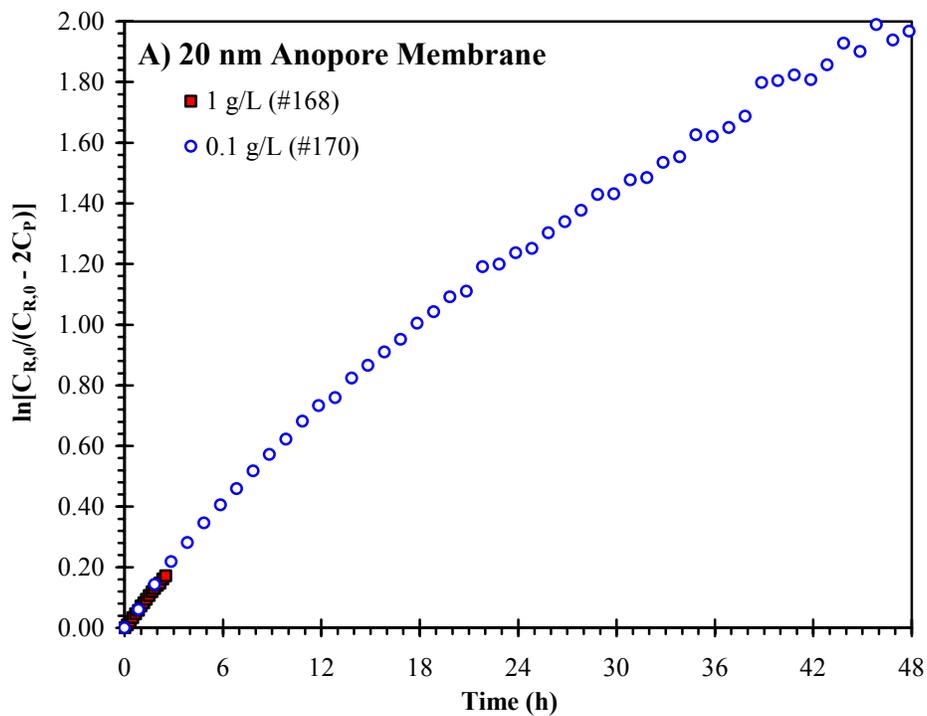
Figure 4-18: Comparison of diffusion operating line plots (equation {4.9}), quantified at a wavelength of 384.7 nm, as a function of AA concentration in toluene: T = 25.0±0.2°C, stirrer speed = 600 rpm.

collected every 10 minutes and the stirrer was operated at 600 rpm. The absorbance profiles for the above asphaltenes at the three wavelengths used previously are shown in Figure 4-19 (along with the profile for AA for comparison), and the resulting effective diffusion coefficients are listed in Table 4-8.

Table 4-8: Summary of effective diffusion coefficients for asphaltenes of different origins with 1 g/L initial concentration

	$D_{e, AA}$ (x 10^{-6} cm^2/s)					
	Equation {4.9}			Equation {4.18}		
Membrane	*375.8 & 384.7 nm*	*500.8 nm*	*600.1 nm*	*375.8 & 384.7 nm*	*500.8 nm*	*600.1 nm*
Athabasca, AA (#175)	0.51±0.07	0.26±0.04	0.18±0.05	1.2±0.2	0.59±0.09	0.41±0.08
Safaniya, SA (#188)	0.74±0.04	0.36±0.04	0.18±0.05	1.71±0.08	0.82±0.06	0.41±0.07
Venezuelan, VA (#189)	0.74±0.04	0.32±0.03	0.26±0.06	1.70±0.08	0.73±0.06	0.73±0.05
Athabasca Part. Demet., APDA (#190)	0.41±0.03	0.28±0.03	0.13±0.04	0.92±0.06	0.62±0.05	0.29±0.07

The absorbance profiles for all four asphaltene samples are qualitatively similar indicating that the origin of the asphaltenes does not affect their behaviour at the current conditions. The effective diffusion coefficients of SA and VA asphaltenes are virtually identical as are the effective diffusion coefficients of the unadulterated AA and the APDA asphaltenes. The VA and SA asphaltenes have slightly higher diffusion coefficients (~34-45%) than those of Athabasca origins, indicating that perhaps these asphaltenes are smaller and more mobile, although the difference is relatively small making any quantitative conclusions of little value.

4.4.5.1 Safaniya Asphaltenes

The permeate and whole asphaltene spectra for the SA asphaltenes in Figure 4-20 look qualitatively similar to the results obtained with the AA asphaltenes. The UV & violet region (350-500 nm) of the permeate spectra are much steeper, with little or no absorption occurring beyond 600 nm. The height of the metalloporphyrin peak at 407 nm is much lower as a result of the lower vanadium content of this material (discussed later).

4.4.5.2 Venezuelan Asphaltenes

The permeate and whole asphaltene spectra for the VA asphaltenes in Figure 4-21
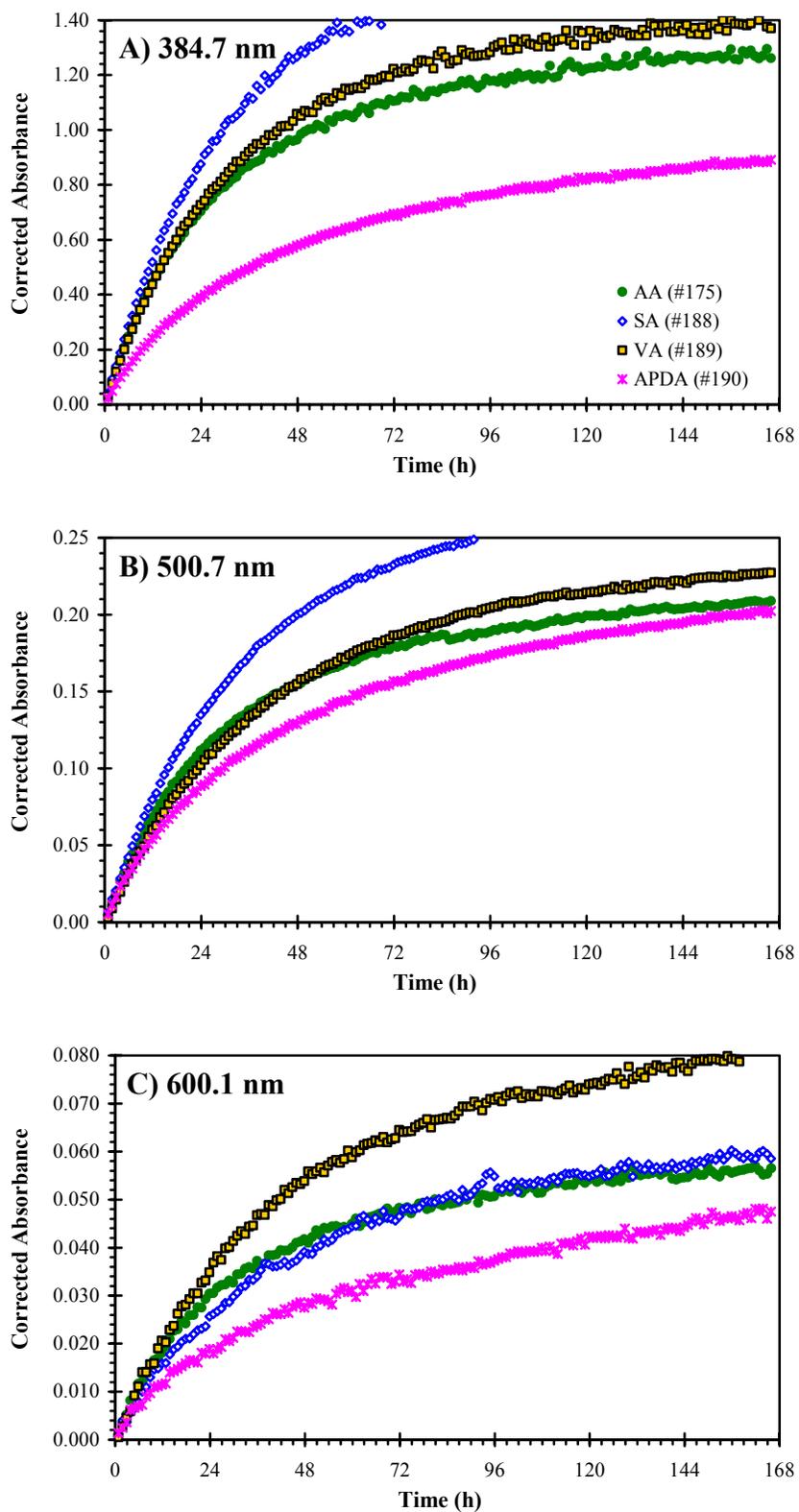
Figure 4-19: Permeate absorbance profiles for diffusion of asphaltenes from different origins in toluene: T = 25.0±0.2°C, stirrer speed = 600 rpm, initial asphaltene concentration = 1 g/L, membrane = Ultracel YM30 (5 nm). (NOTE: the legend in A applies to all three figures)
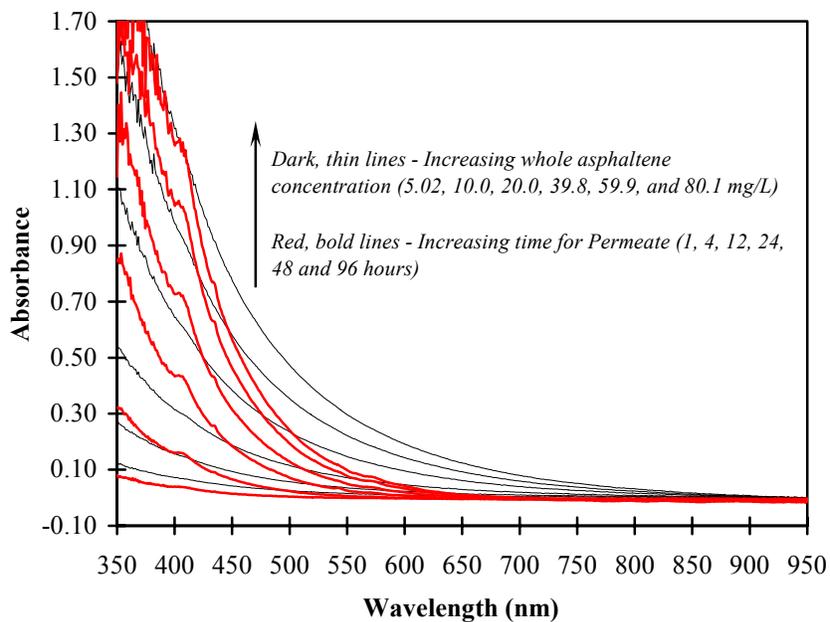
Figure 4-20: Comparison of raw permeate spectra to whole asphaltene spectra for diffusion of SA in toluene (Expt #188): Ultracel YM30 membrane (5 nm), T = 25±0.2°C, initial concentration = 1 g/L, stirrer speed = 600 rpm.
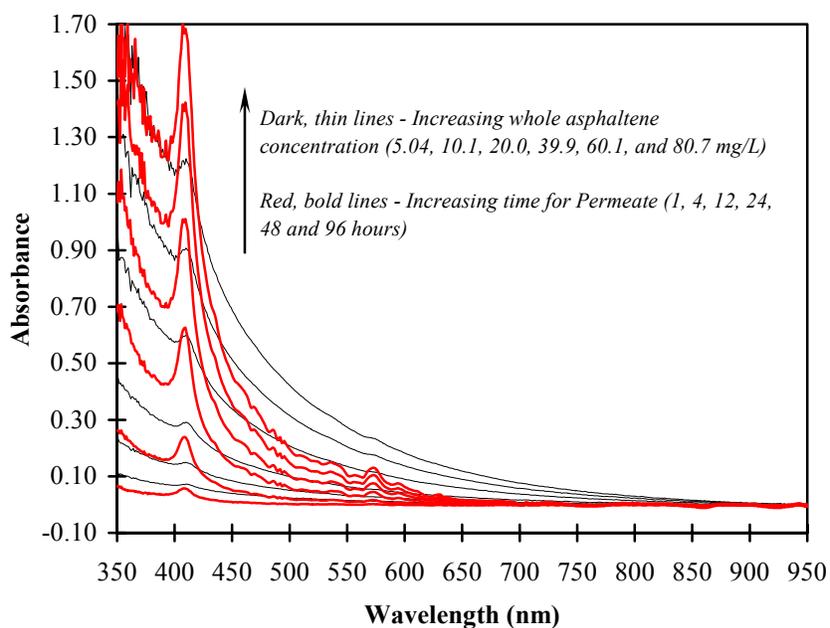
Figure 4-21: Comparison of raw permeate spectra to whole asphaltene spectra for diffusion of VA in toluene (Expt #189): Ultracel YM30 membrane (5 nm), T = 25±0.2°C, initial concentration = 1 g/L, stirrer speed = 600 rpm.

once again look qualitatively similar to the results obtained with the AA asphaltenes. The UV & violet region (350-500 nm) of the permeate spectra are much steeper, with little or no absorption occurring beyond 600 nm. The height of the metalloporphyrin peak at 407 nm is much higher as a result of the higher vanadium content of this material (discussed later). There is also an additional small peak at 577 nm, which can be attributed to the α peaks of metalloporphyrins. The other features appearing between 450 and 550 nm are too small to clearly identify, but it is possible that they are also attributable to the higher concentration of metalloporphyrins.

4.4.5.3 Athabasca Partially Demetallated Asphaltenes

The permeate and whole asphaltene spectra for the APDA asphaltenes in Figure 4-22 look qualitatively similar to the results obtained with the AA asphaltenes. The UV & violet region (350-500 nm) of the permeate spectra are much steeper, with little or no absorption occurring beyond 600 nm. There is no metalloporphyrin peak at 407 nm which fits with the origin of the sample since it has been processed to remove a large portion of the vanadium. These spectra are also notably smoother with very little if any spectral features emerging. It is not clear why this is, although it is likely that the process for removal of the vanadium has removed the chromophores that are responsible for the
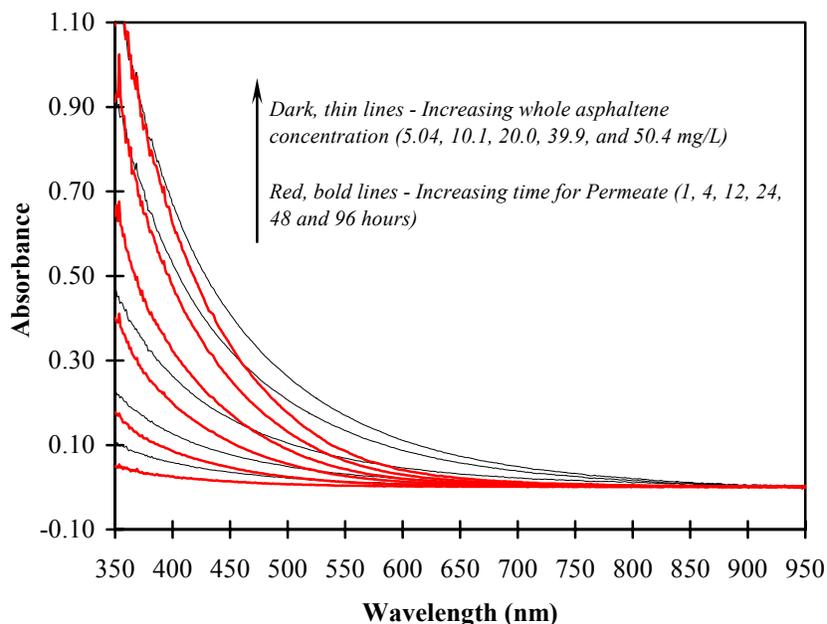
Figure 4-22: Comparison of raw permeate spectra to whole asphaltene spectra for diffusion of APDA in toluene (Expt #190): Ultracel YM30 membrane (5 nm), T = 25±0.2°C, initial concentration = 1 g/L, stirrer speed = 600 rpm.

features evident with the other asphaltene samples.

4.4.6 GENERAL DISCUSSION

The main conclusions that can be drawn from these results are:

1. The size of the asphaltene structures in toluene at 1 g/L are between 5 and 9 nm based on the significant jump in effective diffusivities observed between these pore sizes.

2. An increase in temperature results in an increase in asphaltene mobility but does not reduce the size of the asphaltene structures below 5 nm.

3. A decrease in concentration to 0.1 g/L results in a significant decrease in the size of the asphaltene structures to < 3 nm.

4. The exclusion of a large portion of the total asphaltenes by pores < 5 nm eliminates the absorbance of visible light (>600 nm) by asphaltenes.

The sizes reported in the literature for asphaltenes in toluene vary over a sizeable range. Spiecker *et al.*[103] reported a correlation length (radius of gyration) of 4.5 nm at 25°C for a Hondo asphaltene in toluene (1 wt%, ~10 g/L) using SANS. Gawrys and Kilpatrick[265] reported radii of gyration ranging from 0.06-7.5 nm at 25°C depending on the form assumed for the aggregated species (e.g. monodisperse spheres, prolate cylinders, oblate cylinders etc.) using SANS for 1 wt% Canadon Seco and Arab heavy asphaltenes. Rajagopal and Silva[266] reported a radius of 21-24 nm at 20°C for 1 mg/L Brazilian asphaltenes in toluene using light-scattering. Fenistein *et al.*[267] reported a radius of gyration of 6.1 and 6.9 nm at 20°C for 3.6 wt% asphaltenes using SANS. Obviously, the results obtained using scattering measurements are highly variable, although they seem to be in the general range of 4-6 nm. It should also be noted that very few results were available for toluene solutions at low concentrations (0.1 wt% or 1 g/L) and as such the above results are expected to be a little higher. Note also that the results from scattering experiments yield a mass-average size as opposed to the number-average size implied by the Stokes-Einstein (hydrodynamic) radius[268] and as such there are bound to be some discrepancies. Despite these caveats, all of the data reported above using scattering techniques imply aggregate sizes which are in the correct order of magnitude reported by this work (5-9 nm), with the exception of the result of Rajagopal and Silva[266] which is significantly higher than all other measurements.

As for the size of the asphaltene monomers, there is very little data available from scattering techniques at the low concentrations required to obtain this information. The majority of the debate surrounding the low concentration regime surrounds the molecular weight, which is in turn a function of the physical size. The infinite dilution diffusivities reported previously all point to a monomer size on the order of $r_s = 0.6 – 1.8$ nm. This size range fits well with the current observations based on the ability of the smaller fractions to diffuse across even the tightest (3 nm) membrane.

The majority of the discussion thus far has been done under the assumption that the asphaltenes are composed of two components: a monomer of lower molecular weight and an aggregated species with higher molecular weight consisting of several monomers. The analysis was done using the VPO data of Yarranton *et al.*[111, 112] which put the monomer and aggregate molecular weights at 1,800 Da and 4,000 Da, respectively. These molecular weights imply that the aggregate is roughly a dimer. This simplified picture is somewhat misleading since it is likely that the asphaltenes consist of a distribution of species of higher molecular weights rather than a simple bimodal distribution. The molecular weight distributions for AA in toluene at different concentrations and temperatures predicted by the model of Agrawala and Yarranton[112] are shown in Figure 4-23. The predictions at 25°C were done by extrapolating the constants given at 50°C and 70°C down to 25°C. This simplified model assumes that the asphaltenes consist of two types of molecules: propagator molecules (P) which polymerize in integer multiples, and terminator molecules (T) which bind to the propagators/polymers to halt or terminate subsequent higher order association[112]. For the models in Figure 4-23, the propagator and terminator molecular weights were chosen as 1,800 Da and 800 Da, respectively. The calculated average molecular weight for each distribution is included in Figure 4-23 for reference.

This type of step-wise aggregation/association model and the resulting predicted molecular weight distributions shown in Figure 4-23 fit well with the behaviour observed in this work. The fact that there is some permeation of asphaltenes occurring even with the tightest membrane implies that there are components smaller than 3 nm (i.e. monomers). According to the distribution for 1 g/L AA at 25°C in Figure 4-23, approximately 20% of the total sample would have a molecular weight of 1,800 Da or less which fits with this observation. As well, the fact that less than 10% of the total asphaltenes are able to permeate the tightest membranes implies that there is a significant
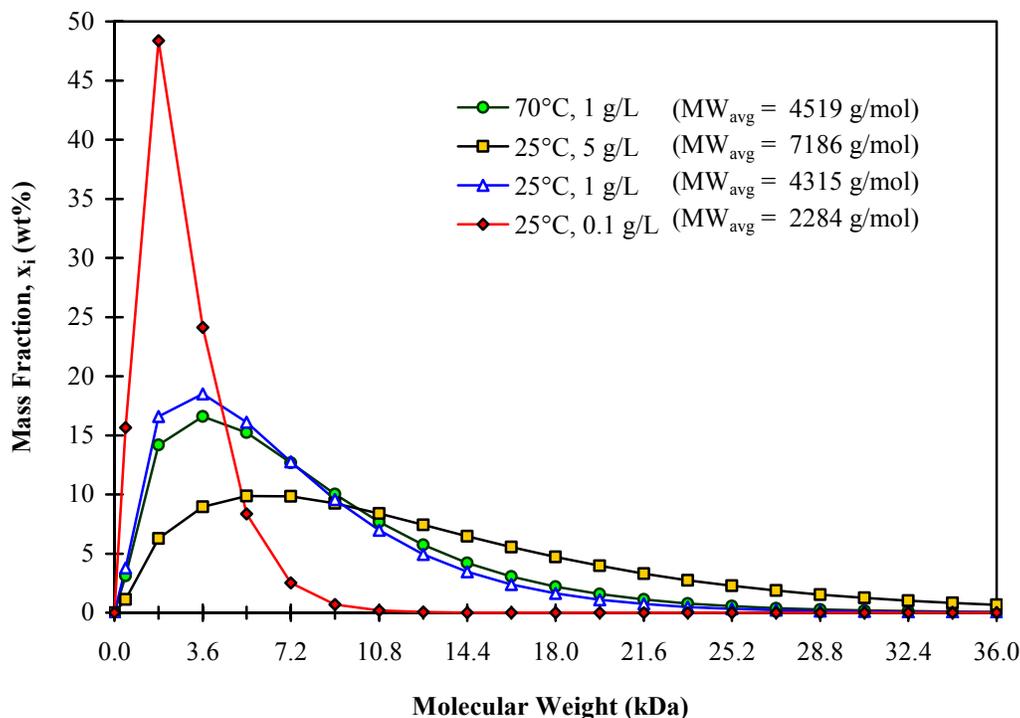
Figure 4-23: Molecular weight distributions for AA in toluene as a function of concentration estimated using the stepwise association model of Agrawala and Yarranton[112] with a terminator and propagator MW of 800 and 1,800 Da, respectively. The average molecular weight for each distribution is included for reference.

portion of the asphaltenes that are in an aggregated state, again in full agreement with the predicted distribution (>60% of the asphaltenes have a MW > 4,500 Da). The fact that the rate of transfer of the smaller monomers is very slow in the latter stages of the experiments (between 4 to 7 days) implies that the aggregated species are relatively stable and that the exchange of the monomers between the solution and the aggregates is very slow.

The results at low concentration (0.1 g/L) are also in qualitative agreement with this model. The effective diffusivity determined for the asphaltenes at 0.1 g/L is 4 times higher than the value reported at 1 g/L. As well, the analysis of the low concentration data was well described using the standard analysis with the total retentate concentration (i.e. no MW correction), indicating that the molecular weight of both the retained and permeating species were essentially the same. In other words, the asphaltenes are no longer large aggregates but rather are primarily in monomer form. The molecular weight distribution in Figure 4-23 suggests that over 60% of the total asphaltenes have a MW of 1,800 Da or less which would certainly lead to higher diffusion across the membrane.

In the case of the high temperature measurements, once again the molecular weight distributions predicted by the step-wise association model are still qualitatively supported. The increases in diffusivity at 70°C observed in this work can be explained using the Stokes-Einstein relationship (equation {4.21}) to correct for temperature and viscosity with no need for a substantial decrease in aggregate size. This result is in qualitative agreement with the predicted distributions in Figure 4-23 which show a relative insensitivity as a result of the change in temperature from 25 – 70°C.

Finally, the last observation that has not been explained is the lack of absorption in the visible region (>600 nm) for the permeate spectra when using the tighter (3 and 5 nm) membranes. It is clear that the asphaltenes present in the permeate are smaller than the retained species and as such the main explanation is likely tied to the size of the asphaltenes. When the radius of molecules and/or particles is significantly shorter than the wavelength of the incident radiation ($r < 0.1\lambda$), Rayleigh scattering can occur[269]. The total measured absorbance of a sample (also referred to as extinction) is given by Beers' law:

$$A = \varepsilon bC \quad\quad\quad\quad\quad\quad \{4.22\}$$

where A = Absorbance = $-\log_{10}(I/I_0)$
            I = intensity of light transmitted through sample
            I_0 = baseline intensity of light through solvent
            ε = total extinction coefficient
            C = analyte concentration

In the case of a standard UV/Vis experiment, the detector is in a straight line with the incident light. Light that is scattered by solutes in the solution will not reach the detector and will be interpreted as an absorbance. Therefore, the measured extinction coefficient, ε, is the sum of the scattering and absorption contributions[269]:

$$\varepsilon = \frac{N_A}{2.303}\left(a_{C,A} + a_{C,S}\right) \quad\quad\quad\quad \{4.23\}$$

where N_A = Avogadro's number = 6.0221415 x 10^{23}
            $a_{C,A}$ = Absorption cross-section
            $a_{C,S}$ = Scattering cross-section

The Rayleigh scattering cross-section for a spherical particle of radius r is given by[269]:

$$a_{C,S-Rayleigh} = \frac{128\pi^5 n_S^4}{3} \left[\frac{\left(n_P/n_S\right)^2 - 1}{\left(n_P/n_S\right)^2 + 2} \right]^2 \frac{r^6}{\lambda^4} \quad \text{.......................} \{4.24\}$$

where n_S = Refractive index of the solvent
n_P = Refractive index of the particle

If it is assumed that the observed extinction is a function of scattering only (i.e. $a_{C,A} = 0$), then equations $\{4.22\}$ - $\{4.24\}$ give:

$$A = bC\xi \frac{r^6}{\lambda^4} \quad \text{...} \{4.25\}$$

where $\xi = \text{constant} = \frac{128\pi^5 n_S^4 N_A}{3 \cdot 2.303} \left[\frac{\left(n_P/n_S\right)^2 - 1}{\left(n_P/n_S\right)^2 + 2} \right]^2$

Equation $\{4.25\}$ indicates that if Rayleigh scattering is responsible for the measured extinction in the visible region (> 600 nm), then the measured absorbance should vary linearly with the inverse 4th power of the wavelength ($1/\lambda^4$). In contrast, if the observed extinction were due to absorption then the measured absorbance would vary with $1/\lambda$[269].

Figure 4-24 shows several spectra of AA in toluene plotted in the form of equation $\{4.25\}$. It is immediately apparent from this figure that all of these spectra are linear within this region (R^2 for all of the linear fits were > 0.996). The fact that these curves are highly linear would indicate that the primary mechanism for the observed extinction in the visible region is indeed Rayleigh scattering. If absorption was significant in this region, it would be expected that the coefficient for λ would be somewhere between 1 (absorption) and 4 (Rayleigh scattering). In fact, Owen[270] states that for complex chemical systems, the effective exponent can vary between 2 to 4. However, none of the spectra in Figure 4-24 show any signs of significant deviations from linearity indicating limited absorption in this region.

This analysis also agrees with the observation that the permeate spectra have no absorbance in the visible region. As indicated by equation $\{4.25\}$, the absorbance due to scattering is directly proportional to r^6 and hence the magnitude of the scattering extinction will increase dramatically with the size of the solute. By retaining the large aggregated asphaltene species, the scattering effect is effectively eliminated and as such there is no absorbance observed beyond 600 nm.
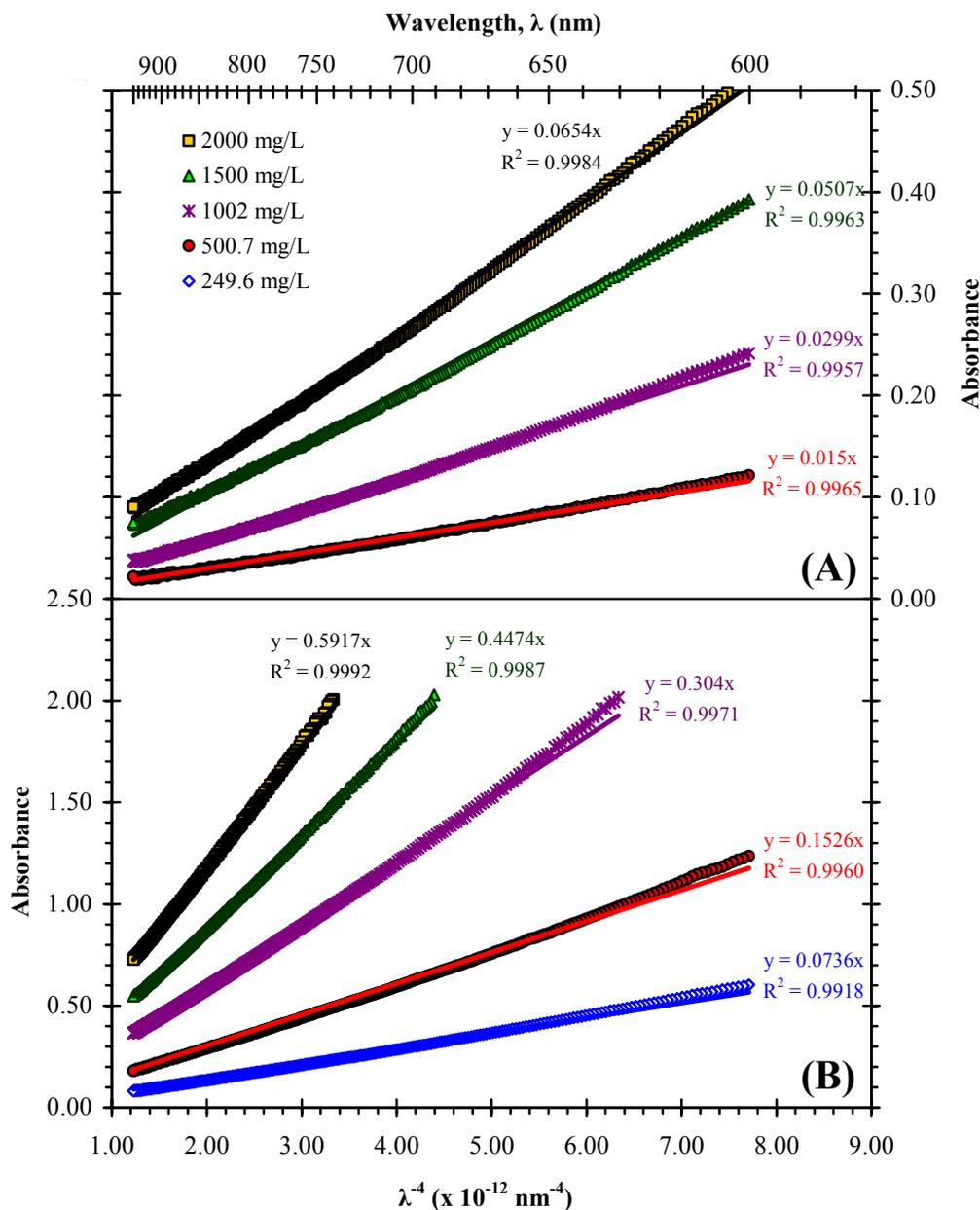
Figure 4-24: Rayleigh scattering curves for AA in toluene: (A) 1 mm Cuvette, (B) 10 mm Cuvette

The above scattering justification is in stark contrast to the analysis of Ruiz-Morales *et al.*[271, 272], whom explained the absorbance in the visible region (>600 nm) using molecular orbital calculations. They propose that the absorbance in the visible region is due to large fused-ring systems with 4-10 fused rings per molecule. However, a large part of this explanation relies on the claim that the absorbance in this region is linear when plotted as a function of $1/\lambda$. Closer examination of their measured

absorbances indicates that their data is clearly not linear in this region. As well, their analysis does not take into account the effects of association on the absorption of the asphaltene systems, which as the preceding results indicate clearly occurs for these systems.

Evdokimov *et al.*[273-276] have studied the optical absorption behaviour of crude oils and asphaltenes in depth. They observed a power law relationship of $A \propto \lambda^{-m}$ with m ranging between 3.14 and 4.33[273] which fits with the trends observed in this work. In fact, their analysis included some of the same data used by Ruiz-Morales *et al.*[271, 272] noted above. The varying value of m is indicative of a heterogeneous chemical system, although the fact that the observed exponents are centered on a value of 4 indicates that Rayleigh scattering is the dominant mechanism. Further scattering measurements at 633 nm[274] supported the contention that Rayleigh scattering was occurring within similar concentration ranges and wavelengths as used in this work.

4.5 Diffusion of Metalloporphyrins

4.5.1 UV/VIS QUANTITATION OF METALLOPORPHYRINS IN ASPHALTENE MIXTURES

Prior to performing diffusion studies involving model and native metalloporphyrins mixed with asphaltenes, the effect of the asphaltene matrix on the UV/Visible response of the metalloporphyrins must be determined. Effectively, it must be verified whether the presence of the asphaltenes will cause significant deviations from Beer's law[277]:

$$A = \varepsilon bC \quad \text{...} \quad \{4.26\}$$

where A = Absorbance = $-\log_{10}(I/I_0)$
I = intensity of light transmitted through sample
I_0 = baseline intensity of light through solvent
ε = molar absorptivity of analyte (L/mol·cm)
C = analyte concentration (mol/L)

Equation {4.26} is the standard method for correlating spectroscopic measurements (absorbance) to quantitative concentration measurements and it requires that the response of the analyte to the specified radiation be linear. One major cause for a non-linear relationship is the presence of so-called "matrix effects". The presence of a different chemical species can cause the electronic environment of the analyte to change and result in a change in its absorbance of electromagnetic radiation[277]. Therefore, any

quantitative calibration should include as many of the matrix components as possible in order to account for any or all interactions which may affect the absorption. The metalloporphyrin calibrations given in Appendix B only include toluene and n-heptane as matrix components and as such the presence of asphaltenes in the system could lead to a deviation from these calibration curves.

The effect of asphaltenes on the absorption characteristics of VOOEP were tested in detail by mixing VOOEP with AA in toluene and measuring the spectra of the mixtures. The concentrations of VOOEP were tested at three different levels to optimize the height of the VOOEP peaks with different pathlengths: 1.12 μmol/L VOOEP (Soret band @ 407 nm with a 10 mm pathlength), 12.0 μmol/L VOOEP (Soret band @ 407 nm with a 1 mm pathlength and visible bands @ 533 & 572 nm with a 10 mm pathlength), and 100 μmol/L VOOEP (visible bands @ 533 & 572 nm with a 1 mm pathlength). The asphaltene concentration was varied from 0 – 2,000 mg/L, and all of the spectra collected were done using both light sources with a crossover wavelength of 460 nm.

In order to assess the effect of the asphaltenes on the VOOEP spectra, the spectrum of pure AA in toluene at the same concentration was subtracted from the mixture spectrum. The pure asphaltene spectra were corrected for slight differences in concentration using Beer's law as follows:

$$A_2 = A_1 * \frac{C_2}{C_1}$$ .... {4.27}

The corrected spectra (mixture spectrum – pure AA spectrum) are shown in Figure 4-25 and Figure 4-26 below. The fact that all of the corrected spectra are virtually superimposed on the pure VOOEP spectrum indicated that the spectra were additive and as such any interactions that did occur between VOOEP and AA in toluene did not impact the UV/Visible spectra of either analyte. Therefore, it is valid to use the calibration curves listed in Appendix B for quantifying the concentration of vanadyl porphyrins in the presence of asphaltenes in toluene.

Now that asphaltene matrix effects have been ruled out, it is necessary to test the overall quantitative method for VOOEP concentration in the presence of asphaltenes. Unfortunately, it is not possible to subtract an entire asphaltene spectrum from the mixture spectrum in the case of the asphaltene diffusion studies since the shape and nature of the asphaltene spectrum changes through the course of the diffusion process
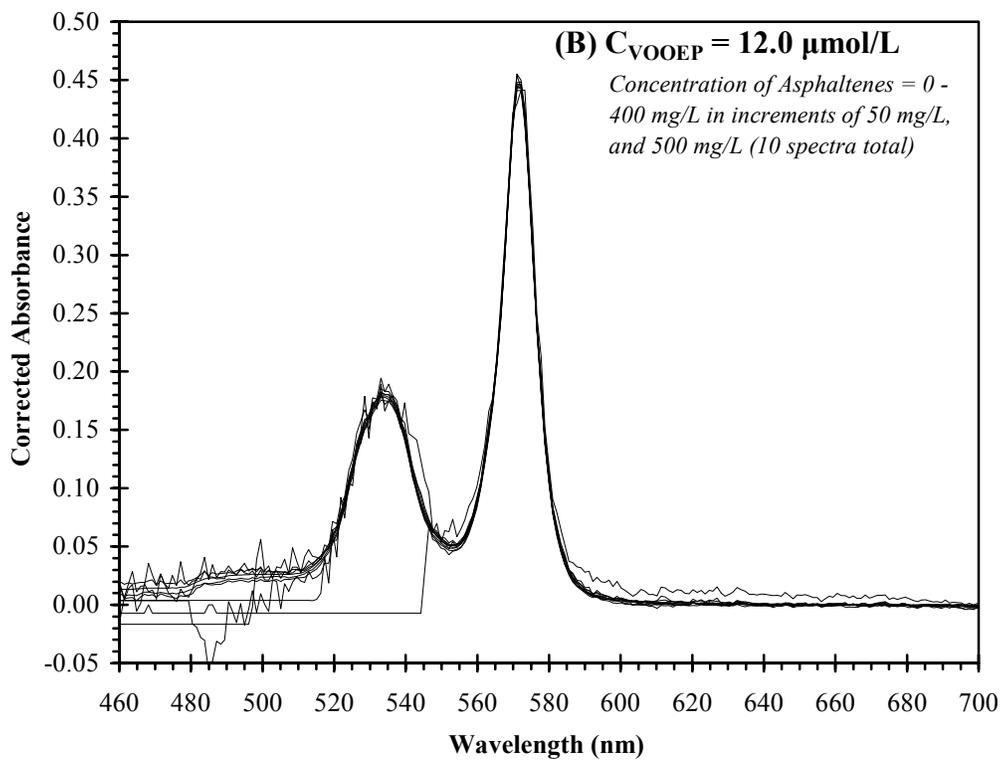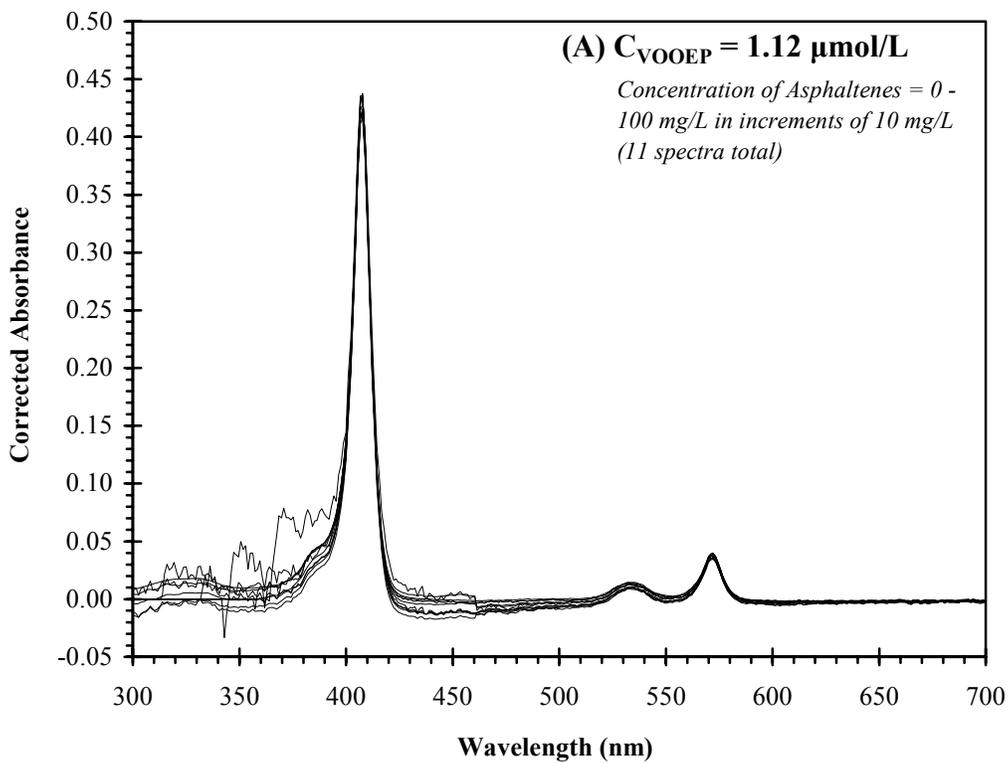
Figure 4-25: Corrected Spectra for VOOEP + AA in toluene with the 10 mm pathlength cuvette
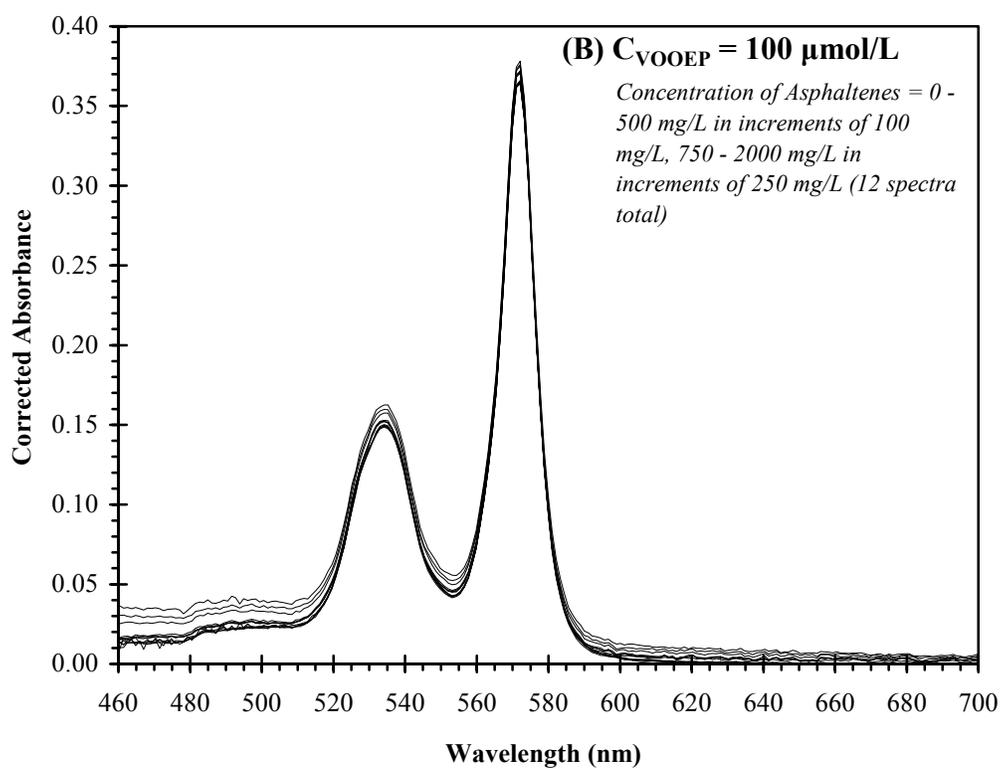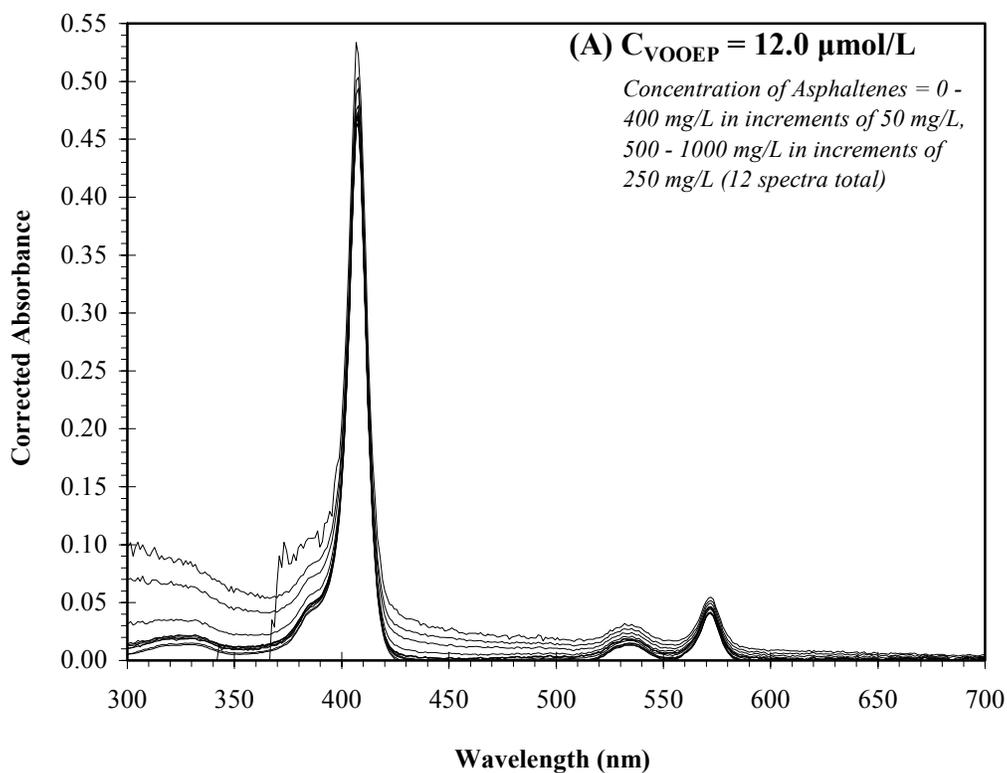
Figure 4-26: Corrected Spectra for VOOEP + AA in toluene with the 1 mm pathlength cuvette

(see section 4.4). Therefore, some other means of baseline correction was necessary to correct for the absorption of the asphaltenes (A_b) in the vicinity of the porphyrin peaks. This correction was of the form:

$$A_{C,porphyrin} = A_{max} - A_b$$ .... {4.28}

where $A_{C, Porphyrin}$ = Corrected absorbance of porphyrin @ λ_{max}
            A_{max} = Raw absorbance @ λ_{max}
            A_b = Estimated asphaltene absorbance @ λ_{max}
            λ_{max} = Wavelength of porphyrin peak

Two different methods were tested for estimating the asphaltene baseline absorbance (A_b) @ λ_{max}:

1. Linear Correction: This method assumes that the shape of the asphaltene spectrum is a straight line in the vicinity of the metalloporphyrin peak. This method uses two points (A_i,λ_i) from the mixture spectrum (one at a wavelength preceding the metalloporphyrin peak, and one at a wavelength following it) to define the asphaltene baseline. The absorbance of the asphaltenes (A_b) at the metalloporphyrin peak wavelength (λ_{max}) is then calculated by linear interpolation between the two baseline points.

2. Cubic Lagrange Polynomial Correction: This method assumes that the shape of the asphaltene spectrum is curved in the vicinity of the metalloporphyrin peak. This method uses four points (A_i,λ_i) from the mixture spectrum (two at wavelengths preceding the metalloporphyrin peak, and two at wavelengths following it) to define the asphaltene baseline. The absorbance of the asphaltenes (A_b) at the metalloporphyrin peak wavelength (λ_{max}) is then calculated using a cubic Lagrange polynomial[278]:

$$A_b(\lambda_{max}) = \sum_{j=1}^{4} A_j \left(\prod_{i=1, i \neq j}^{4} \frac{\lambda_{max} - \lambda_i}{\lambda_j - \lambda_i} \right)$$ .... {4.29}

These two baseline correction methods are illustrated graphically in Figure 4-27 for 2 different mixtures. The VOOEP peaks appear at 407.8 nm (Soret), 533.0 nm (α_1) and 572.2 nm (α_2). The corresponding baseline coordinates used for each baseline method are summarized in Table 4-9.

Table 4-9: Summary of wavelengths used for baseline correction data points

| Correction Method | Baseline Coordinates | |
	Soret Peak	α_1 & α_2 Peaks
Linear	375 and 440 nm	510 and 600 nm
Cubic Lagrange Polynomial	360, 370, 439, and 449 nm	480, 510, 600, and 620 nm
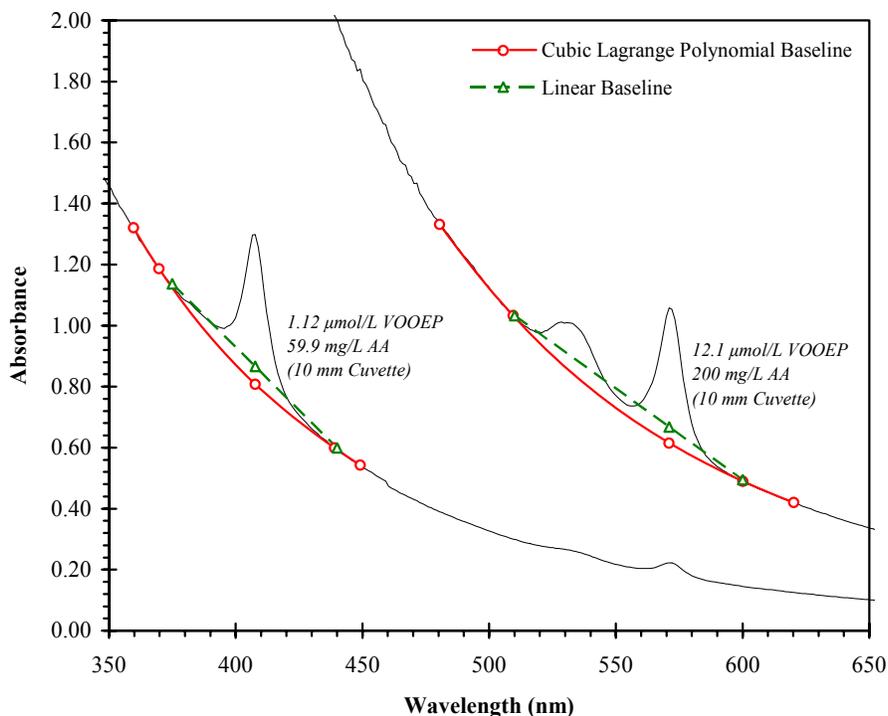
Figure 4-27: Implementation of baseline corrections to raw spectra

The two baseline correction methods were then used to estimate the concentration of VOOEP in the different solutions using the VOOEP calibration listed in Appendix B. The estimated concentration was then compared to the known concentration of VOOEP to test the accuracy of the two methods. In the case of the Soret peak (407 nm), the absorbance had to be corrected for the petroporphyrins peak that is present in the AA (see Appendix C). The results of these calculations are summarized in Figure 4-28.

It is immediately evident that the cubic Lagrange polynomial is a much better approximation for the asphaltene baseline than the linear approximation. In all cases, the linear baseline significantly under-predicts the concentration of VOOEP in the solution. The magnitude of this error increases with increasing asphaltene concentration since as
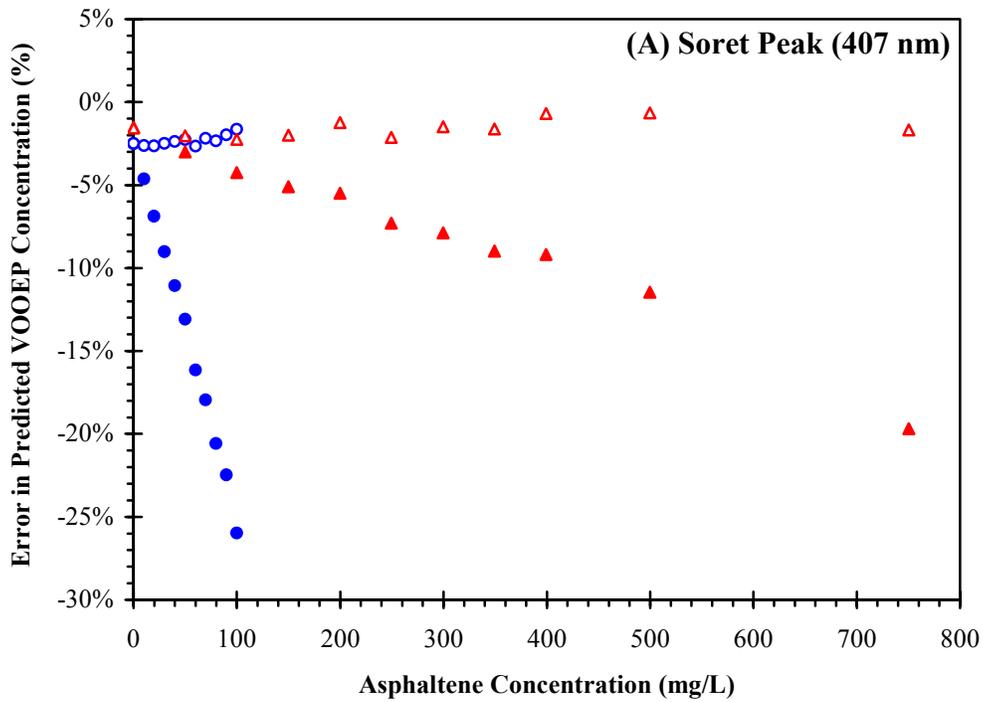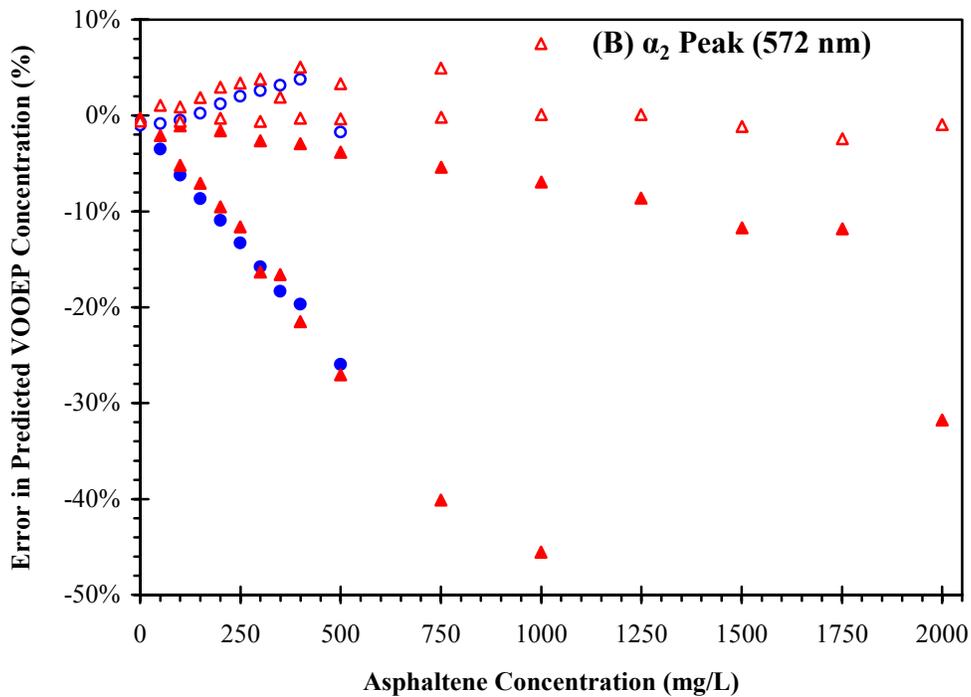
Figure 4-28: Comparison of the error in measured VOOEP concentration using the linear and cubic Lagrange polynomial baseline correction methods. Open symbols = cubic Lagrange polynomial, Closed symbols = linear baseline.

asphaltene concentration increases, so too does the degree of curvature of the asphaltene spectrum. As the curvature increases, the inherent error of a linear approximation will also increase, as is the case in Figure 4-28.

In the case of the α_2 peak (572.2 nm, Figure 4-28B), the cubic Polynomial correction does show signs of over-prediction for one series of solutions with the 1 mm cuvette. However, it should be noted that the concentration of VOOEP for that series of solutions was 12.0 μmol/L, resulting in corrected absorbances ranging from 0.044-0.047. This is towards the low end of the usable range of the calibration for VOOEP. The accuracy of the instrument is ±0.005 absorbance units, which corresponds to a concentration accuracy of ±1.3 μmol/L (10.8%) for the 1 mm cuvette. All of the data points for the cubic Lagrange polynomial therefore fall within the accuracy limits of the instrument and are not a concern. Quantitation of the concentration of metalloporphyrins in the presence of asphaltenes, therefore, used the cubic Lagrange polynomial correction scheme with the wavelengths listed in Table 4-9.

4.5.2 DIFFUSION OF MODEL PORPHYRINS

The diffusive behaviour of two model vanadyl porphyrins (VOOEP and VOTPP) in toluene was tested at 25.0±0.2°C using an Anopore® 20 nm membrane, and the results are shown in Figure 4-29 in the form of equation {4.9}. In each case, the initial concentration of vanadyl porphyrin was ~ 30 μmol/L. Using the results for H$_2$TPP (D = 7.18±0.05x10^{-6} cm^2/s[227]) as a calibration for the membrane, the diffusion coefficients for VOTPP and VOOEP are 6.7±0.9 and 6.9±0.7 x 10^{-6} cm^2/s, respectively. The value obtained for VOTPP compares favorably with the value 6.4±0.1 x 10^{-6} cm^2/s reported by Hejtmánek and Schneider[228].

The diffusive behaviour of these same two model vanadyl porphyrins was then tested at the same conditions using a much tighter Ultracel YM10 (3.0 nm) membrane, and the results are shown in Figure 4-30 in the form of equation {4.9}. Using the results for H$_2$TPP (D = 7.18±0.05x10^{-6} cm^2/s[227]) as a calibration for the membrane, the diffusion coefficients for VOTPP and VOOEP are 6.7±0.9 and 7.1±0.7 x 10^{-6} cm^2/s, respectively. The value obtained for VOTPP once again compares favorably with the value 6.4±0.1 x 10^{-6} cm^2/s reported by Hejtmánek and Schneider[228], and both values compare very well with the values obtained with the Anopore® membrane. Therefore, even though a membrane with pores this small should exhibit significant diffusive
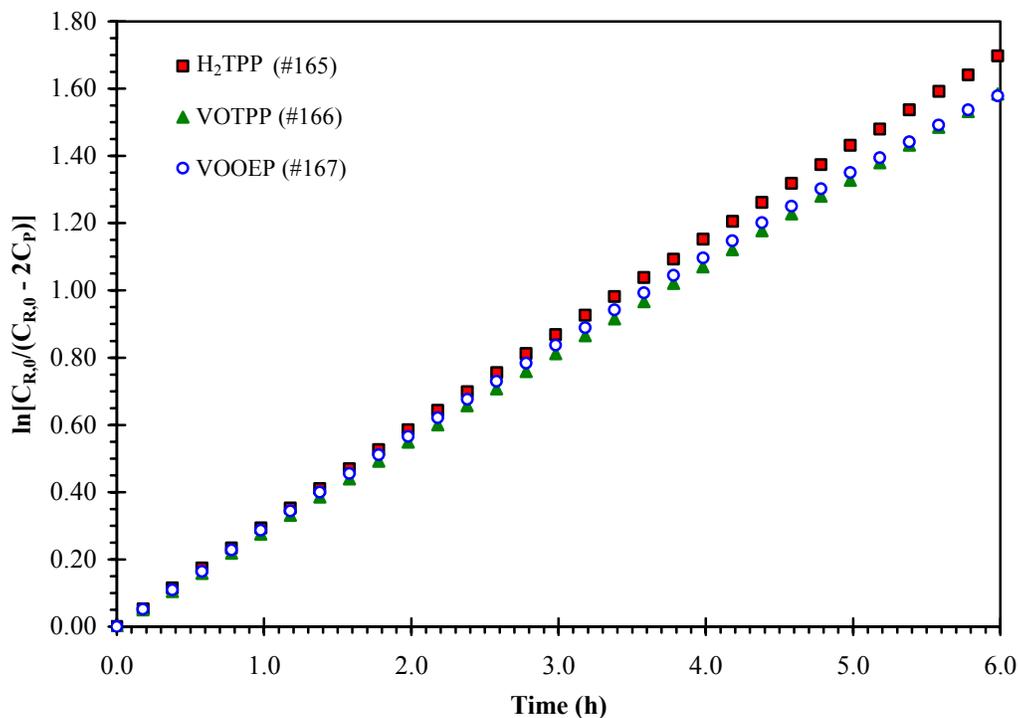
Figure 4-29: Diffusion of model porphyrins in toluene with an Anopore® 20 nm membrane: T = 25.0±0.2°C, stirrer = 600 rpm
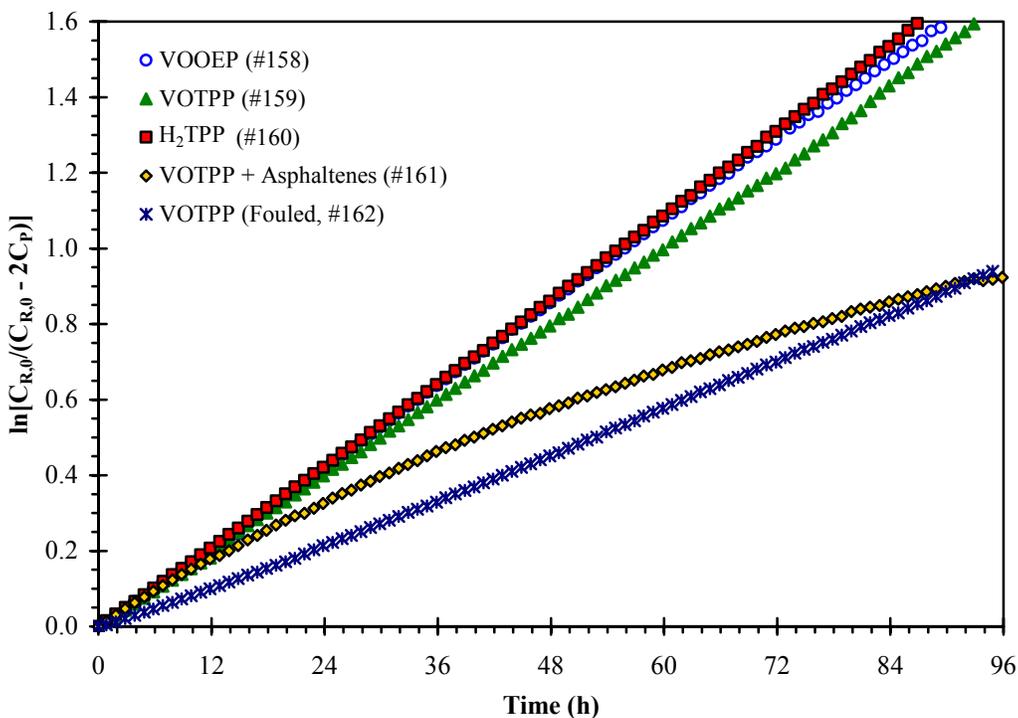
Figure 4-30: Diffusion of model porphyrins in toluene with an Ultracel YM10 (3.0 nm) membrane: T = 25.0±0.2°C, stirrer = 600 rpm

hindrance (see equation {4.19}), calibrating it with a molecule of comparable size (H_2TPP in this case) helps account for these effects. The mean values of the two determinations for VOOEP and VOTPP give diffusion coefficients of 7.0±0.4 and 6.7±0.4 x 10^{-6} cm^2/s, respectively. An additional test was done using VOTPP (29.6 µmol/L) mixed with AA (1.01 g/L) with the Ultracel YM10 membrane, and the results are shown in Figure 4-30. The initial solution was made by weighing out the two solids independently and transferring to a volumetric flask. The flask was filled to the base of the neck with toluene (not quite to the mark) and sonicated for 1 hour prior to topping off to the mark to dissolve the solids completely and ensure good contact and mixing between the two solutes. The total time that the solutes were in contact with each other was ~2 hours to ensure that any molecular interactions that may occur between them had time to develop.

It is immediately apparent that the transport of VOTPP was significantly affected by the presence of the asphaltenes. As mentioned in section 4.4.1, this membrane is susceptible to fouling by the asphaltenes and therefore it is likely that the significant decline in VOTPP flux is a result of fouling. The first 12 hours of this run show a VOTPP flux that is comparable to the pure VOTPP with a steady decline thereafter. If the first 12 hours are regressed, the resulting diffusion coefficient for VOTPP is 6.2±1.8 x 10^{-6} cm^2/s which is very close to the previously measured value and the value reported by Hejtmánek and Schneider[228]. This result indicated that fouling was responsible for the decline in the effective diffusion coefficient at longer times. Immediately following this test, another run was done using VOTPP without rinsing the membrane and the results are included in Figure 4-30 (noted as VOTPP (fouled) in the legend). These results show that indeed the membrane was fouled or plugged by asphaltenes. This would result in a decrease in the cell constant β and would cause the non-linearity of the operating plot noted above. These results also indicate that any analysis of the diffusion rates of petroporphyrins will need to be confined to the first 12 hours of data to avoid incorporating fouling effects in the results.

The fact that the first 12 hours of data are the same as for the pure VOTPP also indicates that there are little or no molecular interactions taking place between the model porphyrin and the asphaltenes. This simple model vanadyl porphyrin was not aggregating or adsorbing onto the asphaltene aggregates as evidenced by its relatively constant mobility at the start of the run. It is possible that over longer periods, molecular

interactions are taking place and contributing to the decline in VOTPP flux. However, it is not possible to differentiate between this type of effect and the fouling noted above and therefore it is not possible to draw any concrete conclusions at this stage.

4.5.3 DIFFUSION OF NATIVE PETROPORPHYRINS

Now that a method has been developed for quantifying the concentration of metalloporphyrins in the presence of asphaltenes, the diffusion cell described in section 4.3.1 can be used to study the diffusion of petroporphyrins in the presence of asphaltenes. The concentration of petroporphyrins in the permeate was quantified using the aforementioned method for an experiment with AA using an Ultracel YM30 membrane (Expt #175, 1 g/L initial AA concentration, $T = 25 \pm 0.2°C$, stirrer = 600 rpm) and the results are shown in Figure 4-31. All calculations of concentration of petroporphyrins were done making the implicit assumption that they have the same molecular weight and molar absorptivity (ε) as VOOEP. In order to analyze the data in Figure 4-31 using the diffusion cell operating equation (equation {4.9}), it is necessary to estimate the initial concentration of metalloporphyrins on the retentate side of the cell ($C_{R,0}$).
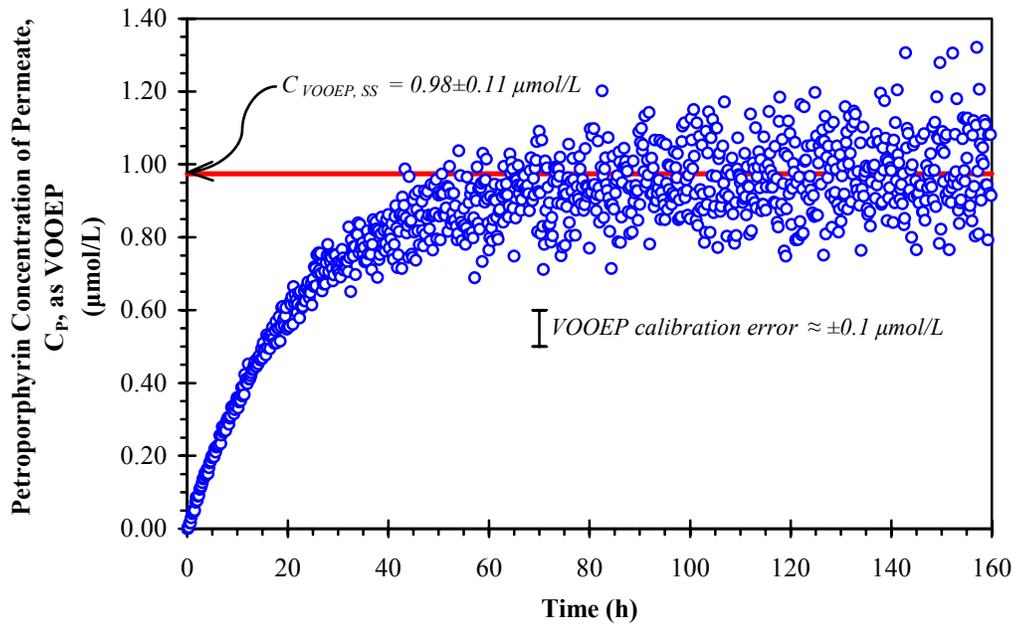
Figure 4-31: Petroporphyrin concentration profile in the permeate for diffusion of AA in toluene (Expt #175): Ultracel YM30 membrane (4.5 nm), $T = 25 \pm 0.2°C$, initial concentration = 1 g/L, stirrer speed = 600 rpm.

The first and most obvious method is to assume that all of the vanadium initially present in the asphaltenes would constitute the initial vanadyl porphyrin concentration. For the experiment above, the concentration of vanadium in the AA asphaltenes is 850 ppmw. This corresponds to an initial VOOEP concentration of $16.8\pm0.2\mu mol/L$ in the retentate.

The second method for estimating $C_{R,0}$ is to use the peak at 407 nm evident in the spectra of the whole asphaltenes in toluene to estimate the concentration of petroporphyrins in free solution. This was done using the extensive data set in Appendix C for whole AA in toluene, and the data and analysis are summarized in Figure 4-32. The data only extend up to an AA concentration of 750 mg/L since beyond this point the detector becomes saturated. Extrapolating this model to 1 g/L gives an initial petroporphyrin concentration of 2.6 ± 0.1 μmol/L for the above experiment. Although it is always dangerous to extrapolate an empirical correlation beyond its experimental limits, the degree of extrapolation in this case is small ($750 \rightarrow 1000$ mg/L) and the degree of linearity is high and as such it is deemed appropriate.

The third and final method for estimating $C_{R,0}$ recognizes that the concentration of porphyrins in the permeate plateaus at long times, as is expected for this type of experiment at steady state. According to the analysis for this experimental setup (section

slope = 0.002566 (μmol/L VOOEP)/(mg/L AA)
R^2 = 0.994
s.e. of slope = 0.000042
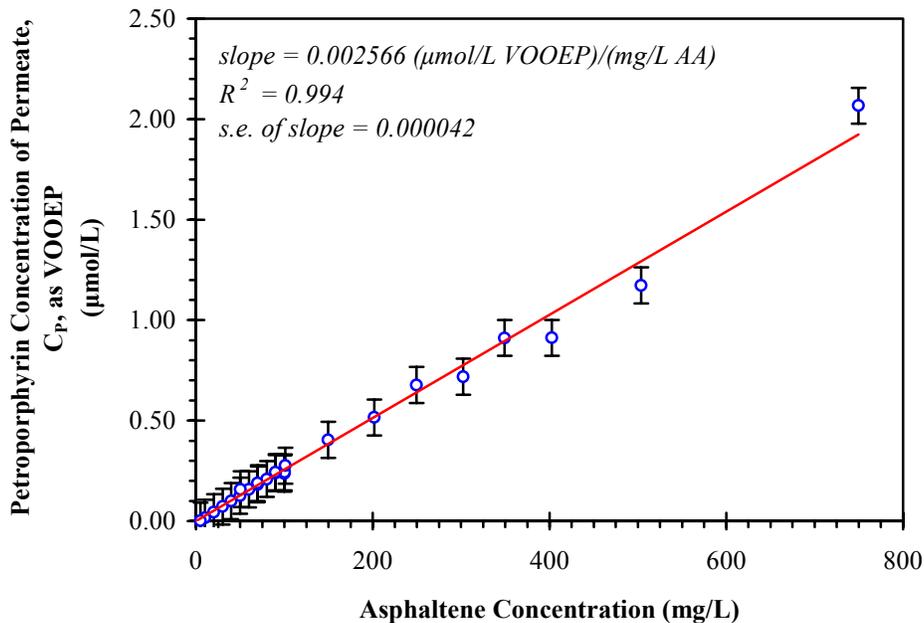
Figure 4-32: Estimate of the petroporphyrin concentration in free solution for AA in toluene

137

4.2.2), the concentration of solute in the permeate at steady state would be half of the initial concentration loaded to the cell (assuming constant volume). Therefore, it is possible to use the value of the concentration plateau to estimate $C_{R,0}$. Applying this concept to the data in Figure 4-31 yields a steady state permeate concentration of 0.98±0.11 μmol/L and a corresponding initial concentration of $C_{R,0} = 1.9±0.2$ μmol/L. This value is quite close to the value obtained in method 2 above and should therefore yield very similar results for the diffusion coefficient of the petroporphyrins.

The analysis of the concentration profile in Figure 4-31 using the three different values for $C_{R,0}$ are shown in Figure 4-33, along with the resulting diffusion coefficients for the petroporphyrins obtained by regressing the first 24 hours of data. When the total initial vanadium content is used, the resulting operating curve is non-linear and results in a diffusion coefficient that is an order of magnitude lower than those obtained by the other 2 methods. The steady state amount of vanadyl porphyrin in the permeate corresponds to 5.8% of the total vanadium (or 11.6% of the total vanadium is in free solution), and therefore using the total vanadium content as an estimate of the initial concentration significantly overestimates the amount of vanadyl porphyrins available for

Method 1
Slope = 0.00367 ($R^2 = 0.959$)
$D_{VOOEP} = Slope/\beta = 0.40±0.06 \times 10^{-6}$ cm^2/s
Method 2
Slope = 0.0306 ($R^2 = 0.984$)
$D_{VOOEP} = Slope/\beta = 3.4±0.45 \times 10^{-6}$ cm^2/s
Method 3
Slope = 0.0460 ($R^2 = 0.983$)
$D_{VOOEP} = Slope/\beta = 5.1±0.7 \times 10^{-6}$ cm^2/s

y-axis: **ln [$C_{R,0}/(C_{R,0} - 2C_P)$]**

x-axis: **Time, t (h)**
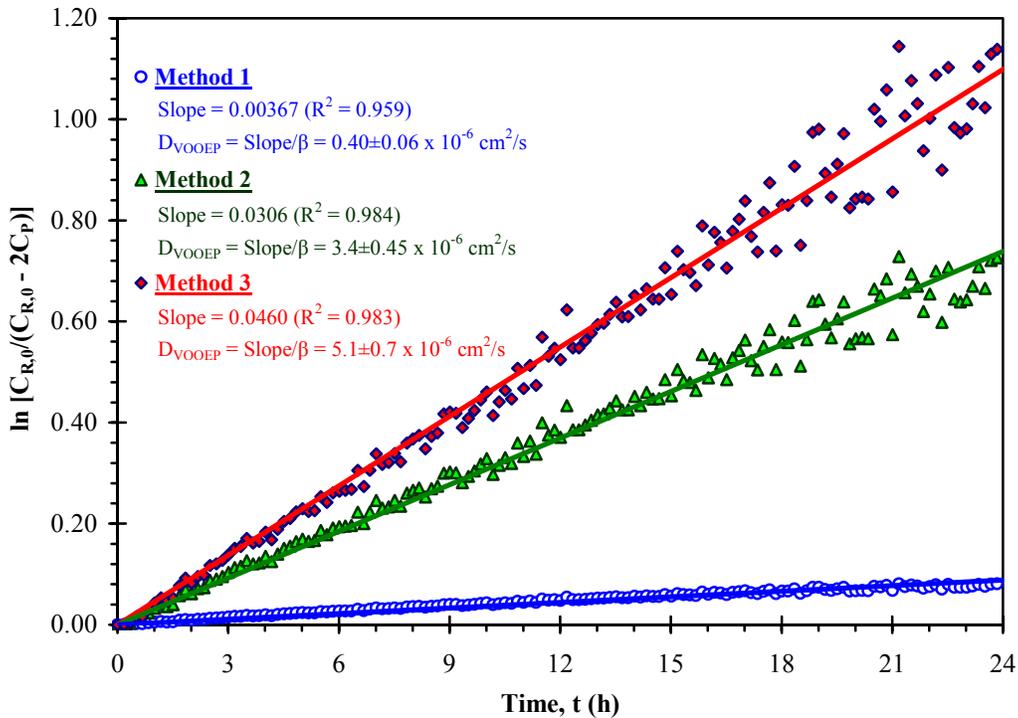
Figure 4-33: Operating equation plots for Expt #175 using the three different methods for quantifying $C_{R,0}$

diffusion. The fact that the vanadyl porphyrin concentration reaches such a low steady state value indicates that a relatively large portion of the total vanadium (~88.4%) is unaccounted for. This could be as a result of petroporphyrins being tightly bound by the asphaltenes and therefore they are not able to diffuse. Alternatively, it is possible that the Soret band for some of the petroporphyrins is not located at 407 nm and as such they are not "visible" at this wavelength. As discussed in Chapter 2, possible causes of such a shift include binding or agglomeration with asphaltenes or annulation of the porphyrin backbone. The net effect of these phenomena would be a systematic underestimation of the concentration of the petroporphyrins in solution, both for the retentate (method two) and the permeate.

When using the other two methods for quantifying $C_{R,0}$, the resulting diffusion coefficients (3.4 ± 0.45 and 5.1 ± 0.7 x 10^{-6} cm^2/s, respectively) are both in the right order of magnitude compared to the previously obtained diffusion coefficients for VOOEP and VOTPP ($6.7 – 7.1$ x 10^{-6} cm^2/s). Considering the number of assumptions and simplifications that went into determining these values, to be this close to the value for the pure porphyrin is very encouraging. In fact, it must be noted that the likelihood of the petroporphyrins all having the same form as VOOEP is very low. The petroporphyrins that are contributing to the observed Soret peak are likely a mixture of several forms such as vanadyl etioporphyrin (VOEtio) and vanadyl DPEP (see Chapter 2) and this could affect both their mobility and their molar absorptivity. Based on the data in Figure 4-2, as well as the experimentally determined diffusion coefficients for H$_2$TPP (7.18 ± 0.05x10^{-6} cm^2/s[227]), VOTPP (6.7 ± 0.4 x 10^{-6} cm^2/s), and VOOEP (7.0 ± 0.4 x 10^{-6} cm^2/s), the physical shape of the porphyrin doesn't seem to have a large effect on the diffusivity and therefore the different physical forms of the native petroporphyrins should not have a large impact on the value of the mean diffusion coefficient. The extinction coefficient being used here to quantify the petroporphyrin concentration using the Soret peak is 3.90 x 10^5 L/mol·cm. This compares well with the values given by Foster *et al.*[38] for VODMEP (3.90 x 10^5 L/mol·cm) and VOEtio (4.00 x 10^5 L/mol·cm) and therefore it is believed that the estimated petroporphyrin concentration is a reasonable approximation.

4.5.4 EFFECT OF MEMBRANE PORE SIZE

The effect of pore size on the diffusive behaviour of vanadyl petroporphyrins can be analyzed using the same data as was used in section 4.4 for asphaltenes. In this case, the analysis focuses on the porphyrin peak at 407 nm. 4 different membranes were

tested: Ultracel YM10 (10 kDa, ~3 nm pores), Ultracel YM30 (30 kDa, ~5 nm pores), Ultracel YM100 (100 kDa, ~9 nm pores), and Anopore® 20 nm membranes. In each case, the starting solution is a 1 g/L solution of AA in toluene and the experiments were all done at 25±0.2°C. The vanadyl petroporphyrin concentration profiles (as VOOEP) for the above membranes are shown in Figure 4-34. This concentration data is then used to calculate the effective diffusion coefficient of the petroporphyrins in toluene using the methods discussed in the previous section, and the results are summarized in Table 4-10. The data for the estimated initial retentate concentration of vanadyl petroporphyrins are also included in Table 4-10 for comparison.

With the exception of the Anopore® 20 nm membrane, all of the permeate profiles are in the same comparable range. The profiles for the Ultracel YM100 and Anopore® membranes are cut short because eventually the detector becomes saturated (due to high asphaltene concentration) and it is no longer possible to quantify the concentration of vanadyl petroporphyrins. Both of the experiments using the YM30 membranes seemed to eventually reach a steady state concentration, while the YM10 membrane was not run long enough to reach steady state. Because of this, only the experiments with the YM30 membranes could be analyzed using the third method of estimating $C_{R,0}$. In all cases, using the total vanadium content as an estimate of the initial concentration significantly overestimates the amount of vanadyl porphyrins available for diffusion and results in diffusion coefficients that are an order of magnitude lower. This result indicated that a relatively large portion of the total vanadium (~88.4%) is unaccounted for (see previous section).

Table 4-10: Summary of estimated initial retentate porphyrin concentration and effective diffusion coefficients of vanadyl petroporphyrins as a function of membrane pore size.

Method / Membrane	$C_{R,0} = V$ total		$C_{R,0} =$ from Figure 4-32		$C_{R,0} = 2*C_{P,SS}$	
	$C_{R,0}$ (μmol/L)	$D_{e, Porph}$ (x 10^{-6} cm^2/s)	$C_{R,0}$ (μmol/L)	$D_{e, Porph}$ (x 10^{-6} cm^2/s)	$C_{R,0}$ (μmol/L)	$D_{e, Porph}$ (x 10^{-6} cm^2/s)
YM10 (#156)	17.0±0.2	0.65±0.02	2.56±0.04	4.4±0.1		
YM30 (#175)	17.1±0.3	0.46±0.06	2.57±0.04	3.4±0.4	1.9±0.2	5.1±0.7
YM30 (#185)	17.1±0.2	0.58±0.02	2.57±0.04	4.0±0.1	1.34±0.05	10.3±0.1
YM100 (#179)	17.0±0.3	0.74±0.02	2.56±0.04	5.2±0.2		
YM100 (#182)	17.0±0.3	0.68±0.02	2.56±0.04	5.4±0.2		
Anopore 20 nm (#168)	17.0±0.3	0.84±0.04	2.56±0.04	7.3±0.5		
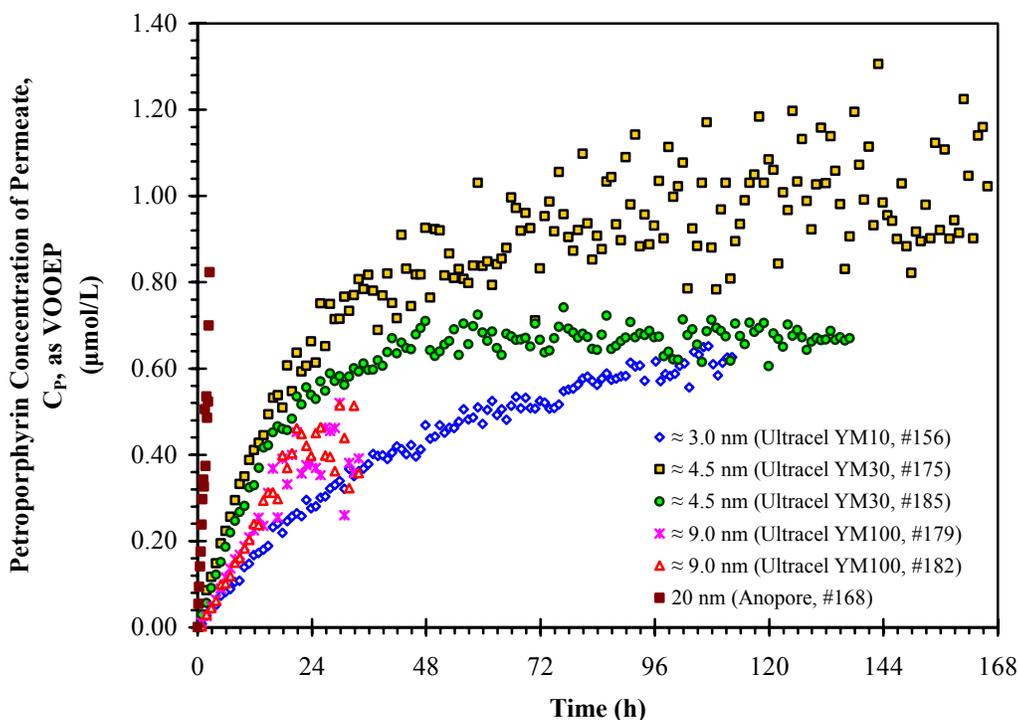
Figure 4-34: Petroporphyrin concentration profile in the permeate for diffusion of AA in toluene as a function of membrane pore size: T = 25.0±0.2°C, stirrer speed = 600 rpm, initial AA concentration = 1 g/L.

If the values predicted by the second method ($C_{R,0}$ from Figure 4-32) are examined further, it appears that the pore size of the membrane has a small effect on the diffusion coefficient values, with the exception of the value obtained with the Anopore® 20 nm membrane. When compared with the previously obtained diffusion coefficients for VOOEP and VOTPP (6.7 – 7.1 x 10^{-6} cm^2/s), the value obtained with the Anopore® membrane is very close to these pure values, while the others are all lower. Based on the results obtained with the pure porphyrins through the YM10 membrane, it is not likely that pore hindrance is the cause of these lower values since this is accounted for by the calibration using H_2TPP. Also, the values in Table 4-10 were obtained using the data up to 12 or 24 hours and so the effects of fouling should also not be a factor.

The data from method two are examined further by plotting the diffusion coefficient as a function of the pore size in Figure 4-35. This curve is in stark contrast to the curves obtained for asphaltenes. Rather than a step change between the YM30 and YM100 membranes, we see a continuous rise in the mobility of the porphyrins as a function of pore size. This same behaviour was not seen with the pure porphyrins where
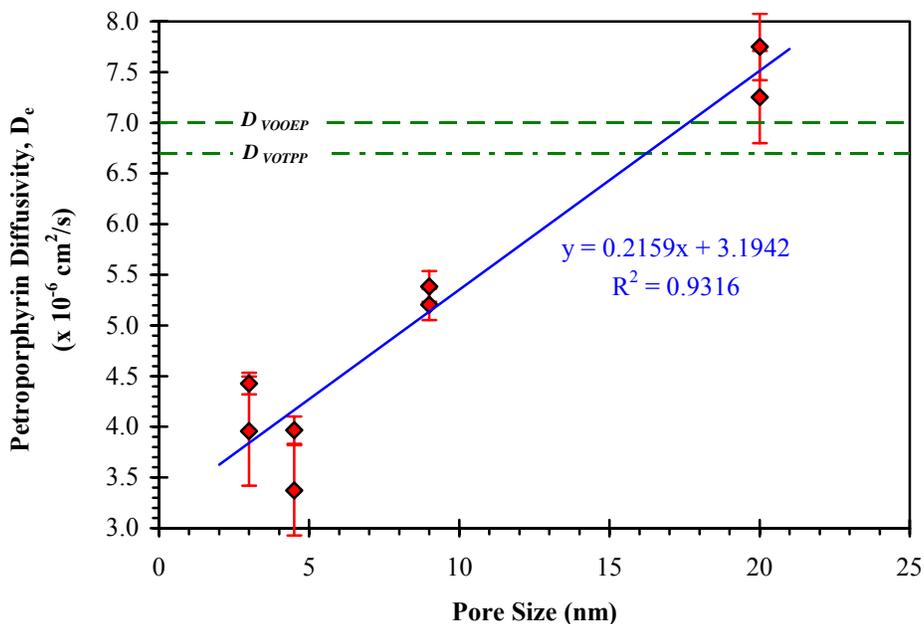
Figure 4-35: Effect of Pore size on the diffusion coefficient of vanadyl petroporphyrins. (NOTE: The data from section 0 have been included)

the diffusion coefficient was the same for both the YM10 and the Anopore® membranes (mean values are shown in Figure 4-35 for VOOEP and VOTPP). Therefore, the presence of asphaltenes did affect the mobility of the petroporphyrins.

This behaviour can be explained using the step-wise association model discussed in section 0. If the vanadyl petroporphyrins are participating as a propagator or terminator molecule in the step-wise association, then their effective hydrodynamic radius would increase as a result of being attached to another molecule(s). This would lead to increased hindrance from the pores of the membranes and hence the behaviour observed in Figure 4-35. As well, if the petroporphyrins are participating in the step-wise association, then there would be a significant portion of the total petroporphyrins that would be tethered to aggregates with sizes significantly larger than the pores and hence are retained by the membrane entirely, which was observed in this work.

A second possible explanation for this behaviour would be that the vanadyl petroporphyrins have a significantly different chemical structure than the model porphyrins, and in particular than the membrane calibration standard H_2TPP. This difference in structure would result in added pore resistance and would lead to a decrease in the effective diffusivity, D_e. Equation {4.20} can be used with the diffusivity of

VOOEP (7.0×10^{-6} cm^2/s) as an approximation to D_∞ to estimate the size of these petroporphyrins. The estimated Stokes radii calculated using the effective diffusivities from method 2 are shown below in Table 4-11. The values predicted using this correction all yielded comparable Stokes radii (mean = 1.14 nm), indicating that indeed the vanadyl petroporphyrins are larger than the model porphyrins studied in section 0. It is important to note that "larger" refers to the Stokes (hydrodynamic) radius and is not a reference to the physical structure of the petroporphyrins. There is no way to reconcile the Stokes radius to the MW or structure of the petroporphyrins. However, in general, the hydrodynamic radius will scale with MW and therefore it is likely that the petroporphyrins are of higher MW than the model porphyrins. This result would imply additional substitution on the periphery of the porphyrin backbone and hence a larger molecule than the model porphyrins.

Table 4-11: Summary of estimated vanadyl petroporphyrin Stokes radii using equation {4.20}, as a function of membrane pore size.

Membrane	r_S (nm)
YM10 (#156)	0.90
YM30 (#175)	1.4
YM30 (#185)	1.2
YM100 (#179)	1.2
YM100 (#182)	1.2

Mean =   1.18

4.5.5 EFFECT OF TEMPERATURE

Diffusion runs were performed at 70.0±0.2°C to assess the effect of temperature on the behaviour of AA vanadyl petroporphyrins. Three different membranes were run at this elevated temperature: an Ultracel YM30 (30 kDa, 5 nm pores), an Ultracel YM100 (100 kDa, 9 nm pores), and an Anopore® 20 nm membrane. In each case, the starting solution was a 1 g/L AA solution. A full permeate spectrum was collected every 10 minutes and the stirrer was operated at 600 rpm. The vanadyl petroporphyrin concentration profiles (as VOOEP) for the above experiments are shown in Figure 4-36. The effective diffusion coefficients for these runs are summarized in Table 4-12.

Table 4-12: Summary of estimated initial retentate porphyrin concentration and effective diffusion coefficients of vanadyl petroporphyrins at 70°C.

Method / Membrane	$C_{R,0} = V$ total		$C_{R,0} =$ *from Figure 4-32*		$C_{R,0} = 2*C_{P,SS}$	
	$C_{R,0}$ (μmol/L)	$D_{e, Porph}$ (x 10^{-6} cm²/s)	$C_{R,0}$ (μmol/L)	$D_{e, Porph}$ (x 10^{-6} cm²/s)	$C_{R,0}$ (μmol/L)	$D_{e, Porph}$ (x 10^{-6} cm²/s)
YM30 (#176)	16.2±0.3	0.98±0.13	2.44±0.04	9.1±1.2	1.8±0.2	15±2
YM100 (#192)	16.6±0.3	1.75±0.06	2.53±0.04	14.4±0.5		
Anopore 20 nm (#172)	16.8±0.3	2.0±0.1	2.58±0.04	17±1		
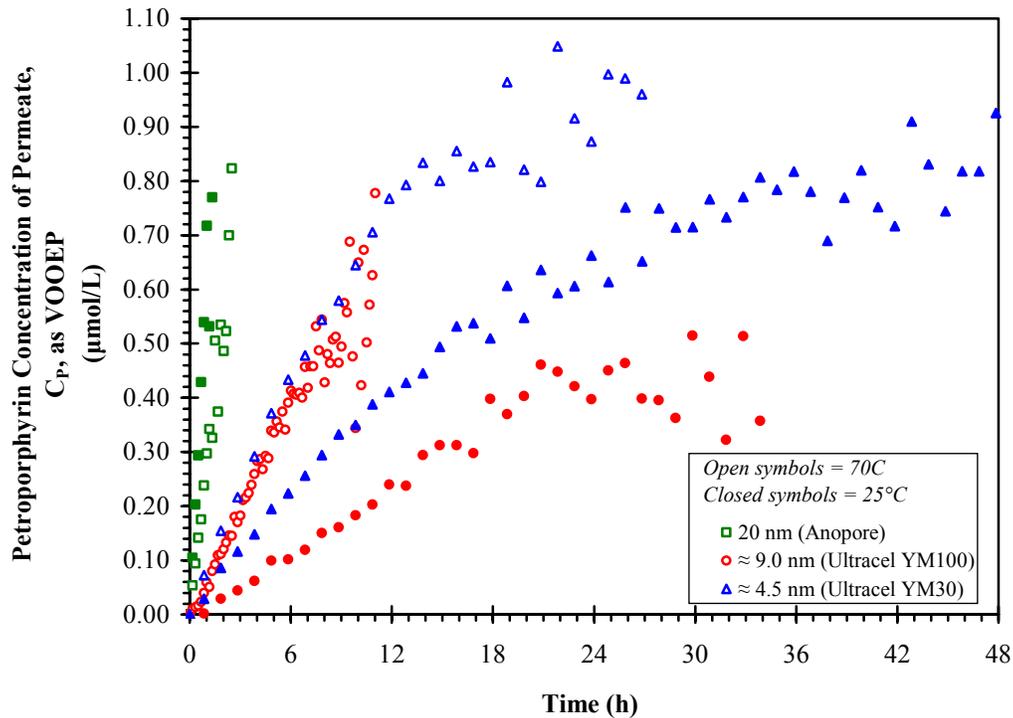
Figure 4-36: Petroporphyrin concentration profile in the permeate for diffusion of AA in toluene as a function of membrane pore size and temperature: stirrer speed = 600 rpm, initial AA concentration = 1 g/L.

From equation {4.21} and the viscosity data in section 4.4.3, increasing the temperature from 25°C to 70°C should result in an increase in the diffusion coefficient by a factor of 1.83. In the case of porphyrins, Saiki *et al.*[227] showed that the diffusivity varies with the viscosity to the power -0.972 rather than -1 as stipulated by the Stokes-Einstein equation (see line in Figure 4-2). Using this exponent yields an increase in diffusivity by a factor of 1.81 for the same conditions. In all three cases, the observed increase in effective diffusivity ranged from 1.7 to 2.4. This seems to fit reasonably well

with the Stokes-Einstein analysis (factor = 1.81 or 1.83) indicating that temperature had little effect on the size (and hence mobility) of the asphaltene aggregates with which the petroporphyrins are associated.

4.5.6 EFFECT OF CONCENTRATION

Two runs were performed at a concentration of 0.1 g/L to assess the effect of concentration on the behaviour of AA derived vanadyl petroporphyrins. Two different membranes were tested at this concentration: an Ultracel YM10 (10 kDa, ~3 nm pores) and an Anopore® 20 nm membrane. In each case, the temperature was 25.0±0.2°C. A full permeate spectrum was collected every 10 minutes and the stirrer was operated at 600 rpm. The vanadyl petroporphyrin concentration profiles (as VOOEP) for these experiments are shown in Figure 4-37. The resulting effective diffusion coefficients for these runs are summarized in Table 4-13. Comparing the data in Table 4-13 to the data at 1 g/L in Table 4-10 indicates that concentration has no effect on the mobility of the vanadyl petroporphyrins in toluene.
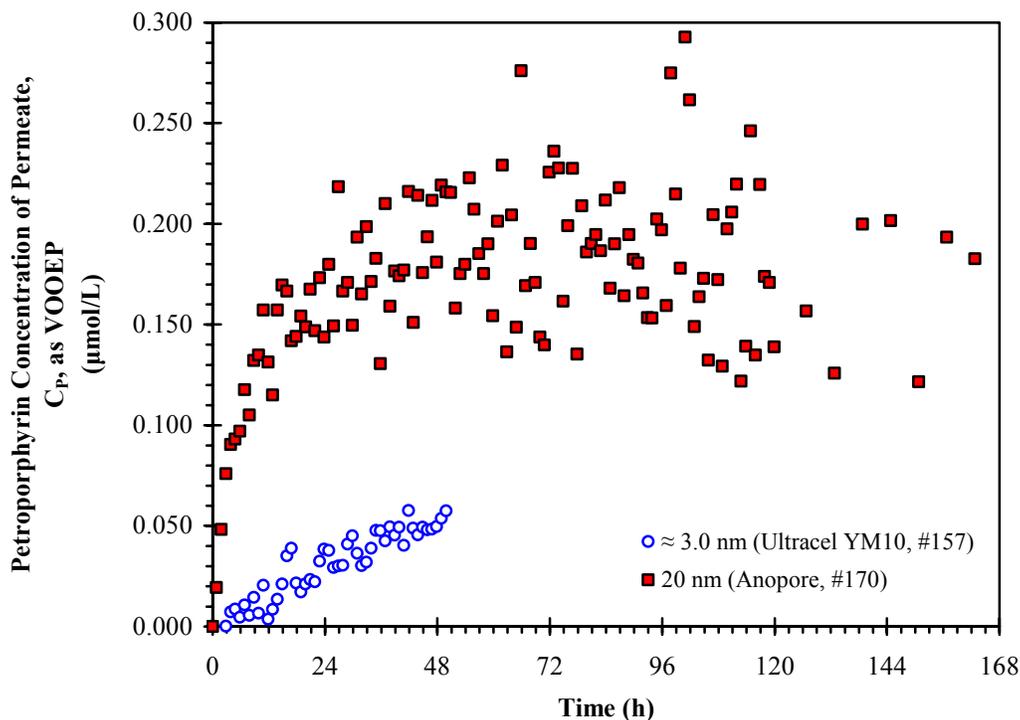
Figure 4-37: Petroporphyrin concentration profile in the permeate for diffusion of AA in toluene for an initial AA concentration = 0.1 g/L : T = 25.0±0.2°C, stirrer speed = 600 rpm.

145

Table 4-13: Summary of effective diffusion coefficients of
vanadyl petroporphyrins with 0.1 g/L AA initial concentration

Method / Membrane	$C_{R,0} = V$ total		$C_{R,0} = $ from Figure 4-32	
	$C_{R,0}$ (µmol/L)	$D_{e, Porph}$ (x 10^{-6} cm^2/s)	$C_{R,0}$ (µmol/L)	$D_{e, Porph}$ (x 10^{-6} cm^2/s)
YM10 (#157)	1.73±0.03	0.62±0.02	0.261±0.004	4.0±0.5
Anopore 20 nm (#170)	1.73±0.03	0.80±0.03	0.260±0.004	7.7±0.3

4.5.7 EFFECT OF ASPHALTENE ORIGIN

Three runs were performed using asphaltenes from different origins: Safaniya
asphaltenes (SA), Venezuelan asphaltenes (VA), and asphaltenes from an Athabasca
bitumen that has been partially demetallated (APDA, see section 4.3.5.3). These tests
were all carried out using an Ultracel YM30 membrane with an initial asphaltene
concentration of 1 g/L and a temperature of 25.0±0.2°C. A full permeate spectrum was
collected every 10 minutes and the stirrer was operated at 600 rpm. The vanadyl
petroporphyrin concentration profiles (as VOOEP) for these experiments are shown in
Figure 4-38 (along with the profiles for the AA samples with the same membrane).

The partially demetallated Athabasca asphaltenes showed no vanadyl
petroporphyrin peaks either before or after diffusion (as would be expected) and therefore
were not analyzed any further. This indicates that the partial demetallation procedure has
removed the labile metalloporphyrins and the remaining vanadium (180±2 ppmw) is
tightly bound and not "visible" via UV/Visible spectroscopy. The concentration data is
then used to calculate the effective diffusion coefficient of the petroporphyrins in toluene
using the methods discussed in the previous section, and the results are summarized in
Table 4-14. The data for the estimated initial retentate concentration of vanadyl
petroporphyrins are also included in Table 4-14 for comparison. Safaniya
petroporphyrins could only be analyzed using the first method ($C_{R,0}$ = total vanadium)
since there is no petroporphyrin peak at 407 nm for the whole sample prior to diffusion.
The Venezuelan petroporphyrins were analyzed by all three methods. For method two, a
separate calibration for the free VOOEP concentration was done and the results are
shown in Figure 4-39.

Based on the results in Table 4-14, the Safaniya petroporphyrins seem to be the
most mobile based on the diffusion coefficient obtained using method one.

Unfortunately, the diffusion coefficient for Safaniya petroporphyrins could not be estimated using method two, which seems to be the best method for assessing the mobility of the free petroporphyrins. Venezuelan petroporphyrins appear to be more mobile than the Athabasca petroporphyrins with all three methods, although it is not clear at this point why this is the case.

Table 4-14: Summary of estimated initial retentate porphyrin concentration and effective diffusion coefficients @ 25°C of vanadyl petroporphyrins as a function of the asphaltene origin (membrane = YM30).

Method / Source	$C_{R,0}$ = V total		$C_{R,0}$ = from Figure 4-32		$C_{R,0}$ = $2*C_{P,SS}$	
	$C_{R,0}$ (μmol/L)	$D_{e, Porph}$ (x 10^{-6} cm²/s)	$C_{R,0}$ (μmol/L)	$D_{e, Porph}$ (x 10^{-6} cm²/s)	$C_{R,0}$ (μmol/L)	$D_{e, Porph}$ (x 10^{-6} cm²/s)
Safaniya (#188)	4.3±0.02	1.39±0.05				
Venezuelan (#189)	22.9±0.2	1.03±0.04	4.34±0.07	6.4±0.2	4.0±0.3	7.0±0.2
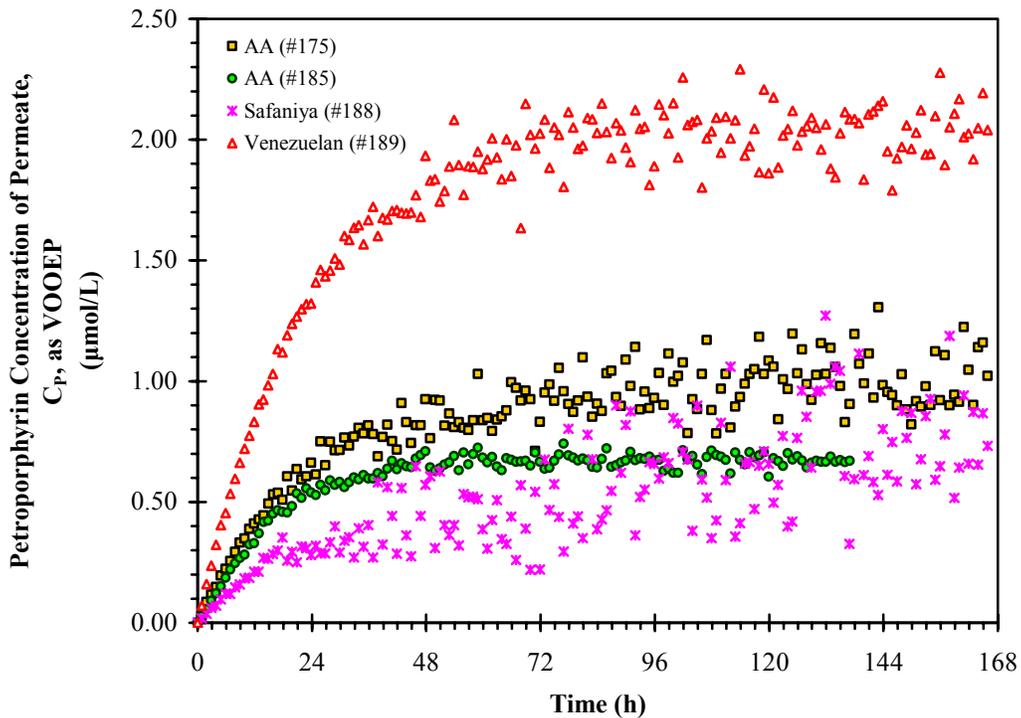
Figure 4-38: Petroporphyrin concentration profile in the permeate for diffusion of asphaltenes in toluene as a function of origin: T = 25.0±0.2°C, stirrer speed = 600 rpm, initial asphaltene concentration = 1 g/L, membrane = YM30.
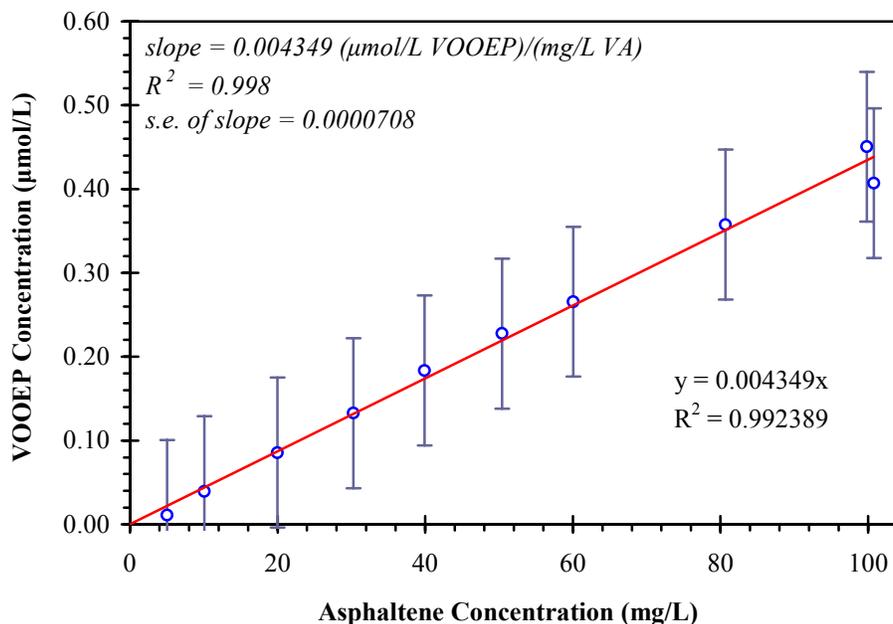
Figure 4-39: Estimate of the petroporphyrin concentration in free solution for Venezuelan asphaltenes in toluene

4.5.8 GENERAL DISCUSSION

The main conclusions that can be drawn from the petroporphyrin analysis are:

1. The petroporphyrins appear to be larger than the model vanadyl porphyrins as indicated by the presence of pore hindrance effects with the tighter membranes.

2. An increase in temperature results in an increase in petroporphyrin mobility that is proportional to the viscosity and temperature according to the Stokes-Einstein equation.

3. Decreasing the asphaltene concentration does not result in an increase in the mobility of the vanadyl petroporphyrins.

4. The mobility of the vanadyl petroporphyrins is affected by the origin of the sample and is therefore not universal.

In general, a large fraction of the total vanadium present does not participate in the diffusion process indicating that they are interacting strongly with the asphaltene aggregates even in a strong solvent such as toluene. Reducing the concentration of the asphaltenes did not increase the amount of petroporphyrins accounted for, which is not surprising in light of the lack of any effect of lower concentration on asphaltenes (see

sections 4.4.4 and 0). Since the asphaltene aggregation process is not disrupted at lower concentrations, it is not anticipated that the amount of petroporphyrins visible and available for diffusion would increase, which was indeed observed.

It is possible that the petroporphyrins are still associated to asphaltenes at these low concentrations in the form of a dimer (1 porphyrin molecule + 1 asphaltene molecule). This would result in a larger effective Stokes radius (as was observed) and could also affect the UV/Visible spectrum of the petroporphyrin. If the association results in a decrease in the molar absorptivity and/or in a shift in the location of the Soret peak, then it is possible that these species are not being properly quantified by the analytical method. In other words, the petroporphyrins may very well be more mobile at low concentration, but this effect is not "visible" to the spectrophotometer. This behaviour would also explain why a large portion of the total vanadium is unaccounted for by UV-Visible spectroscopy (see Chapter 2).

As was the case for the asphaltenes, increasing the temperature did not have a major effect on petroporphyrins. There was an increase in mobility (i.e. effective diffusivity) at 70°C but the magnitude of this increase can be explained using the Stokes-Einstein relationship (equation {4.21}) to correct for temperature and viscosity with no need for a substantial decrease in association of the petroporphyrins to asphaltenes.

Chapter 5

General Discussion: Tying it all Together

The solubility behaviour of the model compounds studied herein match the criteria of an asphaltene: they are "insoluble" in n-heptane and "soluble" in toluene. The solubility in toluene was several orders of magnitude higher than in n-heptane and therefore all of these compounds meet the operational definition of asphaltenes. This is not entirely surprising for PBP since this molecule is being used as a model for asphaltenes and this behaviour would be a minimum for it to be considered as such. In the case of the porphyrins, the fact that they meet the operational definition of an asphaltene would certainly help to explain their inclusion with the asphaltene fraction.

This simple fact (i.e. vanadyl porphyrins = asphaltenes) also has significant implications for the design of selective vanadium separation processes. The fact that the porphyrins are in and of themselves an asphaltene implies that a selective vanadium separation process is in fact an asphaltene separation process. It just so happens that the specific asphaltene molecule being targeted has a vanadyl group as part of its structure. Therefore, the effective design of such a process must take into account the solution behaviour of asphaltenes in general and not just of the vanadyl porphyrins. Based on the extensive discussions regarding the associative behaviour of the asphaltene fraction, therefore, any discussion of vanadium separation will need to contend with the issues of asphaltene association and in particular the inclusion of metalloporphyrins within the aggregated structures.

The proposed mechanisms for inclusion of metalloporphyrins within the aggregate structure are illustrated schematically in Figure 5-1. The first class of bound metalloporphyrins is the so-called "loosely" bound molecules which are retained in the
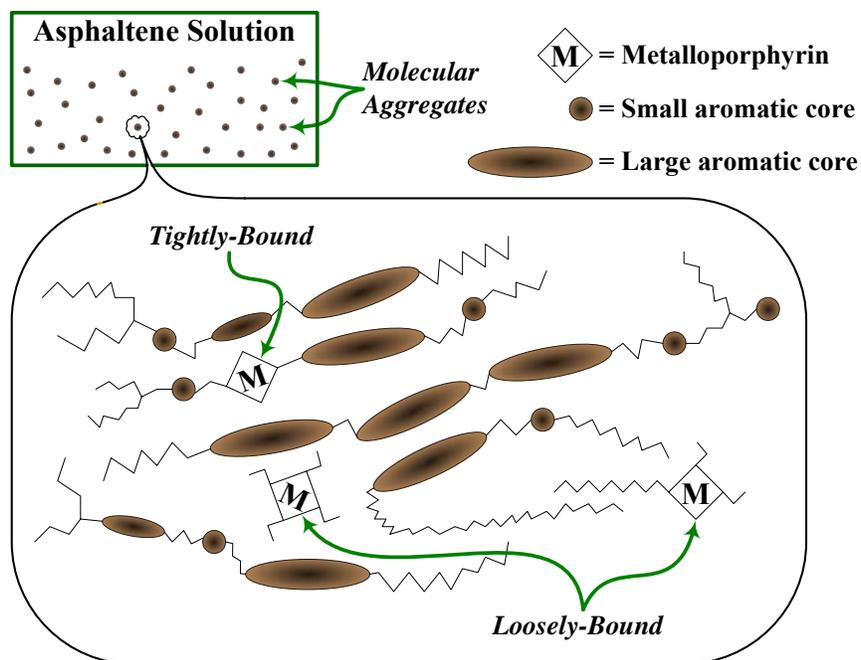
Figure 5-1: Schematic of asphaltene nano-aggregate containing metalloporphyrins

aggregates either by non-covalent bonds or by occlusion as a result of precipitation type mechanisms. These metalloporphyrins would be the smallest, simplest structures and would be the easiest to selectively remove from the asphaltenes since they are not strongly retained within the aggregate structure. These are the metalloporphyrins that have been so extensively studied in the past since they can be removed using simple solvent extraction procedures. However, this class of metalloporphyrins only makes up a small portion of the total vanadium present. The second class of bound metalloporphyrins is the so-called "tightly" bound molecules. They would either be covalently bound to asphaltene moieties, representing larger, more complex metalloporphyrin structures or they would have peripheral substitutions capable of additional non-covalent bonding with the asphaltene molecules (e.g. benzo groups for π-π bonding, carboxylic acid groups for hydrogen bonding etc.). They would participate strongly in the aggregation process and as such would be the hardest to remove selectively.

The persistence of aggregates (or at least dimers) even at relatively low concentrations of 1 g/L in a strong solvent has important implications for any attempt to separate vanadium from crude oil based on interactions with ligands or surfaces. Rather

than interacting with other species in solution as molecular species, a significant fraction of the total asphaltene behaved as a colloid with a size in the range 5-9 nm. These aggregates could exhibit multiple functional groups on their surfaces, possibly without exposing the vanadyl group on their surfaces. Consequently, the molecular interactions would be much less specific than would be obtained from any single species. The stability of the aggregates and the complete lack of their permeation through the small-pore membranes after 7 days indicated that the rate of exchange or transport of the metals between the aggregate phase and the monomers in solution is extremely slow. At temperatures up to 70°C and time scales up to 7 days, the aggregation was largely locked in. Unless the aggregation can be suppressed, separation of a significant portion of the vanadium due to its unique properties cannot be achieved. By extension, the aggregation behavior of the asphaltenes would interfere with the selective separation of any component based on molecular properties, such as acidity, basicity, and molecular size (as in gel permeation chromatography).

The persistence of relatively stable aggregates even at low concentrations also helps to explain the avid and irreversible interaction of asphaltenes with surfaces and chromatographic materials such as silica and alumina. Due to the multiple components and large size of the aggregates, a portion of this material would interact with a surface at multiple sites via multiple functional groups. This multi-point interaction with a surface would give much stronger adsorption than with a single molecule, giving rise to strong interactions.

Although the above discussion paints a rather bleak picture regarding selective removal of vanadium, there is hope. Now that a more direct link has been established between asphaltene and vanadyl porphyrin chemistry, it is clear that the design of a selective removal process will require significant disruption of the asphaltene association behaviour. Unfortunately, temperature and concentration alone are not effective within the context of conventional solvents. Therefore, significant efforts should be directed at locating solvents or solvent mixtures that are capable of significantly disrupting this association. Efforts can now be directed specifically at this issue in the hopes of liberating the metalloporphyrins from their shackles to be plucked away at our leisure.

Chapter 6

Conclusions and Recommendations

6.1 Conclusions

As outlined in the previous section, the primary conclusion from this work is that asphaltene and metalloporphyrin chemistry in solution are intrinsically linked. In order to successfully design a selective vanadium removal process, asphaltene association must be disrupted to liberate the metalloporphyrins and allow removal. Some of the more specific conclusions coming out of this work are:

6.1.1 SOLUBILITY OF VANADYL PORPHYRINS

Based on equilibrium solubility in toluene and n-heptane, simple model porphyrins fit the operational definition of an asphaltene and hence any discussion of native petroporphyrins is intrinsically tied to that of asphaltenes. As well, simple solubility theories incorporating the solubility parameter (Regular Solution theory and Flory Huggins theory) are not capable of properly describing the behaviours of model porphyrins or a model asphaltene molecule in solution. Therefore, it is not anticipated that these simple theories will work any better on a complex mixture such as asphaltenes.

6.1.2 SIZE AND DIFFUSION OF ASPHALTENES

The size of the asphaltene structures in toluene at 1 g/L are between 5 and 9 nm based on the significant jump in effective diffusivities observed between these pore sizes. This size range fits well with scattering measurements from the open literature. These aggregates were very stable, remaining essentially intact even after 7 days in toluene. An increase in temperature to 70°C results in an increase in asphaltene mobility (as described

by the Stokes-Einstein relationship) but does not reduce the size of the asphaltene structures below 5 nm, while a decrease in concentration in toluene to 0.1 g/L results in a significant decrease in the size of the asphaltene structures to < 3 nm. Finally, the exclusion of a large portion of the total asphaltenes by pores < 5 nm eliminates the absorbance of visible light (>600 nm) by asphaltenes, indicating that the absorbance of asphaltene solutions in this range is due to aggregation (e.g. Rayleigh scattering).

6.1.3 SIZE AND DIFFUSION OF NATIVE VANADYL PETROPORPHYRINS

The petroporphyrins present in Athabasca asphaltenes appear to be larger than the model vanadyl porphyrins studied as indicated by the presence of pore hindrance effects with the tighter membranes. An increase in temperature results in an increase in petroporphyrin mobility that is proportional to the viscosity and temperature according to the Stokes-Einstein equation, while decreasing the asphaltene concentration does not result in an increase in the mobility of the vanadyl petroporphyrins. The mobility of the vanadyl petroporphyrins is affected by the origin of the sample and is therefore not universal.

6.2 Recommendations

Although a wealth of information has been derived from the apparatus and membranes used in this work, there are a number of improvements that can and need to be made in order to carry this technique forward and continue to extract useful information.

6.2.1 FUTURE DIFFUSION MEASUREMENTS WITH ASPHALTENES

One particular area that would require improvement is the membranes. Although the polymeric ultrafiltration membranes served their purpose, there is some uncertainty surrounding the exact pore size of these membranes which leads to uncertainty in the conclusions drawn regarding the size of the aggregated asphaltene aggregates. Also, in order to get the small pore sizes required for ultrafiltration, polymeric membranes generally have a corresponding low porosity, which necessitates longer experiments.

For future diffusion measurements of this kind, the use of anodic alumina membranes with well defined pore structures in the desired size range (2-10 nm), synthesized by anodization followed by atomic layer deposition should be investigated.

Membranes synthesized in this manner have well defined pore structures and would reduce some of the uncertainty in drawing conclusions regarding size. As well, an alumina matrix would have near universal solvent compatibility at temperatures well in excess of polymeric membranes. This would allow the technique to be operated at higher temperatures and pressures in the hope of probing these effects on the association behaviour of asphaltenes. Finally, membranes synthesized in this manner generally have higher porosity and are thinner than their polymeric counterparts and would result in a significant reduction in the length of experiments.

Another area that requires improvement is the issue of fouling. When dealing with asphaltenes in solution, it is unlikely that any membrane will be immune to fouling phenomena. Therefore, if more accurate and detailed quantitative information is to be extracted from this technique a means for accounting for this phenomenon is required. To this end, future diffusion measurements with asphaltenes should consider incorporating an internal diffusion standard. In this fashion, fouling could be quantified for each experiment and allow for improved quantitative assessments of the rates of diffusion of the asphaltene species as well as the rates of exchange between the aggregated and free states. Selection of a suitable standard would be difficult since it must not interact strongly with the asphaltenes nor can its primary absorption bands obscure the regions of interest within the metalloporphyrin or asphaltene absorption spectrum. However, if a suitable standard can be identified, the quality of the quantitative measurements would improve dramatically.

6.2.2 SOLVENTS FOR DISRUPTING ASPHALTENE ASSOCIATION

As mentioned above, any process for selective removal of vanadium must first disrupt the associative behaviour of asphaltenes since the metalloporphyrins are intrinsically tied to this phenomenon. Unfortunately, temperature and concentration alone were not sufficient to disrupt the association in toluene. To this end, the next step in this work should investigate multifunctional solvents capable of disrupting the asphaltene association behaviour. The solvents should incorporate polar, hydrogen bonding, and aromatic functionalities to counteract the primary mechanisms for asphaltene association in order to liberate the metalloporphyrins. It is unlikely that a single solvent will be capable of meeting these criteria and as such it is likely that mixtures of solvents will be required. Once a suitable solvent system has been identified

for large scale disruption of the asphaltene association, then, and only then, can a process be successfully designed for selective vanadium removal.

6.2.3 MODEL PORPHYRINS

Another area that warrants further investigation would be the synthesis of more relevant model porphyrin structures to elucidate the specific interactions occurring between the asphaltenes and the metalloporphyrins. VOOEP was used in this study since it closely matches the structure of the Etio porphyrins, one of the more abundant porphyrin structures identified in petroleum systems. As shown in Chapter 4, this model porphyrin displayed no significant interactions with asphaltenes in solution and therefore it is not capturing the behaviour of the majority of the metalloporphyrins which are retained by the asphaltene aggregates.

Therefore, it would appear that to gain additional insight into the specific interactions that are leading to retention of the vanadyl porphyrins within the aggregated structures, the other structures that have been identified (DPEP and Rhodo forms) should be synthesized and tested to determine whether or not the additional functionalities present on these porphyrins can explain the enhanced retention within the asphaltene fractions. The use of these additional model compounds would also help define the spectroscopic behaviour of these series of porphyrins in order to enhance their identification and quantitation within the asphaltene fraction.

6.2.4 RAYLEIGH SCATTERING MEASUREMENTS WITH ASPHALTENES

In the latter stages of this work, it was identified that the larger asphaltene aggregates were showing signs of Rayleigh scattering behaviour. The equipment used in this work is not capable of probing this behaviour in detail, although this phenomenon may hold a great deal of promise for elucidating asphaltene behaviour in solution, particularly at low concentrations. To this end, it is suggested that perhaps this phenomenon (Rayleigh scattering) be explored further by using an integrating sphere to elucidate the size and MW of asphaltenes in the low concentration limit. If successful, this type of analysis would pickup where many other techniques leave off and may provide the answer to the fundamental question: how big is an asphaltene monomer? This would also provide a rapid screening mechanism for evaluating potential solvents as outlined in section 6.2.2.

Bibliography

[1] Branthaver, J.F., Influence Of Metal Complexes In Fossil Fuels On Industrial Operations. *ACS Symp. Ser.* **1987,** 344 (12), 188-204.

[2] Zychlinski, L., J.Z. Byczkowski, and A.P. Kulkarni, Toxic effects of long-term intratracheal administration of vanadium pentoxide in rats. *Arch. Environ. Contam. Toxicol.* **1991,** 20 (3), 295-298.

[3] Cooper, R.G., Vanadium Pentoxide Inhalation. *Indian Journal of Occupational and Environmental Medicine.* **2007,** 11 (3), 97-102.

[4] Occupational Safety & Health Administration , U.S. Occupational Safety and Health Guideline for Vanadium Pentoxide. www.osha.gov (Jan 7, 2010).

[5] Drbal, L.F., P.G. Boston, and K.L. Westra, *Power plant engineering by Black & Veatch*. Springer: New York, NY, **1996**

[6] Siskin, M., S.R. Kelemen, C.P. Eppig, L.D. Brown, and M. Afeworki, Asphaltene Molecular Structure and Chemical Influences on the Morphology of Coke Produced in Delayed Coking. *Energy & Fuels* **2006,** 20 (3), 1227-1234.

[7] Brons, G. and J.M. Yu, Solvent Deasphalting Effects on Whole Cold Lake Bitumen. *Energy & Fuels* **1995,** 9 (4), 641-647.

[8] Reynolds, J.G., Characterization Of Heavy Residua By Application Of A Modified D 2007 Separation And Electron Paramagnetic Resonance. *Liq. Fuels Technol.* **1985,** 3 (1), 73-105.

[9] Gray, M.R., *Upgrading petroleum residues and heavy oils*. Marcel Dekker, Inc.: New York, NY, **1994**

[10] Freeman, D.H., I.D. Swahn, and P. Hambright, Spectrophotometry and solubility properties of nickel and vanadyl porphyrin complexes. *Energy & Fuels* **1990,** 4 (6), 699-704.

[11] Stokes, R.H., The diffusion coefficients of eight uni-univalent electrolytes in aqueous solution at 25 Deg. *J. Am. Chem. Soc.* **1950,** 72, 2243-2247.

[12] Van Geet, A.L. and A.W. Adamson, Diffusion in liquid hydrocarbon mixtures. *J. Phys. Chem.* **1964,** 68 (1), 238-246.

[13] Robinson, R.L., Jr., W.C. Edmister, and F.A.L. Dullien, Calculation of diffusion coefficients from diaphragm cell diffusion data. *J. Phys. Chem.* **1965,** 69 (1), 258-261.

[14] Barwise, A.J.G. and E.V. Whitehead, Characterization Of Vanadium Porphyrins In Petroleum Residues. *Preprints - Div. Petrol. Chem. ACS* **1980,** 25 (2), 268-279.

[15] Pearson, C.D. and J.B. Green, Comparison Of Processing Characteristics Of Mayan And Wilmington Heavy Residues .1. Acid-Base Neutral Fractionation And Characterization. *Fuel* **1989,** 68 (4), 456-464.

[16] Pearson, C.D. and J.B. Green, Comparison Of Processing Characteristics Of Mayan And Wilmington Heavy Residues .2. Characterization Of Vanadium And Nickel-Complexes In Acid-Base Neutral Fractions. *Fuel* **1989,** 68 (4), 465-474.

[17] Altgelt, K.H. and M.M. Boduszynski, *Composition and Analysis of Heavy Petroleum Fractions*. Marcel Dekker, Inc.: New York, NY, Vol. 54, **1994**

[18] Filby, R.H. and D. Strong, Nickel (II) and vanadium (IV) complexes in Alberta oil-sand bitumens. *AIChE Symp. Ser.* **1991,** 87 (282), 1- 9.

[19] Pena, M.E., A. Manjarréz, and A. Campero, Distribution of vanadyl porphyrins in a Mexican offshore heavy crude oil. *Fuel Process. Technol.* **1996,** 46 (3), 171-182.

[20] Yang, X., H. Hamza, and J. Czarnecki, Investigation of subfractions of Athabasca asphaltenes and their role in emulsion stability. *Energy & Fuels* **2004,** 18 (3), 770-777.

[21] Yen, T.F., Chemical Aspects of Metals in Native Petroleum. In *The Role of Trace Metals in Petroleum*, Yen, T. F., Ed. Ann Arbor Science Publichers Inc.: Ann Arbor, **1975**, 1-30.

[22] Czernuszewicz, R.S., E.M. Maes, and J.G. Rankin, Resonance Raman Spectroscopy of Petroporphyrins. In *The Porphyrin Handbook*, Kadish, K. M.; Smith, K. M.; Guilard, R., Eds. Academic Press: San Diego, CA, **2000**, Vol. 7, 293-335.

[23] Qian, K., A.S. Mennito, K.E. Edwards, and D.T. Ferrughelli, Observation of vanadyl porphyrins and sulfur-containing vanadyl porphyrins in a petroleum asphaltene by atmospheric pressure photonionization Fourier transform ion cyclotron resonance mass spectrometry. *Rapid Commun. Mass Spec.* **2008,** 22 (14), 2153-2160.

[24] Smith, K.M., General Features of the Structure and Chemistry of Porphyrin Compounds. In *Porphyrins and Metalloporphyrins*, Smith, K. M., Ed. Elsevier Scientific Publishing Company: New York, **1975**, 1-28.

[25] Senglet, N., C. Williams, D. Faure, T. Des Courieres, and R. Guilard, Microheterogeneity study of heavy crude petroleum by u.v.-visible spectroscopy and small angle X-ray scattering. *Fuel* **1990,** 69 (1), 72-77.

[26] Sugihara, J.M. and R.M. Bean, Direct Determination of Metalloporphyrins in Boscan Crude Oil. *J. Chem. Eng. Data* **1962,** 7 (2), 269-271.

[27] Goulon, J., A. Retournard, P. Friant, C. Goulonginet, C. Berthe, J.F. Muller, J.L. Poncet, R. Guilard, J.C. Escalier, and B. Neff, Structural Characterization By X-Ray Absorption-Spectroscopy (EXAFS/XANES) Of The Vanadium Chemical Environment In Boscan Asphaltenes. *J. Chem. Soc. Dalton* **1984,** (6), 1095-1103.

[28] Goulon, J., C. Esselin, P. Friant, C. Berthe, J.F. Muller, J.L. Pncet, R. Guilard, J.C. Escalier, and B. Neff In *Structural Characterization by X-Ray Absorption Spectroscopy (EXAFS/XANES) of the Vanadium Chemical Environment in Various Asphaltenes*, Characterization of heavy crude oils and petroleum residues: International Symposium on Characterization of Heavy Crude Oils and Petroleum Residues, Lyon, France, June 25 - 27, 1984, Lyon, France, 1984, pp 158-163.

[29] Poncet, J.L., R. Guilard, P. Friant, C. Goulonginet, and J. Goulon, Vanadium (IV) Porphyrins - Synthesis And Classification Of Thiovanadyl And Selenovanadyl Porphyrins - EXAFS And RPE Spectroscopic Studies. *New J. Chem.* **1984,** 8 (10), 583-590.

[30] Berthe, C., J.-F. Muller, D. Cagniant, J. Grimblot, and J.-P. Bonnelle In *Caracterisation des Fractions Lourdes du Pétrole par Spectroscopie IR, UV-Visible, Spectroscopie Photoélectronique ESCA et Spectrométrie LAMMA en Relation avec L'environnement du Vanadium*, Characterization of heavy crude oils and petroleum residues: International Symposium on Characterization of Heavy Crude Oils and Petroleum Residues, Lyon, France, June 25-27, 1984, Lyon, France, 1984, pp 164-168.

[31] Loos, M., I. Ascone, P. Friant, M.F. Ruiz-Lopez, J. Goulon, J.M. Barbe, N. Senglet, R. Guilard, D. Faure, and T. Des Courieres, Vanadyl Porphyrins: Evidence for Self-Association and for Specific Interactions with Hydroprocessing Catalysts Shown from X.A.F.S and E.S.R. Studies. *Catal. Today* **1990,** 7 (4), 497-513.

[32] Zhang, G. and M.M. Boduszynski In *The Binding Structure of Vanadium in Arabian Heavy Petroleum: An X-Ray Absorption Investigation*, International Conference on Petroleum Refining and Petrochemical Processing, Beijing, China, September 11-15, 199, Xianglin, H., Ed. International Academic Publishers, Beijing, China, 1991, pp 821-826.

[33] Miller, J.T., R.B. Fisher, P. Thiyagarajan, R.E. Winans, and J.E. Hunt, Subfractionation and characterization of Mayan asphaltene. *Energy & Fuels* **1998,** 12 (6), 1290-1298.

[34] Miller, J.T., R.B. Fisher, A.M. van der Eerden, and D.C. Koningsberger, Structural determination by XAFS spectroscopy of non-porphyrin nickel and vanadium in Maya residuum, hydrocracked residuum, and toluene-insoluble solid. *Energy & Fuels* **1999,** 13 (3), 719- 727.

[35] Reichardt, C., *Solvents and Solvent Effects in Organic Chemistry*. 3rd ed.; Wiley-VCH: Weinheim, **2003**

[36] Jauquet, M. and P. Laszlo, Influence of Solvents on Spectroscopy. In *Solutions and Solubilities*, Dack, M. R. J., Ed. John Wiley & Sons: New York, **1975**, Vol. VIII, 195-258.

[37] Smith, B.C., *Quantitative Spectroscopy: Theory and Practice*. Academic Press: Amsterdam, **2002**

[38] Foster, N.S., J.W. Day, R.H. Filby, A. Alford, and D. Rogers, The role of Na-montmorillonite in the evolution of copper, nickel, and vanadyl geoporphyrins during diagenesis. *Org. Geochem.* **2002,** 33 (8), 907-919.

[39] Ferrer, E.G. and E.J. Baran, Electronic and photoelectron spectra of vanadyl(IV) tetraphenylporphyrin. *J. Electron Spectrosc.* **1991,** 57 (2), 189-197.

[40] Freeman, D.H., D.C. Saint Martin, and C.J. Boreham, Identification of metalloporphyrins by third-derivative UV/vis diode array spectroscopy. *Energy & Fuels* **1993,** 7 (2), 194-199.

[41] Cantu, R., J.R. Stencel, R.S. Czernuszewicz, P.R. Jaffe, and T.D. Lash, Surfactant-enhanced partitioning of nickel and vanadyl deoxophylloerythroetioporphyrins from crude oil into water and their analysis using surface-enhanced resonance Raman spectroscopy. *Environ. Sci. Technol.* **2000,** 34 (1), 192-198.

[42] Trofimenko, G.M., A.S. Semeikin, M.B. Berezin, and B.D. Berezin, The Influence of Isomerism of Etioporphyrins on Their Physicochemical Properties. *Russ. J. Coord. Chem.* **1996,** 22 (6), 476-480.

[43] Berezin, D.B., V.G. Andrianov, and A.S. Semeikin, Manifestation of structural features of porphyrin molecules in their electronic absorption spectra. *Opt. Spectrosc.* **1996,** 80 (4), 554-561.

[44] Berezin, B.D., *Coordination Compounds of Porphyrins and Phthalocyanines*. John Wiley & Sons: Chichester, **1981**

[45] Gouterman, M., Optical Spectra and Electronic Structure of Porphyrins and Related Rings. In *The Porphyrins*, Dolphin, D., Ed. Academic Press: New York, **1978**, Vol. III - Physical Chemi, 1-165.

[46] Berezin, B.D., Mutual Atomic Effect in Porphyrin Molecules and its Manifestation in Their Structure and Electronic Absorption Spectra. *J. Appl. Spectrosc.* **1999,** 66 (4), 521-527.

[47] White, W.I., Aggregation of Porphyrins and Metalloporphyrins. In *The Porphyrins*, Dolphin, D., Ed. Academic Press: New York, **1978**, Vol. 5, 303-339.

[48] Walker, F.A., E. Hui, and J.M. Walker, Electronic Effects In Transition-Metal Porphyrins .1. Reaction Of Piperidine With A Series Of Para-Substituted And Meta-Substituted Nickel(Ii) And Vanadium(Iv) Tetraphenylporphyrins. *J. Am. Chem. Soc.* **1975,** 97 (9), 2390-2397.

[49] Bonnett, R., P. Brewer, K. Noro, and T. Noro, Chemistry of Vanadyl Porphyrins. *Tetrahedron* **1978,** 34 (3), 379-385.

[50] Drew, M.G.B., P.C.H. Mitchell, and C.E. Scott, Crystal and Molecular Structure of three Oxovanadium(IV) Porphyrins: Oxovanadium Tetraphenylporphyrin(I), Oxovanadium(IV) Etioporphyrin(II) and the 1: 2 Adduct of (II) with 1,4-Dihydroxybenzene(III). Hydrogen Bonding Involving the VO Group. Relevan. *Inorg. Chim. Acta* **1984,** 82 (1), 63-68.

[51] Shelnutt, J.A., E.W. Findsen, M.R. Ondrias, and K. Alston, Axial Coordination In Nickel And Vanadium Porphyrins: Transient And Difference Raman Spectroscopy. *ACS Symp. Ser.* **1987,** 344 (24), 368-383.

[52] Bencosme, C.S., C. Romero, and S. Simoni, Axial Interaction Of Vanadyl Tetraphenylporphyrin With Lewis-Bases. *Inorg. Chem.* **1985,** 24 (10), 1603-1604.

[53] Ozawa, T. and A. Hanaki, Axial Ligation Of Some Lewis-Bases To Oxo-Metalloporphyrins. *Inorg. Chim. Acta* **1988,** 141 (1), 49-51.

[54] Boyd, P.D.W., T.D. Smith, J.H. Price, and J.R. Pilbrow, Electron Spin Resonance Study of Metal Ion Separations in Dimeric Copper (II) and Vanadyl Porphyrins. *J. Chem. Phys.* **1972,** 56 (3), 1253-1263.

[55] Banci, L., Homo- and Heterodimer Formation in Metalloporphyrins. *Inorg. Chem.* **1985,** 24 (5), 782-786.

[56] Maiya, G.B. and V. Krishnan, Electrochemical Redox Properties and Spectral Features of Supermolecular Porphyrins. *Inorg. Chem.* **1985,** 24 (20), 3253-3257.

[57] Lemtur, A., B.K. Chakravorty, T.K. Dhar, and J. Subramanian, Electron Spin Resonance of Dimeric Species from the Radical Cations of Vanadyl Porphyrins. *J. Phys. Chem.* **1984,** 88 (23), 5603-5608.

[58] Thanabal, V. and V. Krishnan, Cation-Induced Crown Porphyrin Dimers of Oxovanadium(IV). *Inorg. Chem.* **1982,** 21 (10), 3606-3613.

[59] Groennings, S., Quantitative determination of porphyrin Aggregate in petroleum. *Anal. Chem.* **1953,** 25 (6), 938- 941.

[60] Biggs, W.R., J.C. Fetzer, R.J. Brown, and J.G. Reynolds, Characterization of vanadium compounds in selected crudes. I. Porphyrin and non-porphyrin separation. *Liq. Fuels Technol.* **1985,** 3 (4), 397- 421.

[61] Reynolds, J.G., W.R. Biggs, and S.A. Bezman, Reaction Sequence Of Metallopetroporphyrins During Heavy Residuum Upgrading. *ACS Symp. Ser.* **1987,** 344 (13), 205-219.

[62] Reynolds, J.G., E.L. Jones, J.A. Bennett, and W.R. Biggs, Characterization of nickel and vanadium compounds in tar sand bitumen by UV-VIS spectroscopy and size exclusion chromatography coupled with element specific detection. *Fuel Sci. Technol. Int.* **1989,** 7 (5-6), 625-642.

[63] Van Berkel, G.J. and R.H. Filby, Generation of Nickel and Vanadyl Porphyrins From Kerogen During Simulated Catagenesis. *ACS Symp. Ser.* **1987,** 344 (7), 110-134.

[64] Pearson, C.D. and J.B. Green, Vanadium and nickel complexes in petroleum resid acid, base and neutral fractions. *Energy & Fuels* **1993,** 7 (3), 338-346.

[65] Freeman, D.H. and T.C. O'Haver, Derivative spectrophotometry of petroporphyrins. *Energy & Fuels* **1990,** 4 (6), 688-694.

[66] Rao, C.N.R., *Ultra-Violet and Visible Spectroscopy: Chemical Applications*. 3rd Edition ed.; Butterworths: London, **1975**

[67] Halasinski, T.M., J.L. Weisman, R. Ruiterkamp, T.J. Lee, F. Salama, and M. Head-Gordon, Electronic absorption spectra of neutral perylene (C20H12), terrylene (C30H16), and quaterrylene (C40H20) and their positive and negative ions: Ne matrix-isolation spectroscopy and time-dependent density functional theory calculations. *J. Phys. Chem. A* **2003,** 107 (19), 3660-3669.

[68] Yokota, T., F. Scriven, D.S. Montgomery, and O.P. Strausz, Absorption and Emission Spectra of Athabasca Asphaltene in the Visible and Near Ultraviolet Regions. *Fuel* **1986,** 65 (8), 1142-1149.

[69] Antipenko, V.R. and L.I. Zemtseva, Multiplicative hindrances in the quantitative analysis of petroleum metal porphyrins. *Petrol. Chem.* **1996,** 36 (1), 31-42.

[70] Wertz, J.E. and J.R. Bolton, *Electron Spin Resonance: Elementary Theory and Practical Applications*. McGraw Hill: New York, NY, **1972**

[71] Saraceno, A.J., N.D. Coggeshall, and D.T. Fanale, An Electron Paramagnetic Resonance Investigation Of Vanadium In Petroleum Oils. *Anal. Chem.* **1961,** 33 (4), 500-505.

[72] Tynan, E.C. and T.F. Yen, Association of Vanadium Chelates in Petroleum Asphaltenes as Studied By ESR. *Fuel* **1969,** 48 (2), 191-208.

[73] Selyutin, G.E., A.A. Shklyaev, N.P. Eletskii, V.F. Anufrienko, and V.I. Titov, ESR Spectra of Cationic Forms of Vanadyl and Copper Ethioporphyrinates. Monocation Dimers. *Sov. J. Coord. Chem.* **1979,** 5 (9), 1041-1046.

[74] Yen, T.F., L.J. Boucher, J.P. Dickie, E.C. Tynan, and G.B. Vaughan, Vanadium Complexes And Porphyrins In Asphaltenes. *J. Inst. Petrol.* **1969,** 55 (542), 87- 99.

[75] Dickson, F.E., C.J. Kunesh, E.L. Mcginnis, and L. Petrakis, Use Of Electron-Spin Resonance To Characterize Vanadium(Iv)-Sulfur Species In Petroleum. *Anal. Chem.* **1972,** 44 (6), 978-981.

[76] Dickson, F.E. and L. Petrakis, Application Of Electron-Spin Resonance And Electronic Spectroscopy To Characterization Of Vanadium Species In Petroleum Fractions. *Anal. Chem.* **1974,** 46 (8), 1129-1130.

[77] Reynolds, J.G., W.R. Biggs, and J.C. Fetzer, Characterization of vanadium compounds in selected crudes: II. Electron paramagnetic resonance studies of the first coordination spheres in porphyrin and non-porphyrin fractions. *Liq. Fuels Technol.* **1985,** 3 (4), 423- 448.

[78] Reynolds, J.G., W.R. Biggs, J.C. Fetzer, E.J. Gallegos, R.H. Fish, J.J. Komlenic, and B.K. Wines In *Molecular Characterization of Vanadyl and Nickel Non-Porphyrin Compounds in Heavy Crude Petroleums and Residua*, Characterization of heavy crude oils and petroleum residues: International Symposium on Characterization of Heavy Crude Oils and Petroleum Residues, Lyon, France, June 25-27, 1984, Lyon, France, 1984, pp 153-157.

[79] Graham, W.R.M., Analysis Of Metal Species In Petroleum And Tar Sands Using The Electron Paramagnetic Resonance And Fourier Transform Infrared Techniques. *ACS Symp. Ser.* **1987,** 344 (23), 358-367.

[80] Reynolds, J.G., E.J. Gallegos, R.H. Fish, and J.J. Komlenic, Characterization of the Binding Sites of Vanadium Compounds in Heavy Crude Petroleum Extracts by Electron Paramagnetic Resonance Spectroscopy. *Energy & Fuels* **1987,** 1 (1), 36-44.

[81] Malhotra, V.M. and H.A. Buckmaster, 34 GHz E.P.R. Study Of Vanadyl Complexes In Various Asphaltenes: Statistical Correlative Model Of The Coordinating Ligands. *Fuel* **1985,** 64 (3), 335- 341.

[82] Malawer, E.G. and L. Senak, Introduction to Size Exclusion Chromatography. In *Handbook of Size Exclusion Chromatography and Related Techniques*, 2nd ed.; Wu, C.-s., Ed. Marcel Dekker, Inc.: New York, **2004**, Ch. 1.

[83] Skoog, D.A. and J.J. Leary, *Principles of Instrumental Analysis*. 4th Edition ed.; Saunders College Publishing: Fort Worth, TX, **1992**

[84] Fish, R.H. and J.J. Komlenic, Molecular Characterization And Profile Identifications Of Vanadyl Compounds In Heavy Crude Petroleums By Liquid Chromatography/Graphite Furnace Atomic Absorption Spectrometry. *Anal. Chem.* **1984,** 56 (3), 510-517.

[85] Fish, R.H., J.J. Komlenic, and B.K. Wines, Characterization And Comparison Of Vanadyl And Nickel Compounds In Heavy Crude Petroleums And Asphaltenes By Reverse-Phase And Size-Exclusion Liquid Chromatography/Graphite Furnace Atomic Absorption Spectrometry. *Anal. Chem.* **1984,** 56 (13), 2452-2460.

[86] Biggs, W.R., R.J. Brown, and J.C. Fetzer, Elemental profiles of hydrocarbon materials by size-exclusion chromatography/inductively coupled plasma atomic emission spectrometry. *Energy & Fuels* **1987,** 1 (3), 257-262.

[87] Fish, R.H., J.G. Reynolds, and E.J. Gallegos, Molecular Characterization Of Nickel And Vanadium Nonporphyrin Compounds Found In Heavy Crude Petroleums And Bitumens. *ACS Symp. Ser.* **1987,** 344 (21), 332-349.

[88] Reynolds, J.G. and W.R. Biggs, Analysis Of Residuum Desulfurization By Size Exclusion Chromatography With Element Specific Detection. *Preprints - Div. Petrol. Chem. ACS* **1987,** 32 (1-2), 398-405.

[89] Sundararaman, P., W.R. Biggs, J.G. Reynolds, and J.C. Fetzer, Vanadylporphyrins, indicators of kerogen breakdown and generation of petroleum. *Geochim. Cosmochim. Acta* **1988,** 52 (9), 2337-2341.

[90] Davison, R.R., C.J. Glover, B.L. Burr, and J.A. Bullin, Size Exclusion Chromatography of Asphalts. In *Handbook of Size Exclusion Chromatography and Related Techniques*, 2nd ed.; Wu, C.-s., Ed. Marcel Dekker, Inc.: New York, **2004**, Ch. 8.

[91] Nguyen, S.N. and R.H. Filby, Interaction Of Ni(Ii) Complexes With Athabasca Asphaltenes. *ACS Symp. Ser.* **1987,** 344 (25), 384-401.

[92] Baker, E.W. and S.E. Palmer, Geochemistry of Porphyrins. In *The Porphyrins*, Dolphin, D., Ed. Academic Press: New York, **1978**, Vol. I, 486-552.

[93] Blumer, M. and M. Rudrum, High molecular weight fossil porphyrins. Evidence for monomeric and dimeric tetrapyrroles of about 1100 molecular weight. *J. Inst. Petrol.* **1970,** 57 (548), 99-106.

[94] Baker, E.W., T.F. Yen, J.P. Dickie, R.E. Rhodes, and L.F. Clark, Mass Spectrometry of Porphyrins. II. Characterization of Petroporphyrins. *J. Am. Chem. Soc.* **1967,** 89 (14), 3631-3639.

[95] Thomas and Blumer, Porphyrin pigments of a Triassic sediment. *Geochim. Cosmochim. Acta* **1964,** 28 (7), 1147-1154.

[96] Strong, D. and R.H. Filby, Vanadyl Porphyrin Distribution In The Alberta Oil-Sand Bitumens. *ACS Symp. Ser.* **1987,** 344 (10), 154-172.

[97] Van Berkel, G.J., M.A. Quinoñes, and M.E.J. Quirke, Geoporphyrin Analysis Using Electrospray Ionization-Mass Spectrometry. *Energy & Fuels* **1993,** 7 (3), 411-419.

[98] Xu, H., G. Que, D. Yu, and J.R. Lu, Characterization of petroporphyrins using ultraviolet-visible spectroscopy and laser desorption ionization time-of-flight mass spectrometry. *Energy & Fuels* **2005,** 19 (2), 517-524.

[99] Beato, B.D., R.A. Yost, G.J. Van Berkel, R.H. Filby, and J.M.E. Quirke, Henryville bed of the New Albany shale. III. Tandem mass spectrometric analyses of geoporphyrins from the bitumen and kerogen. *Org. Geochem.* **1991,** 17 (1), 93-105.

[100] Grigsby, R.D. and J.B. Green, High-Resolution Mass Spectrometric Analysis of a Vanadyl Porphyrin Fraction Isolated from the >700 °C Resid of Cerro Negro Heavy Petroleum. *Energy & Fuels* **1997,** 11 (3), 602-609.

[101] Rodgers, R.P., C.L. Hendrickson, M.R. Emmett, A.G. Marshall, M. Greaney, and K. Qian, Molecular characterization of petroporphyrins in crude oil by electrospray ionization Fourier transform ion cyclotron resonance mass spectrometry. *Can. J. Chem.* **2001,** 79 (5-6), 546-551.

[102] Tanaka, R., J.E. Hunt, R.E. Winans, P. Thiyagarajan, S. Sato, and T. Takanohashi, Aggregates structure analysis of petroleum asphaltenes with small-angle neutron scattering. *Energy & Fuels* **2003,** 17 (1), 127-134.

[103] Spiecker, P.M., K.L. Gawrys, and P.K. Kilpatrick, Aggregation and solubility behavior of asphaltenes and their subfractions. *J. Colloid Interf. Sci.* **2003,** 267 (1), 178-193.

[104] Thiyagarajan, P., J.E. Hunt, R.E. Winans, K.B. Anderson, and J.T. Miller, Temperature-dependent structural changes of asphaltenes in 1-methylnaphthalene. *Energy & Fuels* **1995,** 9 (5), 829-833.

[105] Cosultchi, A., P. Bosch, and V.H. Lara, Small-angle X-ray scattering study of oil- and deposit-asphaltene solutions. *Colloid. Polym. Sci.* **2003,** 281 (4), 325-330.

[106] Savvidis, T.G., D. Fenistein, L. Barre, and E. Behar, Aggregated structure of flocculated asphaltenes. *AIChE J.* **2001,** 47 (1), 206-211.

[107] Bardon, C., L. Barre, D. Espinat, V. Guille, M.H. Li, J. Lambard, J.C. Ravey, E. Rosenberg, and T. Zemb, Colloidal structure of crude oils and suspensions of asphaltenes and resins. *Fuel Sci. Technol. Int.* **1996,** 14 (1-2), 203-242.

[108] Kim, H.-g. and R.B. Long, Characterization Of Heavy Residuum By A Small Angle X-Ray Scattering Technique. *Ind. Eng. Chem Fundam.* **1979,** 18 (1), 60-63.

[109] Strausz, O.P., P. Peng, and J. Murgich, About the colloidal nature of asphaltenes and the MW of covalent monomeric units. *Energy & Fuels* **2002,** 16 (4), 809-822.

[110] Andersen, S.I., Effect of precipitation temperature on the composition of n-heptane asphaltenes. *Fuel Sci. Technol. Int.* **1994,** 12 (1), 51-74.

[111] Yarranton, H.W., H. Alboudwarej, and R. Jakher, Investigation of asphaltene association with vapor pressure osmometry and interfacial tension measurements. *Ind. Eng. Chem. Res.* **2000,** 39 (8), 2916-2924.

[112] Agrawala, M. and H.W. Yarranton, An asphaltene association model analogous to linear polymerization. *Ind. Eng. Chem. Res.* **2001,** 40 (21), 4664-4672.

[113] Yarranton, H.W., W.A. Fox, and W.Y. Svrcek, Effect of resins on asphaltene self-association and solubility. *Can. J. Chem. Eng.* **2007,** 85 (5), 635-642.

[114] Wong, G.K. and T.F. Yen, Electron spin resonance probe method for the understanding of petroleum asphaltene macrostructure. *J. Petrol. Sci. Eng.* **2000,** 28 (1), 55-64.

[115] Tanaka, R., E. Sato, J.E. Hunt, R.E. Winans, S. Sato, and T. Takanohashi, Characterization of asphaltene aggregates using X-ray diffraction and small-angle X-ray scattering. *Energy & Fuels* **2004,** 18 (4), 1118-1125.

[116] Mamardashvili, G.M., N.Z. Mamardashvili, O.A. Golubchicov, and B.D. Berezin, The influence of alkyl bridge substitution on the porphyrin solubility. *J. Mol. Liq.* **2001,** 91 (1-3), 189-191.

[117] Mamardashvili, G.M., N.Z. Mamardashvili, O.A. Golubchikov, and B.D. Berezin, The effect of Zn2+ coordination on the solubility of porphyrins. *Russ. J. Phys. Chem.* **1999,** 73 (6), 894-898.

[118] Trofimenko, G.M., N.Z. Mamardashvili, O.A. Golubchikov, and B.D. Berezin, Solubility of beta-Octaalkylporphirin Derivatives in Organic Solvents. *Russ. J. Phys. Chem.* **1997,** 71 (2), 240-243.

[119] Berezin, B.D., O.I. Koifman, and G.E. Nikitina, Solubility of Porphyrins of the Protoporphyrin Group in Ethanol. *Russ. J. Phys. Chem.* **1980,** 54 (10), 1413-1415.

[120] Berezin, B.D., O.I. Koifman, V.V. Zelov, and G.E. Nikitina, Thermodynamics of the Dissolution of Tetraphenylporphin in Alcohols. *Russ. J. Phys. Chem.* **1978,** 52 (9), 1281-1282.

[121] Koifman, O.I., B.D. Berezin, V.V. Zelov, and G.E. Nikitina, Thermodynamics of the Dissolution of Tetraphenylporphin in Cyclic Solvents and Ketones. *Russ. J. Phys. Chem.* **1978,** 52 (7), 1032-1034.

[122] Salcedo, R., I.P. Zaragoza, J.M. Martinez-Magadan, and I. Garcia-Cruz, Electronic structure in different environments for vanadyl porphyrinate molecules present in crude oil. *J. Mol. Struc. - THEOCHEM* **2003,** 626 (1-3), 195-201.

[123] Pfeiffer, J.P. and R.N.J. Saal, Asphaltic bitumen as colloid system. *J. Phys. Chem.* **1940,** 44, 139-149.

[124] Yen, T.F., J.G. Erdman, and S.S. Pollack, Investigation of the structure of petroleum asphaltenes by x-ray diffraction. *Anal. Chem.* **1961,** 33, 1587-1594.

[125] Speight, J.G., Asphaltenes and the Structure of Petroleum. In *Petroleum Chemistry and Refining*, Speight, J. G., Ed. Taylor and Francis: Washington, DC, **1998**, 103-120.

[126] Merino-Garcia, D. and S.I. Andersen, Thermodynamic Characterization of Asphaltene-Resin Interaction by Microcalorimetry. *Langmuir* **2004,** 20 (11), 4559-4565.

[127] Merino-Garcia, D. and S.I. Andersen, Interaction of Asphaltenes with Nonylphenol by Microcalorimetry. *Langmuir* **2004,** 20 (4), 1473-1480.

[128] Merino-Garcia, D., J. Murgich, and S.I. Andersen, Asphaltene self-association: Modeling and effect of fractionation with a polar solvent. *Petrol. Sci. Technol.* **2004,** 22 (7 & 8), 735-758.

[129] Juyal, P., D. Merino-Garcia, and S.I. Andersen, Effect on Molecular Interactions of Chemical Alteration of Petroleum Asphaltenes. I. *Energy & Fuels* **2005,** 19 (4), 1272-1281.

[130] Merino-Garcia, D. and S.I. Andersen, Calorimetric evidence about the application of the concept of CMC to asphaltene self-association. *J. Disper. Sci. Technol.* **2005,** 26 (2), 217-225.

[131] Verdier, S., F. Plantier, D. Bessieres, S.I. Andersen, E.H. Stenby, and H. Carrier, Study of Asphaltene Precipitation by Calorimetry. *Energy & Fuels* **2007,** 21 (6), 3583-3587.

[132] Akbarzadeh, K., H. Alboudwarej, W.Y. Svrcek, and H.W. Yarranton, A generalized regular solution model for asphaltene precipitation from n-alkane diluted heavy oils and bitumens. *Fluid Phase Equilibria* **2005,** 232 (1-2), 159-170.

[133] Akbarzadeh, K., A. Dhillon, W.Y. Svrcek, and H.W. Yarranton, Methodology for the characterization and modeling of asphaltene precipitation from heavy oils diluted with n-alkanes. *Energy & Fuels* **2004,** 18 (5), 1434-1441.

[134] Alboudwarej, H., K. Akbarzadeh, J. Beck, W.Y. Svrcek, and H.W. Yarranton, Regular Solution Model for Asphaltene Precipitation from Bitumens and Solvents. *AIChE J.* **2003,** 49 (11), 2948-2956.

[135] Yarranton, H.W. and J.H. Masliyah, Molar mass distribution and solubility modeling of asphaltenes. *AIChE J.* **1996,** 42 (12), 3533- 3543.

[136] Cimino, R., S. Correra, P.A. Sacomani, and C. Carniani In *Thermodynamic modelling for prediction of asphaltene deposition in live oils*, International Symposium on Oilfield Chemistry, Feb 14-17 1995, San Antonio, TX, USA, Society of Petroleum Engineers (SPE), 1995, pp 499-512.

[137] Cimino, R., S. Correra, A. Del Bianco, and T.P. Lockhart, Solubility and Phase behaviour of Asphaltenes in Hydrocarbon Media. In *Asphaltenes: Fundamentals and Applications*, Sheu, E. Y.; Mullins, O. C., Eds. Plenum Press: New York, **1995**, 97-130.

[138] Akbarzadeh, K., S. Ayatollahi, M. Moshfeghian, H. Alboudwarej, and H.W. Yarranton, Estimation of SARA fraction properties with the SRK EOS. *J. Can. Pet. Technol.* **2004,** 43 (9), 31-39.

[139] Sabbagh, O., K. Akbarzadeh, A. Badamchi-Zadeh, W.Y. Svrcek, and H.W. Yarranton, Applying the PR-EoS to asphaltene precipitation from n-alkane diluted heavy oils and bitumens. *Energy & Fuels* **2006,** 20 (2), 625- 634.

[140] Buenrostro-Gonzalez, E., C. Lira-Galeana, A. Gil-Villegas, and J. Wu, Asphaltene precipitation in crude oils: Theory and experiments. *AIChE J.* **2004,** 50 (10), 2552-2570.

[141] Wu, J., J.M. Prausnitz, and A. Firoozabadi, Molecular thermodynamics of asphaltene precipitation in reservoir fluids. *AIChE J.* **2000,** 46 (1), 197-209.

[142] Akbarzadeh, K., D.C. Bressler, J. Wang, K.L. Gawrys, M.R. Gray, P.K. Kilpatrick, and H.W. Yarranton, Association behavior of pyrene compounds as models for asphaltenes. *Energy & Fuels* **2005,** 19 (4), 1268-1271.

[143] Rakotondradany, F., H. Fenniri, P. Rahimi, K.L. Gawrys, P.K. Kilpatrick, and M.R. Gray, Hexabenzocoronene model compounds for asphaltene fractions: Synthesis & characterization. *Energy & Fuels* **2006,** 20 (6), 2439-2447.

[144] Tan, X., H. Fenniri, and M.R. Gray, Pyrene Derivatives of 2,2'-Bipyridine as Models for Asphaltenes: Synthesis, Characterization, and Supramolecular Organization. *Energy & Fuels* **2008,** 22 (2), 715-720.

[145] Tan, X., H. Fenniri, and M.R. Gray, Water Enhances the Aggregation of Model Asphaltenes in Solution via Hydrogen Bonding. *Energy & Fuels* **2009,** 23 (7), 3687-3693.

[146] Yudin, I.K., G.L. Nikolaenko, E.E. Gorodetskii, E.L. Markhashov, D. Frot, Y. Briolant, V.A. Agayan, and M.A. Anisimov, Universal behavior of asphaltene aggregation in hydrocarbon solutions. *Petrol. Sci. Technol.* **1998,** 16 (3-4), 395-414.

[147] Yin, C.-X. , X. Tan, K. Mullen, J.M. Stryker, and M.R. Gray, Associative pi-pi Interapictions of Condensed Aromatic Compounds with Vanadyl or Nickel Porphyrin Complexes Are Not Observed in the Organic Phase. *Energy & Fuels* **2008,** 22 (4), 2465-2469.

[148] Sirota, E.B., Physical structure of asphaltenes. *Energy & Fuels* **2005,** 19 (4), 1290-1296.

[149] Lerner, B.J. *Removing metals with a 2-pyrrolidone-alcohol mixture*. US patent no. 3052627, **1959**

[150] Kimberlin, C.N.J. and W.J. Mattox *Butyrolactone solvent extraction process for removal of metal contaminants*. US patent no. 2913394, **1959**

[151] Overfield, R.E. *Integrated method for extracting nickel and vanadium compounds from oils*. US patent no. 4643821, **1987**

[152] Galimov, R.A., L.B. Krivonozhkina, V.V. Abushayeva, and G.V. Romanov, Extraction of vanadyl porphyrins from petroleum asphaltenes. *Petrol. Chem.* **1993,** 33 (6), 539-543.

[153] Yin, C.-X. , J.M. Stryker, and M.R. Gray, Separation of Petroporphyrins from Asphaltenes by Chemical Modification and Selective Affinity Chromatography. *Energy & Fuels* **2009,** 23 (5), 2600-2605.

[154] Speronello, B.K. and W.J. Reagan, Test measures FCC catalyst deactivation by nickel and vanadium. *Oil Gas J.* **1984,** 82 (5), 139-143.

[155] Tsiatouras, V.A., N.P. Evmiridis, V.A. AF Tsiatouras, and N.P. Evmiridis, FCC Catalysts: Cu(II)-Exchanged USY-Type. Stability, Dealumination, and Acid Sites after Thermal and Hydrothermal Treatment before and after Vanadium Impregnation. *Ind. Eng. Chem. Res.* **2008,** 47 (23), 9288-9296.

[156] Kimberlin, C.N.J., H.G. Ellert, C.E. Adams, and G.P. Hamner *Demetallization with Hydrofluoric Acid*. US patent no. 3,203,892, **1965**

[157] Sugihara, J.M., J.F. Branthaver, and K.W. Willcox, Oxidative demetallation of oxovanadium(IV) porphyrins. In *The Role of Trace Metals in Petroleum*, Yen, T. F., Ed. Ann Arbor Science Publichers Inc.: Ann Arbor, MI, **1975**, 183-193.

[158] Gould, K.A., Oxidative demetallization of petroleum asphaltenes and residue. *Fuel* **1980,** 59 (10), 733-736.

[159] Mann, D.P., S.G. Kukes, and D.M. Coombs *Metals Removal with a Light Hydrocarbon and an Organophosphorous Compound*. US patent no. 4,518,484, **1985**

[160] Fedorak, P.M., K.M. Semple, R. Vazquez-Duhalt, and D.W.S. Westlake, Chloroperoxidase-mediated modifications of petroporphyrins and asphaltenes. *Enzyme Microb. Tech.* **1993,** 15 (5), 429-437.

[161] Xu, G.-W. , K.W. Mitchell, and D.J. Monticello *Fuel Product Produced by Demetalizing a Fossil Fuel with an Enzyme*. US patent no. 5,726,056, **1998**

[162] Dedeles, G.R., A. Abe, K. Saito, K. Asano, K. Saito, A. Yokota, and F. Tomita, Microbial demetallization of crude oil: nickel protoporphyrin disodium as a model organo-metallic substrate. *J. Biosci. Bioeng.* **2000,** 90 (5), 515-521.

[163] Greaney, M.A., M.C. Kerby, Jr., W.N. Olmstead, and I.A. Wiehe *Method for Demetallating Refinrey Feedstreams*. US patent no. 5,529,684, **1996**

[164] Ovalles, C., I. Rojas, S. Acevedo, G. Escobar, G. Jorge, L.B. Gutierrez, A. Rincon, and B. Scharifker, Upgrading of Orinoco Belt crude oil and its fractions by an electrochemical system in the presence of protonating agents. *Fuel Process. Technol.* **1996,** 48 (2), 159-172.

[165] Sakanishi, K., N. Yamashita, D.D. Whitehurst, and I. Mochida, Depolymerization and demetalation treatments of asphaltene in vacuum residue. *Catal. Today* **1998,** 43 (3-4), 241-247.

[166] Shiraishi, Y., T. Hirai, and I. Komasawa, A Novel Demetalation Process for Vanadyl- and Nickelporphyrins from Petroleum Residue by Photochemical Reaction and Liquid-Liquid Extraction. *Ind. Eng. Chem. Res.* **2000,** 39 (5), 1345-1355.

[167] Sakanishi, K., I. Saito, I. Watanabe, and I. Mochida, Dissolution and demetallation treatment of asphaltene in resid using adsorbent and oil-soluble Mo complex. *Fuel* **2004,** 83 (14-15), 1889-1893.

[168] Hansen, C.M., Universality of the solubility parameter. *Ind. Eng. Chem Prod. Res. Dev.* **1969,** 8 (1), 2-11.

[169] Wiehe, I.A., *Process Chemistry of Petroleum Macromolecules*. CRC Press: Boca Raton, FL., **2008**

[170] Fleischer, E.B., C.K. Miller, and L.E. Webb, Crystal and molecular structures of some metal tetraphenylporphines. *J. Am. Chem. Soc.* **1964,** 86 (12), 2342-2347.

[171] Lauher, J.W. and J.A. Ibers, Structure of octaethylporphyrin. Comparison with other free base porphyrins. *J. Am. Chem. Soc.* **1973,** 95 (16), 5148-5152.

[172] Molinaro, F.S. and J.A. Ibers, Crystal and Molecular Structure of 2,3,7,8,12,13,17,18-Octaethylporphinatooxovanadium(IV). *Inorg. Chem.* **1976,** 15 (9), 2278-2283.

[173] Prausnitz, J.M., R.N. Lichtenthaler, and E. Gomes de Azevedo, *Molecular Thermodynamics of Fluid Phase Equilibria*. 2nd ed.; Prentice-Hall Inc.: Englewood Cliffs, NJ, **1986**

[174] Design Institute for Physical Properties, A., *DIPPR Project 801 - Full Version*. Design Institute for Physical Property Data/AIChE: **2008**

[175] Walas, S.M., *Phase Equilibria in Chemical Engineering*. Butterworth Publishers: Boston, MA, **1985**

[176] Wong, W.K. and E.F. Westrum, Jr., Thermodynamics of polynuclear aromatic molecules. I. Heat capacities and enthalpies of fusion of pyrene, fluoranthene, and triphenylene. *J. Chem. Thermodyn.* **1971,** 3 (1), 105-124.

[177] Ali, S.H., F.S. Al-Mutairi, and M.A. Fahim, Solubility of polycyclic aromatics in binary solvent mixtures using activity coefficient models. *Fluid Phase Equilibria* **2005,** 230 (1-2), 176-183.

[178] Holzhauer, J.K. and W.T. Ziegler, Temperature dependence of excess thermodynamic properties of n-heptane-toluene, methylcyclohexane-toluene, and n-heptane-methylcyclohexane systems. *J. Phys. Chem.* **1975,** 79 (6), 590-604.

[179] Shahidi, F., P.G. Farrell, J.T. Edward, and P. Canonne, Partial molal volumes of organic compounds in carbon tetrachloride. 3. Aromatic hydrocarbons: steric effects. *J. Org. Chem.* **1979,** 44 (6), 950-953.

[180] Wakeham, W.A., G.S. Cholakov, and R.P. Stateva, Liquid Density and Critical Properties of Hydrocarbons Estimated from Molecular Structure. *J. Chem. Eng. Data* **2002,** 47 (3), 559-570.

[181] McLaughlin, E. and A.R. Ubbelohde, Structure and viscosity of melts of aromatic hydrocarbons. *Trans. Farad. Soc.* **1957,** 53, 628-634.

[182] Baxter, G.P. and A.H. Hale, A revision of the atomic weight of carbon. *J. Am. Chem. Soc.* **1936,** 58, 510-515.

[183] Roux, M.V., M. Temprado, J.S. Chickos, and Y. Nagano, Critically evaluated thermochemical properties of polycyclic aromatic hydrocarbons. *J. Phys. Chem. Ref. Data* **2008,** 37 (4), 1855-1996.

[184] Bissell, T.G., G.E. Okafor, and A.G. Williamson, Enthalpies and volumes of mixing of alkanes with carbon tetrachloride, chloroform, and methylene chloride at 25°C. *J. Chem. Thermodyn.* **1971,** 3 (3), 393-399.

[185] Rothemund, P. and A.R. Menotti, Porphyrin studies. IV. The synthesis of alpha ,beta ,gamma ,delta -tetraphenylporphine. *J. Am. Chem. Soc.* **1941,** 63, 267-270.

[186] Bergstresser, T.R. and M.E. Paulaitis, Solubility of meso-tetraphenylporphyrin in two supercritical fluid solvents. *ACS Symp. Ser.* **1987,** 329 (Supercrit. Fluids:), 138-148.

[187] Neau, S.H., S.V. Bhandarkar, and E.W. Hellmuth, Differential Molar Heat Capacities to Test Ideal Solubility Estimations. *Pharmaceut. Res.* **1997,** 14 (5), 601-605.

[188] Neau, S.H., G.L. Flynn, and S.H. Yalkowsky, The Influence of Heat Capacity Assumptions on the Estimation of Solubility Parameters from Solubility Data. *Int. J. Pharm.* **1989,** 49 (3), 223-229.

[189] Mishra, D.S. and S.H. Yalkowsky, Solubility of organic compounds in non-aqueous systems: polycyclic aromatic hydrocarbons in benzene. *Ind. Eng. Chem. Res.* **1990,** 29 (11), 2278-2283.

[190] Neau, S.H. and G.L. Flynn, Solid and liquid heat capacities of n-alkyl para-aminobenzoates near the melting point. *Pharmaceut. Res.* **1990,** 7 (11), 1157-1162.

[191] Pappa, G.D., E.C. Voutsas, K. Magoulas, and D.P. Tassios, Estimation of the Differential Molar Heat Capacities of Organic Compounds at Their Melting Point. *Ind. Eng. Chem. Res.* **2005,** 44 (10), 3799-3806.

[192] Wu, M. and S. Yalkowsky, Estimation of the Molar Heat Capacity Change on Melting of Organic Compounds. *Ind. Eng. Chem. Res.* **2009,** 48 (2), 1063-1066.

[193] Koifman, O.I., B.D. Berezin, V.V. Zelov, and G.E. Nikitina, Thermodynamics of tetraphenylporphine dissolution in cyclic solvents and in ketones. *Zh. Fizi. Khim.* **1978,** 52 (7), 1782-1784.

[194] Whitlock, H.W., Jr. and R. Hanauer, Octaethylporphyrin. *J. Org. Chem.* **1968,** 33 (5), 2169-2171.

[195] Eisner, U., A. Lichtarowicz, and R.P. Linstead, Chlorophyll and related compounds. VI. The synthesis of octaethylchlorine. *J. Chem. Soc.* **1957,** , 733-739.

[196] Rogel, E., Theoretical estimation of the solubility parameters distributions of asphaltenes, resins, and oils from crude oils and related materials. *Energy & Fuels* **1997,** 11 (4), 920-925.

[197] Jaffe, S.B., H. Freund, and W.N. Olmstead, Extension of structure-oriented lumping to vacuum residua. *Ind. Eng. Chem. Res.* **2005,** 44 (26), 9840-9852.

[198] Fedors, R.F., Method for Estimating Both the Solubility Parameters and Molar Volumes of Liquids. *Polym. Eng. Sci.* **1974,** 14 (2), 147-154.

[199] Constantinou, L. and R. Gani, New Group Contribution Method for Estimating Properties of Pure Compounds. *AIChE J.* **1994,** 40 (10), 1697-1710.

[200] Constantinou, L., R. Gani, and J.P. O'Connell, Estimation of the Acentric Factor and the Liquid Molar Volume at 298K using a New Group Contribution Method. *Fluid Phase Equilibria* **1995,** 103 (1), 11-22.

[201] Stefanis, E., L. Constantinou, and C. Panayiotou, A group-contribution method for predicting pure component properties of biochemical and safety interest. *Ind. Eng. Chem. Res.* **2004,** 43 (19), 6253-6261.

[202] Stefanis, E. and C. Panayiotou, Prediction of Hansen solubility parameters with a new group-contribution method. *Int. J. Thermophys.* **2008,** 29 (2), 568-585.

[203] Marrero, J. and R. Gani, Group-contribution based estimation of pure component properties. *Fluid Phase Equilibria* **2001,** 183, 183-208.

[204] Northrop, J.H. and M.L. Anson, A method for the determination of diffusion constants and the calculation of the radius and weight of the hemoglobin molecule. *J. Gen. Physiol.* **1928,** 12 (4), 543-554.

[205] Gordon, A.R., The diaphragm-cell method of measuring diffusion. *Ann. N.Y. Acad. Sci.* **1945,** 46, 285-308.

[206] Stokes, R.H., An Improved Diaphragm-cell for Diffusion Studies, and Some Tests of the Method. *J. Am. Chem. Soc.* **1950,** 72, 763-767.

[207] Holmes, J.T., C.R. Wilke, and D.R. Olander, Convective mass transfer in a diaphragm diffusion cell. *J. Phys. Chem.* **1963,** 67 (7), 1469-1472.

[208] Holmes, J.T., Simplified technique for using the diaphragm-type liquid diffusion cell. *Rev. Sci. Instrum.* **1965,** 36 (6), 831-832.

[209] Mills, R. and L.A. Woolf, *The Diaphragm Cell: Theory and Practice of the Diaphragm Cell for Liquid Diffusion Measurements*. Australian National University Press: Canberra, Vol. DRU-RR1, **1968**

[210] Keller, K.H. and S.K. Friedlander, Diffusivity measurements of human methemoglobin. *J. Gen. Physiol.* **1966,** 49 (4), 681-687.

[211] Hashitani, T. and R. Tamamushi, Rapid measurements of diffusion coefficients of electrolytes in aqueous solutions by the diaphragm-cell method. *Trans. Farad. Soc.* **1967,** 63 (2), 369-371.

[212] Bremer, M.F. and E.L. Cussler, Diffusion in the ternary system D-tartaric acid-L-tartaric acid-water at 25°C. *AIChE J.* **1970,** 16 (5), 832-837.

[213] Tanaka, K., T. Hashitani, and R. Tamamushi, Modified diffusion cell and its application to the determination of activity coefficients. *Trans. Farad. Soc.* **1970,** 66 (1), 74-79.

[214] Keller, K.H., E.R. Canales, and S.I. Yum, Tracer and mutual diffusion coefficients of proteins. *J. Phys. Chem.* **1971,** 75 (3), 379-387.

[215] Riveros-Moreno, V. and J.B. Wittenberg, Self-diffusion coefficients of myoblobin and hemoglobin in concentrated solutions. *J. Biol. Chem.* **1972,** 247 (3), 895-901.

[216] Geankoplis, C.J., M.R. Okos, and E.A. Grulke, Diffusion of urea and potassium chloride in albumin solutions. *J. Chem. Eng. Data* **1978,** 23 (1), 40-44.

[217] Geankoplis, C.J., E.A. Grulke, and M.R. Okos, Diffusion and interaction of sodium caprylate in bovine serum albumin solutions. *Ind. Eng. Chem Fundam.* **1979,** 18 (3), 233-237.

[218] Robertson, B.C. and A.L. Zydney, A Stefan-Maxwell analysis of protein transport in porous membranes. *Sep. Sci. Technol.* **1988,** 23 (12-13), 1799-1811.

[219] Tyrrell, H. and Harris, K., *Diffusion in liquids, A theoretical and experimental study*. Butterworths: London, **1984**

[220] Bird, R.B., W.E. Stewart, and E.N. Lightfoot, *Transport Phenomena*. 2nd ed.; John Wiley & Sons: New York, **2002**

[221] Barnes, C., Diffusion through a membrane. *Physics* **1934,** 5, 4-8.

[222] Mills, R., L.A. Woolf, and R.O. Watts, Simplified procedures for diaphragm-cell diffusion studies. *AIChE J.* **1968,** 14 (4), 671-673.

[223] Mills, R., Diffusion relationships in the system benzene-biphenyl at 25°C. *J. Phys. Chem.* **1963,** 67, 600-605.

[224] Kaufmann, T.G. and E.F. Leonard, Mechanism of interfacial mass transfer in membrane transport. *AIChE J.* **1968,** 14 (3), 421-425.

[225] Smith, K.A., C.K. Colton, E.W. Merrill, and L.B. Evans, Convective transport in a batch dialyzer: determination of true membrane permeability form a single measurement. *Chem. Eng. Progr. Symp. Ser.* **1968,** 64 (84), 45-58.

[226] Malone, D.M. and J.L. Anderson, Diffusional boundary-layer resistance for membranes with low porosity. *AIChE J.* **1977,** 23 (2), 177-184.

[227] Saiki, H., K. Takami, and T. Tominaga, Diffusion of porphyrins and quinones in organic solvents. *Phys. Chem. Chem. Phys.* **1999,** 1 (2), 303-306.

[228] Hejtmanek, V. and P. Schneider, Diffusion Coefficients of Some Large Organic Molecules in Acetone, Cyclohexane, and Toluene. *J. Chem. Eng. Data* **1993,** 38 (3), 407-409.

[229] Kapinus, E.I. and Y.V. Kholodenko, Palladium tetraphenylporphyrin diffusion coefficients in organic solvents. *Russ. J. Phys. Chem.* **1991,** 65 (2), 197-199.

[230] Kathawalla, I.A., J.L. Anderson, and J.S. Lindsey, Hindered diffusion of porphyrins and short-chain polystyrene in small pores. *Macromolecules* **1989,** 22 (3), 1215-1219.

[231] Geist, J.M. and M.R. Cannon, Viscosities of pure hydrocarbons. *Ind. Eng. Chem. Anal.* **1946,** 18, 611-613.

[232] Howard, K.S. and R.A. McAllister, The viscosity of acetone-water solutions up to their normal boiling points. *AIChE J.* **1958,** 4, 362-366.

[233] Knapstad, B., P.A. Skjoelsvik, and H.A. Oeye, Viscosity of pure hydrocarbons. *J. Chem. Eng. Data* **1989,** 34 (1), 37-43.

[234] Paez, S. and M. Contreras, Densities and viscosities of binary mixtures of 1-propanol and 2-propanol with acetonitrile. *J. Chem. Eng. Data* **1989,** 34 (4), 455-459.

[235] Tanaka, Y., H. Hosokawa, H. Kubota, and T. Makita, Viscosity and density of binary mixtures of cyclohexane with n-octane, n-dodecane, and n-hexadecane under high pressures. *Int. J. Thermophys.* **1991,** 12 (2), 245-264.

[236] Dymond, J.H. and H.A. Oye, Viscosity of selected liquid n-alkanes. *J. Phys. Chem. Ref. Data* **1994,** 23 (1), 41-53.

[237] Kumagai, A. and S. Takahashi, Viscosity and density of liquid mixtures of n-alkanes with squalane. *Int. J. Thermophys.* **1995,** 16 (3), 773-779.

[238] Nikam, P.S., L.N. Shirsat, and M. Hasan, Density and Viscosity Studies of Binary Mixtures of Acetonitrile with Methanol, Ethanol, Propan-1-ol, Propan-2-ol, Butan-1-ol, 2-Methylpropan-1-ol, and 2-Methylpropan-2-ol at (298.15, 303.15, 308.15, and 313.15) K. *J. Chem. Eng. Data* **1998,** 43 (5), 732-737.

[239] Wu, J., Z. Shan, and A.A. Asfour, Viscometric properties of multicomponent liquid n-alkane systems. *Fluid Phase Equilibria* **1998,** 143 (1-2), 263-274.

[240] Faria, M.A.F., C.F. De Sa, G.R. Lima, Filho, Joaquim I. B. C., Martins, R.J., De Cardoso, Marcio J. E., and Barcia, O.E., Measurement of Density and Viscosity of Binary 1-Alkanol Systems (C8-C11) at 101 kPa and Temperatures from (283.15 to 313.15) K. *J. Chem. Eng. Data* **2005,** 50 (6), 1938-1943.

[241] Santos, F.J.V., Nieto de Castro, Carlos A., Dymond, J.H., N.K. Dalaouti, M.J. Assael, and A. Nagashima, Standard Reference Data for the Viscosity of Toluene. *J. Phys. Chem. Ref. Data* **2006,** 35 (1), 1-8.

[242] Iloukhani, H. and B. Samiey, Excess molar volumes, viscosities, and speeds of sound of the ternary mixture {1-heptanol (1) + trichloroethylene (2) + methylcyclohexane (3)} at T = 298.15 K. *J. Chem. Thermodyn.* **2007,** 39 (2), 206-217.

[243] Dubey, G.P. and M. Sharma, Excess volumes, densities, speeds of sound, and viscosities for the binary systems of 1-octanol with hexadecane and squalane at (298.15, 303.15 and 308.15) K. *Int. J. Thermophys.* **2008,** 29 (4), 1361-1375.

[244] Wankhede, D., N. Wankhede, M. Lande, and B. Arbad, Densities and viscosities of propylene carbonate with aromatic hydrocarbons (benzene, 1,4-dimethylbenzene and ethylbenzene) at 288.15, 298.15 and 308.15 K. *Phys. Chem. Liquids* **2008,** 46 (3), 319-327.

[245] Millipore. Ultrafiltration Disc Membranes for Stirred Cells and Micropartition Systems (TN1000ENUS). .

[246] Uversky, V.N., Use of fast protein size-exclusion liquid chromatography to study the unfolding of proteins which denature through the molten globule. *Biochemistry* **1993,** 32 (48), 13288-13298.

[247] Stefan, G., J. Ralf, and W. Roland, Solvational tuning of the unfolding, aggregation and amyloidogenesis of insulin. *J. Mol. Biol.* **2005,** 351 (4), 879-894.

[248] Tanford, C., Y. Nozaki, J.A. Reynolds, and S. Makino, Molecular characterization of proteins in detergent solutions. *Biochemistry* **1974,** 13 (11), 2369-2376.

[249] Ende, H.A., Sedimentation Constants, Diffusion Constants, Partial Specific Volumes, Frictional Ratios and Second Virial Coefficients of Polymers in Solutions. In *Polymer Handbook*, Brandrup, J.; Immergut, E. H., Eds. Interscience Publishers: New York, **1966**, IV-73.

[250] Boyer, P.M. and J.T. Hsu, Experimental studies of restricted protein diffusion in an agarose matrix. *AIChE J.* **1992,** 38 (2), 259-272.

[251] Joessang, T., J. Feder, and E. Rosenqvist, Photon correlation spectroscopy of human IgG. *J. Protein Chem.* **1988,** 7 (2), 165-171.

[252] Tkacik, G. and S. Michaels, A rejection profile test for ultrafiltration membranes and devices. *Bio-Technol* **1991,** 9 (10), 941-946.

[253] Kim, K.J., A.G. Fane, R. Ben Aim, M.G. Liu, G. Jonsson, I.C. Tessaro, A.P. Broek, and D. Bargeman, A comparative study of techniques used for porous membrane characterization: pore characterization. *J. Membrane Sci.* **1994,** 87 (1-2), 35-46.

[254] Meireles, M., A. Bessieres, I. Rogissart, P. Aimar, and V. Sanchez, An appropriate molecular size parameter for porous membranes calibration. *J. Membrane Sci.* **1995,** 103 (1-2), 105-115.

[255] Zeman, L. and M. Wales, Steric rejection of polymeric solutes by membranes with uniform pore size distribution. *Sep. Sci. Technol.* **1981,** 16 (3), 275-290.

[256] Jonsson, G. and P.M. Christensen, *Separation characteristics of ultrafiltration membranes.* Plenum Press: New York, 1986; p 90.

[257] Zhao, B., X. Zhang, and J.M. Shaw, Interplay between the physical properties of Athabasca bitumen plus diluent mixtures and coke deposition on a commercial hydroprocessing catalyst. *Energy & Fuels* **2008,** 22 (3), 1747-1758.

[258] Herrington, P.R., Effect of concentration on the rate of reaction of asphaltenes with oxygen. *Energy & Fuels* **2004,** 18 (5), 1573-1577.

[259] Ostlund, J.-A. , S.-I. Andersson, and M. Nyden, Studies of asphaltenes by the use of pulsed-field gradient spin echo NMR. *Fuel* **2001,** 80 (11), 1529-1533.

[260] Wargadalam, V.J., K. Noringa, and M. Iino, Size and shape of a coal asphaltene studied by viscosity and diffusion coefficient measurements. *Fuel* **2002,** 81 (11-12), 1403-1407.

[261] Ostlund, J.A., M. Nyden, I.H. Auflem, and J. Sjoblom, Interactions between asphaltenes and naphthenic acids. *Energy & Fuels* **2003,** 17 (1), 113-119.

[262] Andrews, A.B., R.E. Guerra, O.C. Mullins, and P.N. Sen, Diffusivity of asphaltene molecules by fluorescence correlation spectroscopy. *J. Phys. Chem. A* **2006,** 110 (26), 8093-8097.

[263] Lisitza, N.V., D.E. Freed, P.N. Sen, and Y.-Q. Song, Study of Asphaltene Nanoaggregation by Nuclear Magnetic Resonance (NMR). *Energy & Fuels* **2009,** 23 (3), 1189-1193.

[264] Baltus, R.E. and J.L. Anderson, Hindered Diffusion of Asphaltenes Through Microporous Membranes. *Chem. Eng. Sci.* **1983,** 38 (12), 1959-1969.

[265] Gawrys, K. and P.K. Kilpatrick, Asphaltenic aggregates are polydisperse oblate cylinders. *J. Colloid Interf. Sci.* **2005,** 288 (2), 325-334.

[266] Rajagopal, K. and S.M.C. Silva, An experimental study of asphaltene particles sizes in n-heptane-toluene mixtures by light scattering. *Braz. J. Chem. Eng.* **2004,** 21 (4), 601-609.

[267] Fenistein, D., L. Barre, D. Broseta, D. Espinat, A. Livet, J.-N. Roux, and M. Scarsella, Viscosimetric and Neutron Scattering Study of Asphaltene Aggregates in Mixed Toluene/Heptane Solvents. *Langmuir* **1998,** 14 (5), 1013-1020.

[268] Espinat, D., D. Fenistein, L. Barre, D. Frot, and Y. Briolant, Effects of Temperature and Pressure on Asphaltenes Agglomeration in Toluene. A Light, X-ray, and Neutron Scattering Investigation. *Energy & Fuels* **2004,** 18 (5), 1243-1249.

[269] Bohren, C. and D. Huffman, *Absorption and Scattering of Light by Small Particles*. John Wiley & Sons: New York, NY, **1983**

[270] Owen, A., *Quantitative UV-Visible Analysis in the Presence of Scattering*. Report # 5963-3940E, Agilent Technologies Inc.: **1995**

[271] Ruiz-Morales, Y. and O.C. Mullins, Polycyclic Aromatic Hydrocarbons of Asphaltenes Analyzed by Molecular Orbital Calculations with Optical Spectroscopy. *Energy & Fuels* **2007,** 21 (1), 256-265.

[272] Ruiz-Morales, Y., X. Wu, and O.C. Mullins, Electronic Absorption Edge of Crude Oils and Asphaltenes Analyzed by Molecular Orbital Calculations with Optical Spectroscopy. *Energy & Fuels* **2007,** 21 (2), 944-952.

[273] Evdokimov, I.N., N.Y. Eliseev, and B.R. Akhmetov, Assembly of asphaltene molecular aggregates as studied by near-UV/visible spectroscopy. I. Structure of the absorbance spectrum. *J. Petrol. Sci. Eng.* **2003,** 37 (3-4), 135-143.

[274] Evdokimov, I.N., N.Y. Eliseev, and B.R. Akhmetov, Assembly of asphaltene molecular aggregates as studied by near-UV/visible spectroscopy. II. Concentration dependencies of absorptivities. *J. Petrol. Sci. Eng.* **2003,** 37 (3-4), 145-152.

[275] Evdokimov, I.N., N.Y. Eliseev, and B.R. Akhmetov, Asphaltene dispersions in dilute oil solutions. *Fuel* **2006,** 85 (10-11), 1465-1472.

[276] Evdokimov, I.N. and A.P. Losev, On the nature of UV/Vis absorption spectra of asphaltenes. *Petrol. Sci. Technol.* **2007,** 25 (1-2), 55-66.

[277] Smith, B.C., *Quantitative Spectroscopy: Theory and Practice*. Academic Press: Amsterdam, **2002**

[278] Hoffman, J.D., *Numerical Methods for Engineers and Scientists*. McGraw Hill, Inc.: New York, **1992**

Appendix A

External Mass Transfer in the Diffusion Cell

A.1 - Analytical Methods

Aqueous KCl concentrations were measured using a Dionex ICS-2000 Ion Chromatograph (S/N 04020113). The chromatograph was equipped with an AS18 column and a DS6 heated conductivity cell detector (cell constant = 135.14). The eluent used was a Dionex RFIC EluGen KOH cartridge at a flowrate of 1 mL/min. Analysis of the results was done using Dionex Chromeleon v6.50 SP4 Build 1000 software. A gradient elution method was employed with the following settings:

- Starting KOH concentration = 12.00 mM
- ramp from 12 - 44 mM (linear) for 5 minutes
- hold 44 mM for 3 minutes
- ramp from 44 – 52 mM (linear) for 2 minutes
- drop to 12 mM and hold for 3 minutes

The column and eluent are configured for anion analysis and therefore quantitation of KCl is done by measuring the concentration of Cl^- and inferring the concentration of KCl. Unfortunately, the linear range of this instrument and method for Cl^- analysis was found to only extend to 1000 ppmw and therefore most samples used in this work had to be diluted for analysis. SO_4^{2-} was used as an internal standard to improve the accuracy of the analysis[A1]. A certified standard solution (SPEX CertiPrep #AS-SO49-2Y, lot #1-84SO4-2, 1002.0 mg/L SO_4^{2-}) was used as the SO_4^{2-} internal standard.

The instrument and analysis method were calibrated using a certified chloride standard (SPEX CertiPrep #AS-Cl9-2X, lot #1-102Cl-2, 998.0±3 mg/L Cl^-). A series of solutions of $Cl^- + SO_4^{2-}$ solutions were prepared using the above two standards. 2 mL of SO_4^{2-} standard was added to a tared 25 mL class A volumetric flask and the weight recorded. A known amount of Cl^- standard was added to the flask and the weight recorded. The flask was topped to the mark with purified water (Millipore MilliQ Academic A10 system, Resistivity = 18.2 MΩ·cm) and the final weight and temperature recorded.

The solutions synthesized as per the above method were then analyzed using the Ion Chromatograph system as per the procedures listed at the end of this Appendix. Each solution was analyzed in triplicate spanning several different days to ensure that any instrumental variability is captured in the calibration. The order of solutions was randomized to avoid any systematic errors. The results of the injections are summarized in Table A-1 and Table A-2.

The injection results were then regressed to yield a linear calibration curve and the results are shown in Table A-3, Figure A-1, and Figure A-2. Table A-3 includes a full ANOVA analysis, and these results indicate a very good fit. Figure A-1 also includes a 95% prediction interval for the regression curve, which is calculated using the following formula[A2]:

$$\hat{Y}_P \pm t_{\alpha/2}s\sqrt{1+\frac{1}{n}+\frac{\left(X_P-\overline{X}\right)^2}{\sum\left(X_i-\overline{X}\right)^2}} \quad\text{................................} \quad \{A.1\}$$

where $t_{\alpha/2} = t_{0.025}$ with n-1 degrees of freedom = 2.160
        $\hat{Y}_P$ = predicted response
        X_P = value of X where Y is predicted
        $s = \sqrt{s^2}$ = standard error

Table A-1: Ion chromatograph data for Expt #040 Cl^- calibration solutions

Inj. #	Sol'n	Cl^- Concentration (ppmw)	SO_4^{2-} Concentration (ppmw)	Cl^- Peak Ret. Time (min)	Cl^- Peak Area (µS·min)	SO_4^{2-} Peak Ret. Time (min)	SO_4^{2-} Peak Area (µS·min)	x_{Cl^-}/x_{SO4^-}	PA_{Cl^-}/PA_{SO4^-}
1	Pure Water								
1	5	400.09 ±0.65	80.70 ±0.22	4.693	125.5875	6.487	18.9572	4.9579	6.6248
2	5	400.09 ±0.65	80.70 ±0.22	4.703	126.1339	6.500	19.0533	4.9579	6.6201
3	5	400.09 ±0.65	80.70 ±0.22	4.707	126.2302	6.503	19.0589	4.9579	6.6232
4	6	200.66 ±0.33	80.80 ±0.16	4.687	63.4296	6.503	19.0658	2.4835	3.3269
5	6	200.66 ±0.33	80.80 ±0.16	4.690	63.6034	6.507	19.1352	2.4835	3.3239
6	6	200.66 ±0.33	80.80 ±0.16	4.693	63.7948	6.510	19.1528	2.4835	3.3308
7	2	803.93 ±1.3	80.55 ±0.36	4.740	250.3705	6.513	18.7155	9.9803	13.3777
8	2	803.93 ±1.3	80.55 ±0.36	4.743	250.9956	6.517	18.7773	9.9803	13.3670
9	2	803.93 ±1.3	80.55 ±0.36	4.737	251.3810	6.510	18.7968	9.9803	13.3736
10	3	705.31 ±1.2	80.53 ±0.33	4.730	220.4098	6.503	18.7550	8.7582	11.7521
11	3	705.31 ±1.2	80.53 ±0.33	4.730	220.7772	6.510	18.8208	8.7582	11.7305
12	3	705.31 ±1.2	80.53 ±0.33	4.733	220.9914	6.517	18.8252	8.7582	11.7391
13	1	905.19 ±1.5	80.50 ±0.40	4.750	280.1309	6.520	18.5655	11.2446	15.0888
14	1	905.19 ±1.5	80.50 ±0.40	4.747	282.0907	6.513	18.7298	11.2446	15.0611
15	1	905.19 ±1.5	80.50 ±0.40	4.747	282.3629	6.510	18.7309	11.2446	15.0747
16	4	599.58 ±0.98	80.45 ±0.29	4.723	187.7182	6.513	18.9489	7.4525	9.9065
17	4	599.58 ±0.98	80.45 ±0.29	4.730	188.4000	6.520	19.0250	7.4525	9.9028
18	4	599.58 ±0.98	80.45 ±0.29	4.727	188.5112	6.517	19.0360	7.4525	9.9029

Table A-2: Ion chromatograph data for Expt #069 Cl⁻ calibration solutions

Inj. #	Sol'n	Cl^- Concentration (ppmw)	SO_4^{2-} Concentration (ppmw)	Cl^- Peak Ret. Time (min)	Peak Area (µS·min)	SO_4^{2-} Peak Ret. Time (min)	Peak Area (µS·min)	$x_{Cl^-}/x_{SO4^=}$	$PA_{Cl^-}/PA_{SO4^=}$
March 4, 2008									
1	Pure Water			4.520	0.0352	6.8230	0.013		
2	7	279.85 ±0.46	79.86 ±0.13	4.547	83.9809	6.250	18.1599	3.5043	4.6245
3	1	880.04 ±1.45	80.59 ±0.13	4.603	266.1670	6.260	17.9744	10.9206	14.8081
4	2	803.42 ±1.3	80.07 ±0.13	4.597	243.2477	6.253	17.8572	10.0341	13.6218
5	4	600.21 ±1.0	80.23 ±0.13	4.587	179.8311	6.267	18.1242	7.4810	9.9222
6	3	681.51 ±1.1	80.63 ±0.13	4.593	205.6597	6.267	18.3680	8.4527	11.1966
7	8	199.15 ±0.3	79.97 ±0.13	4.547	59.4033	6.257	17.8901	2.4902	3.3205
8	5	480.23 ±0.8	80.44 ±0.13	4.580	142.5544	6.277	18.1365	5.9700	7.8601
9	6	399.24 ±0.66	80.32 ±0.13	4.570	119.7060	6.263	18.2046	4.9706	6.5756
March 5, 2008									
1	Pure Water			4.530	0.3173	6.3330	0.006		
2	3	681.51 ±1.12	80.63 ±0.13	4.590	205.4900	6.263	18.3545	8.4527	11.1956
3	7	279.85 ±0.46	79.86 ±0.13	4.557	84.6723	6.267	18.3169	3.5043	4.6226
4	4	600.21 ±1.0	80.23 ±0.13	4.590	185.9116	6.270	18.7907	7.4810	9.8938
5	6	399.24 ±0.7	80.32 ±0.13	4.577	122.9419	6.277	18.6995	4.9706	6.5746
6	1	880.04 ±1.4	80.59 ±0.13	4.613	269.5508	6.273	18.2226	10.9206	14.7921
7	2	803.42 ±1.3	80.07 ±0.13	4.613	251.5302	6.273	18.4753	10.0341	13.6144
8	8	199.15 ±0.3	79.97 ±0.13	4.563	61.7935	6.280	18.6501	2.4902	3.3133
9	5	480.23 ±0.79	80.44 ±0.13	4.590	148.0174	6.280	18.8300	5.9700	7.8607
March 6, 2008									
1	Pure Water			4.523	0.3894	6.3200	0.434		
2	1	880.04 ±1.45	80.59 ±0.13	4.603	273.0759	6.250	18.4690	10.9206	14.7856
3	5	480.23 ±0.79	80.44 ±0.13	4.577	145.9475	6.257	18.5452	5.9700	7.8698
4	8	199.15 ±0.3	79.97 ±0.13	4.550	61.5045	6.270	18.5726	2.4902	3.3116
5	2	803.42 ±1.3	80.07 ±0.13	4.607	248.5066	6.270	18.2693	10.0341	13.6024
6	3	681.51 ±1.1	80.63 ±0.13	4.607	209.3403	6.280	18.6936	8.4527	11.1985
7	7	279.85 ±0.5	79.86 ±0.13	4.560	85.8880	6.263	18.5811	3.5043	4.6223
8	6	399.24 ±0.7	80.32 ±0.13	4.570	122.1650	6.277	18.6160	4.9706	6.5624
9	4	600.21 ±0.99	80.23 ±0.13	4.590	183.9122	6.277	18.5882	7.4810	9.8940

Table A-3: Regression calculations for Cl^- calibration

	$x_{Cl^-}/x_{SO_4^{2-}}$ X	X^2	$(X-X_{mean})^2$	$\frac{PA_{Cl^-}}{PA_{SO_4^{2-}}}$ Y	Y^2	$X*Y$	$\hat{Y}$	$\hat{Y}^2$	Residual $Y-\hat{Y}$	%	$(Y-\hat{Y})^2$	$(Y-Y_{mean})^2$	$(\hat{Y}-Y_{mean})^2$
	11.24	126.4	17.59	15.09	227.7	169.7	15.10	228.0	-0.012	-0.08%	0.0001	32.10	32.24
	11.24	126.4	17.59	15.06	226.8	169.4	15.10	228.0	-0.040	-0.27%	0.0016	31.79	32.24
	11.24	126.4	17.59	15.07	227.2	169.5	15.10	228.0	-0.026	-0.17%	0.0007	31.94	32.24
	9.98	99.61	8.586	13.38	179.0	133.5	13.39	179.3	-0.012	-0.09%	0.0001	15.64	15.73
	9.98	99.61	8.586	13.37	178.7	133.4	13.39	179.3	-0.023	-0.17%	0.0005	15.55	15.73
	9.98	99.61	8.586	13.37	178.9	133.5	13.39	179.3	-0.016	-0.12%	0.0003	15.61	15.73
Expt #040 Data	8.76	76.71	2.918	11.75	138.1	102.9	11.74	137.7	0.017	0.14%	0.0003	5.424	5.347
	8.76	76.71	2.918	11.73	137.6	102.7	11.74	137.7	-0.005	-0.04%	0.0000	5.324	5.347
	8.76	76.71	2.918	11.74	137.8	102.8	11.74	137.7	0.004	0.03%	0.0000	5.364	5.347
	7.45	55.54	0.162	9.91	98.14	73.83	9.968	99.36	-0.061	-0.62%	0.0038	0.234	0.297
	7.45	55.54	0.162	9.90	98.06	73.80	9.968	99.36	-0.065	-0.66%	0.0042	0.230	0.297
	7.45	55.54	0.162	9.90	98.07	73.80	9.968	99.36	-0.065	-0.66%	0.0042	0.230	0.297
	4.96	24.58	4.377	6.62	43.89	32.84	6.591	43.44	0.034	0.51%	0.0011	7.83	8.02
	4.96	24.58	4.377	6.62	43.83	32.82	6.591	43.44	0.029	0.44%	0.0008	7.86	8.02
	4.96	24.58	4.377	6.62	43.87	32.84	6.591	43.44	0.032	0.48%	0.0010	7.84	8.02
	2.48	6.17	20.85	3.33	11.07	8.262	3.242	10.51	0.085	2.56%	0.0073	37.16	38.21
	2.48	6.17	20.85	3.32	11.05	8.255	3.242	10.51	0.082	2.48%	0.0068	37.20	38.21
	2.48	6.17	20.85	3.33	11.09	8.272	3.242	10.51	0.089	2.68%	0.0080	37.12	38.21
	10.92	119.3	14.98	14.81	219.3	161.7	14.66	215.0	0.146	0.98%	0.0212	29.00	27.45
	10.92	119.3	14.98	14.79	218.8	161.5	14.66	215.0	0.130	0.88%	0.0168	28.83	27.45
	10.92	119.3	14.98	14.79	218.6	161.5	14.66	215.0	0.123	0.83%	0.0152	28.76	27.45
	10.03	100.7	8.904	13.62	185.6	136.7	13.46	181.2	0.159	1.17%	0.0254	17.63	16.32
	10.03	100.7	8.904	13.61	185.4	136.6	13.46	181.2	0.152	1.12%	0.0231	17.57	16.32
	10.03	100.7	8.904	13.60	185.0	136.5	13.46	181.2	0.140	1.03%	0.0196	17.47	16.32
	8.453	71.45	1.967	11.20	125.4	94.64	11.32	128.2	-0.125	-1.12%	0.0157	3.145	3.605
	8.453	71.45	1.967	11.20	125.3	94.63	11.32	128.2	-0.126	-1.13%	0.0159	3.142	3.605
	8.453	71.45	1.967	11.20	125.4	94.66	11.32	128.2	-0.123	-1.10%	0.0152	3.152	3.605
Expt #069 Data	7.481	55.97	0.186	9.922	98.45	74.23	10.01	100.1	-0.084	-0.85%	0.0071	0.249	0.340
	7.481	55.97	0.186	9.894	97.89	74.02	10.01	100.1	-0.113	-1.14%	0.0127	0.222	0.340
	7.481	55.97	0.186	9.894	97.89	74.02	10.01	100.1	-0.112	-1.14%	0.0126	0.222	0.340
	5.970	35.64	1.166	7.860	61.78	46.92	7.961	63.38	-0.101	-1.29%	0.0102	2.443	2.137
	5.970	35.64	1.166	7.861	61.79	46.93	7.961	63.38	-0.100	-1.28%	0.0101	2.441	2.137
	5.970	35.64	1.166	7.870	61.93	46.98	7.961	63.38	-0.091	-1.16%	0.0083	2.413	2.137
	4.971	24.71	4.324	6.576	43.24	32.68	6.608	43.67	-0.033	-0.50%	0.0011	8.108	7.923
	4.971	24.71	4.324	6.575	43.23	32.68	6.608	43.67	-0.034	-0.51%	0.0011	8.114	7.923
	4.971	24.71	4.324	6.562	43.06	32.62	6.608	43.67	-0.046	-0.70%	0.0021	8.184	7.923
	3.504	12.28	12.57	4.625	21.39	16.21	4.623	21.38	0.001	0.02%	0.0000	23.03	23.04
	3.504	12.28	12.57	4.623	21.37	16.20	4.623	21.38	-0.001	-0.02%	0.0000	23.04	23.04
	3.504	12.28	12.57	4.622	21.37	16.20	4.623	21.38	-0.001	-0.02%	0.0000	23.05	23.04
	2.490	6.201	20.79	3.320	11.03	8.269	3.251	10.57	0.070	2.10%	0.0049	37.24	38.10
	2.490	6.201	20.79	3.313	10.98	8.251	3.251	10.57	0.063	1.89%	0.0039	37.33	38.10
	2.490	6.201	20.79	3.312	10.97	8.246	3.251	10.57	0.061	1.84%	0.0037	37.35	38.10
$\Sigma =$	296.1	2446	358.2	395.8	4386	3275	395.8	4386	0.0000		0.2868	656.6	656.3
Mean =	7.050	58.23	8.527	9.423	104.4	77.98	9.423	104.4	0.00000		0.0068	15.63	15.63

SLOPE = 1.3536519
INTERCEPT = -0.12019802

R^2 = 0.9995632
s^2 = 0.0071703
$t_{0.025}$ = 2.020

ANOVA					
Source	Sum of Squares	DF	Mean Square	F	P
Model	656.2730000	1	656.2730000	91,526	8.031E-69
Residual	0.2868123	40	0.0071703		
Total	656.5598123	41			
	0.0000000				

Slope Error Estimate
u_{Slope} = 0.0090362

Intercept Error Estimate
$u_{Intercept}$ = 0.068954

Prediction Uncertainty Estimates
$u_X = -3.335 \times 10^{-8} Y^4 + 1.257 \times 10^{-6} Y^3 + 7.691 \times 10^{-5} Y^2 - 1.673 \times 10^{-3} Y + 0.1366$
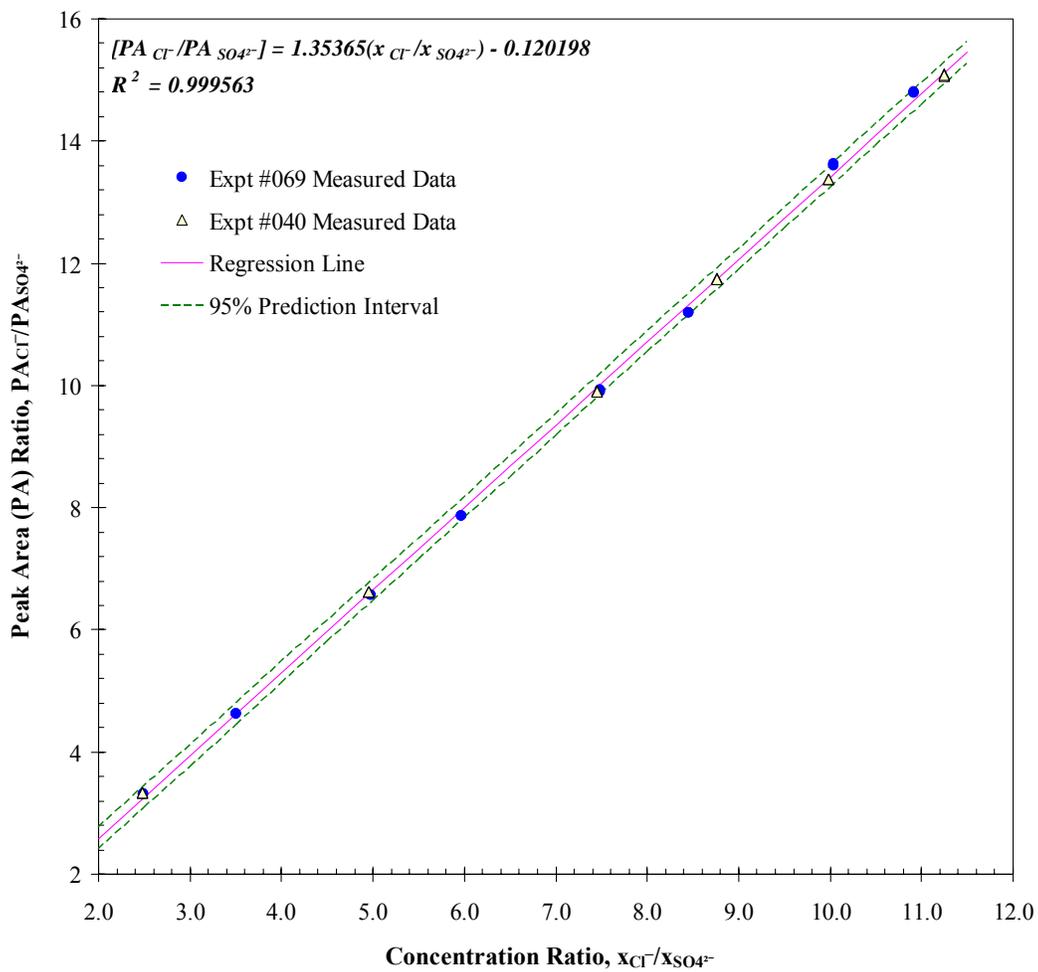
Figure A-1: Ion chromatography calibration curve for Cl⁻ in water
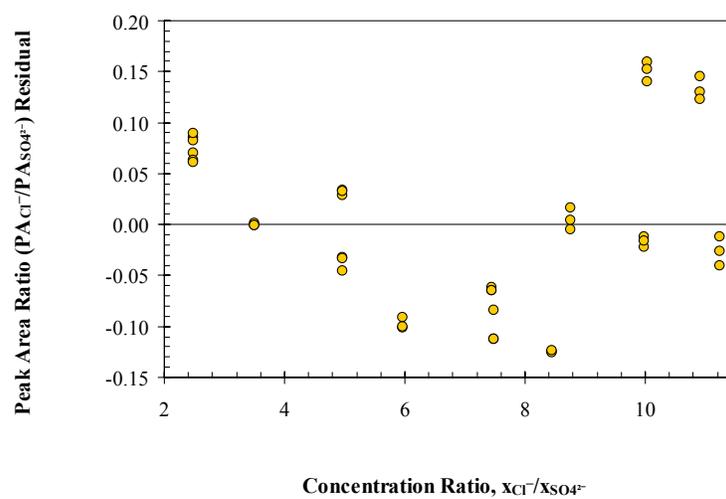
Figure A-2: Residuals for the calibration curve of Cl⁻ in water

A.1.1 - ION CHROMATOGRAPH DETAILED OPERATING PROCEDURES

A.1.1.1 Startup Procedure:

1. Open "Chromeleon" (Software)
2. Go to the "Panels" folder and open (i.e. double-click) the "ICS-2000_Traditional_System_AS40.pan" panel
3. Prime the pump:
   a. Press "Prime" button in Chromeleon
   b. Open front cover on instrument. Open the prime valve (knob with "P" on it)
   c. Press "OK" in Chromeleon
   d. let prime go for ~ 10-20 seconds then press "Off" button (above "Prime" button) in Chromeleon
   e. press the "Off" button (above "Prime" button) in Chromeleon and close the prime valve
   f. Close the prime valve
4. Press "Startup" button
5. Begin data acquisition by:
   a. pressing the button in toolbar (blue circle)
   b. OR go to the "Control" menu and select "Acquisition On"
   c. OR press "Ctrl A"
6. let the system equilibrate until signal is flat (usually approximately 35-60 minutes)

A.1.1.2 Sequence Operation/Run Procedure:

1. In the Chromeleon Data Browser (i.e. folder view), go to the "Sequences" folder
2. Go to the desired folder (e.g. "Greg Dechaine" folder) and make a copy of the sequence which most closely matches the sequence of samples to be analyzed:
   a) Copy the template sequence to a different folder (use either Ctrl C then Ctrl V OR use the edit pull down menu)
   b) Rename the copied sequence to reflect the current experiment
   c) Move the renamed sequence to the correct folder (e.g. "Greg Dechaine" folder)
3. Within the newly created sequence, edit the samples to reflect the samples being currently analyzed:
   a) To add a sample, right click on the list of samples and select "Append Sample"
   b) To delete a sample, right click on the list of samples and select "Delete Sample"
   c) To rename a sample, click on the name and type in the desired name
   d) Change the "status" of each sample from "finished" to "single"
4. Save the sequence. (NOTE: In the save as dialog window, make sure to select "Save Raw Data" check box. Otherwise the raw data will not be recorded.)

5. Run the sequence:
   a) Go to the "Batch" menu and select "Start"
   b) From the list of available sequences, select the new sequence and press "Start"
6. Once the sequence is complete, press "Save" to save the sequence
7. Press the "Shutdown" button to shutdown the instrument and close Chromeleon

A.1.1.3 Sample Analysis Procedure:

1. Rinse the syringe twice with pure water.
2. Fill the syringe a third time with pure water and push the contents through the sample port & syringe filter on the IC instrument
3. Rinse the syringe with the sample being analyzed and discharge the contents into a waste container. Repeat.
4. Fill the syringe a third time with the solution being analyzed and push the contents through the sample port & syringe filter on the IC instrument
5. Fill the syringe with the solution and place it on the injection port.
6. When prompted by the software, inject the sample and press "OK"

A.2 - Calibration of Diffusion Cells with Aqueous KCl

The cell constant, β, defined in equation {4.7} of Chapter 4 is fixed for a given diaphragm/membrane. However, the surface area and length terms appearing in this equation are not the total surface area and length of the diaphragm itself but rather they are the open pore surface area and length of the pores in the diaphragm. Therefore, the ratio $(A/\ell)_{eff}$ will be a function of the diaphragm properties:

$$\left(\frac{A}{\ell}\right)_{eff} = \frac{A_{membrane} \cdot \varepsilon}{\ell \cdot \tau} \quad\text{...} \quad \{A.2\}$$

where ε = membrane porosity and τ = pore tortuosity. Since the tortuosity and porosity are average parameters at best, it is not generally possible to calculate $(A/\ell)_{eff}$ and as such the value of β is usually determined experimentally using a solute with know diffusivity.

The normal calibration standard for determining β is aqueous potassium chloride (KCl)[A3-5]. Accurate differential diffusion coefficients for this system are available covering a relatively wide range of concentrations making it an ideal calibrant. Woolf and Tilley[A6] have tabulated the data from 0-1M and generated an 8th order polynomial to the data as illustrated below in equation {A.3}.

$$D_{KCl}\left(x\,10^{-5}\,cm^2\,/\,s\right) = \sum_{i=0}^{8} A_i \left(\sqrt{C}\right)^i \quad \ldots\ldots\ldots\ldots\ldots\ldots \{A.3\}$$

where $A_0 = 1.9930$ $A_5 = -35.81551219$
           $A_1 = -1.002337601$ $A_6 = 26.75245668$
           $A_2 = 3.235153497$ $A_7 = -7.833317444$
           $A_3 = -9.780514174$ $A_8 = -1.989929326 \times 10^{-5}$
           $A_4 = 24.34187091$

This polynomial can then be used to determine the integral diffusion coefficient given the concentrations at the start and end of the experiment.

Upon further inspection of this polynomial, however, there appear to be some inconsistencies. The equation of Woolf and Tilley is compared with experimental data from the literature in Figure A-3. In the range up to 0.5M, the polynomial seems to do a good job of describing the available data. This is not surprising since this is within the range used to derive the expression. For the range between 0.5 – 1.0M, their equation seems to exhibit an irregular S-shape rather than a smooth curve. When the extended data of Gosting[A7] is considered beyond 1M, the polynomial of Woolf and Tilley quickly
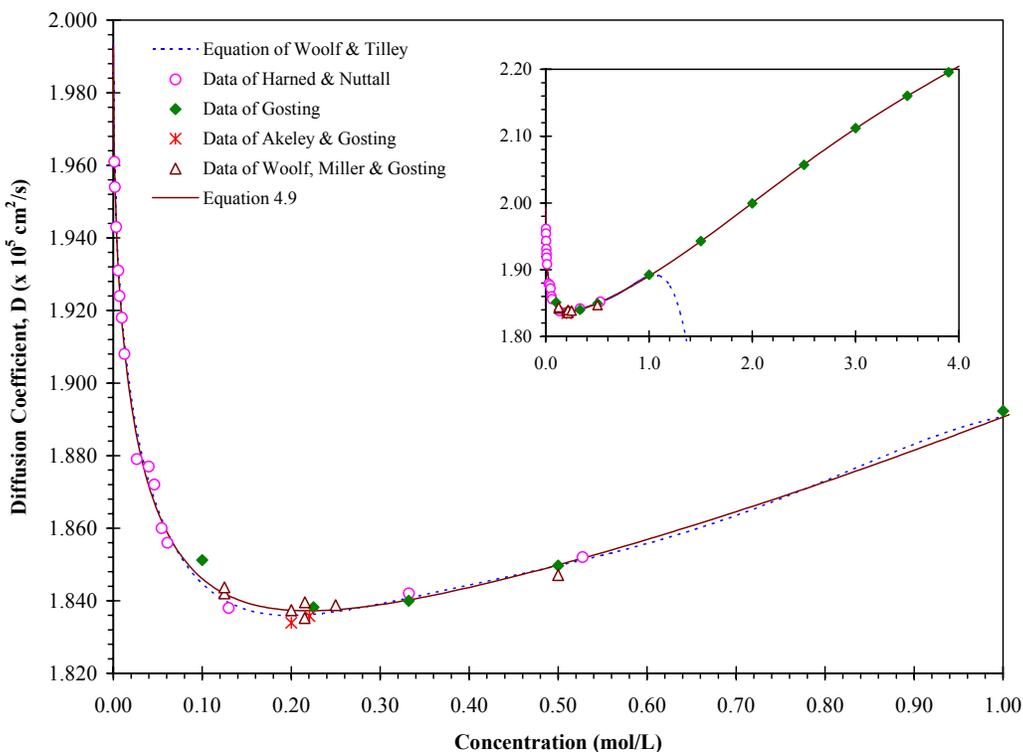
Figure A-3: Comparison of experimental data[A7-10] to the polynomial of Woolf and Tilley[A6] for the diffusivity of aqueous KCl.

breaks down.

If the polynomial coefficients of Woolf and Tilley[A6] are examined closely, it is evident that the last polynomial coefficient deviates significantly from the other parameters by 6 orders of magnitude (their 8th order parameter is of the order 10^{-5} while the other parameters are all of the order 10^{1}). This large discrepancy calls into question the validity of this parameter and the rest of the polynomial as well. The procedure used by Woolf and Tilley[A6] was not a direct regression of the available data. Rather, they first drew a smoothed curve through the data. They then read data points from this smoothed curve and regressed these data points to generate their polynomial. This procedure will undoubtedly incorporate an additional source of error since the actual data were not regressed directly.

The experimental data plotted in Figure A-3 can be regressed directly, including the high concentration data of Gosting[A7]. This was done using a 6th order polynomial rather than the 8th order polynomial used by Woolf and Tilley[A6]. Also, the intercept was set to 1.993×10^{-5} cm^2/s, which according to Woolf and Tilley represents the limiting infinite dilution diffusion coefficient. The results of this regression procedure are given by equation {A.4} and are shown in Figure A-3.

$$D_{KCl}\left(x\,10^{-5}\;cm^2\,/\,s\right) = \sum_{i=0}^{6} A_i \left(\sqrt{C}\right)^i \;\;\;\text{................................}\;\; \{A.4\}$$

where $A_0 = 1.9930$ $A_4 = 2.044280$ $A_3 = -2.910337$
$A_1 = -0.9785858$ $A_5 = -0.7195382$
$A_2 = 2.363147$ $A_6 = 0.09868115$

Based on the curve fits shown in Figure A-3, equation {A.4} provides a much better fit of the available data. It is valid up to 4M and does not display the anomalous S-shaped behaviour between $0.5 - 1M$ that is evident with the equation from Woolf and Tilley[A6].

Applying equation {A.4} to obtain the integral diffusion coefficient for calibrating diaphragm diffusion cells is done using the procedure outlined by Stokes[A11]. The resulting integral diffusion coefficient for an experiment with an initial KCl concentration of 0.5 M and operated for the optimum time outlined in the section 4.2.4 of Chapter 4 would be $\overline{D} = 1.840 \times 10^{-5}$ cm^2/s. This value can then be used in equation {4.7} of Chapter 4 to determine β for a given diaphragm/membrane.

A.3 - External Mass Transfer in the Diffusion Cell

Holmes *et al.*[A12] performed a detailed analysis of the mass transfer occurring in a horizontal stirred diaphragm diffusion cell. They correlated the mass transfer coefficient at the face of the diaphragm (a glass frit in their case) using an expression of the form:

$$Sh = \alpha \, Re^{\gamma} \, Sc^{\eta} \quad \text{...} \quad \{A.5\}$$

where Sh = dimensionless Sherwood number = $\dfrac{kd}{D} = \dfrac{d}{\delta}$

Re = dimensionless Reynolds number = $\dfrac{\omega d^2}{\nu}$

Sc = dimensionless Schmidt number = $\dfrac{\nu}{D}$

k = convective mass transfer coefficient (m/s)
d = length of the stirrer (m)
D = diffusion coefficient (m²/s)
ν = kinematic viscosity (m²/s)
ω = stirrer speed (rps)
δ = thickness of stagnant layer (m)

The values of α, γ, and η were determined experimentally for the specific geometry of their cell by varying the stirrer speed and fluid properties. The diffusion cell constant, β, is then related to the mass transfer coefficient, k, as follows[A12]:

$$\beta = \left(\frac{1}{V_R} + \frac{1}{V_P} \right) \frac{1}{2D/kA + (\ell/A)_{eff}} \quad \text{..............................} \quad \{A.6\}$$

Because the type of stirrer and the geometry of the cell used in this work are different than those used by Holmes *et al.*[A12], it is not possible to use their values for α, γ, and η (0.050, 0.79, and 0.38 respectively). These values must be obtained experimentally for the current cell.

According to hydrodynamic theory[A13], for a laminar boundary layer the mass transfer correlation takes the form:

$$Sh = 0.68 \, Re^{1/2} \, Sc^{1/3} \quad \text{...} \quad \{A.7\}$$

Equation {A.7} is obtained analytically for laminar flow over a flat plate. Geankoplis[A14] gives a similar equation with a value of 0.664 for α for laminar flow over a flat plate.

When the flow regime at the face of the membrane/disc is no longer laminar, the values of α, γ, and η cannot be determined analytically and therefore they must be

derived from experimental data. Several investigators have examined the mass transfer to a circular membrane/disc in a cylindrical cell with the stirrer oriented parallel to the membrane and with a diameter comparable to the diameter of the disc. Malone and Anderson[A15] performed one such study and obtained:

$$Sh = 1.14 \, Re^{0.58}$$ .... {A.8}

They used an exponent of 1/3 for the Schmidt number to obtain the above equation. Smith et al.[A16] and Colton and Smith[A17] performed a similar analysis and obtained:

$$Sh = 0.285 \, Re^{0.57} \, Sc^{1/3}$$ .... {A.9}

$$Sh = 0.0443 \, Re^{0.75} \, Sc^{1/3}$$ .... {A.10}

It should be noted that for equations {A.9} and {A.10}, the Reynolds number uses the diameter of the cell/membrane as the characteristic dimension rather than the stirrer diameter. Equation {A.10} is very similar to the equation obtained by Holmes et al.[A12] despite the drastically different geometry of the stirrer. This would imply that the cell and stirrer employed by Holmes et al. did result in turbulent mixing at the membrane face. In all of the cases noted above, it was demonstrated that assuming additivity of the resistances due to the membrane and the boundary layers was valid for this type of setup.

In most cases (except Holmes et al.[A12]), the exponent for the Schmidt number is fixed at 1/3. Figure A-4 and Figure A-5 show the effect of this exponent on the data of Holmes et al.[A12]. Changing the exponent for the Schmidt number results in a different exponent for the Reynolds number (0.722 vs. 0.78, 7.4% decline) and a different constant, α (0.122 vs. 0.05, an increase of 144%). The quality of the fit is only reduced slightly by constraining the exponent on the Schmidt number. Considering that the Schmidt number was only tested at 3 levels, it is a bit of a stretch to include this exponent as an adjustable parameter in the regression. Therefore, for the mass transfer correlation developed in this work, the exponent for the Schmidt number will be fixed at 1/3 as this value is firmly rooted in hydrodynamic theory.

Another anomaly in the mass transfer correlation of Holmes et al.[A12] was the relatively large exponent for the Reynolds number (0.78 or 0.722), which would imply turbulent mixing according to Smith et al.[A16]. Being that the stirrer is relatively small (2.5 cm stirrer compared to a membrane diameter of 5.0 cm) and not oriented parallel to the membrane, it would be anticipated that the flow pattern at the face of the membrane
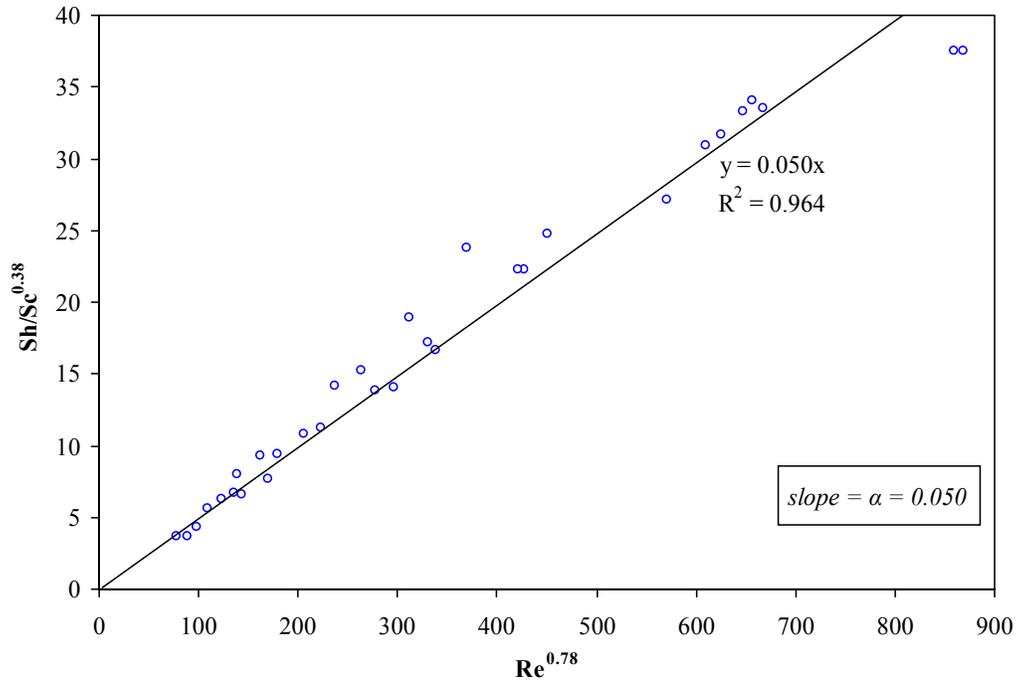
Figure A-4: Original Mass Transfer Correlation of Holmes *et al.*[A12]
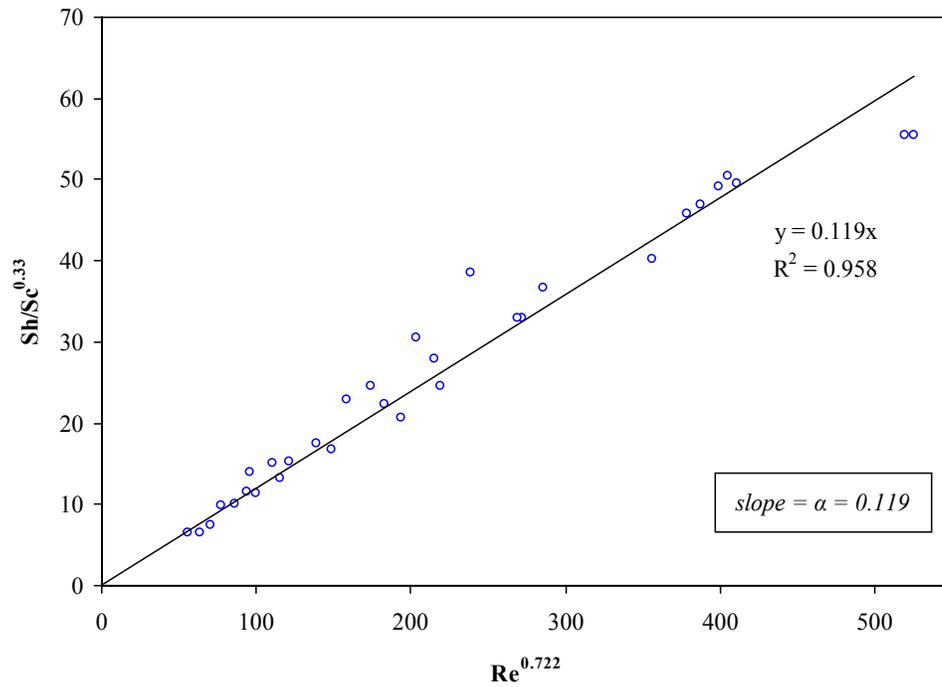
Figure A-5: Modified Mass Transfer Correlation (Schmidt number exponent fixed at 1/3) Using the Data of Holmes *et al.*[A12]
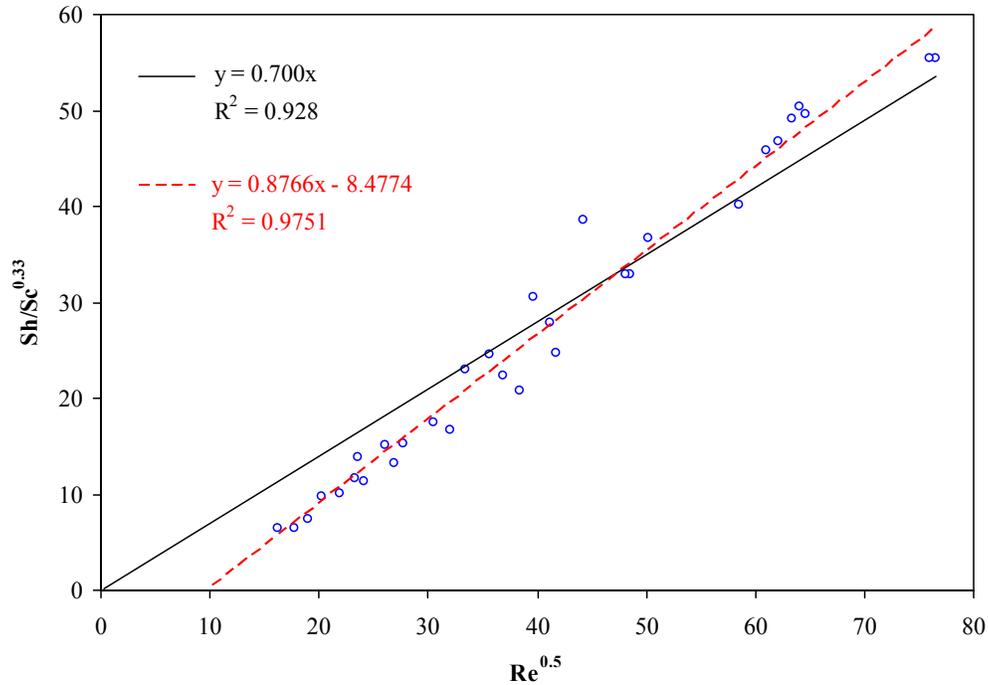
Figure A-6: Modified Mass Transfer Correlation (Schmidt number exponent fixed at 1/3, Reynolds number exponent fixed at 1/2) Using the Data of Holmes et al.[A12]

would be laminar and hence yield an exponent closer to 0.5 (as in equation {A.7}). Figure A-6 shows the effect of a Reynolds exponent of 0.5 on the data of Holmes *et al.*[A12]. It is evident that an exponent of 0.5 does not describe the data as well as the higher exponents. However, if the restriction of a 0 intercept is removed, then the data do follow a linear relationship. It is unclear what a negative intercept would imply relative to the mass transfer occurring at the membrane face, other than to say that the mass transfer coefficient is effectively 0 at a nonzero stirrer speed. Suffice it to say that the exponent for the Reynolds number should be between 0.5 (laminar) and 0.72 (turbulent for this geometry).

If equation {A.5} is expanded in terms of the underlying variables:

$$\frac{kd}{D} = \alpha \left(\frac{\omega d^2}{\nu} \right)^{\gamma} \left(\frac{\nu}{D} \right)^{\eta}$$

$$k = \alpha \, \omega^{\gamma} \, d^{2\gamma - 1} \, \nu^{\eta - \gamma} \, D^{1 - \eta} \quad \text{....................................} \quad \{A.11\}$$

Substituting equation {A.11} into equation {A.6} and assuming $V_1 = V_2 = V$:

185

$$\beta = \frac{2}{V} \left[\frac{1}{\frac{2D}{\left(\alpha\, \omega^{\gamma}\, d^{2\gamma-1}\, \nu^{\eta-\gamma}\, D^{1-\eta} \right)A} + \left(\frac{\ell}{A} \right)_{eff}} \right]$$

$$\therefore\ \frac{2}{\beta V} = \left(\frac{2d^{1-2\gamma}\nu^{\gamma-\eta}D^{\eta}}{\alpha A} \right)\omega^{-\gamma} + \left(\frac{\ell}{A} \right)_{eff} \quad \text{........................ \{A.12\}}$$

Therefore, according to equation {A.12} a plot of $2/\beta V$ vs. $\omega^{-\gamma}$ should be linear with an intercept of $(\ell/A)_{eff}$.

A series of diffusion runs using aqueous potassium chloride as the solute were carried out using a single 5 μm Durapore® membrane (see Chapter 4 for details). The retentate side of the cell was loaded with 55 mL of 0.5 M KCl solution. Each experiment was allowed to run for the approximate optimum length of time (see Chapter 4) after which the cell was emptied using a custom made vacuum apparatus. This vacuum apparatus consisted of 2 parallel 500 mL vacuum flasks connected to the building vacuum system. Each vacuum flask was fitted with a rubber stopper through which a Teflon tube was passed. One end of the tube projected into the vacuum flask past the vacuum port to avoid carryover of liquid, while the other end was equipped with a 6" pipet tip syringe needle. This setup allowed for the simultaneous emptying of both compartments using the vacuum, thus avoiding cross contamination of solutions at the end of the experiment.

The two solutions were then analyzed using ion chromatography. The solutions were diluted such that the concentrations were within the linear calibration range of the instrument (see section A.1). The dilution ratio was quantified gravimetrically and the diluted samples analyzed in triplicate. The speed of the stirrer was varied between 300-650 rpm in 50 rpm increments, and the calibration constant obtained at each speed. Speeds in excess of 650 rpm were not explored since beyond this speed the stirrer became highly unstable, while speeds below 300 rpm were not explored since there are no intentions of running at such low speeds. The raw data are summarized below in Table A-4. The means of the points at each speed are summarized in Table A-5.

The data in Table A-5 was plotted in Figure A-7 as a function of the stirrer speed raised to the two different exponents as discussed previously. Both exponents ($\gamma = 0.5$ and 0.72) provide a reasonable fit to the data for speeds of 550 rpm and below. In each case, the intercept represents $(\ell/A)_{eff}$ for the membrane used, although the two values

Table A-4: Summary of mass transfer data for the glass cell using aqueous KCl diffusion

Expt #	t (min)	ω (rpm)	V_{avg} (mL)	C_0	$C_{H,t}$	$C_{L,t}$	$\ln(\Delta C_0/\Delta C_t)$	β (cm^{-2})	$Y = 2/\beta V_{avg}$ (cm^{-1})
109	230	300	59.69	0.5027	0.3283	0.1777	1.206	4.748±0.044	0.007056±0.000065
105	220	350	59.75	0.5029	0.3289	0.1790	1.210	4.982±0.035	0.006718±0.000065
112	220	350	59.82	0.5028	0.3299	0.1756	1.181	4.863±0.028	0.006875±0.000065
103	210	400	59.84	0.5032	0.3288	0.1786	1.209	5.214±0.029	0.006410±0.000065
108	210	400	59.84	0.5038	0.3296	0.1760	1.188	5.123±0.036	0.006524±0.000065
102	200	450	59.87	0.5050	0.3267	0.1796	1.233	5.584±0.026	0.005983±0.000065
111	200	450	59.85	0.5036	0.3291	0.1748	1.183	5.356±0.057	0.006239±0.000065
101	185	500	59.82	0.5049	0.3312	0.1755	1.176	5.759±0.035	0.005806±0.000065
110	190	500	59.72	0.5035	0.3320	0.1738	1.158	5.520±0.037	0.006067±0.000065
100	175	550	59.80	0.5062	0.3345	0.1728	1.141	5.906±0.061	0.005663±0.000065
107	180	550	59.79	0.5037	0.3298	0.1746	1.178	5.926±0.053	0.005645±0.000065
98	165	600	59.63	0.5043	0.3336	0.1721	1.139	6.250±0.095	0.005366±0.000065
99	165	600	59.74	0.5040	0.3305	0.1753	1.178	6.466±0.075	0.005178±0.000065
106	175	600	59.79	0.5038	0.3295	0.1782	1.203	6.227±0.089	0.005372±0.000065
113	175	600	59.87	0.5031	0.3222	0.1775	1.247	6.453±0.071	0.005177±0.000065
104	165	650	59.87	0.5034	0.3248	0.1821	1.261	6.923±0.036	0.004826±0.000065

Table A-5: Mean calibration constant at each speed

Speed, ω (rpm)	(rps)	$1/\omega^n$ (s^n) (n = 1)	(n = 0.72)	(n = 0.5)	$\beta \pm s$[†] (cm^{-2})		$Y = 2/\beta V_{avg}$ (cm^{-1})
300	5.00	0.200	0.314	0.447	4.748		0.00706
350	5.83	0.171	0.281	0.414	4.923± 0.084	(±1.7%)	0.00680
400	6.67	0.150	0.255	0.387	5.169± 0.064	(±1.2%)	0.00647
450	7.50	0.133	0.234	0.365	5.470± 0.161	(±3.0%)	0.00611
500	8.33	0.120	0.217	0.346	5.640± 0.169	(±3.0%)	0.00594
550	9.17	0.109	0.203	0.330	5.916± 0.014	(±0.2%)	0.00565
600	10.00	0.100	0.191	0.316	6.349± 0.128	(±2.0%)	0.00527
650	10.83	0.092	0.180	0.304	6.923		0.00483

† s = the standard deviation of the replicate data
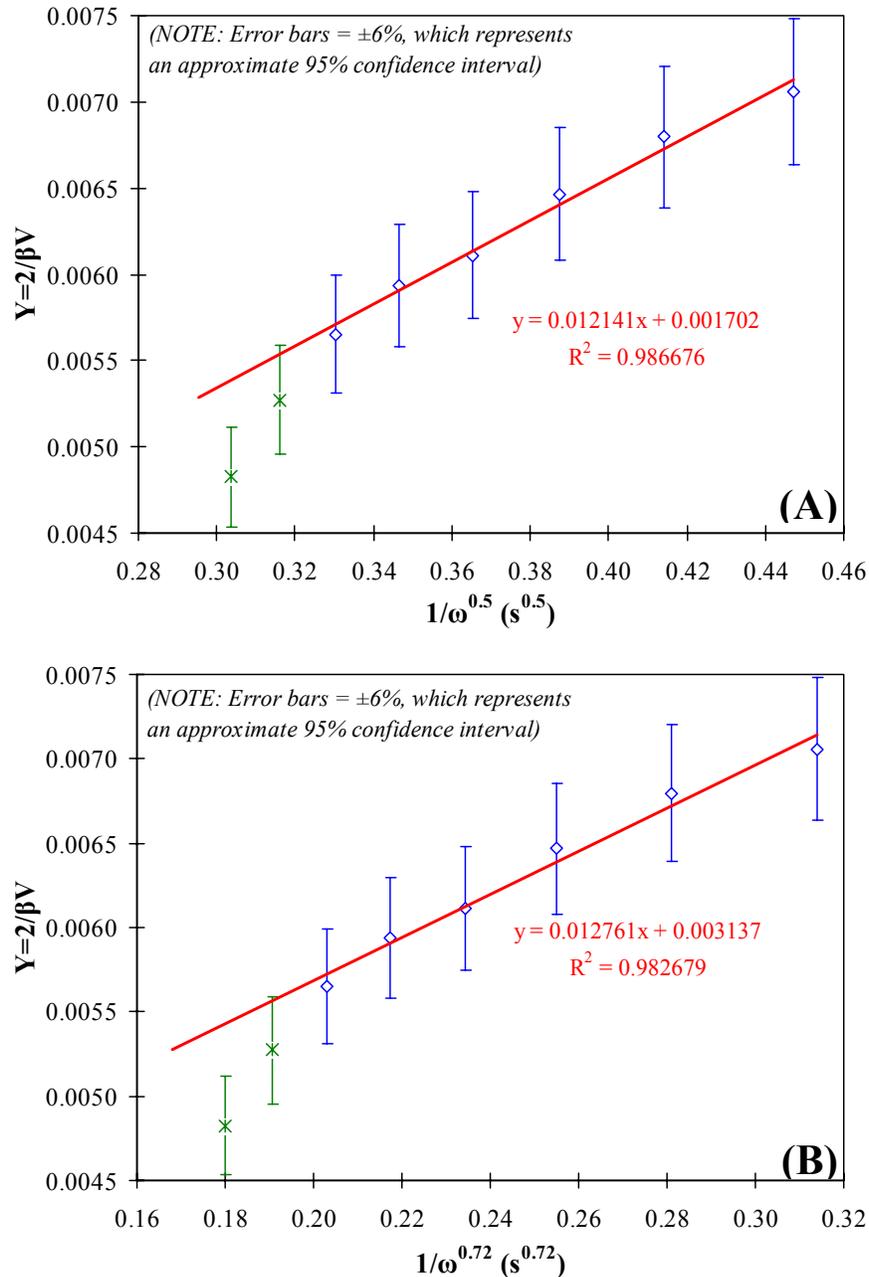
Figure A-7: Plots of equation {A.12} with various Reynolds number exponents: (A) $\gamma = 0.5$, (B) $\gamma = 0.72$

differ significantly from each other. Using an exposed area of 35 mm ($A = 9.621$ cm^2), a membrane thickness of 125 μm, and a porosity of 75% along with equation {4-10} of Chapter 4, the tortuosity, τ, of the membrane is 0.98 (~1) and 1.81 for $\gamma = 0.5$ and 0.72, respectively. A tortuosity of unity is not physically realistic for membranes of this type and therefore the results obtained with $\gamma = 0.72$ would appear to be more realistic.

In order to convert the regression slope from Figure A-7 to a value for α, some properties of aqueous KCl solutions are required. As previously discussed, the integral diffusivity for these conditions is $\overline{D}$ = 1.840 x 10^{-5} cm^2/s. The density of aqueous KCl solutions is calculated using the electrolyte equation of state of Krumgalz et al.[A18] while the dynamic viscosity is calculated using the correlation of Laliberté[A19]. These correlations predict a kinematic viscosity of ν = 0.008806 cm^2/s at the overall average concentration of 0.25 M. The kinematic viscosity only varies by ±2.7% over the range 0-0.5 M and therefore using the overall average does not result in a significant error. Finally, the stirrer is a ¾" starburst stirrer (cross style) and therefore d = 1.905 cm. Using these values along with the slopes in Figure A-7 and equation {A.12} gives values α = 0.205 and 0.0520 for γ = 0.5 and 0.72, respectively.

As expected, varying the value of γ also leads to significantly different values for α. Using the values for γ and α, the data in Table A-5 can now be transformed into dimensionless form as per equations {A.5} and {A.6}. First of all, values for the mass transfer coefficient, k, are calculated from a rearranged form of equation {A.6}:

$$ k = \frac{2D}{A\left[\dfrac{2}{\beta V_{avg}} - \left(\dfrac{\ell}{A}\right)_{eff}\right]} \quad\text{...................................... \{A.13\}} $$

Once the mass transfer coefficient has been determined for each case, the dimensionless Sherwood (Sh), Reynolds (Re), and Schmidt (Sc) numbers are calculated and the data plotted in dimensionless form. These calculations were performed on the data in Table A-5 and the results are summarized in Table A-6 and Figure A-8. Both correlations are capable of adequately describing the low speed data, but both break down for speeds of 600 rpm and above. As described previously, the tortuosity predicted by the correlation using γ = 0.5 seems too low. As well, the correlation with γ = 0.5 predicts that the boundary layer resistances represent a much greater proportion of the total diffusional resistance.

Unfortunately, neither correlation describes the results at speeds of 600 rpm and above. This effect is made worse by the fact that the primary solvent being used in the diffusion cell is toluene. The kinematic viscosity of toluene at 25°C is 6.43 x 10^{-3} cm^2/s[A20, 21]. The maximum Reynolds number allowed by both correlations is 3780, which for toluene corresponds to a stirrer speed of 400 rpm. Therefore, it would not be

possible to use the correlations developed herein to determine the external mass transfer at speeds above 400 rpm in toluene. It is undesirable to only run the cell at 400 rpm instead of 600 rpm since the boundary layer resistance is not minimized.

Also, it should be noted that the failure of the dimensionless correlations to describe the data at 600 and 650 rpm is puzzling, particularly for the turbulent models (i.e. $\gamma = 0.72$). If the flow regime is indeed turbulent at stirrer speeds of 300-550 rpm, then there should not be a step change in the data at higher speeds. The observed step change is indicative of a change in flow regime (e.g. laminar to turbulent), or perhaps indicative of other external forces (e.g. vibration) leading to anomalous behaviour. In either case, the correlations are not suitable for use in any quantitative manner for diffusion measurements.

Table A-6: Dimensionless mass transfer data (Sc = 479)

| Speed, ω | | Re | Re^γ | k_{exptl} (cm/s) | Sh | | $Sh/Sc^{1/3}$ | | $\delta = D/k^\dagger$ (μm) | $R_\delta^\ddagger$ (cm^{-1}) | R_δ/R_T^* (%) |
(rpm)	(rps)				Exptl	Model	Exptl	Model			
$\gamma = 0.72$, $\alpha = 0.05196$, $(l/A)_{eff} = 0.003137$											
300	5.00	2061	243	0.000976	101	98.9	12.9	12.6	189	0.003919	55.5%
350	5.83	2404	272	0.001045	108	110	13.8	14.1	176	0.003659	53.8%
400	6.67	2747	299	0.001149	119	122	15.2	15.5	160	0.003330	51.5%
450	7.50	3091	326	0.001286	133	132	17.0	16.9	143	0.002974	48.7%
500	8.33	3434	351	0.001366	141	143	18.1	18.3	135	0.002799	47.2%
550	9.17	3778	376	0.001520	157	153	20.1	19.6	121	0.002517	44.5%
600	10.00	4121	401	0.001791	185	163	23.7	20.8	103	0.002136	40.5%
650	10.83	4465	424	0.002265	235	173	30.0	22.1	81	0.001689	35.0%
$\gamma = 0.5$, $\alpha = 0.2054$, $(l/A)_{eff} = 0.001702$											
300	5.00	2061	45.4	0.000714	74.0	72.9	9.5	9.3	258	0.005354	75.9%
350	5.83	2404	49.0	0.000751	77.7	78.8	9.9	10.1	245	0.005094	75.0%
400	6.67	2747	52.4	0.000803	83.1	84.2	10.6	10.8	229	0.004765	73.7%
450	7.50	3091	55.6	0.000868	89.8	89.3	11.5	11.4	212	0.004409	72.1%
500	8.33	3434	58.6	0.000903	93.5	94.2	12.0	12.0	204	0.004234	71.3%
550	9.17	3778	61.5	0.000968	100	98.7	12.8	12.6	190	0.003952	69.9%
600	10.00	4121	64.2	0.001071	111	103	14.2	13.2	172	0.003571	67.7%
650	10.83	4465	66.8	0.001224	127	107	16.2	13.7	150	0.003124	64.7%

NOTES:
† δ = the approximate thickness of the boundary layer
‡ R_δ = the resistance due to the 2 boundary layers
* R_T = the total resistance = $2D/kA + (l/A)_{eff}$

A) $\gamma = 0.72$

$$\frac{Sh}{Sc^{1/3}} = 0.0520\,Re^{0.72}$$

B) $\gamma = 0.5$

$$\frac{Sh}{Sc^{1/3}} = 0.205\,Re^{0.5}$$
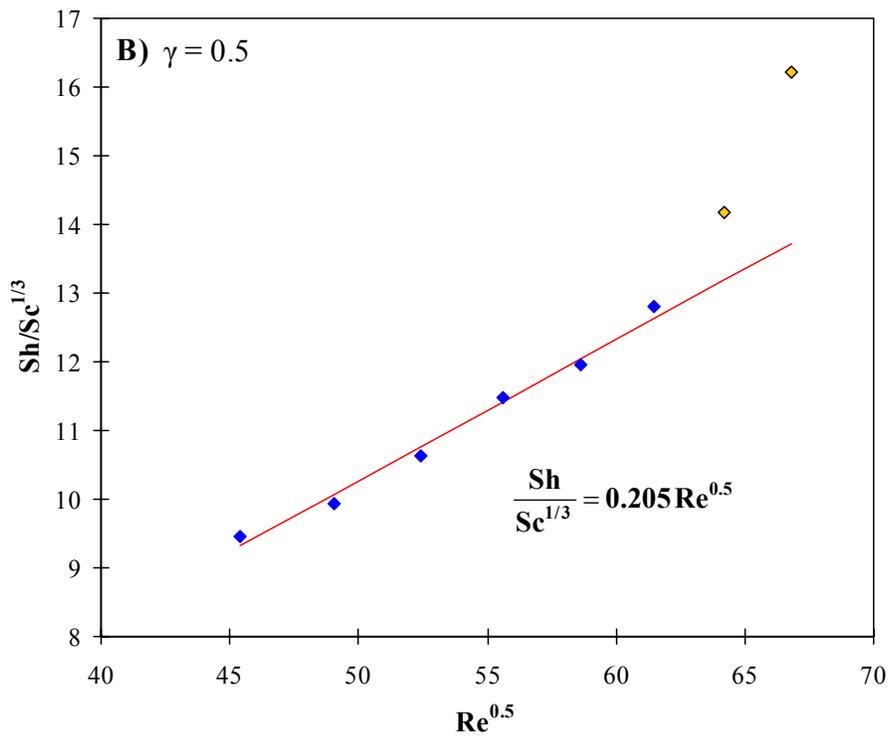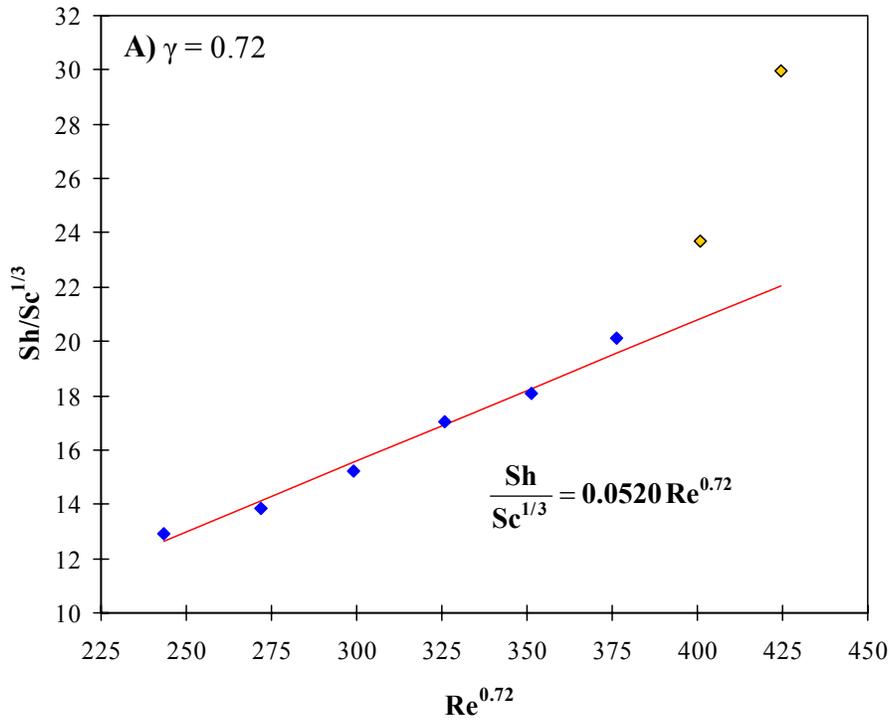
Figure A-8: Dimensionless mass transfer correlations

A.4 - Bibliography

[A1] Rowland, F. W., *The Practice of Gas Chromatography*. Hewlett-Packard Co.: **1974**

[A2] Mullins, E., *Statistics for the Quality Control Chemistry Laboratory*. Royal Society of Chemistry (RSC): Cambridge, UK, **2003**

[A3] Gordon, A. R., The diaphragm-cell method of measuring diffusion. *Ann. N.Y. Acad. Sci.* **1945,** 46, 285-308.

[A4] Mills, R.; Woolf, L. A., *The Diaphragm Cell: Theory and Practice of the Diaphragm Cell for Liquid Diffusion Measurements*. Australian National University Press: Canberra, Vol. DRU-RR1, **1968**

[A5] Tyrrell, H.; Harris, K., *Diffusion in liquids, A theoretical and experimental study*. Butterworths: London, **1984**

[A6] Woolf, L. A.; Tilley, J. F., Revised values of integral diffusion coefficients of potassium chloride solutions for the calibration of diaphragm cells. *J. Phys. Chem.* **1967,** 71 (6), 1962-1963.

[A7] Gosting, L. J., A Study of the Diffusion of Potassium Chloride in Water at 25° with the Gouy Interference Method. *J. Am. Chem. Soc.* **1950,** 72 (10), 4418-4422.

[A8] Harned, H. S.; Nuttall, R. L., The Differential Diffusion Coefficient of Potassium Chloride in Dilute Aqueous SOlution. *J. Am. Chem. Soc.* **1949,** 71 (4), 1460-1463.

[A9] Akeley, D. F.; Gosting, L. J., Studies of the DIffusion of Mixed Solutes with the Gouy Diffusiometer. *J. Am. Chem. Soc.* **1953,** 75 (22), 5685-5696.

[A10] Woolf, L. A.; Miller, D. G.; Gosting, L. J., Isothermal Diffusion Measurements on the System H2O-Glycine-KCl at 25°; Tests of the ONsager Reciprocal Relation. *J. Am. Chem. Soc.* **1962,** 84 (3), 317-&.

[A11] Stokes, R. H., Integral diffusion coefficients of potassium chloride solutions for calibration of diaphragm cells. *J. Am. Chem. Soc.* **1951,** 73, 3527-3528.

[A12] Holmes, J. T.; Wilke, C. R.; Olander, D. R., Convective mass transfer in a diaphragm diffusion cell. *J. Phys. Chem.* **1963,** 67 (7), 1469-1472.

[A13] Levich, V. G., *Physicochemical Hydrodynamics*. Prentice-Hall Inc.: Englewood Cliffs, NJ, **1962**

[A14] Geankoplis, C. J., *Transport Processes and Unit Operations*. 3rd ed.; Prentice-Hall PTR: Englewood Cliffs, NJ, **1993**

[A15] Malone, D. M.; Anderson, J. L., Diffusional boundary-layer resistance for membranes with low porosity. *AIChE J.* **1977,** 23 (2), 177-184.

[A16] Smith, K. A.; Colton, C. K.; Merrill, E. W.; Evans, L. B., Convective transport in a batch dialyzer: determination of true membrane permeability form a single measurement. *Chem. Eng. Progr. Symp. Ser.* **1968,** 64 (84), 45-58.

[A17] Colton, C. K.; Smith, K. A., Mass transfer to a rotating fluid. II. Transport from the base of an agitated cylindrical tank. *AIChE J.* **1972,** 18 (5), 958-967.

[A18] Krumgalz, B. S.; Pogorelskii, R.; Sokolov, A.; Pitzer, K. S., Volumetric Ion Interaction Parameters for Single-Solute Aqueous Electrolyte Solutions at Various Temperatures. *J. Phys. Chem. Ref. Data* **2001,** 29 (5), 1123-1140.

[A19] Laliberte, M., Model for Calculating the Viscosity of Aqueous Solutions. *J. Chem. Eng. Data* **2007,** 52 (2), 321-335.

[A20] Masui, R., Development of a Magnetic Suspension Densimeter and Measurement of the Density of Toluene. *Int. J. Thermophys.* **2002,** 23 (4), 921-935.

[A21] Santos, F. J. V.; Nieto de Castro, Carlos A.; Dymond, J. H.; Dalaouti, N. K.; Assael, M. J.; Nagashima, A., Standard Reference Data for the Viscosity of Toluene. *J. Phys. Chem. Ref. Data* **2006,** 35 (1), 1-8.

Appendix B

UV/Visible Calibration of Porphyrins and PBP

All UV/Visible measurements in this work were done using an SI-Photonics model 440 spectrophotometer (see Chapter 4 for more details). This spectrophotometer is a fiber optic unit capable of accommodating various different sample cells. In this work, 2 different sample cells were used: traditional cuvettes (both 10 mm and 1 mm pathlength) and a quartz sleeved dip probe (C-Technologies Inc. VersaProbe). Therefore, calibrations are required for each sample cell. In the case of the dip probe, calibrations were also done at different temperatures in a jacketed cell.

B.1 - Calibration of H$_2$TPP

Calibrations were done using a series of solutions of H$_2$TPP (Sigma-Aldrich # 247367, lot #25996KH, 99.9% purity) in toluene. First, enough solid H$_2$TPP to yield a 200 μmol/L solution was weighed out on a Mettler-Toledo MX5 micro balance (±0.001 mg) and carefully transferred to a tared class A 100 mL volumetric flask. The flask was filled to the base of the neck with toluene and sonicated for ~ 15 minutes to speed up the dissolution of the solids. Afterwards, the flask was topped to the mark and the final weight recorded on a Sartorius CP224S analytical balance (±0.0001g). This stock solution was then serially diluted to yield solutions with varying concentrations of H$_2$TPP for calibration. The concentrations of these diluted solutions were quantified gravimetrically, and the resulting concentrations are summarized below in Table B-1.

Table B-1: Concentrations of H$_2$TPP Solutions used for calibrating the 10 mm Cuvette

#	Actual H$_2$TPP Concentration			
	Mass Fraction, x$_{H2TPP}$ Value ± Abs. error (% error)		**Molar Concentration @ 20°C, C$_{H2TPP}$** Value ± Abs. error (% error)	
1	142.30 ±0.29ppmw	(0.21%)	200.70 ±0.32 μmol/L	(0.16%)
2	142.41 ±0.29ppmw	(0.21%)	200.93 ±0.32 μmol/L	(0.16%)
3	113.48 ±0.24ppmw	(0.21%)	159.69 ±0.35 μmol/L	(0.22%)
4	85.55 ±0.18ppmw	(0.21%)	120.33 ±0.26 μmol/L	(0.22%)
5	71.21 ±0.15ppmw	(0.21%)	100.22 ±0.22 μmol/L	(0.22%)
6	56.89 ±0.12ppmw	(0.21%)	80.02 ±0.18 μmol/L	(0.22%)
7	42.674 ±0.090ppmw	(0.21%)	60.12 ±0.13 μmol/L	(0.22%)
8	28.380 ±0.060ppmw	(0.21%)	39.917 ±0.088 μmol/L	(0.22%)
9	14.345 ±0.030ppmw	(0.21%)	20.198 ±0.044 μmol/L	(0.22%)
10	7.183 ±0.015ppmw	(0.21%)	10.130 ±0.023 μmol/L	(0.22%)
11	3.4057 ±0.0073ppmw	(0.21%)	4.794 ±0.011 μmol/L	(0.22%)
12	1.7186 ±0.0037ppmw	(0.21%)	2.4207 ±0.0054 μmol/L	(0.22%)
13	0.5739 ±0.0012ppmw	(0.22%)	0.8087 ±0.0018 μmol/L	(0.23%)
14	0.27310 ±0.00059ppmw	(0.22%)	0.38449 ±0.00087 μmol/L	(0.23%)
15	0.021879 ±0.000048ppmw	(0.22%)	0.030788 ±0.000071 μmol/L	(0.23%)

The solutions synthesized as per above were then analyzed in triplicate using the UV/Vis spectrophotometer with the different sample cells as required. The resulting spectra (Figure B-1) were then analyzed to quantify the height of the analyte peaks. H_2TPP contains 5 separate peaks: 418.2 nm (Soret), 513.1 nm, 547.7 nm, 590.1 nm, and 647.0 nm. The baseline correction method of Freeman *et al.*[B1] was used, whereby 2 points on either side of the peak are chosen and a linear, sloping baseline is drawn across the base of the peak. This baseline is then used to interpolate for the background absorbance at the same wavelength as the peak maximum. This interpolated background absorbance is subtracted from the measured peak height to yield a corrected peak height, A_T. This method, shown graphically in Figure B-2, automatically corrects for sloping and/or non-zero baselines, significantly reducing the variability of the concentration measurements. The coordinates used for the baselines are: 375 & 450 nm for the Soret peak, 465 & 675 nm for the visible peaks.

Once the corrected peak height, A_T, has been determined, a linear calibration curve is then constructed for each peak as illustrated for the first visible peak of H_2TPP (513.1 nm) in Table B-2, Figure B-3, and Figure B-4. Decisions about at what concentration to cap the curve and exclude data points at higher concentrations were made based on inspection of the extinction coefficients and the regression residuals. In most cases, the residuals are within the tolerance of the instrument (±0.005 AU). It should also be noted that, strictly speaking, Beer's law does not include an intercept. However, although a zero intercept is theoretically correct, in practice instrumental error generally leads to a non-zero intercept in quantitative applications[B2] and as such an intercept was included in all regressions. In most cases, these intercepts were very small and within the tolerance of the instrument (±0.005 AU). Table B-2 includes a full ANOVA analysis, and these results indicate a very good fit. Figure B-3 also includes a 95% prediction interval for the regression curve, which is calculated using the following formula[B3]:

$$\hat{Y}_P \pm t_{\alpha/2}s\sqrt{1+\frac{1}{n}+\frac{(X_P-\overline{X})^2}{\sum(X_i-\overline{X})^2}} \quad \dots\dots\dots\dots\dots\dots\dots\dots \{B.1\}$$

where $t_{\alpha/2} = t_{0.025}$ with n-1 degrees of freedom
$\hat{Y}_P$ = predicted response
X_P = value of X where Y is predicted
$s = \sqrt{s^2}$ = standard error
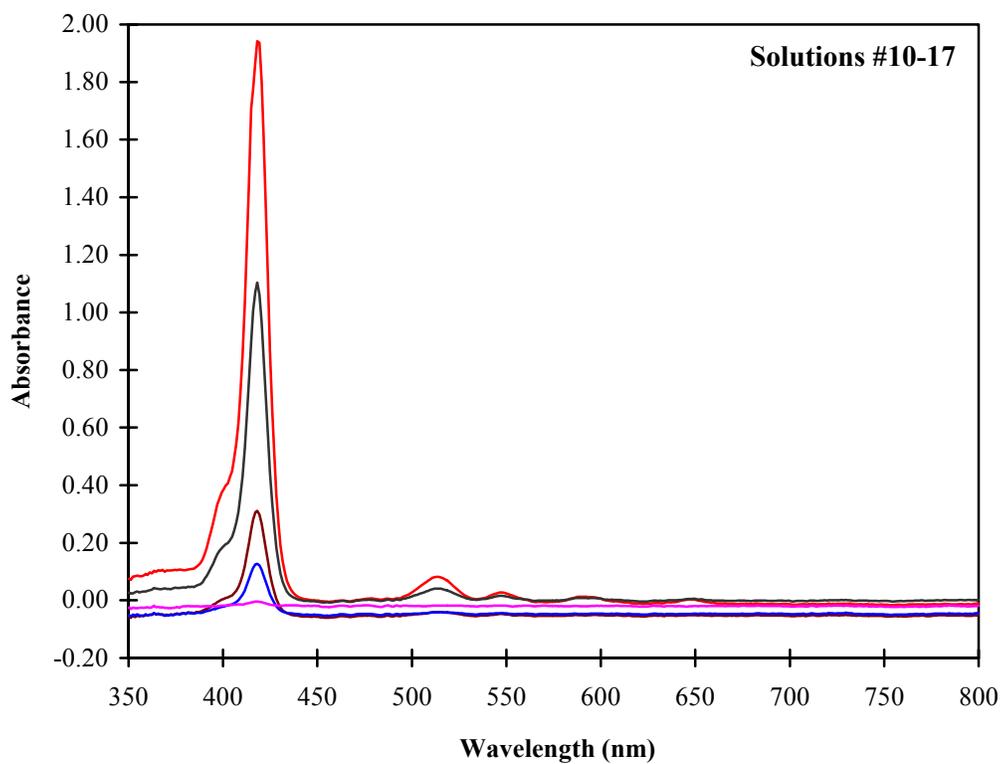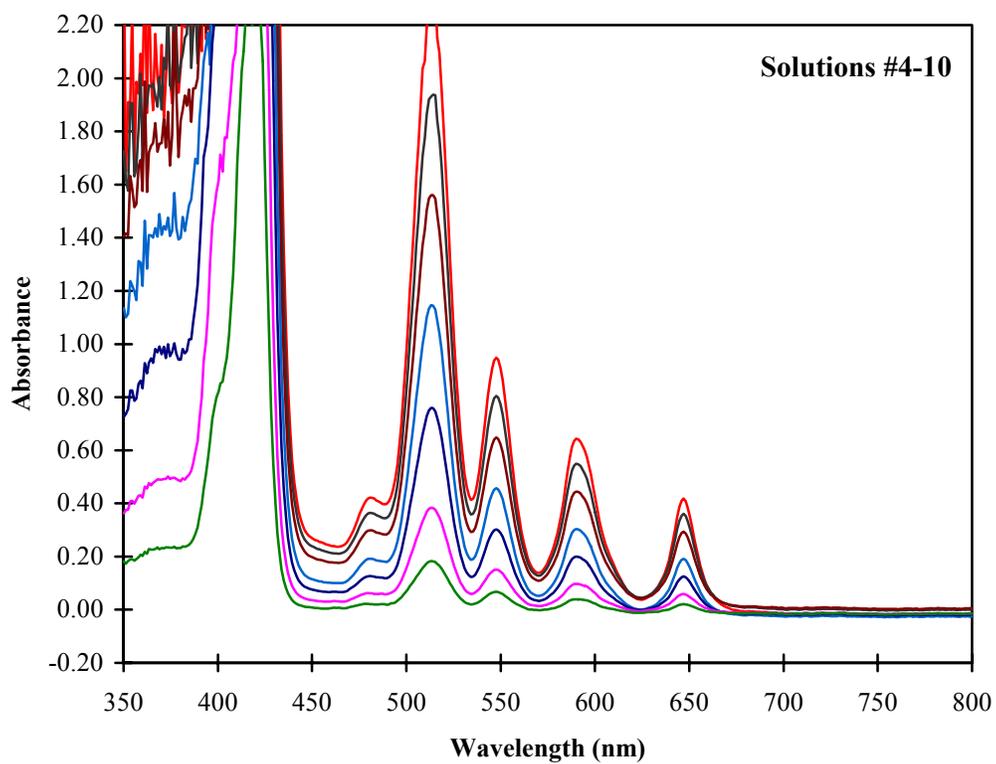
Figure B-1: Raw spectra for H$_2$TPP calibration solutions in 10 mm cuvette (only 1 scan of each is shown for clarity)
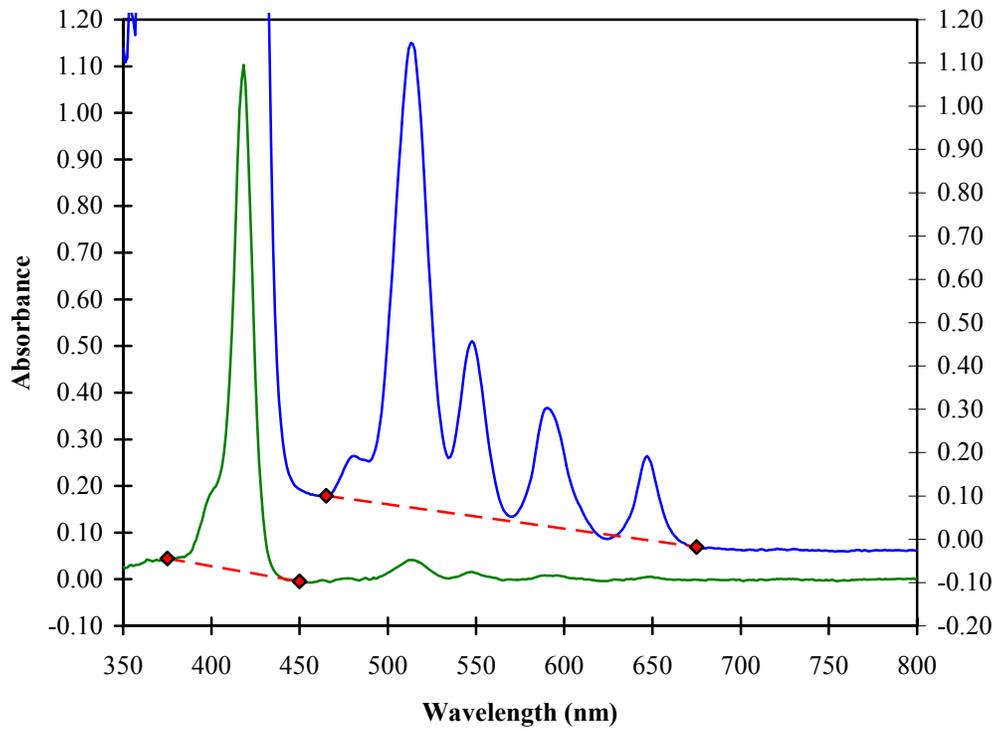
Figure B-2: Graphical illustration of linear baselines used for correcting the peak height

Table B-2: Regression calculations for the calibration of the first visible peak of H_2TPP (513.1 nm) in a 10 mm cuvette

H₂TPP Conc. (µmol/L) X	X²	$(X-X_{mean})^2$	Corrected Peak Height, A_T Y	Y²	X*Y	Ŷ	Ŷ²	Residual Y-Ŷ	%	$(Y-Ŷ)^2$	$(Y-Y_{mean})^2$	$(Ŷ-Y_{mean})^2$
100.225	10045	4944.25	1.7743	3.148	177.83	1.7800	3.1686	-0.00573	-0.3%	0.00003	1.5431	1.5574
100.225	10045	4944.25	1.7782	3.162	178.22	1.7800	3.1686	-0.00180	-0.1%	0.00000	1.5529	1.5574
100.225	10045	4944.25	1.7727	3.143	177.67	1.7800	3.1686	-0.00733	-0.4%	0.00005	1.5392	1.5574
80.017	6403	2510.78	1.4214	2.020	113.73	1.4214	2.0204	-0.00003	0.0%	0.00000	0.7908	0.7909
80.017	6403	2510.78	1.4255	2.032	114.06	1.4214	2.0204	0.00411	0.3%	0.00002	0.7982	0.7909
80.017	6403	2510.78	1.4191	2.014	113.55	1.4214	2.0204	-0.00234	-0.2%	0.00001	0.7867	0.7909
60.117	3614	912.51	1.0733	1.152	64.52	1.0682	1.1411	0.00509	0.5%	0.00003	0.2929	0.2874
60.117	3614	912.51	1.0754	1.156	64.65	1.0682	1.1411	0.00714	0.7%	0.00005	0.2951	0.2874
60.117	3614	912.51	1.0727	1.151	64.49	1.0682	1.1411	0.00444	0.4%	0.00002	0.2922	0.2874
39.917	1593	100.15	0.7110	0.5055	28.38	0.7097	0.5037	0.00125	0.2%	0.00000	0.0320	0.0315
39.917	1593	100.15	0.7129	0.5082	28.46	0.7097	0.5037	0.00318	0.4%	0.00001	0.0327	0.0315
39.917	1593	100.15	0.7118	0.5067	28.41	0.7097	0.5037	0.00212	0.3%	0.00000	0.0323	0.0315
20.198	408	94.30	0.3621	0.1311	7.31	0.3597	0.1294	0.00235	0.6%	0.00001	0.0289	0.0297
20.198	408	94.30	0.3618	0.1309	7.31	0.3597	0.1294	0.00205	0.6%	0.00000	0.0290	0.0297
20.198	408	94.30	0.3613	0.1305	7.30	0.3597	0.1294	0.00156	0.4%	0.00000	0.0292	0.0297
10.130	103	391.22	0.1804	0.0326	1.83	0.1810	0.0328	-0.00061	-0.3%	0.00000	0.1237	0.1232
10.130	103	391.22	0.1813	0.0329	1.84	0.1810	0.0328	0.00028	0.2%	0.00000	0.1230	0.1232
10.130	103	391.22	0.1806	0.0326	1.83	0.1810	0.0328	-0.00039	-0.2%	0.00000	0.1235	0.1232
4.794	23	630.78	0.0852	0.0073	0.41	0.0863	0.0075	-0.00115	-1.4%	0.00000	0.1997	0.1987
4.794	23	630.78	0.0857	0.0074	0.41	0.0863	0.0075	-0.00059	-0.7%	0.00000	0.1992	0.1987
4.794	23	630.78	0.0856	0.0073	0.41	0.0863	0.0075	-0.00073	-0.9%	0.00000	0.1993	0.1987
2.421	6	755.62	0.0432	0.0019	0.10	0.0442	0.0020	-0.00105	-2.4%	0.00000	0.2390	0.2380
2.421	6	755.62	0.0431	0.0019	0.10	0.0442	0.0020	-0.00111	-2.6%	0.00000	0.2391	0.2380
2.421	6	755.62	0.0426	0.0018	0.10	0.0442	0.0020	-0.00164	-3.9%	0.00000	0.2396	0.2380
0.809	1	846.84	0.0146	0.0002	0.01	0.0156	0.0002	-0.00101	-7.0%	0.00000	0.2678	0.2667
0.809	1	846.84	0.0142	0.0002	0.01	0.0156	0.0002	-0.00144	-10%	0.00000	0.2682	0.2667
0.809	1	846.84	0.0141	0.0002	0.01	0.0156	0.0002	-0.00149	-11%	0.00000	0.2683	0.2667
0.384	0	871.71	0.0071	0.0000	0.00	0.0081	0.0001	-0.00102	-14%	0.00000	0.2756	0.2746
0.384	0	871.71	0.0069	0.0000	0.00	0.0081	0.0001	-0.00114	-16%	0.00000	0.2758	0.2746
0.384	0	871.71	0.0068	0.0000	0.00	0.0081	0.0001	-0.00131	-19%	0.00000	0.2760	0.2746
0.031	0	892.72	0.0012	0.0000	0.00	0.0018	0.0000	-0.00058	-48%	0.00000	0.2818	0.2812
0.031	0	892.72	0.0007	0.0000	0.00	0.0018	0.0000	-0.00105	-141%	0.00000	0.2823	0.2812
Σ = 957.1	66586	37960	17.03	21.02	1183.0	17.03	21.02	0.000		0.000	11.957	11.957
Mean = 29.91	2080.8	1186.25	0.5321	0.6568	36.97	0.5321	0.6568	0.0000		0.00001	0.37367	0.37366

SLOPE = 0.01774805
INTERCEPT = 0.001257391

R^2 = 0.999979
s^2 = 0.00000853
$t_{0.025}$ = 2.040

ANOVA					
Source	Sum of Squares	DF	Mean Square	F	P
Model	11.9571170	1	11.9571170	1,402,289	1.300E-71
Residual	0.0002558	30	0.0000085		
Total	11.9573728	31			

Slope Error Estimate
u_{Slope} = 0.0000306

Intercept Error Estimate
$u_{Intercept}$ = 0.001394

Prediction Uncertainty Estimates
$u_X = -0.00044985Y^3 + 0.014601Y^2 - 0.015050Y + 0.34469$

$$A_T = 0.0177481 \cdot C_{H2TPP}(\mu mol/L) + 0.00125739$$

$$R^2 = 0.999979$$

- ○ Measured Data
- —— Overall Regression Curve
- – – – 95% Prediction Interval
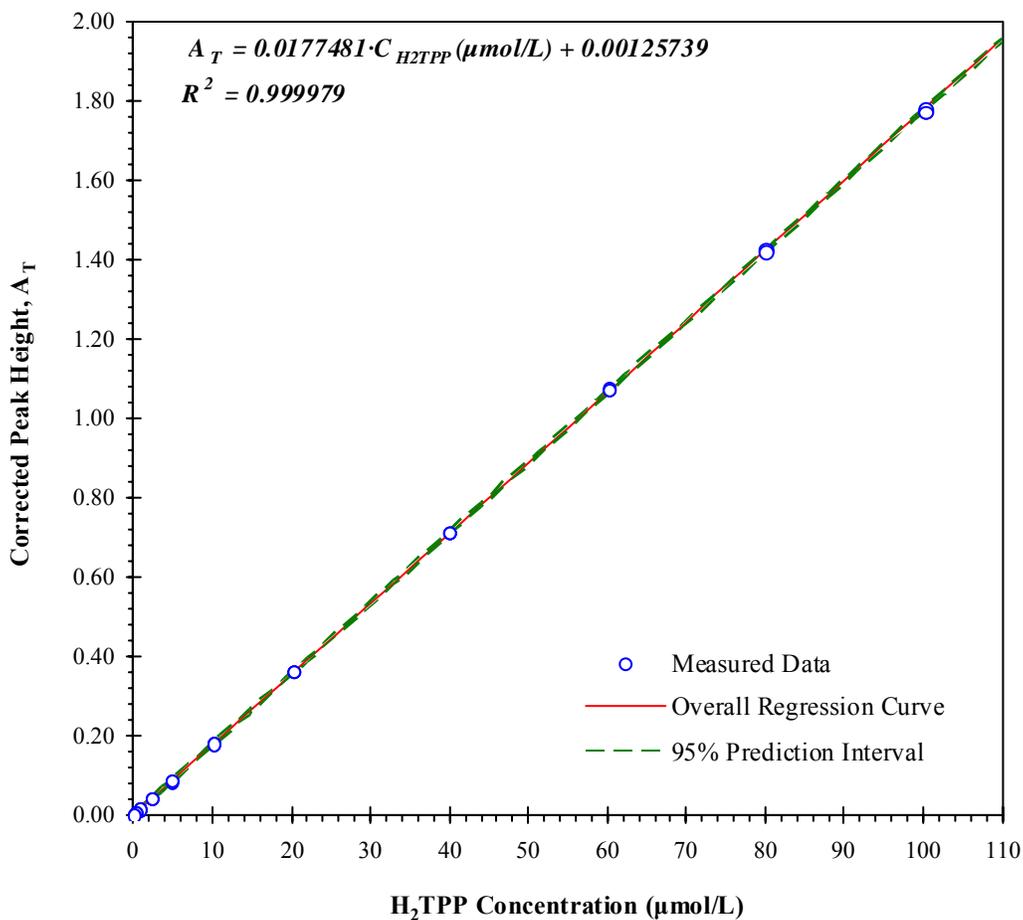
Figure B-3: Calibration curve for the first visible peak of H_2TPP (513.1 nm) in a 10 mm cuvette
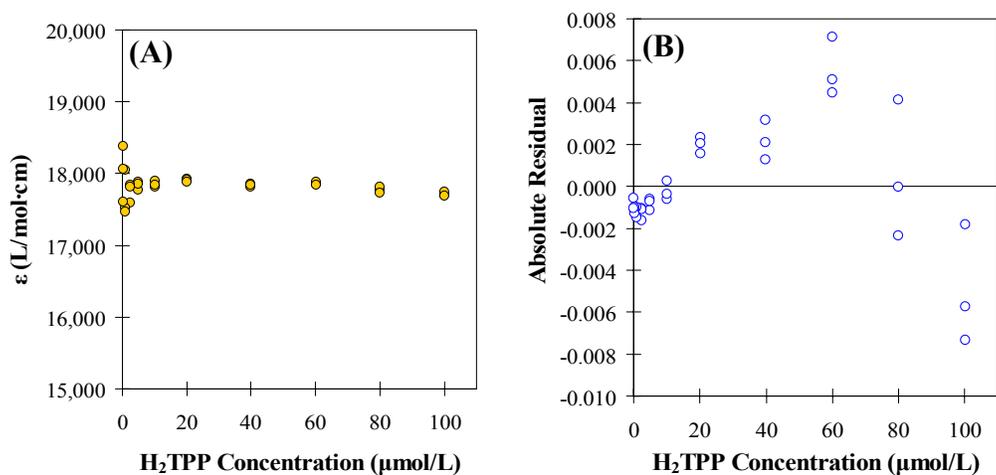

Figure B-4: A) Extinction coefficients, and B) regression residuals for the calibration curve of the first visible peak of H_2TPP (513.1 nm) in a 10 mm cuvette

For the sake of brevity, the preceding analysis will not be repeated for each peak since the methods are all the same. From hereon, only the final calibration equations and some diagnostic information will be given.

Table B-3: Calibration data for H_2TPP in toluene: 10 mm Cuvette @ ambient temperature

Peak (nm)	Slope/Extinction Coefficient, ε (L/mol·cm)	Intercept	R^2	C_{max} (μmol/L)
418.1	446,956	0.003317	0.999982	2.5
513.1	17,748	0.001257	0.999979	100
547.7	6,720	-0.0003679	0.999979	200
590.1	4,568	-0.001479	0.999980	200
647.0	3,222	-0.0009025	0.999961	200

Table B-4: Calibration data for H_2TPP in toluene @ 25°C: VersaProbe with 10mm Tip

Peak (nm)	Slope/Extinction Coefficient, ε (L/mol·cm)	Intercept	R^2	C_{max} (μmol/L)
418.1	432,630	0.006310	0.999881	2.5
513.1	17,549	0.001867	0.999980	80
547.7	6,700	0.0001477	0.999969	180
590.1	4,519	0.001345	0.999973	200
647.0	3,134	0.001604	0.999958	200

B.2 - Calibration of H_2OEP

The procedures used for developing calibration curves for H_2OEP were the same as those used for H_2TPP. The resulting spectra for H_2OEP (Figure B-5) contain 5 separate peaks that can be used for quantitation: 401.5 nm (Soret), 497.4 nm, 530.9 nm, 567.8 nm, 622.4 nm. The baseline correction method of Freeman *et al.*[B1] was used as before with the following coordinates for the baselines: 360 & 460 nm for the Soret peak, 460 & 645 nm for the four visible peaks. The final calibration equations are listed in Table B-5.
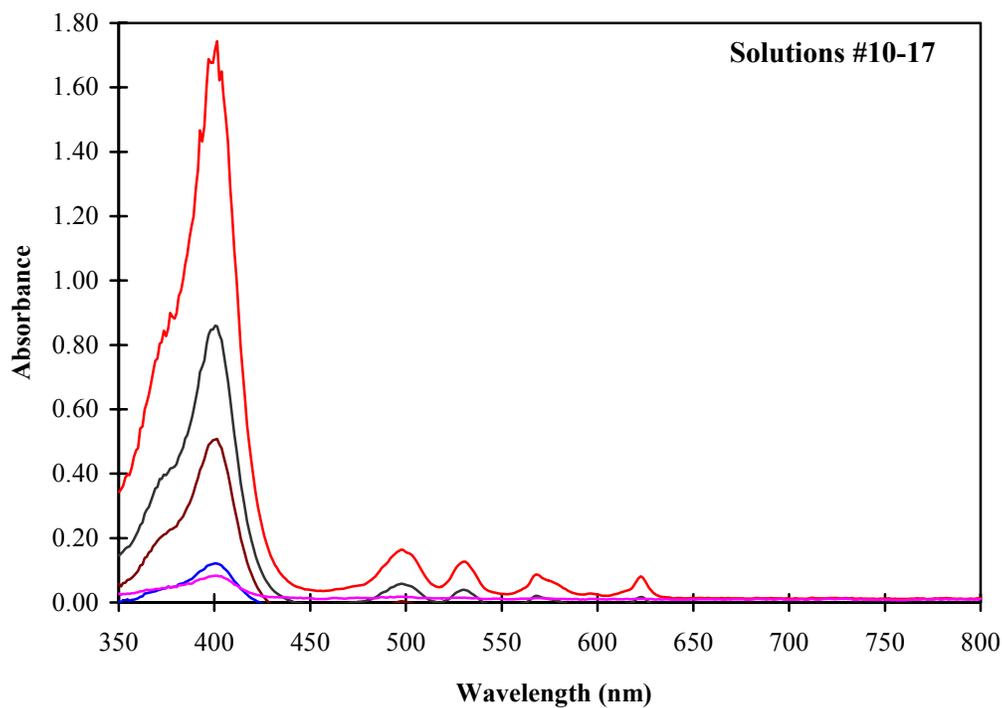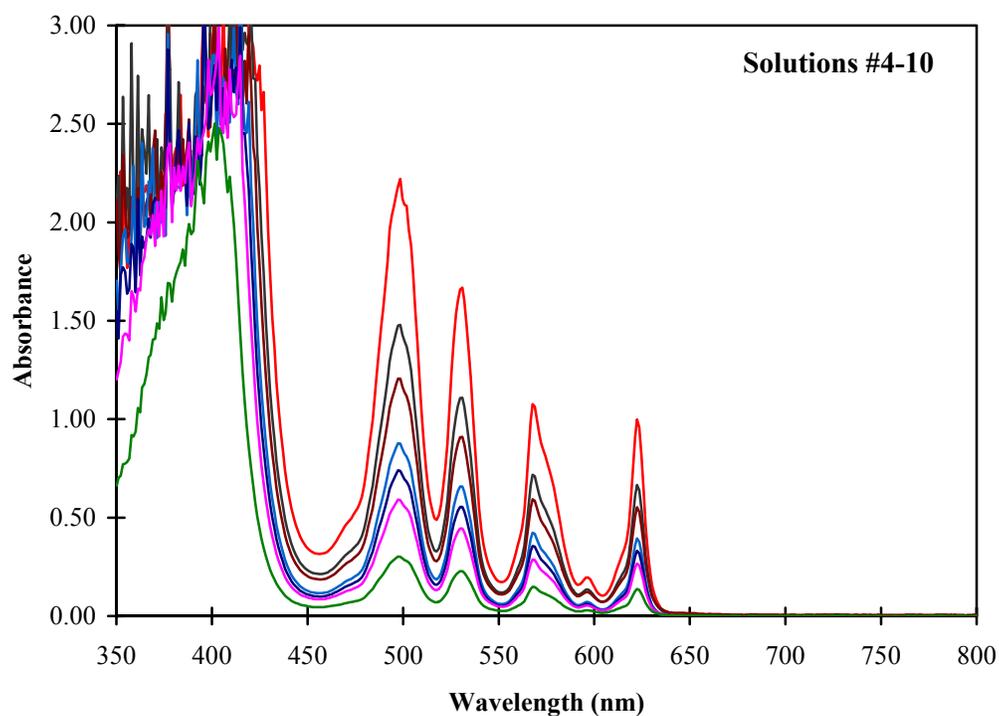
Figure B-5: Raw spectra for H_2OEP calibration solutions in 10 mm cuvette (only 1 scan of each is shown for clarity)

Table B-5: Calibration data for H_2OEP in toluene: 10 mm Cuvette @ ambient temperature

Peak (nm)	Slope/Extinction Coefficient, ε (L/mol·cm)	Intercept	R^2	C_{max} (µmol/L)
401.5	143,922	0.005842	0.99984	10
497.4	13,002	0.002496	0.999969	100
530.9	9,737	0.001697	0.999983	150
567.8	6,224	0.002649	0.999971	200
622.4	6,335	0.002019	0.999908	200

B.3 - Calibration of VOTPP

The procedures used for developing calibration curves for VOTPP were the same as those used for H_2TPP. The resulting spectra for VOTPP (Figure B-6) contain 2 peaks that can be used for quantitation: 422.7nm (Soret) and 547.7 nm. The baseline correction method of Freeman *et al.*[B1] was used as before with the following coordinates for the baselines: 375 & 460 nm for the Soret peak, 480 & 620 nm for the visible peak. In the case of VOTPP, calibrations were performed in various mixtures of n-heptane and toluene. The change in solvent from toluene to n-heptane had no impact on the extinction coefficient of VOTPP. The final calibration equations are listed in Table B-6 and Table B-7.

Table B-6: Calibration data for VOTPP in heptol: 10 mm Cuvette @ ambient temperature

| Peak (nm)	Slope/Extinction Coefficient, ε (L/mol·cm)	Intercept	R^2	C_{max} (µmol/L)
422.7	501,372	0.008616	0.9975	2.6
547.7	20,408	-0.0004954	0.9998	75
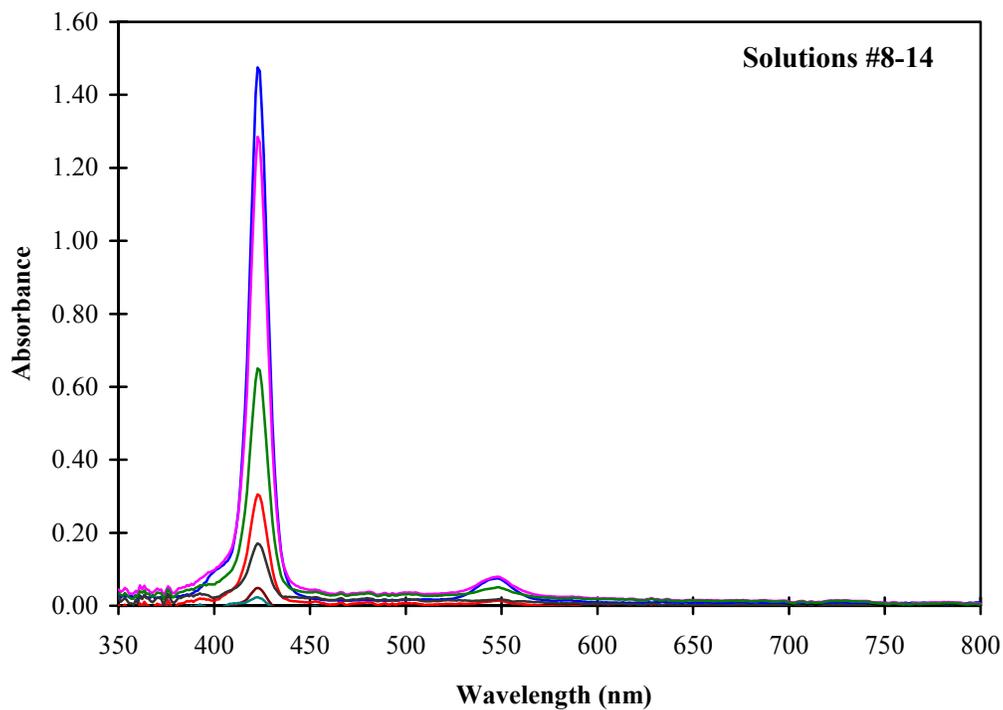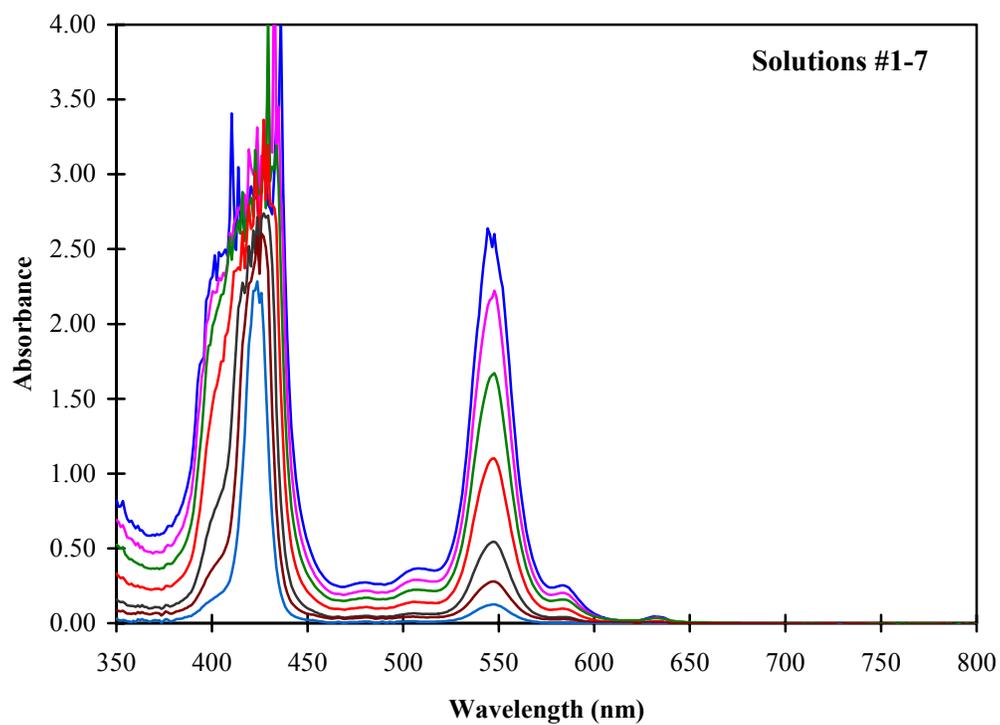
Figure B-6: Raw spectra for VOTPP calibration solutions in 10 mm cuvette (only 1 scan of each is shown for clarity)

Table B-7: Calibration data for VOTPP in heptol: VersaProbe with 10mm Tip

Peak (nm)	Temperature (°C)	Slope/Extinction Coefficient, ε (L/mol·cm)	Intercept	R^2	C_{max} (µmol/L)
422.7	25	494,055	0.009401	0.9981	2.6
	40	485,386	0.007355	0.9971	2.6
	60	465,533	0.008329	0.9936	2.6
547.7	25	20,546	0.001403	0.9997	75
	40	20,446	-0.0003250	0.9993	75
	60	19,971	0.001160	0.9994	75

B.4 - Calibration of VOOEP

The procedures used for developing calibration curves for VOOEP were the same as those used for H_2TPP. The resulting spectra for VOOEP (Figure B-7) contain 3 peaks that can be used for quantitation: 407.0 nm (Soret), 533.2 nm, and 571.1 nm. The baseline correction method of Freeman *et al.*[B1] was used as before with the following coordinates for the baselines: 360 & 460 nm for the Soret peak, 470 & 630 nm for the visible peaks. In the case of VOOEP, calibrations were performed in various mixtures of n-heptane and toluene (heptol). The change in solvent from toluene to n-heptane had no impact on the extinction coefficient of VOOEP. The final calibration equations are listed in Table B-8 and Table B-9.

Table B-8: Calibration data for VOOEP in heptol: 10 mm Cuvette @ ambient temperature

| Peak (nm)	Slope/Extinction Coefficient, ε (L/mol·cm)	Intercept	R^2	C_{max} (µmol/L)
407.0	386,963	0.004735	0.9979	3.5
533.2	13,707	0.001559	0.9994	115
571.1	35,969	0.003567	0.9982	45
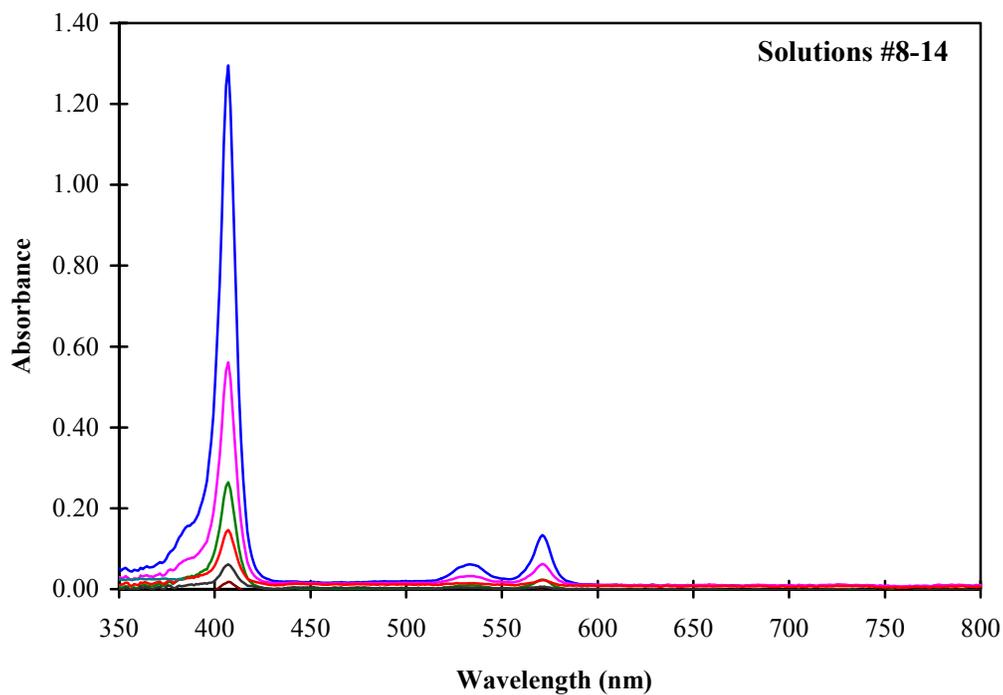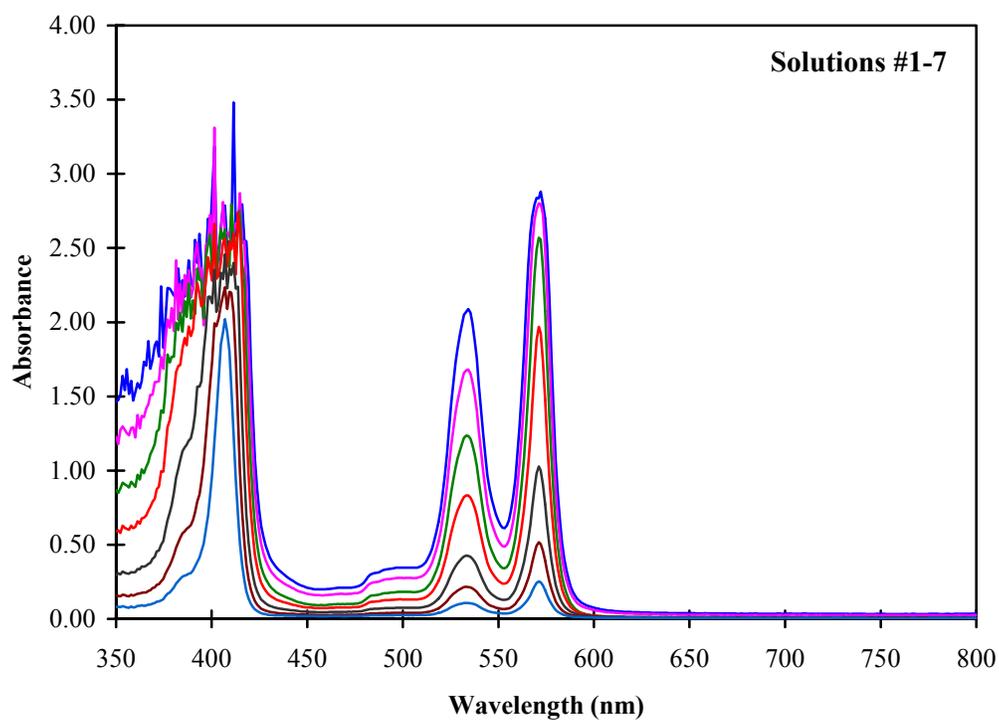
Figure B-7: Raw spectra for VOOEP calibration solutions in 10 mm cuvette (only 1 scan of each is shown for clarity)

: Calibration data for VOOEP in heptol: VersaProbe with 10mm Tip

Peak (nm)	Temperature (°C)	Slope/Extinction Coefficient, ε (L/mol·cm)	Intercept	R^2	C_{max} (µmol/L)
407.0	25	390,768	0.0008811	0.9992	3.5
	40	383,627	-0.001606	0.9990	3.5
	60	368,339	-0.0000066	0.9989	3.5
533.2	25	13,550	0.001437	0.9996	115
	40	13,443	0.0006415	0.9996	115
	60	13,179	0.0009028	0.9997	115
571.1	25	35,750	0.002410	0.9989	45
	40	34,621	0.002057	0.9991	45
	60	33,341	0.001836	0.9990	45

B.5 - Calibration of PBP

The procedures used for developing calibration curves for PBP were the same as those used for H_2TPP. The resulting spectra for PBP (Figure B-8) contain 3 separate peaks that can be used for quantitation: 314.4 nm, 328.9 nm, 345.7 nm. The baseline correction method of Freeman et al.[B1] was used as before with 307 & 360 nm as baseline coordinates. The final calibration equations are listed in Table B-10.

Table B-10: Calibration data for PBP in toluene: 10 mm Cuvette @ ambient temperature

Peak (nm)	Slope/Extinction Coefficient, ε (L/mol·cm)	Intercept	R^2	C_{max} (µmol/L)
314.4	12,887	0.007857	0.9982	50
328.9	42,142	0.001210	0.9999	35
345.7	66,257	-0.003558	0.9997	25
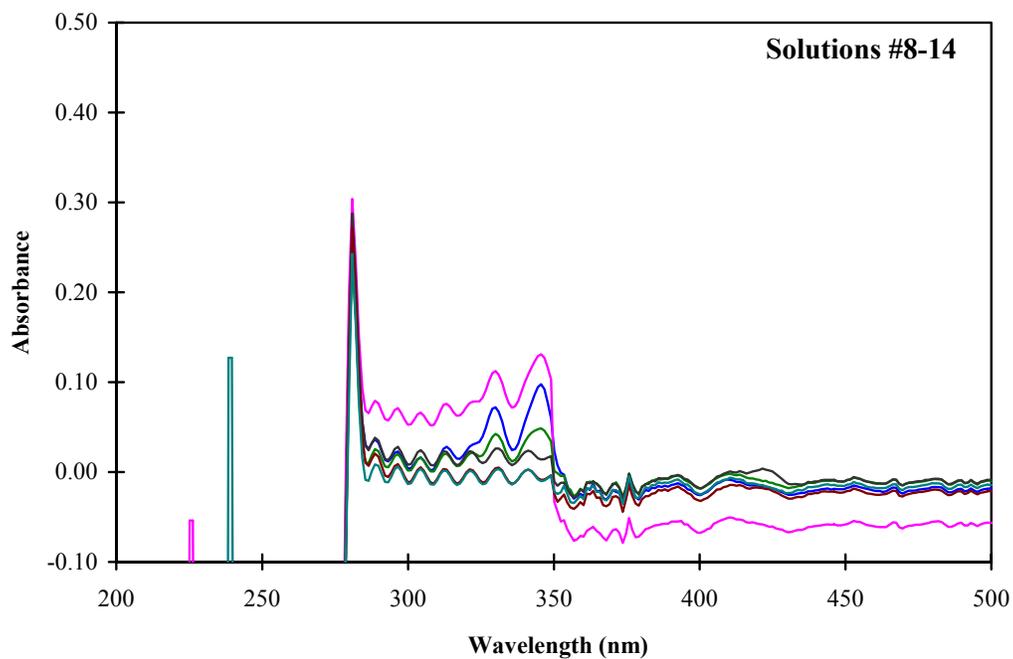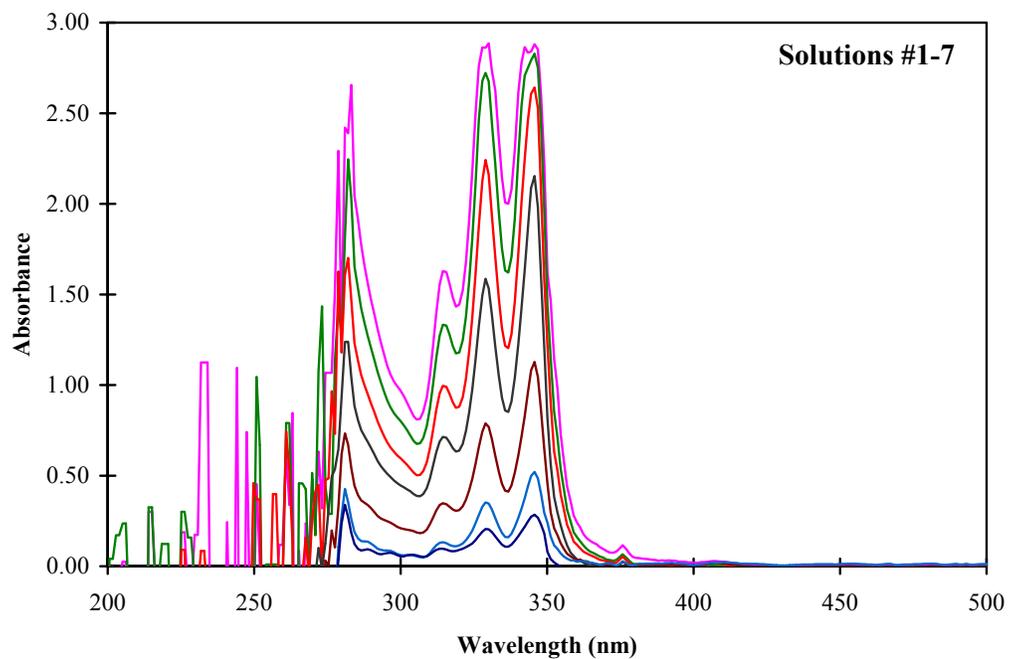
Figure B-8: Raw spectra for PBP calibration solutions in 10 mm cuvette (only 1 scan of each is shown for clarity)

B.6 - Bibliography

[1] Freeman, D. H.; Swahn, I. D.; Hambright, P., Spectrophotometry and solubility properties of nickel and vanadyl porphyrin complexes. *Energy & Fuels* **1990,** 4, (6), 699-704.

[2] Smith, B. C., *Quantitative Spectroscopy: Theory and Practice*. Academic Press: Amsterdam, **2002**

[3] Mullins, E., *Statistics for the Quality Control Chemistry Laboratory*. Royal Society of Chemistry (RSC): Cambridge, UK, **2003**

Appendix C

UV/Visible Calibration of Asphaltenes

All UV/Visible measurements in this work were done using an SI-Photonics model 440 spectrophotometer (see Chapter 4 for more details). This spectrophotometer is a fiber optic unit capable of accommodating various different sample cells. In this work, 2 different sample cells were used: traditional cuvettes (both 10 mm and 1 mm pathlength) and a quartz sleeved dip probe (C-Technologies Inc. VersaProbe). Therefore, calibrations are required for each sample cell. In the case of the dip probe, calibrations were also done at different temperatures in a jacketed cell.

C.1 - Calibration of Athabasca Asphaltenes (AA) in Toluene

Calibrations were done using a series of solutions of AA in toluene. First, enough solid asphaltenes to yield a 1000 mg/L solution was weighed out on a Mettler-Toledo MX5 micro balance (±0.001 mg) and carefully transferred to a tared class A 100 mL volumetric flask. The flask was filled to the base of the neck with toluene and sonicated for at least 1 hour to speed up the dissolution of the solids. Afterwards, the flask was allowed to cool, topped to the mark, and the final weight recorded on a Sartorius CP224S analytical balance (±0.0001g). Three of these stock solutions were made and serially diluted to yield calibration solutions with varying concentrations of asphaltenes. The concentrations of these solutions were quantified both volumetrically and gravimetrically, and the resulting mean concentrations are summarized below in Table C-1.

The solutions synthesized as per above were then scanned in triplicate using the UV/Vis spectrophotometer using the different sample cells as required. The resulting spectra (Figure C-1) were then analyzed to quantify the height of the analyte peaks. Unlike the pure compounds in Appendix B, the asphaltene spectra in Figure C-1 do not contain any distinct peaks for analysis. Rather, the spectra are characterized by a continuous, downward sloping curve. As such, calibration curves can be generated for any specific wavelength to suit different needs. In the case of the 10 mm cuvette, the calibration wavelengths chosen were: 350.1 nm, 500.8 nm, 600.1 nm, 700.6 nm, and 799.9 nm. Because the curve displays a continuous curvature, and because at higher concentrations the absorbance at the maximum wavelength of the instrument is non-zero, it is difficult to apply any specific baseline correction scheme. Instead, the absorbance at each wavelength is corrected by subtracting the absorbance at 950.6 nm (instrument max. wavelength) to yield a corrected peak height measurement.

Table C-1: Concentrations of asphaltene solutions used for calibrating the 10 mm Cuvette

#	Actual Asphaltene Concentration			
	Mass Fraction, x_{Asph}		Concentration @ 20°C†, C_{Asph}	
	Value ± Abs. error (% error)		Value ± Abs. error (% error)	
1	1155.1 ±2.4ppmw	(0.20%)	1002.0 ±1.6 mg/L	(0.16%)
2	1156.3 ±2.4ppmw	(0.20%)	1002.5 ±1.6 mg/L	(0.16%)
3	923.7 ±1.9ppmw	(0.21%)	801.2 ±1.2 mg/L	(0.15%)
4	693.5 ±1.4ppmw	(0.21%)	601.3 ±0.9 mg/L	(0.15%)
5	459.45 ±0.95ppmw	(0.21%)	399.37 ±0.62 mg/L	(0.15%)
6	231.29 ±0.48ppmw	(0.21%)	200.59 ±0.31 mg/L	(0.15%)
7	115.24 ±0.24ppmw	(0.21%)	99.96 ±0.15 mg/L	(0.15%)
8	115.47 ±0.24ppmw	(0.21%)	100.14 ±0.15 mg/L	(0.15%)
9	92.26 ±0.19ppmw	(0.21%)	80.00 ±0.12 mg/L	(0.15%)
10	69.22 ±0.14ppmw	(0.21%)	60.034 ±0.093 mg/L	(0.15%)
11	46.136 ±0.096ppmw	(0.21%)	40.013 ±0.062 mg/L	(0.15%)
12	23.037 ±0.049ppmw	(0.21%)	19.980 ±0.031 mg/L	(0.16%)
13	11.507 ±0.024ppmw	(0.21%)	9.979 ±0.016 mg/L	(0.16%)
14	5.787 ±0.012ppmw	(0.21%)	5.020 ±0.008 mg/L	(0.16%)
15	1155.5 ±2.4ppmw	(0.20%)	1001.9 ±1.6 mg/L	(0.16%)
16	577.5 ±1.2ppmw	(0.21%)	500.74 ±0.77 mg/L	(0.15%)
17	346.73 ±0.72ppmw	(0.21%)	300.76 ±0.46 mg/L	(0.15%)
18	207.45 ±0.43ppmw	(0.21%)	179.91 ±0.28 mg/L	(0.15%)
19	161.91 ±0.34ppmw	(0.21%)	140.38 ±0.22 mg/L	(0.15%)
20	57.60 ±0.12ppmw	(0.21%)	49.947 ±0.078 mg/L	(0.16%)
21	34.627 ±0.073ppmw	(0.21%)	30.026 ±0.047 mg/L	(0.16%)

Once the corrected peak height, A_T, has been determined, a linear calibration curve is then constructed for each peak as illustrated for the first wavelength (350.1 nm) in Table C-2, Figure C-2, and Figure C-3. Decisions about at what concentration to cap the curve and exclude data points at higher concentrations were made based on inspection of the extinction coefficients and the regression residuals. In most cases, the residuals are within the tolerance of the instrument (±0.005 AU). As discussed in Appendix B, strictly speaking Beer's law does not include an intercept. However, although a zero intercept is theoretically correct, in practice instrumental error generally leads to a non-zero intercept in quantitative applications and as such an intercept was included in all regressions. In most cases, these intercepts were very small and within the tolerance of the instrument (±0.005 AU). Table C-2 includes a full ANOVA analysis, and these results indicate a very good fit. Table C-2 also includes a 95% prediction interval for the regression curve, which is calculated using the formula given in Appendix B.
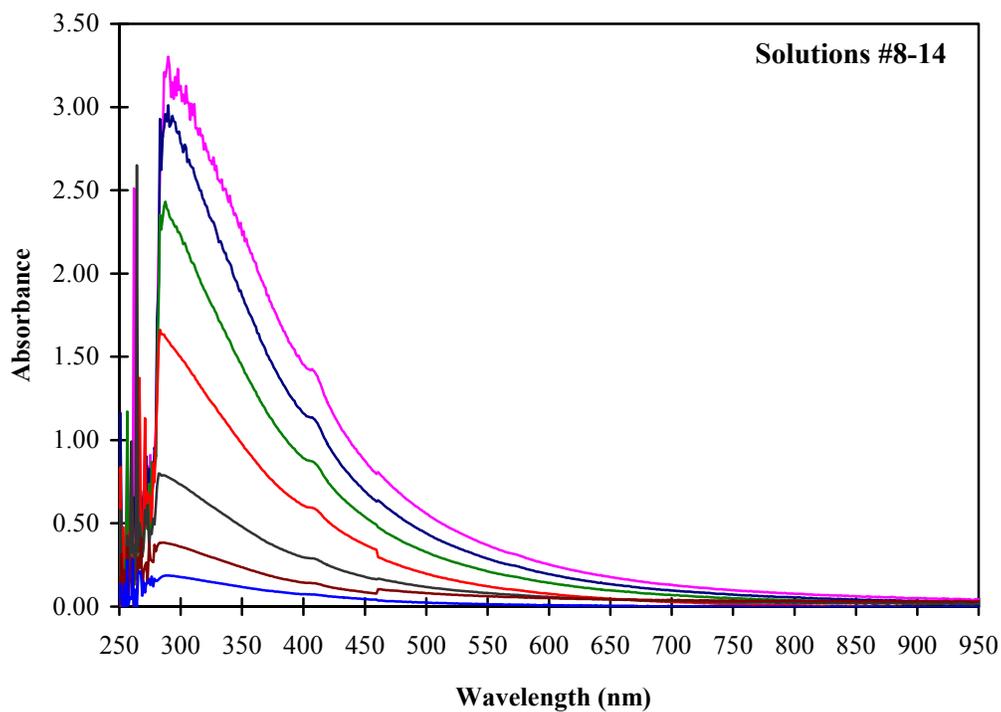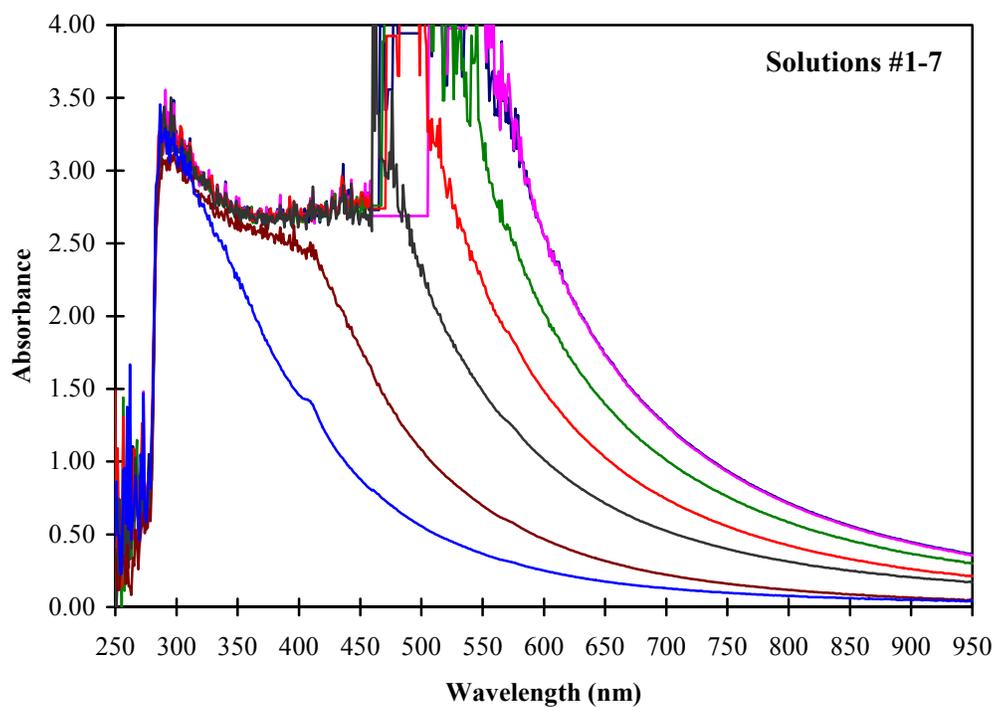
Figure C-1: Raw spectra for AA calibration solutions in 10 mm cuvette (only 1 scan of each is shown for clarity)

Table C-2: Regression calculations for the calibration curve at 350.1 nm for AA in toluene in a 10 mm cuvette.

Asph Conc. (mg/L) X	X²	(X-X$_{mean}$)²	Corrected Peak Height, A$_T$ Y	Y²	X*Y	Ŷ	Ŷ²	Residual Y-Ŷ	%	(Y-Ŷ)²	(Y-Y$_{mean}$)²	(Ŷ-Y$_{mean}$)²
60.034	3604	859.64	0.9397	0.8831	56.42	0.9382	0.8803	0.00151	0.2%	0.00000	0.2114	0.2100
60.034	3604	859.64	0.9368	0.8776	56.24	0.9382	0.8803	-0.00143	-0.2%	0.00000	0.2087	0.2100
60.034	3604	859.64	0.9369	0.8779	56.25	0.9382	0.8803	-0.00129	-0.1%	0.00000	0.2089	0.2100
40.013	1601	86.46	0.6275	0.3938	25.11	0.6253	0.3910	0.00226	0.4%	0.00001	0.0218	0.0211
40.013	1601	86.46	0.6298	0.3966	25.20	0.6253	0.3910	0.00450	0.7%	0.00002	0.0225	0.0211
40.013	1601	86.46	0.6278	0.3942	25.12	0.6253	0.3910	0.00256	0.4%	0.00001	0.0219	0.0211
19.980	399	115.22	0.3123	0.0975	6.24	0.3121	0.0974	0.00016	0.1%	0.00000	0.0281	0.0282
19.980	399	115.22	0.3136	0.0984	6.27	0.3121	0.0974	0.00147	0.5%	0.00000	0.0277	0.0282
19.980	399	115.22	0.3133	0.0982	6.26	0.3121	0.0974	0.00121	0.4%	0.00000	0.0277	0.0282
9.979	100	429.94	0.1566	0.0245	1.56	0.1558	0.0243	0.00084	0.5%	0.00000	0.1045	0.1051
9.979	100	429.94	0.1542	0.0238	1.54	0.1558	0.0243	-0.00161	-1.0%	0.00000	0.1061	0.1051
9.979	100	429.94	0.1553	0.0241	1.55	0.1558	0.0243	-0.00052	-0.3%	0.00000	0.1054	0.1051
5.020	25	660.17	0.0767	0.0059	0.39	0.0783	0.0061	-0.00158	-2.1%	0.00000	0.1626	0.1613
5.020	25	660.17	0.0757	0.0057	0.38	0.0783	0.0061	-0.00259	-3.4%	0.00001	0.1634	0.1613
5.020	25	660.17	0.0775	0.0060	0.39	0.0783	0.0061	-0.00080	-1.0%	0.00000	0.1620	0.1613
49.947	2495	369.91	0.7784	0.6058	38.88	0.7806	0.6093	-0.00220	-0.3%	0.00000	0.0891	0.0904
49.947	2495	369.91	0.7778	0.6049	38.85	0.7806	0.6093	-0.00279	-0.4%	0.00001	0.0887	0.0904
49.947	2495	369.91	0.7766	0.6031	38.79	0.7806	0.6093	-0.00395	-0.5%	0.00002	0.0880	0.0904
30.026	902	0.47	0.4713	0.2221	14.15	0.4692	0.2201	0.00211	0.4%	0.00000	0.0001	0.0001
30.026	902	0.47	0.4708	0.2217	14.14	0.4692	0.2201	0.00164	0.3%	0.00000	0.0001	0.0001
30.026	902	0.47	0.4697	0.2206	14.10	0.4692	0.2201	0.00052	0.1%	0.00000	0.0001	0.0001
Σ = 645.0	27376	7565	10.08	6.69	427.8	10.08	6.69	0.000		0.000	1.849	1.849
Mean = 30.71	1303.6	360.26	0.4799	0.3184	20.37	0.4799	0.3184	0.0000		0.00000	0.08803	0.08803

SLOPE = 0.0156314898
INTERCEPT = -0.00018481

R^2 = 0.999951
s^2 = 0.00000477
$t_{0.025}$ = 2.086

ANOVA					
Source	*Sum of Squares*	*DF*	*Mean Square*	*F*	*P*
Model	1.8485684	1	1.8485684	387,297	2.08E-42
Residual	0.0000907	19	0.0000048		
Total	1.8486590	20			

Slope Error Estimate
u_{Slope} = 0.0000524

Intercept Error Estimate
$u_{Intercept}$ = 0.001892

Prediction Uncertainty Estimates
u_X (mg/L) = -0.00060626Y^3 + 0.075811Y^2 - 0.072280Y + 0.31575

$$A_T = A_{350.1\ nm} - A_{458.3\ nm} = 0.0156315 \cdot C_{Asphaltene}\ (mg/L) - 0.00018481$$

$$R^2 = 0.999951$$
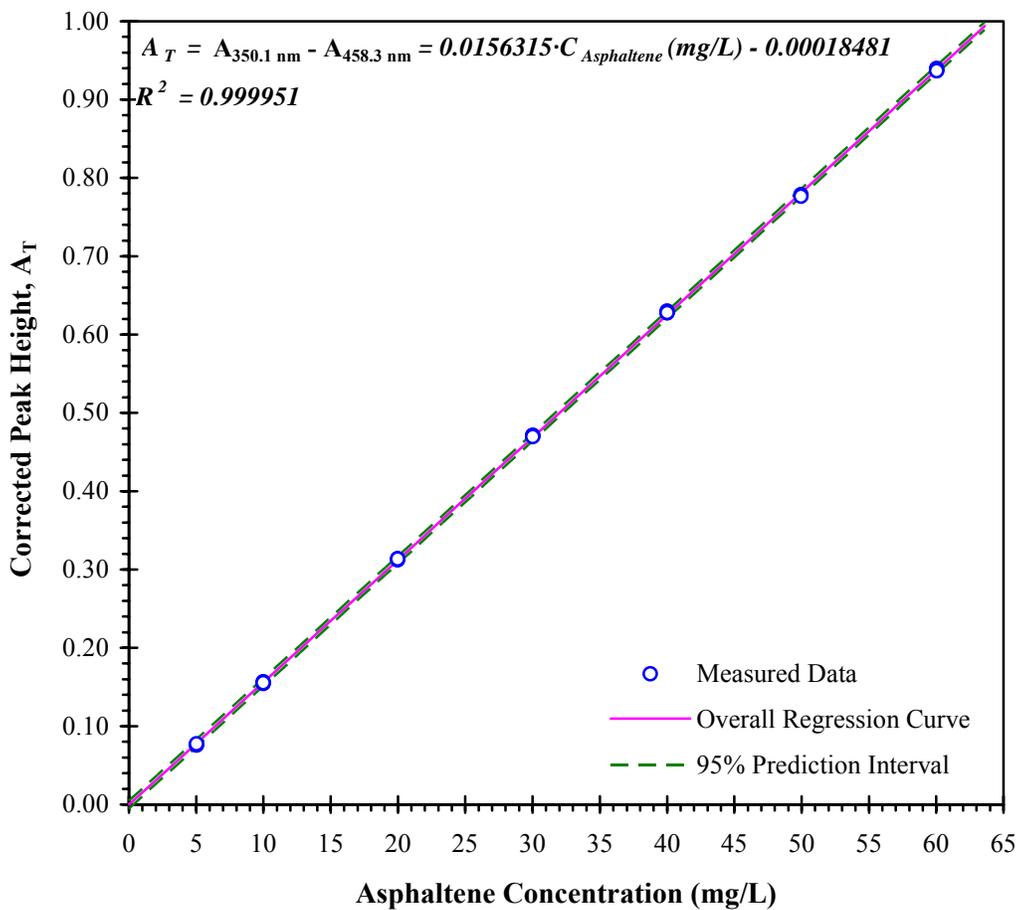
Figure C-2: Calibration curve at 350.1 nm for AA in toluene in a 10 mm cuvette e
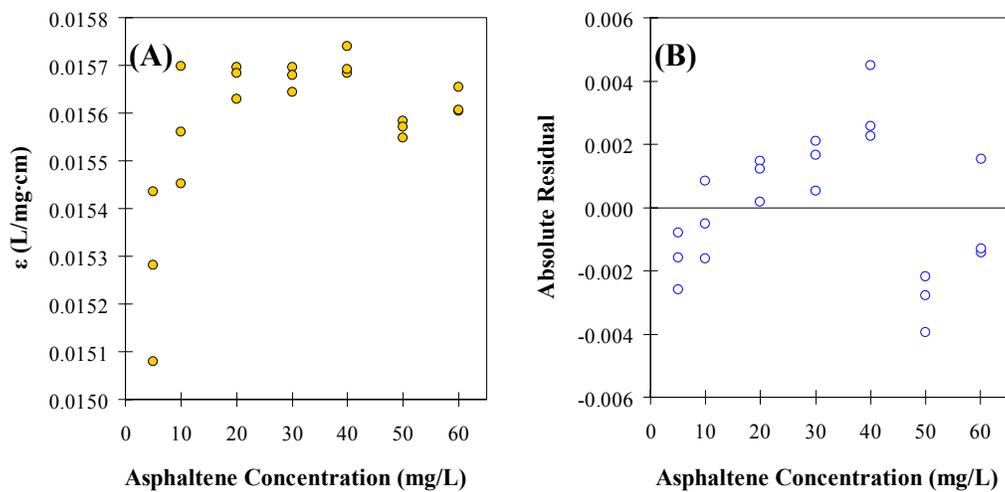

Figure C-3: A) Extinction coefficients, and B) regression residuals for the calibration curve at 350.1 nm for AA in toluene in a 10 mm cuvette

For the sake of brevity, the preceding analysis will not be repeated for each wavelength since the methods are all the same. From hereon, only the final calibration equations and some diagnostic information will be given.

Table C-3: Calibration data for AA in toluene: 10 mm Cuvette @ ambient temperature

Wavelength (nm)	Slope/Extinction Coefficient, ε (L/g·cm)	Intercept	R^2	C_{max} (mg/L)
350.1	15.63	-0.0001848	0.999951	60
500.8	5.179	-0.001479	0.999975	200
600.1	2.113	-0.003023	0.999970	600
700.6	0.8980	-0.004341	0.999958	1000
799.9	0.3587	-0.002203	0.999926	1000

Table C-4: Calibration data for AA in toluene @ 25°C: VersaProbe with 10mm Tip

Wavelength (nm)	Slope/Extinction Coefficient, ε (L/mol·cm)	Intercept	R^2	C_{max} (mg/L)
375.8	18.41	0.01687	0.999558	60
384.7	16.89	0.01133	0.999796	60
500.8	5.176	0.008757	0.999961	200
600.1	2.099	0.005939	0.999987	600
700.6	0.8874	0.001950	0.999991	1000
799.9	0.3553	0.002190	0.999945	1000

Table C-5: Calibration data for AA in toluene @ 60°C: VersaProbe with 10mm Tip

Wavelength (nm)	Slope/Extinction Coefficient, ε (L/mol·cm)	Intercept	R^2	C_{max} (mg/L)
384.7	17.11	0.003181	0.999710	60
500.8	5.212	0.003576	0.999983	200
600.1	2.101	0.002392	0.999987	600
700.6	0.8841	-0.0007846	0.999964	1000
799.9	0.3529	0.001087	0.999928	1000

C.2 - Calibration of Venezuelan Asphaltenes (VA) in Toluene

The procedures used for developing calibration curves for VA were the same as those used for AA. The resulting spectra for VA (Figure C-4) have a similar shape to those for AA and as such the wavelengths chosen for calibration, as well as the baseline correction method, are the same as for AA. The final calibration equations are listed in Table C-6.

Table C-6: Calibration data for VA in toluene: 10 mm Cuvette @ ambient temperature (23°C)

| Wavelength (nm)	Slope/Extinction Coefficient, ε (L/g·cm)	Intercept	R^2	C_{max} (µmol/L)
375.3	17.87	-0.01223	0.999662	60
384.3	16.03	-0.007688	0.999896	60
500.6	5.217	-0.003569	0.999958	200
600.1	2.333	-0.006943	0.999920	600
700.8	1.002	-0.006654	0.999941	1000
800.3	0.4062	-0.003747	0.999919	1000
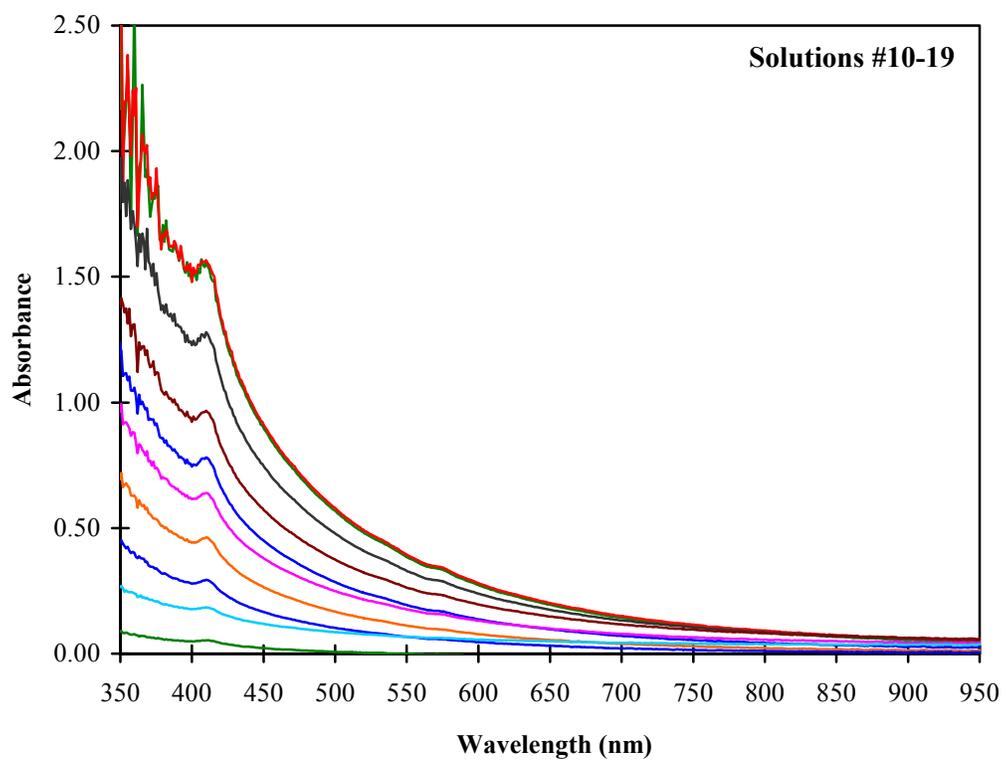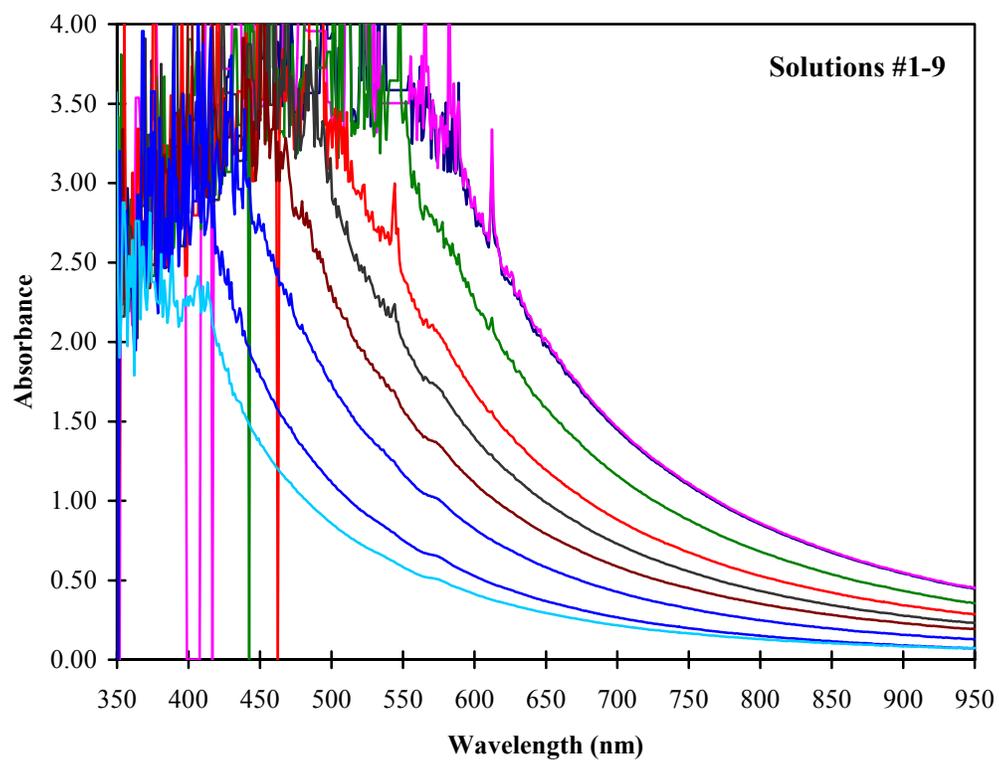
Figure C-4: Raw spectra for VA calibration solutions in 10 mm cuvette (only 1 scan of each is shown for clarity)

C.3 - Calibration of Safaniya Asphaltenes (SA) in Toluene

The procedures used for developing calibration curves for SA were the same as those used for AA. The resulting spectra for SA (Figure C-5) have a similar shape to those for AA and as such the wavelengths chosen for calibration, as well as the baseline correction method, are the same as for AA. The final calibration equations are listed in Table C-7.

Table C-7: Calibration data for SA in toluene: 10 mm Cuvette @ ambient temperature (23°C)

| Wavelength (nm)	Slope/Extinction Coefficient, ε (L/g·cm)	Intercept	R^2	C_{max} (µmol/L)
375.3	21.71	-0.01649	0.998765	60
384.3	19.42	-0.01310	0.999841	60
500.6	5.979	-0.005855	0.999930	200
600.1	2.460	-0.004026	0.999952	600
700.8	1.027	-0.004581	0.999959	1000
800.3	0.4006	-0.0009767	0.999961	1000
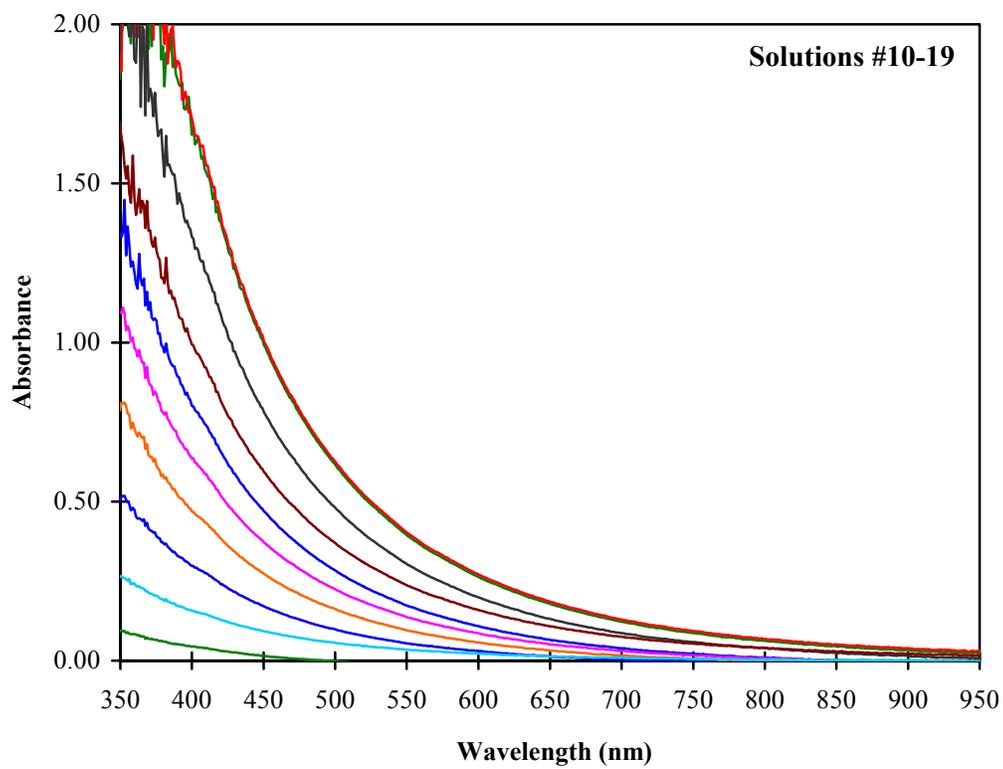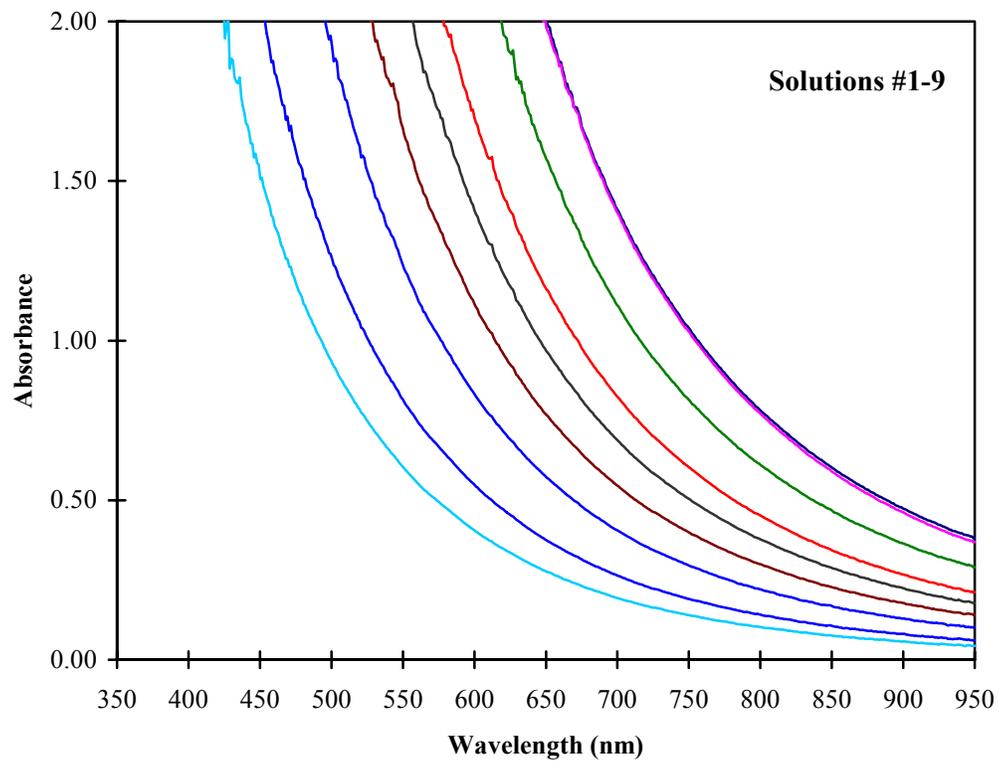
Figure C-5: Raw spectra for SA calibration solutions in 10 mm cuvette (only 1 scan of each is shown for clarity)

C.4 - Calibration of Athabasca Partially-Demetallated Asphaltenes (APDA) in Toluene

The procedures used for developing calibration curves for APDA were the same as those used for AA. The resulting spectra for APDA (Figure C-6) have a similar shape to those for AA and as such the wavelengths chosen for calibration, as well as the baseline correction method, are the same as for AA. The final calibration equations are listed in Table C-8.

Table C-8: Calibration data for APDA in toluene: 10 mm Cuvette @ ambient temperature (23°C)

| Wavelength (nm)	Slope/Extinction Coefficient, ε (L/g·cm)	Intercept	R^2	C_{max} (µmol/L)
375.3	18.00	-0.01523	0.999661	60
384.3	16.09	-0.01420	0.999677	60
500.6	5.233	-0.003652	0.999982	200
600.1	2.271	-0.004859	0.999942	600
700.8	1.004	-0.004429	0.999930	1000
800.3	0.4130	-0.001853	0.999943	1000
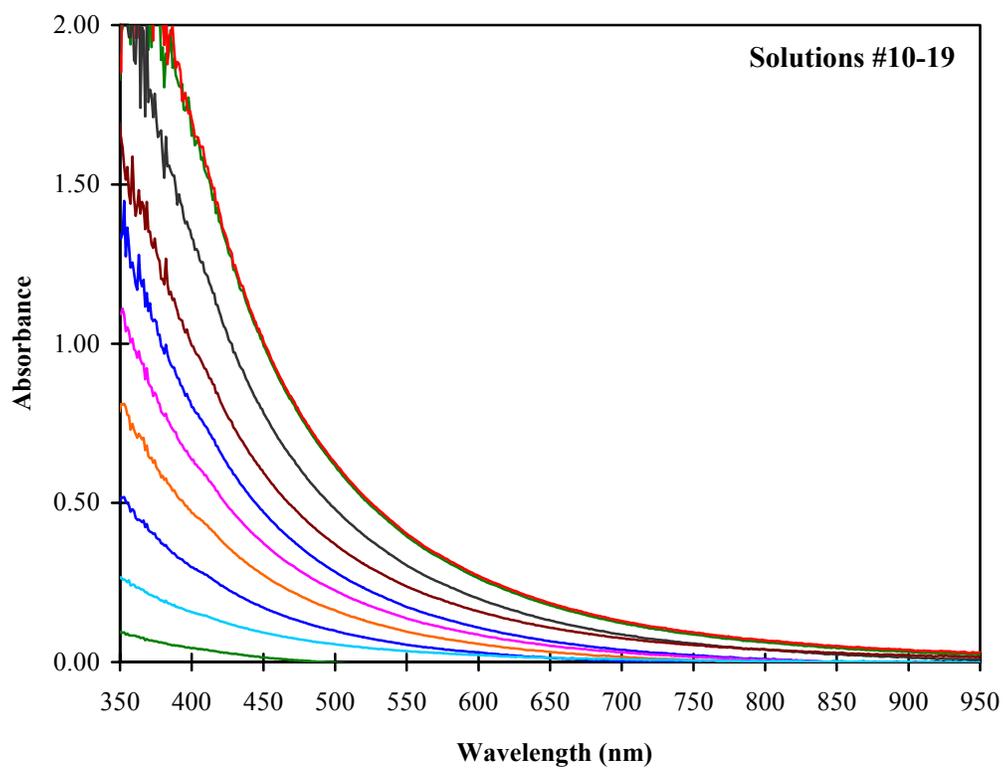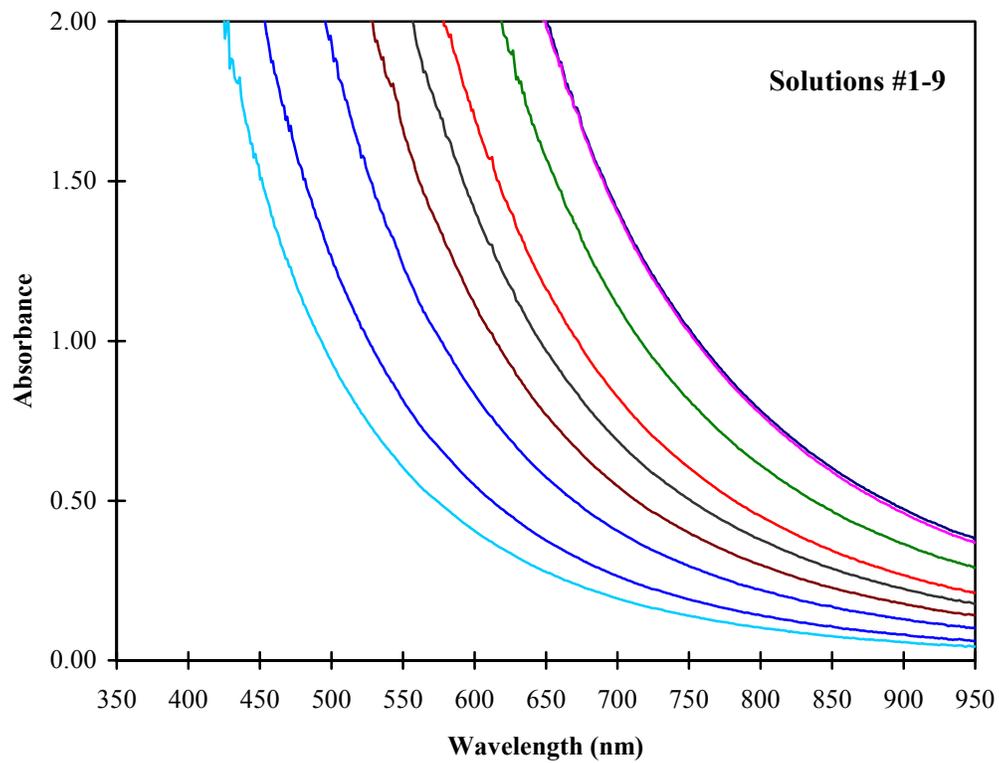
Figure C-6: Raw spectra for APDA calibration solutions in 10 mm cuvette (only 1 scan of each is shown for clarity)

Appendix **D**

Chromatographic Purification of Vanadyl Porphyrins

D.1 - Purification of VOTPP

VOTPP was purified using a Biotage SP-1 Flash chromatography unit equipped with a FLASH 25+M compression module (25 mm diameter x 150 mm long, Part# FC-022-16044). This compression module was used in conjunction with Biotage pre-made silica gel columns (FLASH 25+M KP-Sil columns, 48 mL volume, 40 g silica gel, #FPK0-1107-16016). The VOTPP solids (~700 mg) were dissolved in dichloromethane at a concentration of ~3 mg/mL. The solution was sonicated for 1 hour to fully disperse the solids. 10 FLASH 25+ KP-Sil samplets (4.8 mL, 0.9 g silica gel, Part #SAM-1107-16016) were loaded with this VOTPP/DCM solution in 4.5 mL increments. The samplet was dried under vacuum for at least 1 hour between each addition.

After extensive testing using both thin layer chromatography and small scale flash chromatography, the separation parameters and mobile phase used for this separation are summarized in Table D-1. The resulting elution curve for the first of 10 runs is shown in Figure D-1. Fractions 14-23 were collected as the VOTPP product (shaded region in Figure D-1). The remaining 9 runs were all very similar and as such are not shown here. The collected fractions were combined and the solvent removed by rotary evaporation followed by evaporation in a fume hood.

The recovered VOTPP solids (87.3% recovery) were then redissolved in DCM at a concentration of 3 mg/mL as before and loaded to another 10 samplets as before. These 10 samplets were processed using the same parameters as before (Table D-1) and the

Table D-1: Summary of instrument parameters and gradient program for flash chromatographic purification of VOTPP with flash 25+M columns

|	
Flowrate =	4 mL/min
Weak solvent =	30% n-heptane/70% P-xylene (by volume)
Strong Solvent =	Dichloromethane (DCM)
Gradient:	- Equilibrate (100% weak) for 3 CVs
	- 0% strong (100% weak) for 6 CVs
	- 0-100% strong for 2 CVs (linear)
	- 100% strong for 10 CVs
Collection:	- First 2 CVs to waste
	- Collect the rest in 24 mL (½ CV) fractions

CV = Column volume
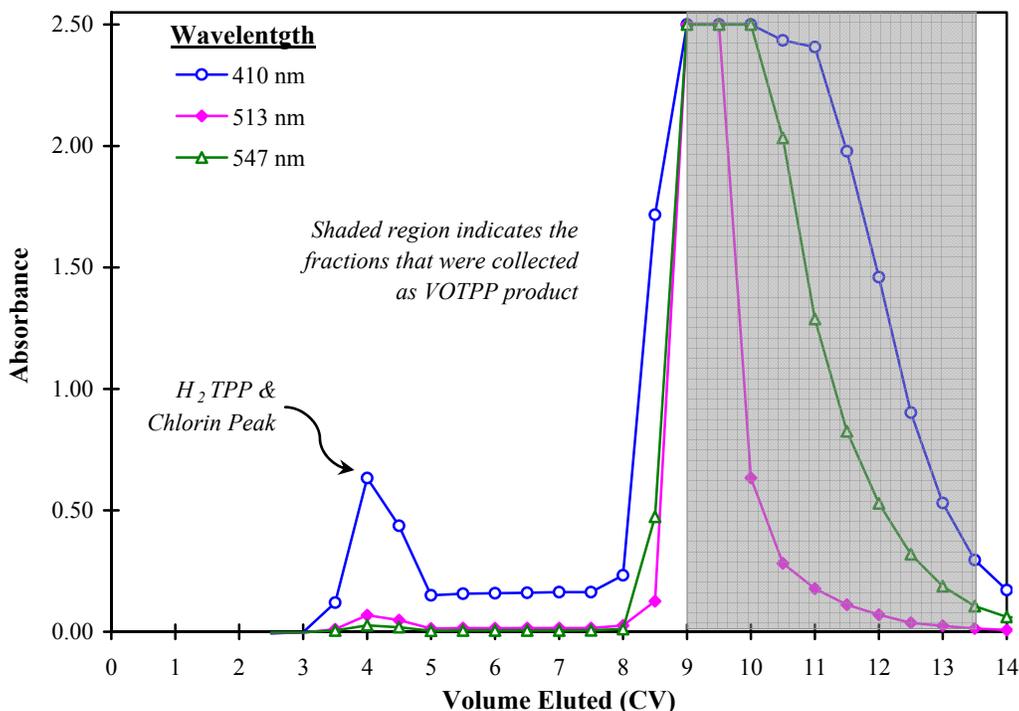
Figure D-1: Elution Curves for VOTPP Run #1 (Baseline corrected & capped peak height)

resulting elution curve for the first of 10 runs is shown in Figure D-2. Fractions 13-23 were collected as the VOTPP product (shaded region in Figure D-2). The remaining 9 runs were all very similar and as such are not shown here. The collected fractions were combined and the solvent removed by rotary evaporation followed by evaporation in a fume hood. The final recovered solids were dried under vacuum at 130°C constituting the final purified product (82.7% recovery, 572 mg total).

The final product was submitted to the Dept. of Chemistry analytical laboratory here at the U of A for purity analysis using HPLC (performed by Dr. Wayne Moffat). The HPLC is a Beckman equipped with model 1350 dual pumps, model 1305A variable wavelength UV-Vis detector, data acquisition, and the pumps are controlled using Beckman ValuChrom software. The chromatographic column is a Supelcosil LC-ABZ 150 x 4.6 mm, 5 μm particle size. The eluent is isocratically programmed at 20% methanol and 80% acetonitrile at a flow rate of 1.0 mL/min with detection at 410 nm. The injection volume is fixed at 20 μL. Using this system, the retention time for the VOTPP is 3.9 minutes and the H_2TPP is 7.4 minutes with a total run time of 10 minutes. The peaks are symmetrical and well resolved from each other. A 2-3 mg sample of
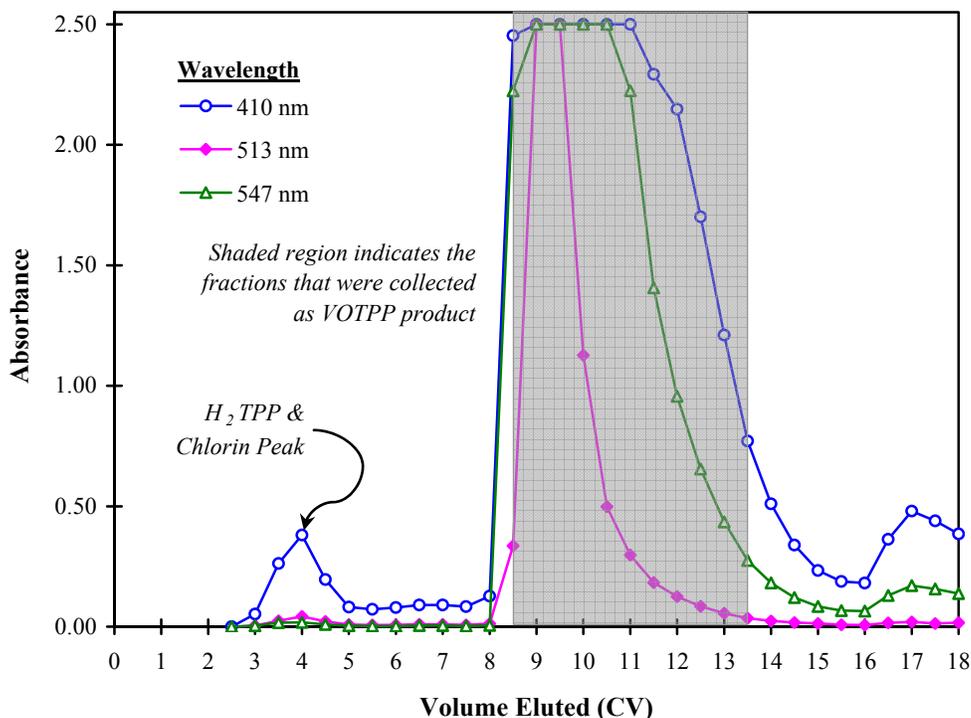
Figure D-2: Elution Curves for VOTPP Run #11 (Baseline corrected & capped peak height)

H$_2$TPP was accurately weighed to the nearest 0.0001 mg and quantitatively transferred to a 10 mL volumetric flask. The solid was completely dissolved in CHCl$_3$ and diluted to volume. Just prior to injection, an aliquot of the stock solution was diluted 100 fold using methanol. The methanol solution was immediately injected. The methanol solution was discarded after each injection and a fresh one prepared. A 2-3 mg sample of VOTPP was accurately weighted to the nearest 0.0001 mg and quantitatively transferred to a 1 ml volumetric flask. The solid was completely dissolved in CHCl$_3$ and diluted to volume. Just prior to injection, an aliquot of the stock solution was diluted 25 fold using methanol. The methanol solution was immediately injected. The methanol solution was discarded after each injection and a fresh one prepared.

The weight percent result was obtained by calculating a response factor for H$_2$TPP (area counts per mg) from the H$_2$TPP standard solution injections. That response factor was used to obtain the amount of H$_2$TPP in the VOTPP solution based on the area counts of the H$_2$TPP peak found. Knowing the weight of H$_2$TPP from the response factor calculation and the weight of VOTPP in the solution injected, the weight percent of

H_2TPP is determined by a simple ratio multiplied by 100. The final result is **0.25 ± 0.06 wt%** H_2TPP in the VOTPP product.

D.2 - Purification of VOOEP

VOOEP was also purified using the same Biotage SP-1 Flash chromatography unit. In this case, the unit was equipped with a 340g SNAP column (71 mm diameter x 168 mm long, 450 mL column volume, 340g KP-Sil 60Å, Part# FSK0-1107-0340). The VOOEP solids (~500 mg) were dissolved in dichloromethane at a concentration of ~2.6 mg/mL. The solution was sonicated for 1 hour to fully disperse the solids. This solution was loaded onto a SNAP samplet (34 g KP-Sil silica gel, 45 mL) in 45 mL increments and dried in the vacuum oven between additions.

After extensive testing using both thin layer chromatography and small scale flash chromatography, the separation parameters and mobile phase used for this separation are summarized in Table D-2. The resulting elution curve is shown in Figure D-3. Fractions 12-34 were collected as the VOOEP product (shaded cross-hatched region in Figure D-3). The collected fractions were combined and the solvent removed by rotary evaporation followed by evaporation in a fume hood.

Table D-2: Summary of instrument parameters and gradient program for flash chromatographic purification of VOOEP with a SNAP 340g column

Flowrate =	40 mL/min
Weak solvent =	n-heptane
Strong Solvent =	Dichloromethane (DCM)
Gradient:	- Equilibrate (30% strong) for 3.5 CVs
	- 30% strong for 2 CVs
	- 30-92% strong for 7 CVs (linear)
Collection:	- First 4 CVs to waste
	- Collect the rest in 48 mL fractions

CV = Column volume

The final recovered solids were dried under vacuum at 100°C constituting the final purified product (86.9% recovery, 440 mg total). In the case of VOOEP, the sample was only purified once and was not submitted for purity analysis for several reasons:

1. The VOOEP solids had a much lower concentration of impurities than did the VOTPP and therefore it should be easier to separate them.

2. The SNAP column used for the VOOEP separation is transparent and as such it was possible to monitor the separation visually through the column. The leading impurity band was visible and was seen to pass through first. As well, three impurity bands (brown, green, violet, identities unknown) were visible after the VOOEP peak and retained on the column.

3. Thin layer chromatography of the preliminary runs indicated very high purity.

For the reasons above, it is anticipated that the VOOEP product will have a comparable purity (or better) than the VOTPP product in the previous section without the need for additional analysis.
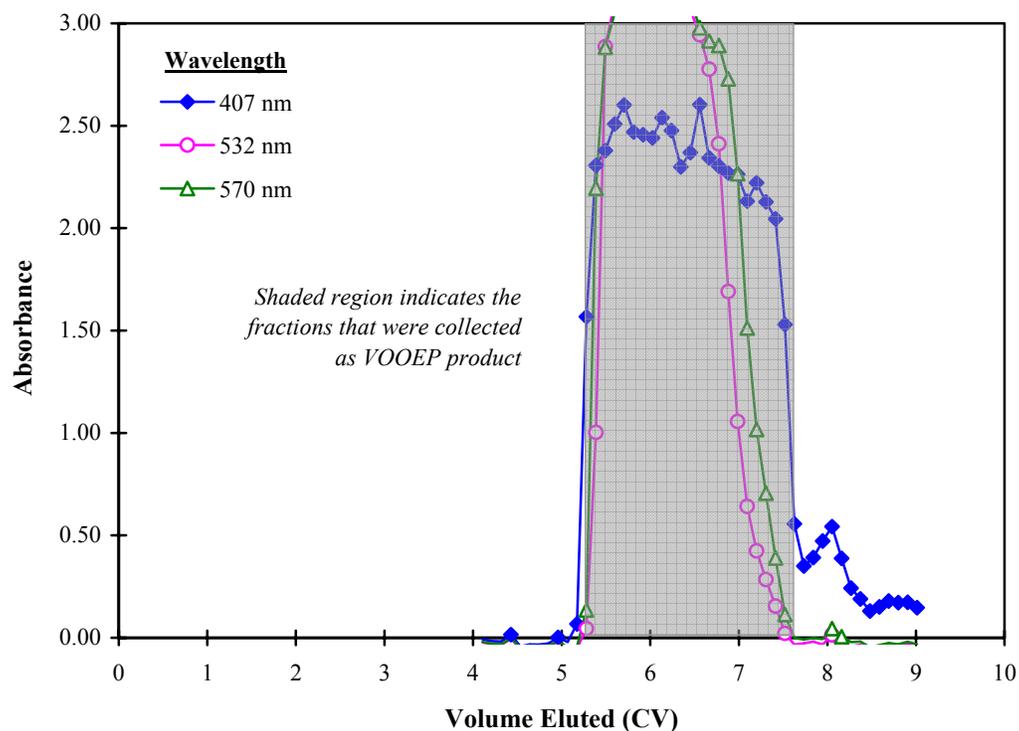

Figure D-3: Elution Curve for purification of VOOEP